TAL TECH

DOCTORAL THESIS

Dynamic Processes of Air-Water Flows in Urban Water Systems

Katrin Kaur

Dynamic Processes of Air-Water Flows in Urban Water Systems

KATRIN KAUR

TALLINN UNIVERSITY OF TECHNOLOGY
School of Engineering
Department of Civil Engineering and Architecture
This dissertation was accepted for the defence of the degree 01/11/2022

Supervisor:	Tenured Associate Professor **Janek Laanearu** School of Engineering Tallinn University of Technology Tallinn, Estonia
Co-supervisor:	Tenured Assistant Professor **Ivar Annus** School of Engineering Tallinn University of Technology Tallinn, Estonia
Opponents:	Associate Professor **Jose G. Vasconcelos** Samuel Ginn College of Engineering Department of Civil and Environmental Engineering Auburn University
	Professor **Ling Zhou** College of Water Conservancy and Hydropower Engineering Hohai University

Defence of the thesis: 09/12/2022, Tallinn

Declaration:
Hereby I declare that this doctoral thesis, my original investigation and achievement, submitted for the doctoral degree at Tallinn University of Technology has not been submitted for doctoral or equivalent academic degree.

Katrin Kaur

_____
signature

Õhu ja vee koosvoolamise dünaamilised protsessid linna veesüsteemides

KATRIN KAUR

Contents

List of Publications

The list of author's publications, on the basis of which the thesis has been prepared:

Articles in journals

I   Kaur, K.; Laanearu, J.; Annus, I. (2023). Air-Pocket Dynamics in Case of Bridging of Stratified Flow during Rapid Filling of Horizontal Pipe. *Journal of Hydraulic Engineering, 149* (1), 04022030. doi.org/10.1061/(ASCE)HY.1943-7900.0002021.

II Kaur, K.; Vassiljev, A.; Annus, I.; Kändler, N.; Roosimägi, J. (2020). Numerical investigation of the impact of irregular pipe wall build-up on velocity in the water distribution system. *Journal of Water Supply Research and Technology-Aqua, 69* (7), 647–655. doi.org/10.2166/aqua.2020.035.

III Annus, I.; Kartušinski, A.; Vassiljev, A.; Kaur, K. (2019). Numerical and Experimental Investigation on Flow Dynamics in a Pipe with an Abrupt Change in Diameter. *Journal of Fluids Engineering, 141* (10), 101301. doi.org/10.1115/1.4043233.

Articles in proceedings

IV Kaur, K.; Annus, I.; Laanearu, J. (2018). Experimental measurements of momentum changes at hydraulic jump in a transparent horizontal pipe. *13th International Conference on Pressure Surges, 2*, 925–936. BHR Group.

V   Laanearu, J.; Kaur, K. (2018). Two-phase CFD modelling of air-water flow transition in a horizontal circular pipe and comparisons with experimental results. *13th International Conference on Pressure Surges, 2*, 937–948. BHR Group.

VI Kaur, K.; Laanearu, J.; Annus, I. (2017). Numerical study of Tallinn storm-water system flooding conditions using CFD simulations of multi-phase flow in a large-scale inverted siphon. *IOP Conference Series: Materials Science and Engineering, 251*, 012128. doi.org/10.1088/1757-899X/251/1/012128.

Author's Contribution to the Publications

Contribution to the papers in this thesis are:

I   Conducting experiments and numerical simulations, analysing results, deriving, and proposing formulas, preparing manuscript. The author was the main organiser and writer of the publication.

II   Partaking in the numerical analysis, analysing results, preparing manuscript. The author was the main organiser and writer of the publication.

III Partaking in the numerical analysis, conducting the experiments and preparing the manuscript. The author was the co-author of the publication.

IV Conducting experiments and analysis, preparing manuscript. The author was the main organiser and writer of the publication and presented the results at the conference.

V   Set-up and pre-processing of the numerical model. Partaking in analysis. The author was the co-author of the publication.

VI Conducting numerical simulations and preparing manuscript. The author was the main organiser and writer of the publication and presented the results at the conference.

Introduction

Flow in the water collection and conveyance systems of the built environment is very rarely of purely one fluid. On the contrary, in most flow domains, complex combinations of liquids, gases and even solids are common. Urban water systems handle raw water, drinking water, black and grey waste water, stormwater, and effluent. While, in most conventional operational situations, the first half of this sequence can be considered a water-only flow, sanitary sewage and stormwater collection and conveyance includes gas-liquid or gas-liquid-solid interactions in separate or in combined pipelines.

It may further be stated that a stormwater system is an air-filled network which is periodically flushed with a non-stationary flow of water and other substances, resulting in complex air-water flow dynamics. Depending on boundary conditions, such as precipitation volumes, ground water level, and receiving water body level, different filling ratios, i.e. water levels relative to pipe internal diameter, in the sewers may occur. While the water levels in the pipeline are low, the air effect on the flow is negligible. However, the presence of air modifies the flow behaviour with increasing filling ratios in poorly ventilated systems. In practice, the air movement during filling can depend on factors such as manhole placement and, if the sewers are poorly ventilated, air may even become trapped.

If the pipe is filled rapidly and the flow becomes supercritical or the outflow is submerged, transitional flow, combining regimes of gravity and pressure driven flow, sometimes named mixed flow, may occur. The transitions resulting in filling ratio change can be of the surge or bore wave type. The bore wave is a free-surface flow feature characterised by a jump in water depths. If the flow in the conduit bridges, i.e. the interface of air-water flow touches the pipe obvert, the transition is classified as surge wave type, and a suppressed (mobile) hydraulic jump, that is accompanied by a pressure jump, occurs.

In addition to the pipeline failures induced by construction and employment factors such as placement, freezing or load-induced damage, malfunctioning or adversely changing operating conditions of the stormwater system are associated with pressure changes. These may be broadly separated into rapid and prolonged pressure alterations. The high and/or fast pressure peaks that have been studied thoroughly by several authors, are induced by trapped air pockets and their release, and may result in conduit failure or water bursting out of manholes. Conversely, while the transitional flow process results in a mobile hydraulic jump that entrains air into the water column, the result is a more prolonged pressure alteration, which still poses several open questions. This slower process may cause reduced capacity that induces flooding at the manholes and will last until cessation of the mixed regime, viz. until all air is entrained or the inflow is reduced.

While the slopes of a water-only network may be more freely selected, in the gravity-driven stormwater network, where multi-phase flow occurs, choosing the correct slope is of greater importance. Physical conduits may consist of undulating sections, not planned in the engineering design, but resulting from practical constraints in the construction phase. Also, as the conduits age, the shape of the inner walls may change unevenly due to corrosion, sediment build-up, and structural failures, progressing far beyond the applicability of the simple approach of increasing the roughness coefficient while conducting calculations, and potentially causing transitional flow. Currently, there are no clear criteria to predict the flow transitions via the process of the formation of a

mobile hydraulic jump in poorly ventilated closed conduits with concurrent air pocket entrapment during filling, while the air flow velocity is insignificant. It is likely that instabilities resulting from different causes, such as wall roughness, pipe slope changes and shear between air and water, combine and contribute in different proportions at different stages of the flow.

In the stormwater collectors it is necessary to consider the interactions of multiple phases while analysing the flow behaviour. In current engineering applications, these systems are mostly designed under open-channel flow approximations, necessitating a free surface, i.e. a surface only under atmospheric pressure where, contrary to an interface, any mixing between the phases is ignored. In other words, the air effect is not considered in the design. In the case of multi-phase systems, the fluids (such as air and water) are coupled not only by pressure, but also due to drag, and the flow can reveal mixed flow dynamics due to the presence of the interface and its instabilities. The engineering-oriented computational approaches have conventionally not been able to capture the complexities of the mixed flow dynamics.

Advanced numerical models are available to meet the engineering challenges in fluid dynamics associated with interfacial processes or non-uniform conduit geometries. The modelling of flows with interfaces is still an interesting field under theoretical development. The developments in Computational Fluid Dynamics (CFD) solvers have accelerated over recent decades due to advances in numerical methods and increasing capacities of computational power. In the field of civil engineering, CFD applications are more common in ventilation and air conditioning studies, assessing air quality changes due to pollutants. Numerical simulation of the urban water system components is not so common and there is a wide field of challenges that are not thoroughly met yet. While, for pipe flows, the energy loss is due to a friction factor in the hydraulic modelling, in mixed flows the turbulent viscosity becomes a relevant parameter. In the case of multi-phase flows in irregular-geometry domains, the applicability of different turbulence models and respective coefficients are not fully understood.

Novelty and Objectives

The novelty of the thesis is strongly related to the challenges of understanding non-stationary multi-phase fluid flow processes in closed conduits. It is shown that the air-water interactions are important in urban water systems and that air-water flow processes may be associated with the systems' malfunctioning during intense rain events. The dynamic behaviour of flows dominated by multi-phase processes and irregular geometries cannot be governed by hydraulic formulae and therefore advanced numerical simulations should be used to clarify the operating conditions.

Applying experimental, numerical and theoretical techniques, herein the conditions resulting in stratified flow bridging are analysed, a relationship for the speed of the resulting mobile hydraulic jump is derived, and the turbulence energy consumed in the air-water mixing process in the jump is estimated by introducing a mixing efficiency parameter for the immiscible flow. In addition, the relationship defining the mobile hydraulic jump speed allows the assessment of the air-entrainment rate and the duration of the prolonged pressure alteration caused by the presence of an air pocket. This helps to better understand the possible pluvial flood mitigation measures in urban areas.

The objectives of the thesis are:

1. Validation of the applicability of finite volume method solvers for storm sewer flow analysis.
2. Parameterisation of the mobile hydraulic jump in a closed conduit.
3. Introduction of a mixing efficiency parameter for air and water mixed flow.
4. Assessment of the causes and consequences of prolonged pressure alterations in a pipeline.

Layout of the Thesis

The thesis has been prepared based on publications I - VI, included as appendices at the end of the dissertation. The first three papers are articles in peer-reviewed journals and the latter three are peer-reviewed articles in conference proceedings. The thesis comprises three main chapters. First, in chapter 1, a framework for characterising the behaviour of flows with interfaces is overviewed and the herein derived novel relationships demonstrated. Second, in chapter 2, the numerical methodology used is outlined. Last, chapter 3 is dedicated to mixed flow case studies, complemented by investigations of geometry effects.

In the thesis, three methodologies are used:

1. Experiments have been conducted in the laboratory, to characterise the processes under interest and validate the numerical model solutions.
2. Advanced numerical modelling has been used to qualitatively and quantitatively interpret the processes and gain information on parameters that otherwise would not be available from experimental or field observations. Numerical solution results are used as input for the development of parameters and formulae.
3. A control-volume analysis is applied to characterise the process of mobile hydraulic jump advancement.

The approbation of the outcomes of the thesis has been achieved by the afore-listed publications, additional supporting papers and conference presentations included in the references at the close of this thesis.

Symbols

A	flow section of circular pipe [m²]
A_d	flow section downstream of the hydraulic jump [m²]
A_u	flow section upstream of the hydraulic jump [m²]
c_{jump}	hydraulic jump speed [m s⁻¹]
D	pipe internal diameter [m]
F	Flow number
Fr	Froude number
g	acceleration due to gravity [m s⁻²]
h	water level [m]
h_a	hydraulic depth of air [m]
h_w	hydraulic depth of water [m]
k	turbulent kinetic energy [m² s⁻²]
K_f	correction factor
n	normal vector of the free surface
p'	modified pressure [Pa]
p_d	pressure downstream of the hydraulic jump [Pa]
p_u	pressure upstream of the hydraulic jump [Pa]
Q	inflow rate [m³ s]
R_x	friction force [N]
Re	Reynolds number
Ri$_\mathbf{f}$	Flux Richardson number
t	time [s]
$\boldsymbol{U}$	flow velocity of two-phase fluid [m s⁻¹]
u_d	water velocity downstream of the hydraulic jump [m s⁻¹]
u_u	water velocity upstream of the hydraulic jump [m s⁻¹]
U_{VF}	volumetric water inflow velocity [m s⁻¹]
U_{VF1}	air-water front velocity [m s⁻¹]
U_{VF2}	water velocity in the free-surface regime [m s⁻¹]
$\boldsymbol{U_1}$	axial velocity component [m s⁻¹]
$\boldsymbol{U_3}$	vertical velocity component [m s⁻¹]
u_1	axial velocity fluctuation component [m s⁻¹]
u_3	vertical velocity fluctuation component [m s⁻¹]
x	position vector [m]
Zu	Zukoski number
α	void fraction
γ	phase-fraction
ΔQ	volumetric water flux difference [m³ s]
ε	rate of dissipation of turbulent kinetic energy [m² s⁻³]
κ	interface curvature
λ	wavelength of the water wave [m]

μ	dynamic viscosity [Pa s]
ρ	average density of the fluid within a cell [kg m^{-3}]
ρ_a	air density [kg m^{-3}]
ρ_d	air-water mixture density downstream of hydraulic jump [kg m^{-3}]
ρ_u	water density upstream of hydraulic jump [kg m^{-3}]
ρ_w	water density [kg m^{-3}]
σ	surface tension [N m^{-1}]

1 Multi-Fluid Flows

Multi-phase flow can be defined as fluid flow consisting of more than one phase or component (Brennen, 2005). A clear distinction may be made between multi-fluid (two or more different fluids) and multi-phase (same fluid in different phases) (Tryggvason et al., 2011). The form multi-phase is also used to characterise situations where several different phases – liquids, gases, solids – are flowing simultaneously, including chemically different components, e.g. oil and water in the case of liquids (Yadigaroglu & Hewitt, 2018). Within the multi-fluid flows, herein, a distinction is made between the multi-phase flow of fluids and the multi-layer flow of fluids. There are two broad options for classifying multi-fluid flows.

Firstly, they may be classified based on their mixing behaviour. For immiscible fluids, as opposed to miscible fluids, mixing occurs as long as external driving forces are present, but the fluids do not dissolve to form a homogenous substance, i.e. the process of mixing is reversible. Density, viscosity and interfacial surface tension determine the dynamics of the fluid interactions. Therefore, after cessation of the driving force, the mixture separates into the original fluids (phases) with a more-or-less sharp boundary i.e. the interface in-between, and with the placement determined by the relative density. Coincidently, in these processes of multi-phase flows of fluids, the term 'mixture' usually denotes the concurrent flow of two (or more) fluids and does not necessarily imply that these are mixed into a third homogeneous fluid (Yadigaroglu & Hewitt, 2018). The concurrent flow can be parallel (co-current), when the fluids flow in the same direction, or counter-current, when they flow in opposite directions. An additional distinction based on the flow direction distinguishes vertical, horizontal and inclined flows. This directionality is more important in the presence of large differences in the density of the fluids, when gravity plays a more significant role, such as in the case of air-water flow under atmospheric pressure (Yadigaroglu & Hewitt, 2018).

The second broad classification for multi-fluid flows is based on density difference. Flows with large density difference ($(\rho_2 - \rho_1)/\rho_2 \sim 1$, where ρ_i is the density of one fluid), cf. (Zhu & Lawrence, 2000), can often be considered as weakly coupled, or one-way-coupled. This means that the denser fluid phase affects the lighter one but there is no reverse effect. However, while the lighter fluid (e.g. air) cannot move freely because the systems are poorly ventilated, its effect will become non-negligible. Air-water and air-slurry flows are examples relevant to water collection systems. For stratified flows with small density differences ($(\rho_2 - \rho_1)/\rho_2 \ll 1$), the coupling between fluid layers may be considered strong, i.e. the flow is no less than two-way-coupled. Prevalent examples are flows with density stratification induced by salinity or temperature difference. These flows are classified as multi-layer flows of fluids.

This chapter presents a framework for characterising the behaviour of multi-phase flows of fluids under stratified and transitional conditions in the built environment. The focus herein is on special problems of internal flows, viz. mixed-flow-induced dynamics in urban water pipelines. The background is given in terms of two-phase flows of fluids, as even though sewers may experience flow regimes involving solids, imposing additional resistance, these will not cause as severe as complications in the form of pressure fluctuations and instabilities as the two-phase air-water regime does (Hamam, 1982). Furthermore, in a gravity driven urban water system, the air-water flow is the most common type of multi-fluid flow, concurrently often marked as an undesired condition in the built environment (Pothof, 2011). Notably, the amount of research into

issues of mixed flow in conduits (Leon et al., 2010; Li & McCorquodale, 1999; Politano et al., 2007; Vasconcelos et al., 2006, 2015; Vasconcelos & Wright, 2006) indicates that the occurrence of the mixed regime and multi-phase flows are largely unavoidable and should, rather, be planned-for.

1.1 Flow Regimes in Gravity Driven Urban Water Systems

Waste water and stormwater are collected in the urban environment in separate or combined pipelines. The drainage facilities, including all the sewers in the network, are designed to serve all future rainfall events that do not exceed a specified design hydrologic level (Yen, 2001). The as-designed operation of these infrastructure components is vital in terms of environment, health and property protection in the urban space.

Stormwater systems contain, in addition to pipelines, open channel structures, such as ditches. Furthermore, the conveyance pipelines are, in most cases, designed for operation in free water surface gravity flow conditions, with slopes to allow for self-cleaning velocities. The open-channel flow, e.g. flow under atmospheric pressure, can be classified according to change in flow depth with respect to time and coordinates (Chow, 1959). According to the time criterion, the flow may be steady or unsteady if the flow variables do not or do change during a set time interval, respectively. Based on the space criterion, flows in open channels can be uniform, when flow depth is the same at every section or varied otherwise. More specifically, steady uniform flow; steady gradually varied flow; steady rapidly varied flow, e.g. with a free hydraulic jump; gradually varied unsteady flow; and rapidly varied unsteady flow, e.g. with a mobile hydraulic jump, i.e. a bore wave regime may be encountered in open channels (Figure 1).
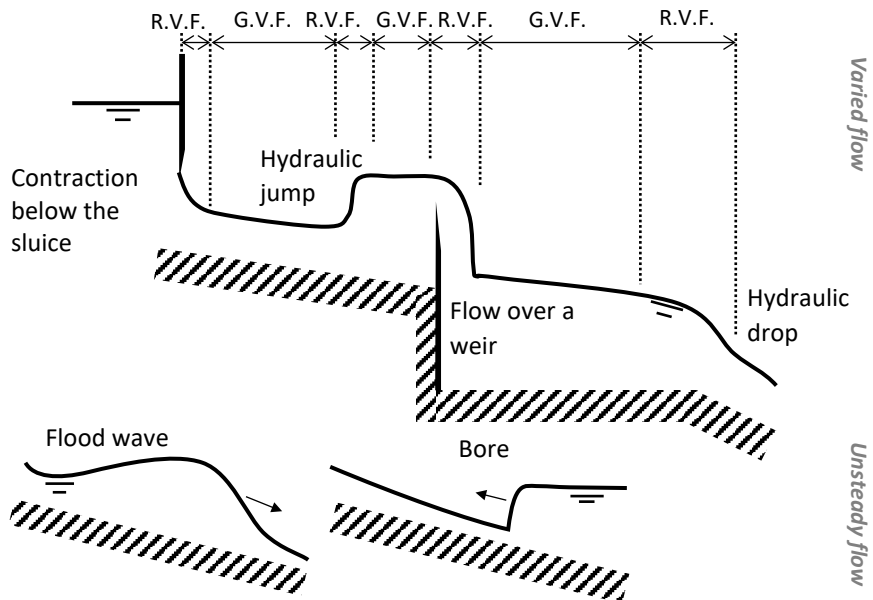
Figure 1. Types of open-channel flow. Adapted from Chow (1959). R.V.F = rapidly varied flow; G.V.F. = gradually varied flow.

The flow in stormwater pipelines can be divided into regions of entrance (inlet), pipe, and exit (outlet). Figure 2 shows the classification of nine flow cases in a pipe, combining subcritical, supercritical and surcharge conditions.

The critical flow corresponds to minimum specific energy for a given flowrate and is assessed based on the Froude number criterion (see subchapter 1.2.4).
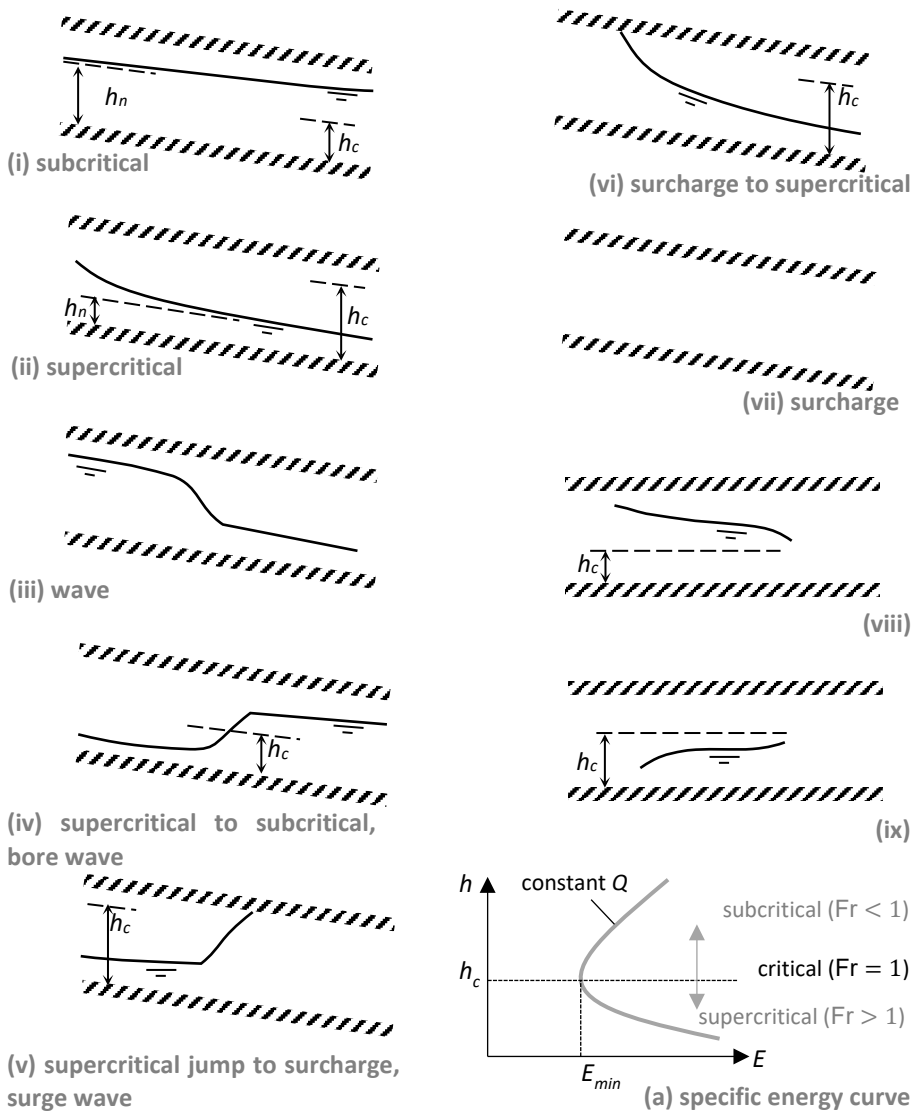
Figure 2. (i – ix) Classification of flow in sewer pipe. h_c is critical depth and h_n is normal depth. For horizontal (and adverse) slope and surcharge flow the normal depth is not defined. Extended from Yen (2001) and Chadwick et al. (2004). (a) Schema of a specific energy curve. h_c is critical depth corresponding to minimum specific energy E_{min}, for constant flowrate Q. Adapted from White (2009).

In Figure 3, case I is associated with downstream control of the pipe flow and case II with upstream control. In case III the flow under the air pocket may be subcritical, supercritical or transitional. In case IV the flow may be controlled by both upstream and downstream conditions. In case V the flow is under exit control. In case VI, under upstream control if it is supercritical, and downstream control, if supercritical. In case VII, the pipe flow is under upstream control, and junction (outlet) water surface is under downstream control. In case VIII, the flow is either under downstream control (more prevalent), or under both upstream and downstream control (Yen, 2001).

Entrance flow   *Exit flow*

(I) nonsubmerged entrance

(V) nonsubmerged entrance, free fall

(II) nonsubmerged entrance

(VI) nonsubmerged entrance, continuous

(III) submerged entrance, air pocket

(VII) nonsubmerged entrance, hydraulic jump

(IV) submerged entrance

(VIII) submerged outlet
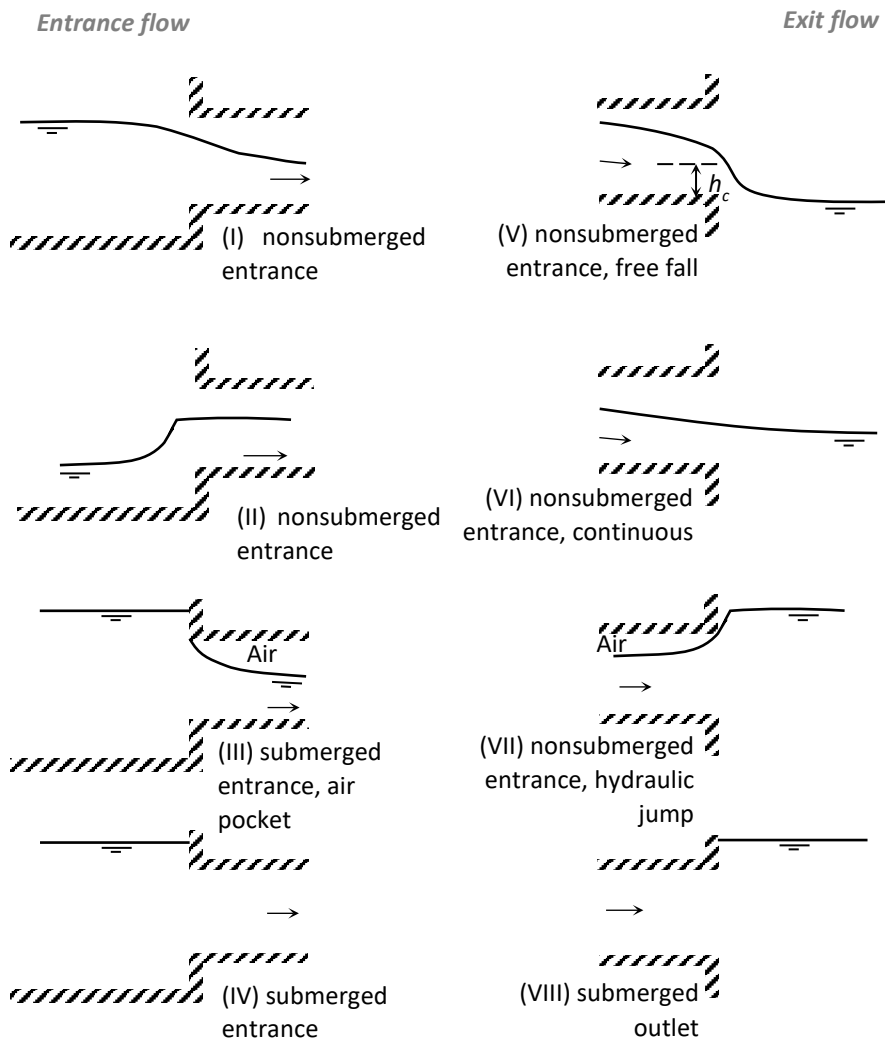
Figure 3. Pipe entrance and exit conditions. Extended from Yen (2001).

Different combinations of the entrance, pipe and exit flow are possible. For instance, the (i) subcritical flow may either develop from non-submerged entrance (I) or from submerged entrance, if the flow under the air pocket is subcritical, and exit condition is through free fall or continuously. Meanwhile, the formation of the hydraulic jump, either resulting in subcritical flow (iv) or surcharge condition (v), is possible if the entrance

condition is supercritical, i.e. case (II), or case (III) while the flow under the air pocket is supercritical. Furthermore, the abrupt flow transitions from gravity to the surcharge flow regime may occur for several reasons. For instance, the change may result from a submerged outflow, inadequate pumping capacity in the case of pumped systems, unsteady or design capacity exceeding inflows due to intense rain events, improper vertical or horizontal pipe alignment, the presence of inverted siphons, drop-pipes, and wells, and control devices such as gates (Hamam, 1982). Transitions may also be caused by pipe-wall roughness or obstructions due to changes in internal wall diameter caused by and uneven roughness build-up, for example (Laanearu & Kaur, 2018).

As a result of the transition, regimes of multi-fluid flow of fluids, viz. two-phase flow of air and water become dominant. Two-phase flow is a general term not related to any specific flow pattern. Filling experiments on a large-scale pipeline carried out by (Hou et al., 2014) confirmed that the stratified flow modifies the dynamics of two-phase flow. It was evident from the experiments that, for a comparatively large cross-sectional area pipeline filling case different fronts appear, which move with different speeds and result in stratified flow. In a comparatively small cross-sectional area pipeline filling case, only a full vertical cross-sectional water-air front is present, and no stratified flow occurs.

The closed conduit two-phase flow can be classified according to the type of developed flow patterns (Falvey, 1980). The flow patterns of a multi-phase flow can fundamentally be characterised based on the extent to which it involves separation, with disperse and separated flows at the two ends of the spectrum (Brennen, 2005). The latter consist of two or more continuous streams of fluids separated by interfaces. The stratified flow is designated as a fully separated flow with coupling between the phases. If the flow is coupled, then an interface (instead of a surface) separates the phases, and their interactions dominate the flow dynamics. Secondly, a basic characteristic for classifying flow patterns is the level of intermittency in the volume fraction (Brennen, 2005). The wavy flow and the slug flow are examples of intermittent flows. Figure 4 represents the regimes according to the flow pattern that may form in two-phase flow systems. The stratified and slug flow regimes are the most relevant in the context of stormwater systems and this thesis. A slug is a liquid blockage propagating downstream in the pipe, and its front may be approximated by a single stage hydraulic jump (Pothof, 2011; Ruder & Hanratty, 1990). Air is entrained into the slug through a hydraulic jump.
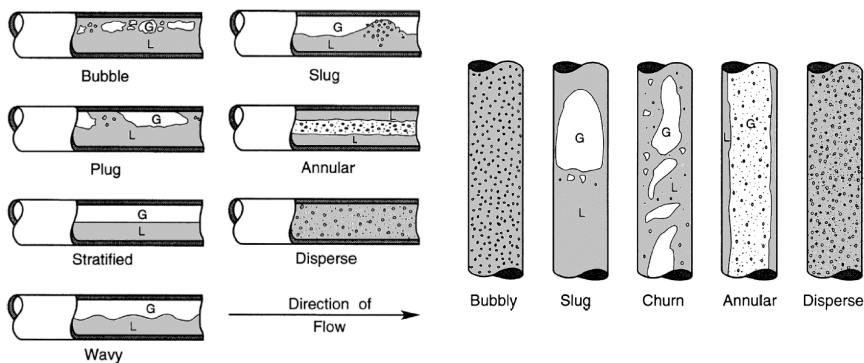
Figure 4. Possible regimes of two-phase liquid (L) gas (G) flow in horizontal and vertical pipes (Brennen, 2005).

The transition to surcharged flow can occur in the supercritical regime due to interfacial instability, and in subcritical regime due to, e.g. submerged or obstructed outflow. In either case, the flow results in a regime with both gravity and pressurised flow, denoted mixed flow (Kaur et al., 2023; Leon et al., 2010; Politano et al., 2007; Vasconcelos et al., 2006).

The transient flow that results in the change in the filling ratio can be of surge or bore wave type (Kaur et al., 2018; Wiggert, 1972). The open-channel bore (Figure 1) is a free-surface concept characterised by a jump of water depths. In (Kaur et al., 2018) the bore wave concept in analysing the transient's advancement in a closed conduit was tested for specific conditions, i.e. accounting that the water column height above the pipe invert after the jump would not exceed the obvert height. If the flow in the conduit bridges, i.e. the interface of air-water flow touches the pipe obvert, the transition is accompanied by the pressure jump and classified as surge wave type (Kaur et al., 2018). This transition is conventionally referred to as pressurisation bore, with bore standing for mobile hydraulic jump.

The mixed flow regime can be accompanied by air pocket entrapment, which in poorly ventilated conduits can result in vacuum creation (Kaur et al., 2018) or otherwise abnormal operating conditions, such as pressure peaks (Vasconcelos & Wright, 2009). Vasconcelos and Wright (2006) presented a systematic study on the filling of a horizontal pipeline, with varying ventilation configurations, inflow rates, and initial depths, and identified that the majority of cases resulted in air pocket entrapment. They detected five different mechanisms related to air pocket entrapment: inadequate amount of ventilation, misplaced ventilation, interface breakdown, shear flow instability, and gradual flow regime transition, and concluded that the entrapment depends strongly on the geometry and inflow configuration of the system.

Unexpected pressure surges in fluid pipelines may be associated with fast pressure fluctuations or prolonged pressure alterations (Kaur et al., 2023). High-pressure peaks in stormwater systems can be induced by the release of trapped air pockets, resulting in flow acceleration that may cause conduit failure or water erupting from manholes. The formation of air pockets in sewers due to bridging of stratified flow during conduit filling may be accompanied by a suppressed mobile hydraulic jump. These flow transients, which are related to changes in pipeline flow depth, will act to entrain air into the water column, resulting in a prolonged pressure change, changing the operating conditions and capacity of the system so that the flooding from the manholes will last until the air pocket collapses (Kaur et al., 2023).

While the prolonged pressure alterations still pose more open questions, the high-pressure peaks have been studied by several authors. When trapped air pockets are released, flow acceleration in the undulating pipeline can result in unexpected high-pressure peaks (Axworthy et al., 1997; Liou & Hunt, 1996). The transient motion of an individual liquid slug in a voided line and the associated pressure peaks due to impacting slugs at the elbow were experimentally and theoretically investigated by Bozkus & Wiggert (1997). If a rapidly advancing water column passes a knee point when undulating pipeline profiles are being filled, negative gauge pressures can arise (Liou & Hunt, 1996; Malekpour & Karney, 2011). This, in turn, can cause structural buckling (Chaudhry, 1979). High-pressure peaks, which are associated with rapid pipe filling accompanied by trapped air and may result in conduit failure, were observed by (F. Zhou et al., 2002) for an experimental horizontal pipeline apparatus and by (Vasconcelos et al., 2015) for an actual stormwater conduit geometry. The relation

between pressure peaks and air-water interaction during rapid air expulsion was studied in horizontal pipes by (L. Zhou et al., 2020) and vertical pipes by (L. Zhou et al., 2019).

The transition from stratified to slug flow in a closed conduit is facilitated by the pressurisation bore forming a non-stationary flow, which results in a mobile hydraulic jump. Depending on the conduit geometry, an air pocket, whose size will depend on pipe age, may become trapped. Within newer, smoother pipes, the captured air volumes are larger, while aged pipelines with rougher internal walls will trap smaller volumes due to the development of gradually varied flow (Laanearu & Kaur, 2018). The hydraulic jump will act to entrain air from the air pocket until the fully filled condition is reached or the water inflow rate reduces (Kaur et al., 2023). The air entrainment rate in mobile hydraulic jumps is influenced by parameters such as the supercritical Froude number, the ratio of the bore velocity and the supercritical velocity, and the pipe slope (Schulz et al., 2020). Concurrently, according to Schulz et al. (2020), intermediate inflow rates may result in the formation of oscillatory jumps with an undular pressurisation interface that is capable of trapping a series of air bubbles larger in comparison to the ones entrained through the jump roller. When an air pocket forms in the pipeline during filling, a volumetric water flux difference can occur between the inflow and outflow. The larger flux difference will result with the pressurisation bore velocity being considerable, accompanied by sub-atmospheric conditions in the pipeline (Kaur et al., 2023; Politano et al., 2007).

1.2 Characterisation of Two-Phase Flows

The prediction of the formation and advance of flow features, e.g. mobile hydraulic jumps, is relevant in terms of stormwater system operation, as they may be accompanied by flooding at manholes. The stability of the air-water interface in the sewer is mainly affected by the relative velocity of the two phases, the filling ratio (water level relative to pipe internal diameter), and the pipe geometry.

The mobile hydraulic jump formation is related to the stratified flow instabilities (Kaur et al., 2023). The onset of slugging in horizontal and near horizontal gas-liquid flows was studied by Wallis & Dodson (1973), who proposed a criterion for the transition from a stratified to a slug or plug flow regime in horizontal rectangular ducts in the case of airflow over a stagnant water column. Lin & Hanratty (1986) employed the viscous Kelvin-Helmholtz analysis to predict the onset of slug flow. Based on the assumption that the interface instability is formed by the air being pushed to create water waves, Li & McCorquodale (1999) proposed a normalised condition for the transition of free surface to a pressurised flow by discontinuity. They built their work on the studies carried out by Milne-Thomson (1938), who had proposed an equation for the instability condition based on the small-amplitude waves between water and air. Taitel & Dukler (1976) introduced a prediction approach to horizontal flow regime transitions in pipes. They explained the formation of slug flow by the Kelvin-Helmholtz instability changing the gas and liquid flow rates. In fact, many authors agree that the transition to slugging is due to the Kelvin-Helmholtz instability, i.e. the shear flow instability (SFI) (Kordyban, 1990). The SFI instability criterion, i.e. the stratified flow instability criterion that is related to the relative velocity between two phases has been used for pipe flow (Eldayih et al., 2020). The advancement of air cavities and long bubbles in pipes was introduced by Benjamin (1968) and Zukoski (1966). Laanearu et al. (2012) made use of the Zukoski number, which is fundamentally related to the stratified flow, to characterise the

air-cavity dynamics in the case of large-scale pipeline emptying in which no air pockets form before the air-water front reaches the pipeline outlet.

There are no clear criteria for predicting the formation of hydraulic jumps in poorly ventilated closed conduits with concurrent air pocket entrapment during filling, where the air flow velocity is insignificant. It is likely that several types of instabilities contribute, in different proportions and at different stages of the flow. Pratt (1986) described the long wave instability of the sill flows resulting from supercritical solutions in which the propagation of the perturbation signal is only possible in the downstream direction of flow. Kaur et al. (2023) proposed that the formation is related to the stratified flow instability of a long-wave type. The condition is applied based on geometrical similarity criterion.

In Kaur et al. (2023) different instability criteria were tested. The interface instability was explained through Zukoski, Froude-like, modified SFI and Froude number. The difference between the different criteria is that the Zukoski number is fundamentally related to the stratified flow, similar to the Froude-like number but, unlike the Froude number, that is only related to the water-layer flow. In the Froude-like number, the relative velocity (between air and water in the free surface regime) is normalised by the square root of gravitational acceleration times the hydraulic depth. At the same time, for the Zukoski number, the velocity of the air cavity is normalised by the square root of gravitational acceleration multiplied by the pipe diameter. For the transitional flow in a pipe the velocity in the Zukoski number is defined by the relative velocity due to the air-cavity motion inside the water column, with respect to the full-pipe flow velocity.

In the following sub-sections, the formation of the water-air front and mobile hydraulic jump is explained. Additionally, the expressions for mixing efficiency in the mobile hydraulic jump roller and the speed of the mobile hydraulic jump c_{jump} are derived. The different stages are depicted in Figure 5 and their representation is largely based on Kaur et al. (2023).
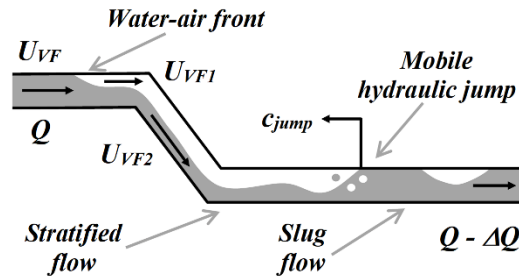
Figure 5. Transitions from fully filled pipe flow to stratified flow via water-air front, and from stratified flow to slug flow via mobile hydraulic jump – the formation of air pocket (Kaur et al., 2023).

1.2.1 Flow Number

The Flow number, sometimes also denoted as the pipe Froude number (Pothof, 2011), is associated with air cavity formation at the horizontal pipe outlet (Hager, 1999):

$$F = \frac{Q}{A\sqrt{g \cdot D}},$$ (1)

where Q is the flowrate, A is the cross-sectional area of the fully filled flow, g is the gravitational acceleration and D is the pipe's internal diameter. The Flow number criterion determines the conditions for air intrusion into the water column and the length

of the cavity at the pipe outlet. Hager (1999) mapped a range of Flow numbers for cavity formation in the horizontal pipe outlet. While there is a sufficiently abrupt slope change present in the stormwater pipeline, it may act to mimic a pipe outlet. Furthermore, if the flow preceding the slope change is fully filled, the stratified flow may occur behind the change. In the present study, the pipe bridge acts as an outlet, traps the upper water-air front at the crown and accelerates the lower water-air front flowing into the horizontal section, eventually bridging.

1.2.2 Zukoski Number

The Zukoski number represents a dimensionless speed that is related to the rate of change of the length of the water column due to the intrusion of air above the water layer (Kaur et al., 2023). In Laanearu et al. (2012) the Zukoski number was defined based on the cavity velocity. The onset of shear-flow-type instability can be characterised by the Zukoski number, as the cavity velocity is the difference between the water inflow velocity of the fully filled section U_{VF}, and the velocity of the upper water-air front at the upstream end of the cavity U_{VF1} (Figure 5). In other words, it represents the relative velocity between the phases, as the water-air front, while it moves, acts to push the upper phase above the lower. The Zukoski number is then expressed as:

$$\text{Zu} = \frac{U_{VF} - U_{VF1}}{\sqrt{g \cdot D}}, \tag{2}$$

In the case of a static water-air upstream front, the velocity U_{VF1} is zero and the Zukoski number can, therefore, be determined by the fully filled inflow velocity U_{VF}. In Kaur et al. (2023), an instability appeared at the positive slope of the pipe bridge (Figure 5). It is thought to be of a Helmholtz type, modified by the influence of the gravitational field, which is not perpendicular to the air-water interface. Zukoski (1966) found that the amplitude of Helmholtz instability in the interface also increased with increasing cavity speed. In emptying of horizontal pipes, non-steady flow emerges, if the Zukoski number is less than 0.5 (Benjamin, 1968; Zukoski, 1966). In this case, the air cavity would not propagate steadily due to the receding flow becoming critical, according to the Froude number criterion, and small disturbances originating at the downstream being able to overtake the cavity advance. Concurrently, if the upper water-air front is static, i.e. the cavity moves with an equal and opposite velocity with respect to the water column, the mobile hydraulic jump in the horizontal region downstream is likely not explained by the Zukoski number criterion. In the case where the water-air front is static and the Zukoski number is determined by the fully filled inflow rate, the Zukoski number value coincides with the value of the Flow number.

1.2.3 Modified Froude-Like Number

The Froude-like number is associated with the shear flow instability (SFI). Based on the assumption that air is pushed to create water waves and causes instability, Li & McCorquodale (1999) proposed a normalised condition for the transition of free surface to pressurised flow by discontinuity. They built on the work of Milne-Thomson (1938), who had proposed an equation for the instability condition based on the small-amplitude waves between water and air:

$$\frac{U_{VF1} + U_{VF2}}{\sqrt{g \cdot h_w}} \geq K_f \sqrt{\left(1 - \frac{\rho_a}{\rho_w}\right)\left(\frac{\rho_w}{\rho_a} \tanh\left(\frac{2\pi h_a}{\lambda}\right) + \tanh\left(\frac{2\pi h_w}{\lambda}\right)\right)} \sqrt{\frac{\lambda}{2\pi h_w}}, \tag{3}$$

A modification in which the condition is normalised based on the square root of the gravitational acceleration and the pipe diameter was proposed by Kaur et al. (2023):

$$\frac{U_{VF1} + U_{VF2}}{\sqrt{g \cdot D}} \geq K_f \sqrt{\left(1 - \frac{\rho_a}{\rho_w}\right)\left(\frac{\rho_w}{\rho_a}\tanh\left(\frac{2\pi h_a}{\lambda}\right) + \tanh\left(\frac{2\pi h_w}{\lambda}\right)\right)}\sqrt{\frac{\lambda}{2\pi D}}, \quad (4)$$

where h_w and h_a are the hydraulic depths of water and air, and ρ_w and ρ_a are the densities of water and air, respectively. If the air velocity is zero, corresponding to a static water-air interface in the pipe, then the instability condition can be determined by the water velocity in the free-surface regime U_{VF2} (see Figure 5).

The water-air front velocity U_{VF1}, the fully filled inflow velocity U_{VF} and the water velocity in the free-surface regime U_{VF2} are related through the void fraction $\alpha = 1 - \gamma$ (where γ is phase fraction, representing excess density, that describes the fraction occupied by water), which represents the effective cross-sectional area of air and is equal to unity when the cross-section contains no water (Laanearu et al., 2015):

$$U_{VF1} = \frac{U_{VF}}{\alpha} - \frac{U_{VF2}(1 - \alpha)}{\alpha} \quad (5)$$

Based on this relationship, U_{VF2}, on the left-hand-side of Eq. (4) can be expressed in terms of U_{VF} and U_{VF1}. Since U_{VF1} is assumed to be practically zero, the SFI criterion can be expressed as:

$$\frac{U_{VF}}{\sqrt{g \cdot D}} \geq K_f(1 - \alpha)\sqrt{\left(1 - \frac{\rho_a}{\rho_w}\right)\left(\frac{\rho_w}{\rho_a}\tanh\left(\frac{2\pi h_a}{\lambda}\right) + \tanh\left(\frac{2\pi h_w}{\lambda}\right)\right)}\sqrt{\frac{\lambda}{2\pi D}}, \quad (6)$$

by applying the definition of the Zukoski number. In this modified SFI criterion, λ is the wavelength of the free-surface water wave, which may vary from 20 mm (for capillary waves) to a few times the water depth. The correction factor value K_f depends on the reduction in the air flow area, and the entrance and alignment conditions. K_f value should be of the order of magnitude of 1/10 for the instability to arise according to the criterion (Eq. 6), since the criterion value herein varies in the range of 2.8–5.7 while λ varies from the capillary wavelength to a wavelength equal to the pipe diameter (Li & McCorquodale, 1999). The defined SFI criterion would be applicable to the herein described type of instability if the setup produced a significantly higher air velocity, i.e. U_{VF1} would not be negligible. As the mobile hydraulic jump in the horizontal pipe section is formed while the air velocity is nearly zero, it is not likely to be due to the presence of shear flow instability, which is parameterised with respect to the Froude-like number (and, herein, with respect to the Zukoski number). The Zukoski and Froude-like numbers are fundamentally related to the stratified flow, unlike the Froude number that is related only to the water-layer flow. Therefore, a criterion for the onset of long-wave-type instability governed by the Froude number, is presented below.

1.2.4 Froude Number

The water-layer flow regime can be sub or supercritical, according to the Froude number criterion. The Froude number is a free-surface criterion. There also exists an interfacial Froude number that employs a density difference parameter which, for air-water flows, approaches unity. The Froude number is a ratio between inertial and gravity forces that incidentally compares the flow velocity and the celerity of shallow water flow wave propagation (Schall & Richardson, 1997). The square root of gravitational acceleration, multiplied by the local water depth, gives the speed of the fastest small-amplitude water

wave. If the Froude number is less than unity, the surface waves may propagate upstream as well as downstream. When the Froude number is greater than unity, then the fluid speed exceeds the speed of the fastest waves and surface disturbances can propagate only in the downstream direction; and the flow is supercritical. The onset of long-wave-type instability during free-surface inflow, which results in the formation of a pressurisation bore, is indicated by the Froude number derived in Kaur et al. (2023) by solving for the cross-section minimum specific energy:

$$\frac{dE}{dh} = \frac{d}{dh}\left(h + \frac{Q^2}{2gA^2}\right) = 1 - \frac{Q^2}{gA^3}\frac{dA}{dh} = 0 \tag{7}$$

The area of the circular conduit flow section is expressed as follows:

$$A \approx \frac{1}{8}\pi D^2 \left[1 + \frac{2}{\pi}\sin^{-1}\left(2\frac{h}{D} - 1\right) + \frac{4}{\pi}\left(2\frac{h}{D} - 1\right)\sqrt{\frac{h}{D} - \left(\frac{h}{D}\right)^2}\right] \tag{8}$$

Taking the derivative of A, assuming A and h are positive, the resulting Froude number equation is:

$$\mathrm{Fr}^2 = \frac{Q^2}{gA^3} \cdot 2 \cdot \sqrt{h(D-h)} \tag{9}$$

1.2.5 Flux Richardson Number

The water level is increased due to long-wave instability, forming a mobile hydraulic jump that mixes the air and water phases, virtually mimicking a single-phase-like state in the roller. The mixing efficiency is introduced for coupled air-water flows to estimate the turbulence energy consumed in the air-water mixing process in the pressurisation bore (Kaur et al., 2023). In the transitional flow process, the mixing of air and water and the formation of the mobile hydraulic jump are responsible for the entrainment of air in water (the formation of air bubbles) and water in air (the formation of water droplets in air) inside the pipeline, which is quantified in the numerical model by the phase-fraction γ. In the air-water mixing flow process, such as the hydraulic jump, the kinetic energy can be converted to potential energy due to increased water level and negative buoyancy fluxes. The concept of mixing efficiency can be used to relate the amount of mixing in the stratified flow to the amount of energy available to support mixing (Davies Wykes et al., 2015). The parameter is typically used to characterise two-phase flows with a small density difference for internal hydraulic jumps (Ogden & Helfrich, 2016). However, the density variations inside the bore roller are small enough for the mixing efficiency to be applicable in a general way. As per its definition, the mixing efficiency parameter for stratified fluid dynamic processes is formulated based on the flux Richardson number. It should be noted that, in the case of temperature-stratified multi-layer flow of fluids, as the shear production is positive with the minus sign displayed, the sign of the flux Richardson number depends on the sign of the heat flux (Kundu et al., 2012). In the case of mixing air and water, the flux Richardson number can be represented as the ratio of buoyant destruction to shear production (Kundu et al., 2012). In the case of a horizontal flow with a vertical jump, the flux Richardson number takes the form:

$$\mathrm{Ri_f} \approx \frac{-g\,\gamma\,U_3}{-\overline{u_1 u_3}\,\dfrac{dU_1}{dx_3}}, \tag{10}$$

where U_1 and U_3 are the axial and vertical velocity components, respectively, and u_1 and u_3 are the respective fluctuating velocity components. It should be noted that, in the numerator of Eq. (10), the buoyant destruction is replaced with the loss to potential energy, the parameter that appears in an equation for the mean flow's kinetic energy per unit mass (Kundu et al., 2012) and, therefore, Eq. (10) is approximately equal to flux Richardson number. In the denominator of Eq. (10), the shear production term is used.

The mixing efficiency parameter can be used to assess the energy balance in the air-water concurrent flow. If the measurements demonstrate the presence of turbulent fluctuations, but at the same time the value of Ri_f is positive, then it can be concluded that the turbulence is decaying. The mixing efficiency of air-water interface roller (i.e. at bridging location) was determined based on the results of full-scale numerical modelling using the RANS equations (in Kaur et al., 2023). The maximum of the profile was located in the region in which the volume fraction gradients occurred, i.e. near the interface (Figure 6). The experiments also indicated that the fluid phases were not well mixed near the pipe obvert ($Ri_f < 0$, Figure 6). In accordance with the positive flux Richardson number, the buoyancy fluxes are suppressing the turbulence through the hydraulic jump development stage, facilitating the re-separation of the mixed phases (Kaur et al., 2023).
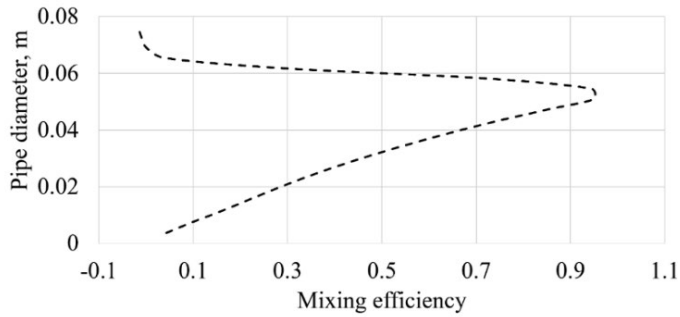
Figure 6. Mixing efficiency in the roller region of mixed flow in pipe (Kaur et al., 2023).

1.2.6 Mobile Hydraulic Jump Speed

Control volume analysis was used to characterise mobile hydraulic jump advancement in a closed conduit by Kaur et al. (2023). The stratified flow transition to slug flow was modelled within the framework of a finite control volume (CV) using the principles of conservation of mass and momentum. The aim of the integral analysis of the flow transition process was to establish a relationship for the hydraulic jump speed as a function of flow velocities, pressure jump, density jump, void fraction of the stratified flow part, and air-water mixing in the roller that merges stratified and slug flow. Figure 7 shows the hydraulic jump in a finite-size control volume.
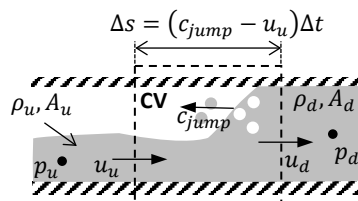
Figure 7. Diagram of hydraulic jump in Control Volume (CV).

The mass conservation of fixed-size control volume is given by the following integral equation:

$$\int\limits_{V(t)} \frac{\partial \rho}{\partial t}\, dV + \int\limits_{A(t)} \rho\, \vec{u} \cdot d\vec{A} = 0 \qquad (11)$$

The first term in Eq. (11) is the rate of change of mass within the fixed control volume V and the second is the mass flux across the bounding surface of V. In the simplified 1D CV model, the hydraulic jump can be approximated as mathematical discontinuity between two uniform flows. In reality, the uniform flow exists at some distance upstream and downstream of the jump. It is mathematically approximated that the uniform flows merge at the discontinuity. The finite-size volume mass-conservation principle that follows the air-water front's movement through the control volume is:

$$0 = \frac{(c_{jump} - u_u)\Delta t}{\Delta t}(\rho_d A_d - \rho_u A_u) + \rho_d A_d u_d - \rho_u A_u u_u, \qquad (12)$$

where $(c_{jump} - u_u)\Delta t$ corresponds to the finite length Δs of CV, c_{jump} is the mobile hydraulic jump speed, Δt is time interval, and (u_u, A_u, ρ_u) and (u_d, A_d, ρ_d) denote the water velocity, flow section area and density immediately upstream and downstream of the jump, respectively. Herein it is considered that no external forces act on the fluid discontinuity due to the gravity in the flow direction. However, an additional pressure force due to the air pressure changes is possible.

The momentum conservation of fixed-size Control Volume is given by the integral equation:

$$\int\limits_{V(t)} \frac{\partial (\rho \vec{u})}{\partial t}\, dV + \int\limits_{A(t)} \vec{u}\, \rho\, \vec{u} \cdot d\vec{A} = \sum \vec{F}_{CV} \qquad (13)$$

The first term on the left-hand-side of Eq. (13) is the rate of momentum change, the second momentum flux across the control surfaces. On the right-hand-side are the resultant forces acting on the control volume. The finite-size volume momentum-conservation principle that follows the air-water front's movement is:

$$-\Delta p A - R_x = \frac{(c_{jump} - u_u)\Delta t}{\Delta t}(\rho_d A_d u_d - \rho_u A_u u_u) + \rho_d A_d u_d{}^2 - \rho_u A_u u_u{}^2 \qquad (14)$$

On the left-hand-side of the equation are the forces acting on the control volume, viz. pressure and friction force.

From Eq. (12), a form is derived for u_u:

$$u_u = (c_{jump} - u_u)\left(\frac{A_d \rho_d}{A_u \rho_u} - 1\right) + \frac{A_d \rho_d}{A_u \rho_u} u_d \qquad (15)$$

After plugging Eq. (15) for u_u into the momentum conservation Eq. (14) and carrying out mathematical manipulation, an interim formula is achieved:

$$\left(u_d + (c_{jump} - u_u)\right)^2 = \frac{A_u \rho_u (A_u p_u - A_d p_d + R_x)}{A_d \rho_d (A_u \rho_u - A_d \rho_d)} \qquad (16)$$

where the assumption of a real solution is made. Then, the speed of the mobile hydraulic jump can be expressed as:

$$c_{jump} = (u_u - u_d) - \sqrt{\frac{A_u\rho_u(A_up_u - A_dp_d + R_x)}{A_d\rho_d(A_u\rho_u - A_d\rho_d)}}, \qquad (17)$$

It is apparent that the pressurisation bore that merges stratified flow and slug flow during the filling process of the pipeline can be characterised by the mobile hydraulic jump speed, which is essentially determined by the pressure, the cross-sectional area of water flow and density jumps. The friction force can be omitted as per the energy balance found using the mixing-efficiency parameter, $R_x \to 0$.

1.3 Summary of Findings

In this chapter, the stratified flow is parameterised. The formation of stratified flow at the pipe bridge was explained by the Flow number. To explain the instability that results in air pocket formation, different criteria were presented, i.e. the Zukoski number, modified Froude-like number and Froude number. Concurrently, the Froude-like number was modified and a Froude number equation for a circular cross-sectional pipe was derived in this thesis. Thus far, the validity of stratified flow instability criteria in closed conduits is unclear, with respect to the presence of a shear flow and a long wave, while the water-air interface at the upstream end of the air pocket is static. Based on the parameterisation via different dimensionless numbers, it is concluded that, in the case where air flow rate is negligible, the instability can be predicted based on a single-phase flow concept. In forced emptying experiments, in which air is used to expel water at high speeds, the relative velocity between the phases may become relevant and give rise to conditions related to shear flow instability.

The mixing efficiency parameter, formulated based on the Flux Richardson number, was herein introduced for air-water mixed flow conditions in conduits to explain the dissipation of turbulent energy in the transitional flow due to a suppressed hydraulic jump, which merged the stratified flow with slug flow. The energy released due to the presence of transitional flow was distributed between turbulent air-water mixing and turbulent dissipation. The mixing efficiency revealed that the energy in the roller is predominantly used by air-water mixing. This finding suggested neglecting the friction force effects when determining the speed of the mobile hydraulic jump.

The transition from stratified to slug flow was modelled within the framework of the principles of conservation of mass and momentum of a CV to determine the speed of the mobile hydraulic jump. Thus, the pressurisation bore in the pipeline filling process was characterised by the mobile hydraulic jump speed, which was essentially determined by the pressure, the cross-sectional area of water flow, and the density jumps.

2 Numerical Methods

This chapter presents the framework for numerical modelling of flows under stratified and transitional conditions in urban water systems. Numerical modelling has three broad steps: pre-processing, processing and post-processing. In the pre-processing phase, the geometry is generated and discretised, and boundary conditions and solution algorithms are chosen. In this chapter, the focus is on the brief overview of the discretisation procedure, the algorithms to solve the Navier-Stokes equation and a stability criterion. The method used for resolving the flow and the approach to turbulence modelling are introduced. Finally, the software structure is briefly touched upon together with the inputs for initialising the computational cases.

Advanced numerical modelling can be used to qualitatively and quantitatively interpret the flow processes and gain information on parameters that otherwise would not be available from experimental and field observations. Computational Fluid Dynamics (CFD) models are powerful tools that model the physical phenomena of fluid flows mathematically and solve them numerically. For the purpose of resolving multi-phase flows, several numerical methods have been developed, such as Marker-and-Cell (Harlow & Welch, 1965), Level set (Sussman et al., 1994) and Volume-of-Fluid (Hirt & Nichols, 1981). These methods are able to accurately capture most of the physics of the flows, while the solution grid is chosen with a suitable resolution.

In recent decades, stratified flows have been increasingly modelled with CFD codes (Höhne & Vallée, 2010). One of the first attempts to simulate mixed flows was presented by Černe et al. (2001). They combined the approaches of the VOF method with a two-fluid model. The slugging phenomena in horizontal conduits was studied by Issa & Kempf (2003), who presented an approach for characterising slug flow behaviour in pipelines for gas-liquid flows. A standard k-ε turbulence model with wall functions was applied in their simulations. It was shown by Frank (2003) that the formation of the slug flow regime in horizontal pipes strongly depends on the wall friction of the liquid phase. Additionally, in simulations using specific inlet boundary conditions, it was found that the formation of slug flow regimes strongly depends on the perturbations on the inlet boundary. Ghorai & Nigam (2006) proposed and validated the concept of interfacial roughness to account for gas-liquid interactions in their numerical study. L. Zhou et al. (2018) applied the VOF CFD approach to simulate pressure oscillations in air-water flow and provide insight into the mechanism of rapid filling in closed conduits. Air pocket formation associated with rapid filling conduits and the concurrent arrival of pressure fronts was also studied by Eldayih et al. (2020). The cited list of numerical studies is by no means conclusive; however, it clearly shows the wide applicability of CFD models to immiscible two-phase flow problems.

The CFD models can be classified based on the approach they take in discretisation. Finite Volume Method, Finite Element Method and Finite Difference Method are some of the widely used techniques. In this thesis, the OpenFOAM software (ESI Group, n.d.), employing the Finite Volume Method (FVM), is used. The FVM transforms a set of partial differential equations that represent conservation laws over differential volumes into a system of discrete algebraic equations over finite volumes through a distinctive two-step discretisation process (Moukalled et al., 2016). Solvers interFoam, multiphaseInterFoam and simpleFoam were used for the analyses presented.

CFD models solve conservation equations for mass and momentum. When the flow is turbulent and/or more than one phase is present in the solution domain, additional

transport equations need to be solved for scalar quantities. In addition to conservation principles, constitutive assumptions are also needed to solve the fluid flow. Herein, the assumption was made that the fluids are Newtonian, immiscible, incompressible and isothermal. Specifically, the air and water (and denser slurry-fluid) were modelled as immiscible liquids, defining their viscosity, density and surface tension force.

2.1 Navier-Stokes Equations

According to the principle of conservation of mass, a region will conserve its mass on a local level, in the absence of mass sources and sinks (Bird et al., 2002; Moukalled et al., 2016). The flux form of mass conservation can be written as:

$$\frac{\partial \rho}{\partial t} + \nabla \cdot [\rho \mathbf{u}] = 0 \tag{18}$$

In the absence of significant pressure and temperature changes the flow can be assumed to be incompressible, i.e. ρ does not change with the flow, which is mathematically expressed as $D\rho/Dt = 0$. This is equivalent to $\nabla \cdot \mathbf{u} = 0$. The integral form $\int_S (\mathbf{u} \cdot \mathbf{n}) dS = 0$ of the continuity equation for incompressible flows demonstrates the treatment more clearly in terms of the finite volume method, as $D\rho/Dt = 0$ does not imply that density is the same everywhere, but that the net flow across any control volume is zero (Moukalled et al., 2016).

According to the principle of momentum-conservation, the rate of change of fluid momentum in the fixed volume is the difference in momentum flux across its boundary plus the net force, comprising total body and surface forces, acting on the volume. The conservative form of the momentum equation can be written as:

$$\frac{\partial}{\partial t}[\rho \mathbf{u}] + \nabla \cdot \{\rho \mathbf{u}\mathbf{u}\} = -\nabla p + \nabla \cdot \{\mu[\nabla \mathbf{u} + (\nabla \mathbf{u})^T]\} + \mathbf{f}_b \tag{19}$$

where $\rho \mathbf{u}\mathbf{u}$, enclosed in curly brackets, is the dyadic product, which is a special case of a tensor product with its divergence being a vector (Moukalled et al., 2016); p is pressure, μ is dynamic viscosity and $\mathbf{f}_b$ are body forces. Eq. (19) is the momentum equation for incompressible flows. An additional term $(\nabla(\lambda \nabla \cdot \mathbf{u})$ of the stress tensor on the right-hand-side of the equation would be needed to represent compressibility.

For incompressible flows, the continuity equation ($\nabla \cdot \mathbf{u} = 0$) is a restriction on the computed momentum field and there is no equation for pressure. This is known as the pressure-velocity coupling problem. Two basic steps are used to solve the Navier-Stokes equations in numerical approaches. First, an equation is derived for pressure from the momentum and continuity equations. Second, a corrector equation is derived for the velocity field computed from the momentum equation, so that it satisfies the continuity equation. The momentum equation can be expressed in general matrix form:

$$\mathbf{M}\mathbf{u} = -\nabla p \tag{20}$$

where $\mathbf{u}$ and p are the unknown fields and $\mathbf{M}$ is the matrix of coefficients that can be derived by decomposing differential terms in the momentum equation using the finite volume method, for example. This equation is also called the semi-discretised form of the momentum equation. For the x component the equation is:

$$\begin{pmatrix} M_{1,1} & M_{1,2} & \cdots & M_{1,n} \\ M_{2,1} & M_{2,2} & \cdots & M_{2,n} \\ \vdots & \vdots & \vdots & \vdots \\ M_{n,1} & M_{n,2} & \cdots & M_{n,n} \end{pmatrix} \begin{pmatrix} u_1 \\ u_2 \\ \vdots \\ u_n \end{pmatrix} = \begin{pmatrix} (\partial p/\partial x)_1 \\ (\partial p/\partial x)_2 \\ \vdots \\ (\partial p/\partial x)_n \end{pmatrix} \tag{21}$$

There are n equations, corresponding to each cell centroid in the computational mesh. The coefficients $M_{i,j}$ in the matrix are all known. The matrix of coefficients is then separated into diagonal ($\mathbf{A}$) and off diagonal ($\mathbf{H}$) components:

$$\mathbf{A}\mathbf{u} - \mathbf{H} = -\nabla p \qquad (22)$$

The division is carried out because the diagonal matrix is easier to invert. The invert of diagonal matrix $\mathbf{A}$ is:

$$\mathbf{A}^{-1} = \begin{pmatrix} \dfrac{1}{A_{1,1}} & 0 & \dots & 0 \\ 0 & \dfrac{1}{A_{2,2}} & \dots & 0 \\ \vdots & \vdots & \vdots & \vdots \\ 0 & 0 & \dots & \dfrac{1}{A_{n,n}} \end{pmatrix} \qquad (23)$$

The matrix $\mathbf{H}$ is explicitly evaluated from the off-diagonal terms and the velocity from previous iterations and is, therefore, known:

$$\mathbf{H} = \mathbf{A}\mathbf{u} - \mathbf{M}\mathbf{u} \qquad (24)$$

Rearranging the decomposed momentum equation, (Eq. (22)) for the velocity field:

$$\mathbf{u} = \mathbf{A}^{-1}\mathbf{H} - \mathbf{A}^{-1}\nabla p \qquad (25)$$

and by substituting it into the continuity equation, Poisson equation for pressure is obtained:

$$\nabla \cdot (\mathbf{A}^{-1}\nabla p) = \nabla \cdot (\mathbf{A}^{-1}\mathbf{H}) \qquad (26)$$

In computational approaches, the explicit scheme finds a solution using an iterative procedure, where the updated variable is calculated in terms of values from the previous time step. The implicit and semi-implicit schemes make use of the values from the previous and new time steps.

For solving the obtained equations, there are several options. SIMPLE, PISO and PIMPLE algorithms are introduced as they pertain to the thesis.

2.1.1 Solution Algorithms

Caretto et al. (1973) proposed the Semi-Implicit Method for Pressure Linked Equations (SIMPLE) algorithm. SIMPLE is a pressure-based algorithm, as the Poisson equation for pressure is solved. The solution process starts by solving the discretised momentum equation for the intermediate velocity field, based on set boundary conditions (Ferziger & Peric, 2002; OpenFOAMWiki, n.d.; Wimhurst, n.d.). This velocity field does not satisfy the continuity equation. Then, the Poisson equation for the pressure field (Eq. (26)) is solved (and under-relaxation is applied), which is used to correct the velocity field, Eq. (25), so that it satisfies the continuity equation. As a result, the velocity field does not satisfy the momentum equation and the cycle is repeated until a convergence criterion is met.

The turbulence scalar (k, ε, ω) and species transport equations, such as the volume fraction indicator γ, are solved within the loop after the volume flux corrector. The scalar transport equations for turbulent kinetic energy and dissipation are:

$$\mathbf{M}_k k = S_k \qquad (27)$$

$$\mathbf{M}_\varepsilon \varepsilon = S_\varepsilon \qquad (28)$$

These are used to update the kinematic eddy viscosity, which is passed back to the momentum equation for the next loop. An example loop is then:

$$\mathbf{Mu} = -\nabla p$$

$$\mathbf{H} = \mathbf{Au} - \mathbf{Mu}$$

$$\nabla \cdot (\mathbf{A}^{-1}\nabla p) = \nabla \cdot (\mathbf{A}^{-1}\mathbf{H})$$

$$\mathbf{u} = \mathbf{A}^{-1}\mathbf{H} - \mathbf{A}^{-1}\nabla p$$

$$\mathbf{M}_k k = S_k$$

$$\mathbf{M}_\varepsilon \varepsilon = S_\varepsilon$$

where S_k and S_ε are source terms for turbulent kinetic energy and dissipation.

The Pressure-Implicit Split-Operator (PISO) algorithm (Issa, 1986) uses the flux-corrector $\mathbf{u}$ to update $\mathbf{H}$ directly and, hence, the momentum predictor is solved once:

$$\mathbf{Mu} = -\nabla p$$

An inner loop is then performed until the pressure equation convergence is achieved:

$$\mathbf{H} = \mathbf{Au} - \mathbf{Mu}$$

$$\nabla \cdot (\mathbf{A}^{-1}\nabla p) = \nabla \cdot (\mathbf{A}^{-1}\mathbf{H})$$

$$\mathbf{u} = \mathbf{A}^{-1}\mathbf{H} - \mathbf{A}^{-1}\nabla p$$

PISO and SIMPLE algorithm solution loops are combined in the PIMPLE algorithm, which is suitable for larger time steps and allows partial convergence of time steps, allowing the Courant number to be extended.

2.1.2 Stability Criterion

The Courant number (*Co*) of the Courant–Friedrichs–Lewy (CFL) condition (Courant et al., 1928) is important for any non-stationary CFD solution. For some codes, the adjustable time-stepping approach is based on the Courant number.

Over a time step Δt the flow is going to move a distance $\mathbf{u}\,\Delta t$ (see Figure 10). Simply put, the Courant number is the ratio between the two lengths Δx and $\mathbf{u}\,\Delta t$ (the distance the flow travels, divided by the length of the 1D cell Δx). In other words, it is the fraction of the cell that the flow moves across within a time step.
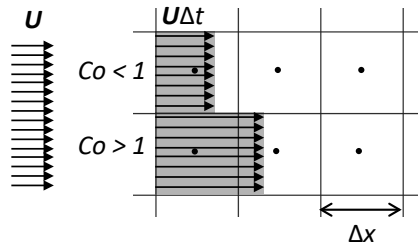
Figure 8. Schematic visualisation of the significance of the CFL stability criteria.

The definition for the CFL criterion in OpenFOAM is general and can account for different shape cells. It is set up by defining the distance across the cell Δx as a cell volume V_p divided by total surface area A_f. Furthermore, the total surface area is made up of the face areas constituting the cell. This approach is valid for any shape and size of cell. Next, the velocity normal to the face is of interest (see Figure 11). Within a given time step, the flow will travel across the shaded portion of the cell towards the cell centroid.

Figure 9. The face normal of a cell is oriented towards the cell centre.

The velocity normal to the face is the dot product between face velocity and the unit normal vector pointing towards the centroid of the cell $\mathbf{u}_f \cdot \mathbf{n}_f$. The Co number is defined as:

$$Co = \sum_{Faces} (\mathbf{u}_f \cdot \mathbf{n}_f) \, \Delta t \, \frac{A_f}{V_p} \qquad (29)$$

The problem with this definition, however, is that the total volume flux across the faces of the cell is zero, due to the conservation of mass, i.e.:

$$\sum_{Faces} (\mathbf{u}_f \cdot \mathbf{n}_f) \, A_f = 0 \qquad (30)$$

Therefore, this definition results in $Co = 0$. To resolve this in CFD, instead of taking the velocity component normal to the face, the magnitude of this term is used. This reverses the flux on half of the faces. Because half of the flux is reversed, a factor of half $(1/2)$ also needs to be introduced. Then, the complete definition of Courant number for arbitrarily shaped cells in 3D is:

$$Co = \frac{1}{2} \, \Delta t \, \frac{\sum_f |\mathbf{u}_f \cdot \mathbf{n}_f| A_f}{V_p} \qquad (31)$$

Every cell in the mesh has a different Courant number, hence it is a field. Broadly speaking, the Courant number is larger were there are large velocities and small cells. CFD solvers will use the maximum Courant number for evaluating stability criteria for the flow field and time step adjustment. Mostly the maximum Co number should be kept below 1, however, this depends on the actual problem under consideration.

In practice, the maximum Co number restricts the time step which can be set for the simulation, as the mesh is set before the simulation and the velocity is resolved during the simulation. If the simulation results in a Co number larger than 1, then the solution is to reduce the time step. For adjustable time stepping, an initial time step is chosen and a limiting value is set for the Co number. The CFD solver then computes the flow field and, after that, the Courant number field; it then evaluates it against the set maximum Courant number. If $Co > Co_{max}$ the time step will be reduced for the next iteration.

For multi-phase flow simulations with the VOF method, the interface Courant number is also tracked separately. Ideally, an upper limit of $Co \approx 0.5$ should not be exceeded in the region of the interface. In some cases, where the propagation velocity is easy to predict, the user should specify a fixed time-step to satisfy the Co criterion. For more complex cases, this is considerably more difficult. Therefore, the automatic adjustment of the time step is often used.

2.2 Volume-of-Fluid Method

In the Volume-of-Fluid (VOF) based method (Bombardelli et al., 2001; Hirt & Nichols, 1981), a transport equation is solved for the fraction of the cell occupied by the liquid phase, the phase fraction indicator function. The transport equations for continuity (Eq. (32)) and momentum (Eq. (33)), where the two immiscible fluids are considered as a single joint fluid through the domain, are:

$$\nabla \cdot \mathbf{u} = 0, \tag{32}$$

$$\frac{\partial}{\partial t}[\rho \mathbf{u}] + \nabla \cdot \{\rho \mathbf{u} \mathbf{u}\} - \nabla \cdot \{\mu \nabla \mathbf{u}\} - \{\nabla \mathbf{u}\} \cdot \nabla \mu = -\nabla p^* - \mathbf{g} \cdot \mathbf{x} \nabla \rho + \sigma \kappa \nabla \gamma, \tag{33}$$

where $\mathbf{u}$ = velocity vector of the two-phase fluid, $\mathbf{u} = \gamma \mathbf{u}_l + (1 - \gamma)\mathbf{u}_g$; ρ = average density of the fluid within a cell, $\rho = \gamma \rho_l + (1 - \gamma) \rho_g$; t = time; μ = average dynamic molecular viscosity, $\mu = \gamma \mu_l + (1 - \gamma) \mu_g$; p^* = pressure, modified to exclude the hydrostatic contribution; $\mathbf{g} = (0, 0, -g)$, where g is acceleration due to gravity, $\mathbf{x}$ = position vector; σ = surface tension; and κ = interface curvature, $\kappa = \nabla \cdot \mathbf{n}$, where $\mathbf{n} = -\nabla \gamma / |\nabla \gamma|$. Subscripts l and g correspond to liquid and gas, respectively.

To define the portion of the cell occupied by the fluid, the phase-fraction γ is used as an indicator function. The transport of γ is expressed by an advection function: $\partial \gamma / \partial t + \nabla \cdot [\gamma \mathbf{u}] = 0$. The phase-fraction γ, representing the excess density, can take values within the range $0 \leq \gamma \leq 1$, with values 0 and 1 corresponding to regions entirely of air and water, respectively. To provide a sharper interface resolution, especially for large density difference two-phase flows, Weller (2005) introduced an extra term of artificial compression in the phase-fraction equation, and so the transport equation takes the form:

$$\frac{\partial \gamma}{\partial t} + \nabla \cdot [\gamma \mathbf{u}] + \nabla \cdot [\gamma(1 - \gamma)\mathbf{u}_r] = 0, \tag{34}$$

where $\mathbf{u}_r$ = velocity field to compress the interface, $\mathbf{u}_r = \mathbf{u}_l - \mathbf{u}_g$.

For the solution of the indicator function, the Multi-Dimensional Universal Limiter for Explicit Solution (MULES) method, developed for OpenFOAM and based on the Flux Corrected Transport technique (Boris & Book, 1973), is used to maintain boundedness of the phase fraction, independent of the underlying numerical scheme, mesh structure, etc.

2.3 Turbulence Modelling

In engineering practice, most flows of interest are turbulent in nature. From a modelling point of view, approaches to predicting turbulent flows can broadly be classified into six categories, four of which, with the specific models exemplified, are represented on Figure 12.

In more general terms the six categories are (Bardina et al., 1980; Ferziger & Peric, 2002):

1. Correlations, applicable to simple flows and characterisable by just a few parameters.
2. Integral equations, derived from the equations of motion by integrating over one or more coordinates.
3. One-point closure approach that leads to Reynolds averaged Navier-Stokes (RANS) equations. This method is based on equations obtained by averaging the equations of motion over time (if the flow is statistically steady), over a coordinate in which

the mean flow does not vary, or over an ensemble of realisations (an imagined set of flows in which all controllable factors are kept fixed).

4. Two-point closure that employs equations for the correlation of the velocity components at two distinct points, or the Fourier transform of these equations.
5. Large eddy simulation (LES) that solves the largest scale motions of the flow while modelling only the small-scale motions.
6. Direct numerical simulation (DNS) where the Navier-Stokes equations are solved for all motions in the turbulent flow.
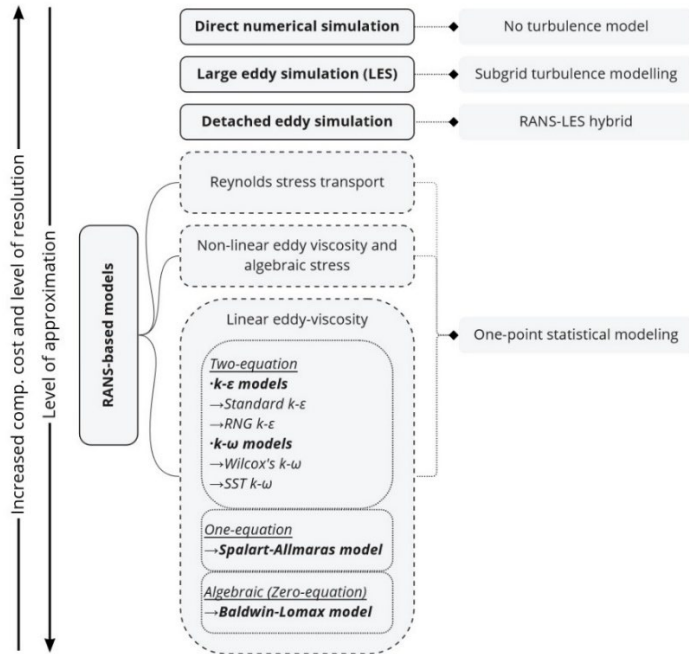
Figure 10. A Schematic overview of turbulence modelling, with a selection of existing specific models listed. Adapted from Andersson (2012).

The Reynolds-Averaged Navier-Stokes (RANS) approach, which requires a solution to the Reynolds stress term, is one of the most widely used methods for turbulent flows. A number of different turbulence models are available for modelling the Reynolds stress term. Two-equation models that simulate the eddy viscosity via turbulent kinetic energy production and dissipation (Launder & Spalding, 1974; Shih et al., 1996) are commonly used. The incompressible RANS equations are based on time-averaged variables and are derived by starting with the Reynolds decomposition, i.e. decomposing the fields into mean and fluctuating parts (see Figure 13).

Decomposing the velocity and pressure fields:

$$\mathbf{u} = \bar{\mathbf{u}} + \mathbf{u}' \tag{35}$$
$$p = \bar{p} + p' \tag{36}$$
$$\bar{\mathbf{u}} = \bar{u}\mathbf{i} + \bar{v}\mathbf{j} + \bar{w}\mathbf{k} \tag{37}$$
$$\mathbf{u}' = u'\mathbf{i} + v'\mathbf{j} + w'\mathbf{k} \tag{38}$$

and by substituting the decomposed expressions in the incompressible continuity and momentum equations (assuming a Newtonian fluid) and taking the time average, the result is:

$$\overline{\nabla \cdot [\rho(\overline{\mathbf{u}} + \mathbf{u}')]} = 0 \qquad (39)$$

and

$$\overline{\frac{\partial}{\partial t}[\rho(\overline{\mathbf{u}} + \mathbf{u}')] + \nabla \cdot \{\rho(\overline{\mathbf{u}} + \mathbf{u}')(\overline{\mathbf{u}} + \mathbf{u}')\} =} $$
$$= -\nabla(\overline{p} + p') + \nabla \cdot \left\{ \mu \left[\nabla(\overline{\mathbf{u}} + \mathbf{u}') + \left(\nabla(\overline{\mathbf{u}} + \mathbf{u}')\right)^T \right] \right\} + \mathbf{f}_b \qquad (40)$$
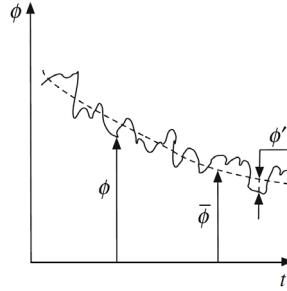
Figure 11. Schematic representation of the mean and fluctuating parts of the flow (Moukalled et al., 2016).

If ϕ and φ are two variables and $\phi'$and φ' are their respective fluctuating components, then the relevant averaging rules are the following:

$$\overline{\phi'} = 0 \qquad (41)$$
$$\overline{\phi} = \overline{\overline{\phi}} \qquad (42)$$
$$\overline{\nabla\phi} = \nabla\overline{\phi} \qquad (43)$$
$$\overline{\phi + \varphi} = \overline{\phi} + \overline{\varphi} \qquad (44)$$
$$\overline{\overline{\phi}\varphi} = \overline{\phi}\overline{\varphi} \qquad (45)$$
$$\overline{\overline{\phi}\varphi'} = 0 \qquad (46)$$
$$\overline{\phi\varphi} = \overline{\phi}\overline{\varphi} + \overline{\phi'\varphi'} \qquad (47)$$

Applying the averaging rules and rearranging, the Reynolds averaged equations are:

$$\nabla \cdot [\rho\overline{\mathbf{u}}] = 0 \qquad (48)$$

and

$$\frac{\partial}{\partial t}[\rho\overline{\mathbf{u}}] + \nabla \cdot \{\rho\overline{\mathbf{u}}\overline{\mathbf{u}}\} = -\nabla\overline{p} + [\nabla \cdot (\overline{\boldsymbol{\tau}} - \rho\overline{\mathbf{u}'\mathbf{u}'})] + \overline{\mathbf{f}_b} \qquad (49)$$

The averaging procedure results in additional averaged products of the fluctuating components, introducing six new unkowns – the components of the Reynolds stress tensor:

$$\boldsymbol{\tau}^R = -\rho\overline{\mathbf{u}'\mathbf{u}'} = -\rho \begin{pmatrix} \overline{u'u'} & \overline{u'v'} & \overline{u'w'} \\ \overline{u'v'} & \overline{v'v'} & \overline{v'w'} \\ \overline{u'w'} & \overline{v'w'} & \overline{w'w'} \end{pmatrix} \qquad (50)$$

Therefore, the RANS equations are not a closed set and equations are needed for the unknown Reynolds stress components. The calculation process of the Reynolds stress components is what is called turbulence modelling. Due to turbulence being an effect of

a non-linear phenomenon, this can not be resolved by linear averaging of equations, like the Reynolds averaging, and, therefore, the turbulence model needs to express the non-linear fluctuating components in terms of the known mean components. A common approach is to use the Boussinesq hypothesis, which assumes the Reynolds stress to be a linear function of the mean velocity gradients:

$$\boldsymbol{\tau}^R = -\rho\overline{\mathbf{u}'\mathbf{u}'} = \mu_t\{\nabla\mathbf{u} + (\nabla\mathbf{u})^T\} - \frac{2}{3}[\rho k + \mu_t(\nabla\cdot\mathbf{u})]\mathbf{I} \tag{51}$$

For incompressible flows the relationship takes the form:

$$\boldsymbol{\tau}^R = -\rho\overline{\mathbf{u}'\mathbf{u}'} = \mu_t\{\nabla\mathbf{u} + (\nabla\mathbf{u})^T\} - \frac{2}{3}\rho k\mathbf{I} \tag{52}$$

The Boussinesq hypothesis relates the Reynolds stress to the mean velocity gradients in the flow by dynamic eddy viscosity, i.e. turbulent viscosity μ_t. Therefore, we need some way of calculating the eddy viscosity μ_t. Different models, such as the k-ε turbulence model, have been developed for this purpose. The choice of turbulence model depends on several criteria: robustness of the computational domain discretisation, computational costs, and physical phenomena that need to be captured.

2.3.1 k-epsilon Turbulence Model

One of the most widely used turbulence models is the RANS standard k-ε turbulence model (Jones & Launder, 1972) based on the Boussineq approximation with the turbulent viscosity μ_t. The turbulent viscosity is:

$$\mu_t = \rho C_\mu \frac{k^2}{\varepsilon} \tag{53}$$

where k is the turbulent kinetic energy, ε is the dissipation rate of turbulent kinetic energy, ρ is fluid density and c_μ is a closure coefficient.

The transport equation for turbulent kinetic energy k, that determines the energy in the turbulence, takes the form:

$$\frac{\partial}{\partial t}(\rho k) + \nabla\cdot(\rho\mathbf{u}k) = \nabla\cdot\left[\left(\mu + \frac{\mu_t}{\sigma_k}\right)\nabla k\right] + P_k - \rho\varepsilon \tag{54}$$

The transport equation for turbulent dissipation ε, that determines the scale of the turbulence, takes the form:

$$\frac{\partial}{\partial t}(\rho\varepsilon) + \nabla\cdot(\rho\mathbf{u}\varepsilon) = \nabla\cdot\left[\left(\mu + \frac{\mu_t}{\sigma_\varepsilon}\right)\nabla\varepsilon\right] + C_{1\varepsilon}\frac{\varepsilon}{k}P_k - C_{2\varepsilon}\rho\frac{\varepsilon^2}{k} \tag{55}$$

P_k is the production of turbulent kinetic energy, given in compact form (Moukalled et al., 2016) by:

$$P_k = \boldsymbol{\tau}^R : \nabla\mathbf{u} \tag{56}$$

which is a scalar computed by applying the double dot product of the tensors.

The model constants are assigned the following standard values:

$$C_{1\varepsilon} = 1.44, C_{2\varepsilon} = 1.92, C_\mu = 0.09, \sigma_k = 1.0, \sigma_\varepsilon = 1.3$$

The model is widely used for its satisfactory performance in a wide range of flows, considering the relatively low computational cost. The model will not, however, perform continuously well for cases where additional vortices are generated due to geometrical or flow-related conditions. It is possible to improve the models behaviour by adjusting the model constants. Annus et al. (2019) demonstrated that the k-ε turbulence model performance for the flow in a conduit with abrupt changes in diameter, can be improved

by considering changes in the model constants. However, for the air-water coupled flow process investigated in this thesis, where the turbulent kinetic energy peaks are mainly associated with interface breaking, suitable concurrence was not achieved with the adjustment and, therefore, a different model was used for analysing multi-phase flow.

2.3.2 RNG k-epsilon Turbulence Model

The RNG k-ε turbulence model was derived from the Navier-Stokes equations using a statistical technique called renormalisation group theory (Smith & Woodruff, 1998; Yakhot et al., 1992; Yakhot & Orszag, 1986). The RNG model contains an additional term in the equation for ε, that improves the accuracy for rapidly strained flows.

$$\frac{\partial}{\partial t}(\rho\varepsilon) + \nabla \cdot (\rho\mathbf{u}\varepsilon) = \nabla \cdot \left[\left(\mu + \frac{\mu_t}{\sigma_\varepsilon}\right)\nabla\varepsilon\right] + C_{1\varepsilon}\frac{\varepsilon}{k}P_k - C_{2\varepsilon}^*\rho\frac{\varepsilon^2}{k} \tag{57}$$

where $C_{2\varepsilon}^*$ is defined as

$$C_{2\varepsilon}^* \equiv C_{2\varepsilon} + \frac{C_\mu\eta^3\left(1 - {}^\eta/_{\eta_0}\right)}{1 + \beta\eta^3} \tag{58}$$

where $\eta \equiv Sk/\varepsilon$ and S is the modulus of the mean rate-of-strain tensor.

The values of the constants in the equations for k and ε are (Orszag et al., 1996; Pope, 2000):

$$C_{1\varepsilon} = 1.42, C_{2\varepsilon} = 1.68, C_\mu = 0.0845, \sigma_k = \sigma_\varepsilon = 0.72, \beta = 0.012, \eta_0 = 4.38$$

All the listed values (except β) are derived explicitly from the RNG analysis. This model showed satisfactory performance for the air-water flow modelling and was used in this thesis.

In regions with a large strain rate ($\eta > \eta_0$), the value of $C_{2\varepsilon}^*$ is less than $C_{2\varepsilon}$, which results in smaller destruction of ε compared to the standard k-ε turbulence model. In turn, this reduces k and, therefore, effective viscosity. As a result, in rapidly strained flows, the RNG model yields a lower turbulent viscosity than the standard model (ANSYS, Inc., 2011; Yakhot et al., 1992). The effect of swirl on turbulence is included in the RNG model, which enhances the accuracy of swirling flows. In addition, the RNG theory provides an analytical formula for turbulent Prandtl numbers, whereas the standard k-ε model uses user-specified, constant values.

2.4 Discretisation

To implement the finite-volume method, it is necessary to set up the geometrical support framework to define discrete locations at which variables are to be calculated. There are also meshless methods such as Lattice-Boltzman (Derksen & Van den Akker, 1999) and smooth particle hydrodynamics (Marongiu et al., 2007, 2010) but, for most CFD codes, discretisation of the solution domain is one of the first steps.

In addition, it is necessary to determine the time at which the solution is sought. The solution will be obtained by marching in time from prescribed initial conditions and, for this, it is sufficient to define the size of time step for the duration of the calculation. Time-step control is an important issue in free surface tracking since the surface-tracking algorithm is considerably more sensitive to the Courant number than in standard fluid flow calculations.

The first component of the process of generating the geometrical support framework for the finite-volume method is mesh generation. This replaces the continuous domain by a discrete one, consisting of a continuous set of non-overlapping volumes, delimited

by a set of faces. The boundary faces are then marked to define the physical boundaries of the computational domain for which boundary conditions will be applied. Then, relevant geometric information is computed for the components of the mesh and the topology is captured by defining how the components are related and located relative to each other. The grid resolution has a significant impact on computation time, solution accuracy and convergence rate or, for some cases, lack of convergence. The mesh resolution, adjacent cell length/volume ratios, skewness, and boundary layer mesh suitability for the problem of interest, are some of the most important quality indicators for the grid.

It is possible to widely classify the computational meshes into two categories. For regular geometries (rectangular and circular), the grid is usually chosen so that the grid lines follow coordinate directions, which results in a structured grid. For more complex geometries, unstructured meshes need to be used. Hybrid grids are often formed from portions of structured and unstructured regions. Figure 8 shows some common mesh elements and structures.
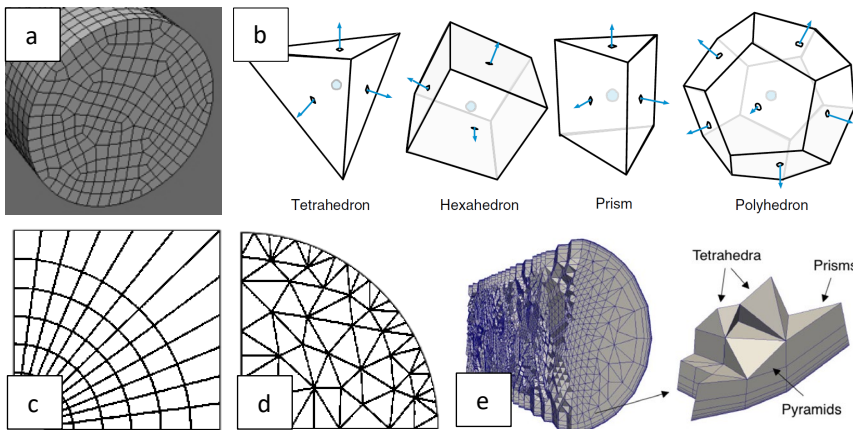
Figure 12. (a) hexahedral mesh; (b) most widely used polyhedron shapes for 3D meshes (Moukalled et al., 2016); (c) 2D curvilinear grid; (d) 2D unstructured (triangulated) grid; (e) boundary layer mesh for a pipe discretised by tetrahedra (Chitale et al., 2014).

Cells that the computational domain is filled with must have the following properties:

- Contiguous - The cells must completely cover the computational domain and must not overlap one another.
- Convex - Every cell must be convex and its cell centre must lie inside the cell.
- Closed - Every cell must be closed, both geometrically and topologically where:
  - geometrical closedness requires that when all face area vectors are oriented to point outwards of the cell, their sum should equal the zero vector to machine accuracy.
  - topological closedness requires that all the edges in a cell are used by exactly two faces of the cell in question.
- Orthogonality - For all internal faces of the mesh, the centre-to-centre vector is defined as that connecting the centres of 2 cells (the centre-to-centre vector is oriented from the centre of the cell with a smaller label to the centre of the cell with a larger label). The orthogonality constraint requires that for each internal face, the angle between the face area vector, oriented as described above, and the centre-to-centre vector must always be less than 90°.

There is a range of different softwares, such as the open source environment Salome, available that are suitable for generating a computational geometry and grid for the use of OpenFOAM simulations. The software itself supplies the snappyHexMesh utility, which automatically generates 3-dimensional meshes containing hexahedra and split hexahedra cells from triangulated surface geometries in Stereolithography (STL) format (Figure 9a). The mesh approximately conforms to the surface by iteratively refining the starting mesh and morphing the resulting split hexahedra mesh to the surface. An optional phase will shrink the resulting mesh and insert cell layers near the specified boundary regions (Figure 9c).
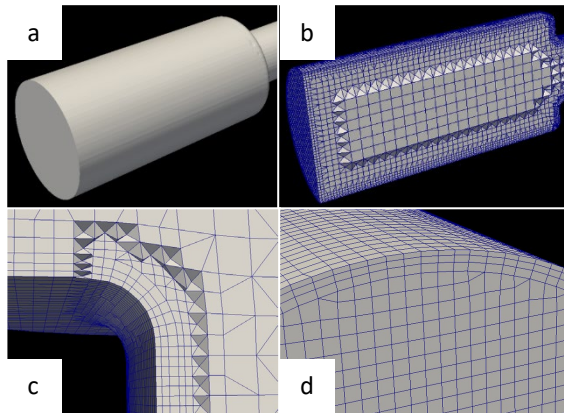
Figure 13. Steps for generating the computational grid with the snappyHexMesh utility (Douglas, 2014).

In addition, specific refinement regions can also be defined within the domain. It is possible to run the mesh generation and refinement processes in parallel with a load balancing step for every iteration. Before snappyHexMesh is executed, the user must create a background mesh of hexahedral cells with the blockMesh utility that will entirely cover the STL geometry and define on which side of the surface the mesh is sought (internal vs. external flow).

Depending on the complexity of the problem and the geometry of the domain, generating meshes for numerical simulation can be one of the most time-consuming steps. It is difficult to assess if the grid is adequate ahead of the simulation and, therefore, the development is iterative; subsequent mesh refinement tends to often be done manually. Validation of the suitable resolution level of the generated grid should always be carried out and the grid independence achieved. To assure that the results do not depend on the mesh density the simulations need to be conducted on different resolutions of the grid. Choosing a variable to study and plotting its value against the number of mesh nodes should reveal a point beyond which an increase in resolution will not further change the variable value. Validation is the assessment of the accuracy of a computational simulation by comparison with experimental data (Oberkampf & Trucano, 2002).

2.5 Computational Solver

The basic directory structure for an OpenFOAM case that contains the minimum set of files required to run an application, is shown in Figure 14. The case directory must include:

- A constant directory that contains a full description of the case mesh in a subdirectory and files specifying physical properties for the application concerned.
- A system directory for setting parameters associated with the solution procedure itself. It contains at least the following entries: controlDict where run control parameters are set, including start/end time, time step and parameters for data output; fvSchemes, where discretisation schemes used in the solution may be selected at run-time; and fvSolution, where the equation solvers, tolerances and other algorithm controls are set for the run.
- The 'time' directories, containing individual files of data for particular fields. The data can be either: initial values and boundary conditions that the user must specify to define the problem or results written to file by OpenFOAM. The OpenFOAM fields must always be initialised, even when the solution does not strictly require it, as in steady-state problems.
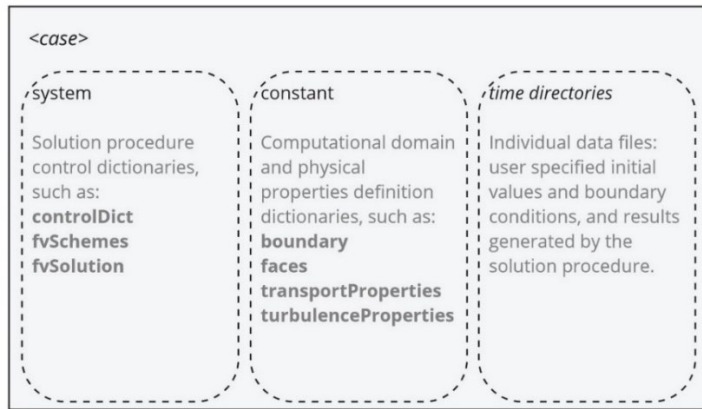
Figure 14. Schematic of the OpenFOAM case folder contents.

For initialising the case, some inputs are required in addition to the velocity and pressure definitions, fluid properties and computational domain information. At appropriate boundaries of the computational domain, the wall-function for turbulent flow over rough walls is applied. The roughness parameter for the wall shear stress in this model is defined via equivalent sand-grain roughness, which can be calculated from the Darcy friction factor f by the relation defined by Adams et al. (2012):

$$k_s = 3.7D \left(10^{-\frac{1}{1.8\sqrt{f}}} - \frac{6.9}{\text{Re}} \right)^{1/1.11} \tag{59}$$

Also, a boundary condition is provided for turbulent kinematic viscosity for rough walls, based on turbulence kinetic energy. This condition manipulates a parameter to account for roughness effects. The modified law of the wall that incorporates surface roughness, proposed by Cebeci & Bradshaw (1977), based on sand-grain mean roughness height k_s, takes the form:

$$u^+ = \frac{1}{K}\ln(y^+) + B - \Delta B(k_s^+) \tag{60}$$

where ΔB is a roughness function of $k_s^+ = {k_s u_\tau}/{\nu}$ based on experimental data, B=5.2, and K=0.41 (OpenCFD Ltd., n.d.) is von Karman's constant.

The initial value for turbulent kinetic energy is set based on the estimation for isotropic turbulence:

$$k = \frac{3}{2}\left(I|u_{ref}|\right)^2 \tag{61}$$

where I is the turbulence intensity and u_{ref} is the reference flow speed.

For isotropic turbulence, the turbulence dissipation rate can be estimated by:

$$\varepsilon = \frac{C_\mu^{0.75} k^{1.5}}{L} \tag{62}$$

where C_μ is a model constant equal to 0.09, by default, and L is a reference length scale.

In OpenFOAM, the SIMPLE algorithm is usually used for stationary and PISO for non-stationary flow analysis. In the latter, the calculation is controlled by the time step that is related to the Courant number (Co < 1). The PISO-SIMPLE merged algorithm, PIMPLE, enables the usage of larger time-steps (Co ≫ 1) (Holzmann, 2019).

2.6 Summary Remarks

In this thesis the numerical technique used in the CFD modelling is the finite volume method and multi-phase flows are solved using a VOF-type method. A pressure-based solver, considering the relationship between velocity and pressure corrections and following mass conservation and momentum changes, is used. The multi-phase solver based on the VOF method calculates a multi-phase mixture, applying an indicator function to find physical properties as weighted averages of the separate fluid properties. The phases are considered as incompressible and immiscible, with the surface tension force taken into account at the interfaces. As the studied air pocket dynamic process is relatively slow and virtually no accelerations were present during the experiments, the incompressibility assumption holds well. This assumption of incompressible air-water mixed flow is further confirmed by the Deltares experiments (Hou et al., 2014) on an large-scale pipeline with higher filling velocities. The multi-phase flow is considered turbulent and, through several validation tests, it has been concluded that the RNG k-ε turbulence model shows better agreement with experimental results (as compared to the k-ε turbulence model). The model was able to capture the periodic movement of air bubbles near the pipe obvert downstream of the hydraulic jump, as well as water droplet formation (see Figure 15). Figure 15 shows part of the pipe where the mobile hydraulic jump is located in the numerical model, at the selected time instance. The blue colour designates the air-water interface.
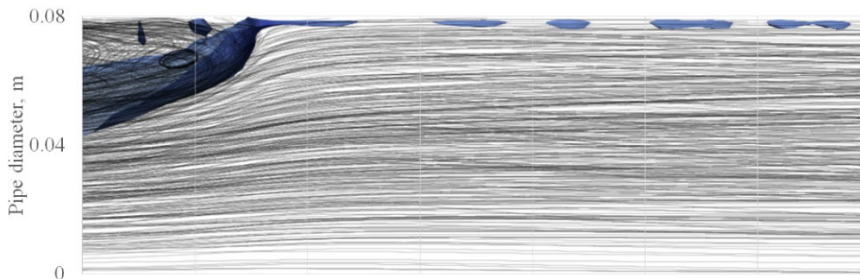
Figure 15. Modelled transitional flow, displaying the presence of swirling flow in the air pocket and the formation of droplets and bubbles at the interface.

3 Mixed Flow Applications

This chapter presents the investigated case studies, based on the journal papers (Annus et al., 2019; Kaur et al., 2020, 2023) and proceedings articles (Kaur et al., 2017, 2018; Laanearu & Kaur, 2018). The laboratory-scale experiments at Tallinn University of Technology were conducted within the duration of this thesis. The large-scale experiments at Deltares (formerly Delft Hydraulics) were carried out by other authors and published in a number of articles (Hou et al., 2014; Laanearu et al., 2012). However, the data pertaining to mobile hydraulic jump formation in the large-scale pipeline has been used for comparison in Kaur et al. (2023) but not been analysed before.

The focus remains on the air-water interaction, and the experimental and numerical investigations supporting an integral view of the processes in urban water systems are part of this work. The flow transitions in storm sewers may take place due to geometry effects, such as uneven sediment build-up and abrupt changes in pipe diameters and slopes. The transitions may also be due to fluid properties, such as denser fluids formed as a result of sediments accumulating in the lower sections of the system, for instance. Therefore, in this chapter, the numerical and experimental investigation of single-phase flow in complex geometry pipes and the numerical investigation of three-phase flow in a distinct-geometry urban sewer section are presented in ensemble with numerical and experimental investigations of the two-phase air-water flow in a horizontal pipe.

3.1 Laboratory-Scale Experimental Investigation

3.1.1 Air-Water Flow

As part of this thesis, an experimental study of pipe filling was conducted at the Fluid Mechanics Laboratory of Tallinn University of Technology (Figure 16).

Figure 16. Transparent pipeline with pipe bridge at Fluid Mechanics Laboratory at TalTech.

Preliminary tests to map the system's behaviour and initial experimental runs were reported in Kaur et al. (2018) and a more rigorous experimental procedure, with several repeats of each measurement stage, was reported in Kaur et al. (2023). The aim of the study was to investigate the dynamics of the air-water flow interface touching the pipe crown, i.e. bridging, and the concurrent air-pocket entrapment in a horizontal pipe. A single air pocket was trapped between a static water-air front and a mobile hydraulic jump (Figure 5); a process that is distinct from the dynamics of water-surface waves generated during super-critical flow, which may touch the conduit crown in a process also referred to as bridging, causing a series of air pockets to form. The investigated filling process had three stages, distinguished as: air cavity formation, air pocket formation, and air entrainment (Kaur et al., 2023).

The specific conditions of the experimental apparatus that produced an air cavity at the pipe bridge were chosen through mapping of the apparatus' operating conditions.

The air cavity formed as two water-air fronts appeared: the upper water-air front static at the pipe bridge crown and the lower front advancing into the horizontal pipe section. The manner of cavity formation demonstrated that the pipe bridge acted as a cavity trap and mimicked pipe outlet conditions as the Flow number value corresponded well with the range of values mapped by (Hager, 1999) for cavity formation in the horizontal pipe outlet. In the preliminary tests Flow numbers in the range of 0.6-0.9 were tested.

The experiments were carried out on an 18 m long horizontal transparent pipeline to allow visual monitoring of the flow development process throughout the pipeline. The components and instrumentation of the experimental apparatus are depicted in Figure 17. The pipeline is composed of transparent polymethyl methacrylate (PMMA) pipe segments 2 m long and with an inner diameter of 0.08 m and a bridge (6), with a height of 0.26 m and length of 1.68 m. The pipeline was fed from an upstream water tank (1), where the pressure head was kept constant throughout the experimental runs to ensure controlled inflow conditions. The aim was to operate the apparatus in a manner that resulted in the formation of a sufficiently long air pocket to be able to investigate the advancement of the pressurisation bore along the pipeline. The bridging location of the stratified flow was determined by adjusting the flow conditions according to a super-critical Froude number value.

1 water tank
2, 5, 7, 11 pressure transducers
3, 13 shut-off valves
4, 12 electromagnetic flow meters
6 pipe bridge
8, 10 water-level meters
9 PIV measurement section

Section	3–4	4–5	5–6	6–7	7–8	8–9	9–10	10–11	11–12	12–13
Length, m	1.1	1.6	7.8	1.8	1.2	0.55	1.7	0.25	1.0	0.65
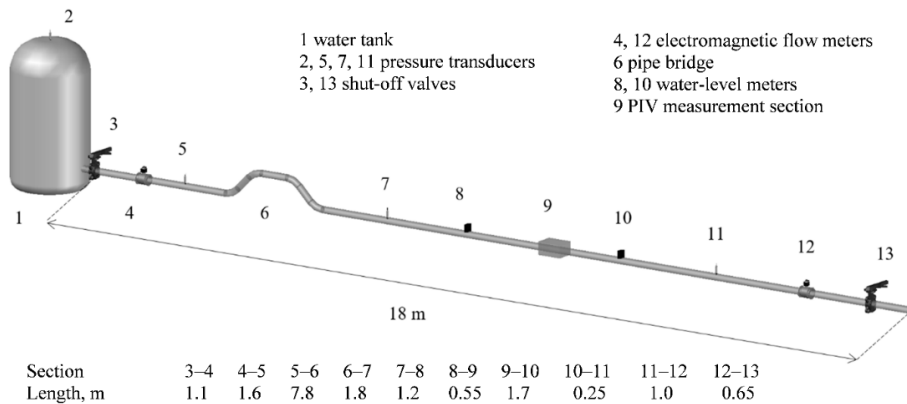
Figure 17. Components and instrumentation of the experimental facility at the Laboratory of Fluid Mechanics, Tallinn University of Technology (Kaur et al., 2023).

Two electromagnetic flow meters (ABB FSM4000 and Aswega VA2304), four strain-gauge pressure probes (Danfoss MBS 4701), a particle image velocimetry (PIV) system consisting of a high-speed camera and a continuous-wave laser (Dantec Dynamics), two capacitive sensors for water level metering, and two synchronised data acquisition modules (HBM QuantumX MX840A) were used to capture the experimental data. The accuracy of the measurements obtained with the instruments and sampling frequency is reported in Kaur et al. (2023). The flow meters were located at the up and downstream ends of the pipeline and the downstream meter data was analysed concurrently, to account for water-only conditions.

For the purpose of capturing the water levels with a suitable accuracy and frequency, a capacitive water level sensor was built in-house. Different configurations, e.g. with probe wires attached to the outside of the pipe wall, with different distances in between, and inside of the pipe (Figure 18), were considered. Due to accuracy and response time

considerations, a measuring system with two vertical parallel rods inside the pipe was found to be most suitable. Depending on the water level, the capacitance between the rods changed in the range 4-35 pF. The capacitance to frequency converter's output was measured by a microcontroller and converted to voltage in the range of 0-10 V DC. The output was updated 1000 times per second. The data acquisition module was used to apply a calibration curve.
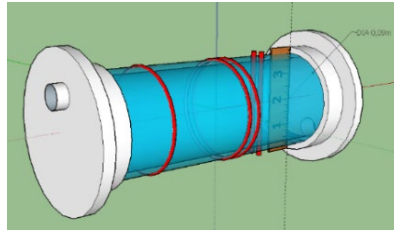
Figure 18. Water level measurement system design.

The experimental procedure is described based on the numbered locations 1 through 13 in Figure 17. At the initiation stage, the section of pipe (3–6) between the upstream tank and the bridge was fully filled with water, expelling all air. The outflow ball valve (13) was fully open and the position of the inflow ball valve (3) was adjusted to achieve the target flow rate $Q = 3.5$ l s^{-1} (Re = 56 000).

The pipe bridge (6) was used to accelerate the flow and mimicked the pipe outlet condition, creating an air cavity in the pipeline, with a static water-air front at the bridge crown. The resulting stratified flow interface advanced into the horizontal section (6–13) after the bridge slope, eventually bridging due to instabilities. Bridging of the stratified flow occurred 5 m after the pipe bridge (6), at section (10–11), resulting in the trapping of an air pocket between the upstream water-air front and a pressurisation bore. The pressurisation bore travelled upstream with a gradually decelerating velocity c_{jump}, as the air was entrained via the air-water roller near the pipe obvert, thereby gradually decreasing the volume of the pocket. The measured flow development stages were defined with respect to the PIV box location (9). Stratified flow measurements were conducted while the mobile hydraulic jump roller was located eight pipe diameters downstream of (9). Roller measurements were conducted, while the jump roller was at (9) and slug flow measurements were conducted while the roller was three pipe diameters upstream of (9). The roller in the PIV box (9) can be seen in Figure 19.
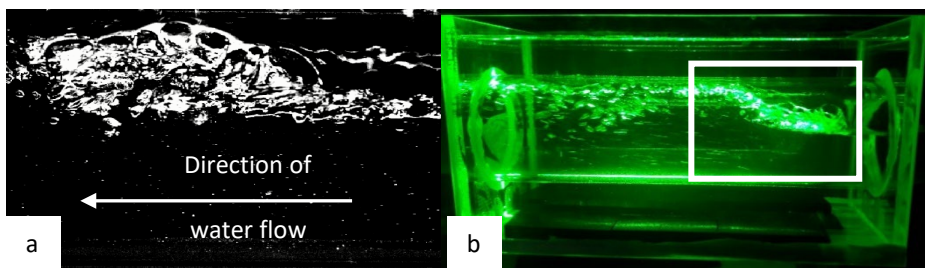
Figure 19. (a) Hydraulic jump roller captured with the PIV camera. (b) Photo of the hydraulic jump in the PIV box, with the white rectangle indicating the PIV camera frame position.

After the first series of measurements of stratified, roller and slug flow stages, the roller was pushed downstream by supplying additional air into the air pocket through a valve at the crown of the pipe bridge (6), therefore restarting the movement of the pressurisation bore towards the pipe bridge, along the horizontal pipe section. The measurements of each stage were repeated fifteen times and before ensemble averaging was conducted, the individual PIV frame sequences were analysed and frames in which the roller was not precisely at the predetermined position were excluded. Additional measurements of fully filled flow were conducted for a numerical model sensitivity study.

Two distinctive regions were observed in the vicinity of the advancing mobile hydraulic jump. The roller acted to entrain air, resulting in bubbles being propelled toward the pipe centreline, forming a bubbly flow (Figure 20c), before aggregating near the obvert and resulting in slug flow. The region of bubbly flow span was approximately two pipe diameters behind the roller, in a pipe with an 80 mm diameter (Kaur et al., 2023).
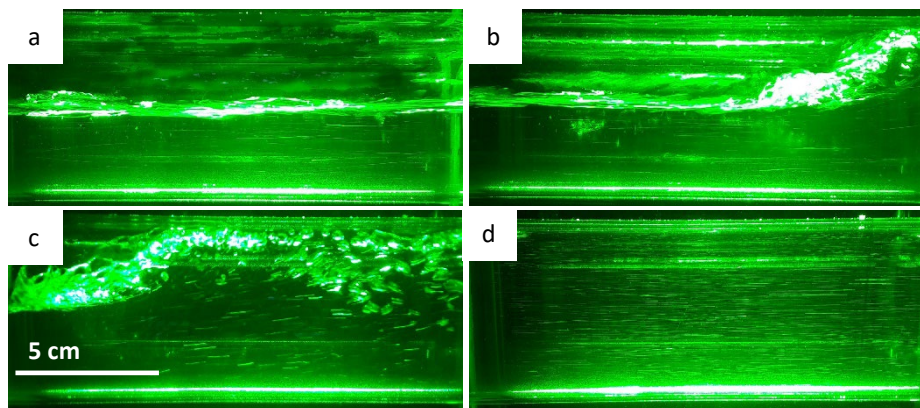
Figure 20. (a) Stratified, (b) roller, (c) bubbly and (d) slug flow stages of pressurisation bore advancement in an 80 mm pipe (Kaur et al., 2023). The filling ratio upstream of the hydraulic jump is 0.63 (frame a).

Calculations using Eq. (17) (subparagraph 1.2.6), which included experimental data captured during the roller measurements, i.e. when the air pocket length was approximately 3.55 m, revealed that the value of the hydraulic jump speed was $c_{jump} \approx$ 0.04 m s^{-1}. Estimating the air entrainment rate, at that time instance, based on the mobile hydraulic jump speed and air pocket thickness, yields 7·10^{-5} m^3 s^{-1}, which corresponds to nondimensional entrained flow rate (air flow rate divided by water flow rate) value 0.02. Schulz et al. (2020) compared empirical equations for nondimensional entrained flow rate and determined a range of uncertainty associated with the expressions. At Froude number value Fr=2, the nondimensional entrained flow rate varies from 0.002 (according to $Q_a/Q_w = 0.00212(\text{Fr}-1)^{1.59}$ based on Kent (1952)) to 0.03 (according to $Q_a/Q_w = 0.03(\text{Fr}-1)^{1.06}$ based on USACE (1980)). Therefore, the herein determined value falls within the range of uncertainty.

The pressure gradient through the jump at this stage was around 200 Pa. A small vacuum was detected once the air pocket had shortened by around a half. It was also apparent that the mobile hydraulic jump decelerated as it neared the pipe bridge and the air pocket shortened, while the water column between the pocket and the pipe outlet lengthened.

3.1.2 Flow in Complex Geometry Pipes

To investigate the effect of complex geometries, experiments of fully filled flow in a pipe with an abrupt diameter change and a pipe with irregular roughness elements were conducted at the Fluid Mechanics Laboratory of Tallinn University of Technology. As the urban water systems age, the shape of the pipes' internal walls may change unevenly due to corrosion, sediment and litter build-up and structural failures, progressing far beyond the applicability of the simple approach of increasing the roughness coefficient while conducting calculations. Additionally, stormwater pipes may be designed with abrupt changes in internal diameter, for instance for the purpose of restricting flow from a specific catchment to a collector pipe. The different configurations of the experimental apparatus are shown in Figure 21.
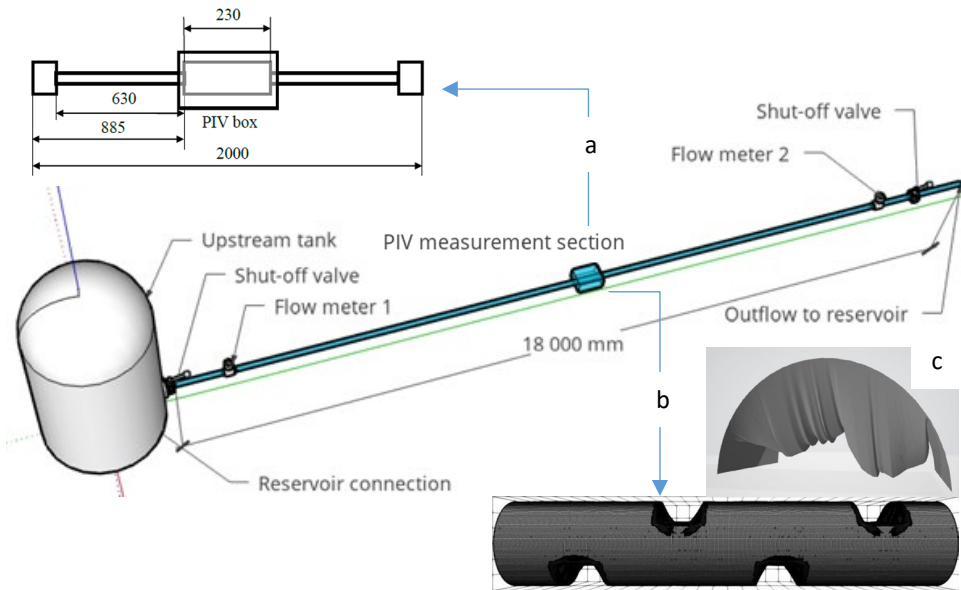
Figure 21. Diagram of the pipeline apparatus used to investigate flow dynamics in (a) a pipe with an abrupt change in diameter (units in mm) and in (b) a pipe containing irregular roughness elements. (c) The irregular roughness element 3D-printed for experiments.

The experimental apparatus consisted of a tank at the upstream end, a horizontal transparent PMMA pipe with a total length L = 18 m and an internal diameter D = 80 mm, and a PIV measurement section. The upstream tank was fed from, and the pipeline emptied into, a 150 cubic metre underground reservoir. The pipeline was assembled from 2 m long hydraulically smooth pipes and the outlet was open to the atmosphere. Shut-off valves were situated at the up and downstream ends of the pipeline, adjacent to electromagnetic flow meters. The two flow meters were simultaneously used at the experiment's initiation stage for the purpose of ensuring that all air was expelled from the flow domain. The pipeline was pressure driven and the flow rate was controlled by the frequency of the upstream-end pump feeding the tank from the reservoir. The velocity field at the location of interest was measured in the streamwise central plane with two-dimensional PIV, in both experimental set-ups. The measurements were carried out using multi-frame single-exposure PIV, with a high-speed camera for image capturing, and a continuous-wave laser for creating the light-sheet. The calibration of the PIV was conducted by capturing a reference images series with rulers inserted into the

measurement section. Any distortion in the capturing was avoided by encasing the pipe in a water-filled Plexiglas PIV box and mounting the camera in a horizontal position. Velocities, standard deviations, and variances were calculated using only valid vectors (i.e. gained from measured particle displacements not approximated by the software's algorithm).

In the first series of experiments, flow dynamics in a pipe with an abrupt change in diameter were investigated. The 2 m long test section consisted of two short pipes at both ends with an internal diameter D = 80 mm, two longer pipes with an internal diameter D = 46.4 mm and length L = 0.63 m, and a 0.23 m long transparent section with an internal diameter D = 80 mm in the middle (Annus et al., 2019). The schema is visible in Figure 21a. PIV was used to capture the velocity field at different flow rates in the 0.23 m long middle section. The measurement frequency of the camera was adjusted according to the Reynolds number (Table 1) and each measurement span 10 s. The cross-correlation method was used over an interrogation window of 16 x 16 pixels with 50% overlap in the analysis.

Table 1. List of experiments. Uncertainty of flow measurements readings ±0.5% (Annus et al., 2019).

Experiment number	Flow rate (Q, l/s)	Reynolds number of the full pipe cross-section (D = 80 mm)	Flow number	PIV measurement frequency (f, Hz)
1	0.750	12 000	0.17	235
2	1.245	19 800	0.28	391

In the flow field, large primary recirculation bubbles evolve behind the sudden expansion and before the sudden contraction. The maximum velocity is highest at the inlet of the larger diameter pipe where the flow is typical for a submerged jet (Figure 22). In the vicinity of the outlet, the effective flow area of the pipe is at its smallest, and the flow direction at the near wall region is the opposite (Annus et al., 2019).
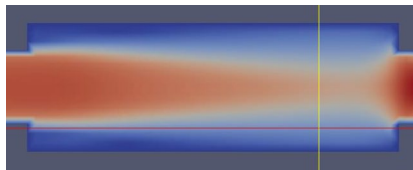
Figure 22. Jet-type flow forming in the middle potion of the experimental section of a pipe with abrupt change in diameter. Red colour indicates higher velocity.

The second series of experimental investigations were conducted on a pipeline containing different configurations of obstructing roughness elements in the flow domain. PIV was used to map the velocity field in the vicinity of the elements, with the PIV box length 0.23 m as in the first series. The experiments were conducted at five different flow rates (Table 2) to characterise the changes of effective flow section in the obstructed conduit (Kaur et al., 2022).

Experiment number	Flow rate (Q, l/s)	Reynolds number of the full pipe cross-section ($D = 80$ mm)	Flow number
1	3.0	47 900	0.68
2	3.8	59 800	0.86
3	4.4	69 800	0.99
4	5.0	79 300	1.13
5	5.6	89 300	1.26

The trigger frequency of the camera was set to 1000 Hz and the flow was measured for 3 s. The data was recorded and processed by Dynamic Studio 4.0 (Dantec Dynamics) software. The cross-correlation method was used to process the PIV data. As a result, velocity vector fields were calculated considering the displacement of the particles between the two frames. An interrogation window of 8 x 8 pixels with 50% overlap was used (1 pix=0.18 mm). The images were pre-processed by subtracting the image mean (including areas covered by the roughness elements) and reflections for generating the vector maps.

Irregular pipe wall build-up elements (Figure 21c) that were first designed for numerical analysis (Annus et al., 2020; Kaur et al., 2020), were 3D printed and attached inside the pipe of the experimental apparatus. The printing was done from a transparent substance, to allow the laser sheet to pass through the elements. Two configurations of the roughness elements were used. Firstly, one element was attached to the pipe obvert and secondly, four elements were inserted into the pipe, two at the obvert and two at the invert, equidistantly (Figure 21b and Figure 23).
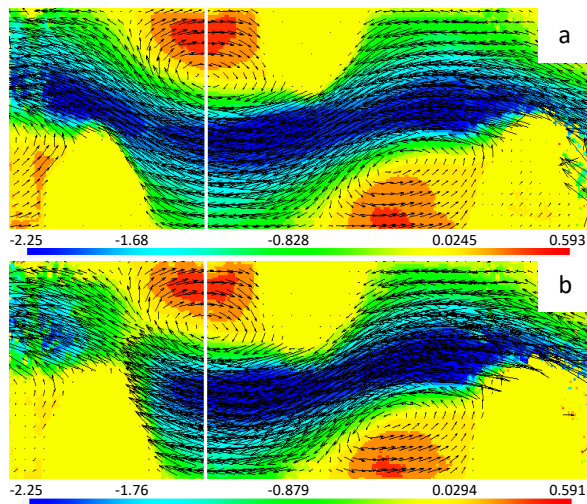
Figure 23. Vector and scalar map in the region of four roughness elements, three of which are in the camera's field of view and one on the right-hand-side, obstructing inflow. Scalar map coloured by axial velocity U. (a) Q=5 l/s, (b) Q = 5.6 l/s (Kaur et al., 2022).

The velocity field mapping at different flow rates in the pipe section, with one roughness element at the pipe obvert, demonstrated how the local disturbance changes the flow dynamics, causing a recirculation area to form that changes in scale with the changing flowrate, indicating a trend in the effective flow area development. The measurements with four elements demonstrated the formation of dead zones between the elements. Concurrently, at higher flowrates, the dynamics start to demonstrate that the flow core is diverted from the central plane (Figure 23b), forcing higher turbulence generation and forecasting conduit choking (Kaur et al., 2022).

3.2 Large-Scale Experimental Investigation of Air-Water Flow

In the lerge-scale pipeline filling experiments conducted at Deltares, the unexpected formation of a hydraulic jump was observed for different filling ratios (h/D), where three stages of mixed flow occurred. These experiments demonstrated that the presence of stratified flow significantly modifies the dynamics of two-phase flow during water-air fronts' intrusion along the pipeline, starting from the full cross-sectional water-air front at the pipe bridge. Measurements of flow rate, pressure and internal water level along the Delft horizontal PVC pipeline (261 m in length and 236 mm internal diameter (Laanearu & van't Westende, 2010)) and camera recordings were available to quantify the transitional-flow process, represented by stratified flow, mobile hydraulic jump and slug flow regions. The Reynolds number for the fully filled flow for the experimental series was 950 000. Even though the scales are different compared to the laboratory-scale experiments (subparagraph 3.1.1), similar behaviour can be detected. Figure 24 shows the stages of stratified, roller, bubbly and slug flow in the D = 236 mm pipe with the stratified flow filling ratio h/D = 0.14. Figure 25 depicts stratified, roller and bubbly flow stages in the same pipe with a filling ratio of 0.53.
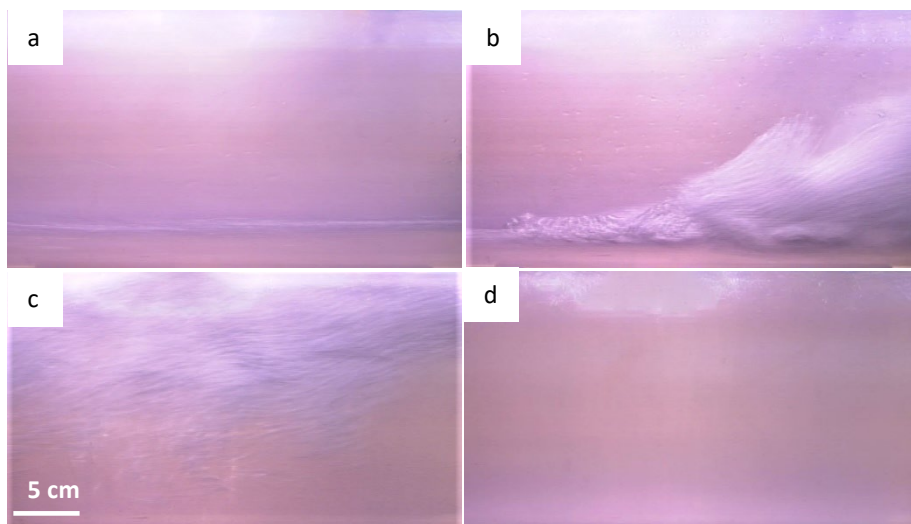
Figure 24. (a) Stratified, (b) roller, (c) bubbly and (d) slug flow stages of pressurisation bore advancement in a 235 mm pipe with comparatively smaller filling ratio (Kaur et al., 2023). The filling ratio upstream of the hydraulic jump is 0.14 (frame a).

Figure 25. (a) Stratified, (b) roller and (c) bubbly flow stages of pressurisation bore advancement in a 235 mm pipe with comparatively larger filling ratio (Laanearu & van't Westende, 2010). The filling ratio upstream of the hydraulic jump is 0.53 (frame a).

Figure 26 represents the trends for water-flux difference and air pocket volume relation trends for comparatively larger and smaller filling ratios in the larger and smaller internal diameter pipes, in normalised form. The length of the air pocket (the end of which is the bridging location) and the region of bubbly flow were dependent on the cross-sectional filling ratio of the pipe h/D and, consequently, the Froude number. Stronger super-critical flow conditions correspond to smaller volumes of captured air. The size of the air pocket is also related to the volumetric water flux difference between the inflow and outflow of the pipeline.
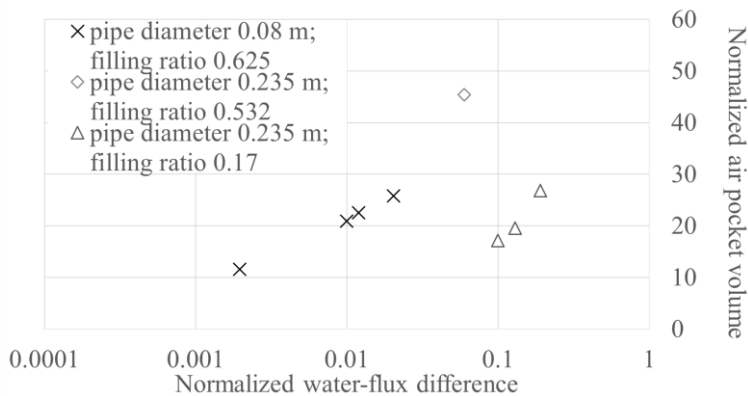
Figure 26. Normalised air pocket volumes and water-flux differences for different diameter pipes with different filling ratios.

Table 3 presents experimentally determined values for the normalised water-flux differences, air pocket volumes, hydraulic jump speeds, Froude, and Flow numbers. The Zukoski number is not presented separately, because the value of Zukoski number and Flow number in the herein presented case coincide for the 0.08 m diameter pipe. For the 0.235 m diameter pipe, Zukoski numbers were calculated for representative experimental runs in the case of pipeline emptying by Laanearu et al. (2012). The Zukoski number value was close to its critical value (≈ 0.5) and changed in the range of 0.33-0.58. The hydraulic jump speed c_{jump} is calculated in the reference frame of the pipe, considering that the bore moves on top of the stratified inflow. Two groups based on the filling ratio, at which point the air pocket formed, are apparent in Table 3. Experiments that resulted in mobile hydraulic jump formation from a filling ratio $h/D > 0.5$ correspond to the lower super-critical Froude number and the higher hydraulic jump speed. The highly super-critical experiments with $h/D < 0.5$ displayed lower air-water front moving speed. Because the two test rigs are of a different scale, water flux

differences between inlet and outlet are normalised by the inflow rate of volumetric flow $\left((Q_{inflow} - Q_{outflow})/Q_{inflow}\right)$, while air pocket volumes are normalised based on the cube of the pipe diameter (V/D^3).

Table 3. Average normalised water flux differences, normalised air pocket volumes, hydraulic jump speeds, Froude and Flow numbers for air pocket formation induced by weaker and stronger super-critical flow conditions (Kaur et al., 2023).

Pipe diameter, m	Filling ratio	Normalised water flux difference	Normalised air pocket volume	c_{jump}	Fr	F
0.080	0.63	0.002	11.6	-	-	-
0.080	0.63	0.010	20.9	0.040	2.00	0.8
0.080	0.63	0.012	22.6	-	-	-
0.080	0.63	0.020	25.6	-	-	-
0.235	0.53	0.060	45.0	0.067	3.55	1.21
0.235	0.14	0.100	17.1	0.015	14.33	0.38
0.235	0.14	0.130	19.5	0.017	16.71	0.41
0.235	0.19	0.190	26.8	0.029	9.64	0.47

3.3 Numerical Investigation

3.3.1 Air-Water Flow

To interpret the different stages of the pressurisation bore development, computational fluid dynamics modelling was applied. Three-dimensional full-scale computational domain geometry was created according to the experimental apparatus. The two-phase flow simulations were conducted using OpenFOAM software's interFoam solver. The flow regime was turbulent and the air and water phases were considered as incompressible, isothermal, Newtonian and immiscible fluids. Interface tracking for the air-water flow was resolved by applying the VOF method. The surface tension coefficient was chosen as σ = 0.073 N m^{-1} for air and water interfaces, corresponding to the laboratory air temperature 20 $^{\circ}$C. The density and dynamic molecular viscosity of water were set as 998.2 kg m^{-3} and $1.002 \cdot 10^{-3}$ kg m^{-1}s^{-1}, respectively. The density and dynamic molecular viscosity of air were set as 1.204 kg m^{-3} and $1.82 \cdot 10^{-5}$ kg m^{-1} s^{-1}, respectively.

RANS model performance in the transitional flow was analysed, comparing measured and modelled velocity and kinetic energy distributions and the formation location and dynamics of the hydraulic jump. It was found that the Renormalization Group (RNG) *k-ε* model performance was superior to the standard *k-ε* model. The standard *k-ε* turbulence model failed to consistently predict the air-water interface bridging location according to the experimental findings. Therefore, in this study the RNG *k-ε* turbulence model was used to resolve the turbulent flow.

For model initialisation, values for turbulent kinetic energy and dissipation were determined from experiments. These were set to k = 0.00124 m^2 s^{-2} and ε = 0.00128 m^2 s^{-3}, respectively. For boundary conditions constant inflow rate was defined based on experiments and the pipe outlet was set to zero gradient pressure condition.

The computational domain was discretised by a hybrid grid, containing a blend of structured and unstructured grid portions. The snappyHexMesh utility, supplied by

OpenFOAM, that creates the grid from triangular surface geometries, was used for the meshing.

Before any conclusions may be drawn from the numerical model results, its validity needs assessment. Conducting a grid independence study is one way of assuring the model fidelity. A grid sensitivity analysis was performed on the full-scale computational domain. A comparison of the measured axial velocity profile was made with the modelled profile obtained from three different grid resolutions. Different refinement levels of the computational domain grid for the study of flow bringing (Kaur et al., 2023) are shown in Figure 27.
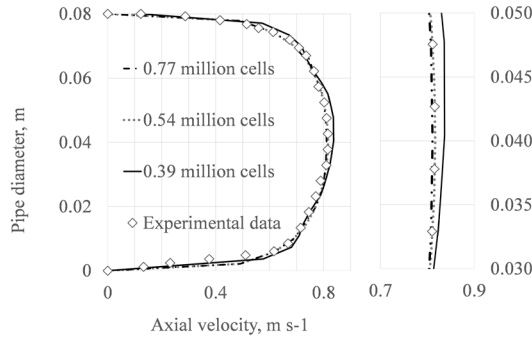
Figure 27. Grid independence study for different mesh refinement levels (Kaur et al., 2023).

It is apparent from the graph, that the finer grid resolutions with 0.54M and 0.77M elements give almost identical results in respect to the velocity distribution. Therefore, 0.54M finite volumes were used for this study. Additionally, for stratified flow, the water level in the pipe and bridging location were compared for the experiments and the modelling and were found to be in good agreement. The model with the above-mentioned set-up and 0.54M mesh elements consistently replicated the bridging location.

In the laboratory experiments, the air entrained through the roller and the jump approached the bridge with a decelerating speed c_{jump}. The numerical modelling also demonstrated the changing speed of the hydraulic jump. During the first 5 s after the bridging event $c_{jump} \approx 0.07$ m s^{-1}, which decreased to 0.01 m s^{-1} over the next 1.5 mins.

The measured and modelled velocity and turbulent kinetic energy profiles of the multi-phase process were compared for model validation purposes. All of the results are presented in normalised form. The PIV velocity field was only captured for the water phase. The PIV measurements were facilitated by flow visualisation, which involved seeding the water flow with oxygen and hydrogen bubbles generated via electrolysis. However, for two-phase mixed flow, visualisation of the air flow was not straightforward and air flow was, therefore, not captured by PIV, and in the comparative figures, only modelling results are shown for both water and air.

Normalisation was consistently carried out based on the maxima of the water flow profiles. The measured profiles were used as the basis, and the axial and vertical velocity profile maxima were found. The modelled axial and vertical velocities were then normalised based on the cell value corresponding to the coordinates of experimentally determined maxima. Turbulent kinetic energies were normalised based on the cell value corresponding to the experimentally determined maxima of the axial velocity. The values of the normalisation constants for the measured and modelled flow profiles and their differences are presented in Table 4.

Table 4. Values of the normalisation constants for measured and modelled flow profiles and their differences (Kaur et al., 2023).

| | | Normalisation Coefficient | | |
		Measured	Modelled	Difference
Stratified Flow	Axial Velocity	1.364	1.185	13%
	Vertical Velocity	0.015	0.013	10%
	Turbulent Kinetic Energy	0.012	0.014	14%
Roller	Axial Velocity	1.336	1.162	13%
	Vertical Velocity	0.107	0.118	10%
	Turbulent Kinetic Energy	0.012	0.014	23%
Slug Flow	Axial Velocity	0.982	1.005	2%
	Vertical Velocity	0.035	0.024	32%
	Turbulent Kinetic Energy	0.017	0.011	32%

The axial velocity component shows better qualitative agreement compared to the vertical component between the measured and modelled transitional flow stage of stratified flow (Figure 28). Comparing the model and experiments of the stratified flow stage revealed slight differences in the interface behaviour. In the experiments, it was visually apparent that the vertical air-water mixing intensity gradually increased, i.e. the mixing was already present at the stratified flow portion leading up to the roller. The numerical model showed similar behaviour to a gradually varied flow, resulting in the same bridging location. Concurrently, the experiment revealed faster growth of the vertical velocity component in this stage.

The measured and modelled axial and vertical velocity components in the roller flow stage show the best overall qualitative (Figure 28) and quantitative (Table 4) agreement. Due to the model's ability to consistently reproduce the roller's behaviour, it was possible to use the modelled velocities in mixing efficiency calculations (subparagraph 1.2.5).

The measured and modelled vertical velocity and turbulent kinetic energy of the slug flow stages show the poorest quantitative agreement, as shown in Table 4. This is primarily due to the frequency of PIV measurements, which was set based on the Reynolds number of the flow, and secondly, because measurement results are slightly affected by the mixed-in air releasing due to buoyancy.

The data in Figure 28 and in Table 4 reveal the qualitative similarity between the measured and modelled profiles. In addition, comparing the qualitative distribution of energy in turbulence with other studies, reveals the apparent similarities. Turbulence intensity and Reynolds stress distributions measured in and behind the hydraulic jump in open channel rectangular flow (Resch & Leutheusser, 1972), revealed turbulence energy maxima near the centre-line of the flow behind the jump, as is also the case in the present study.

Stratified flow
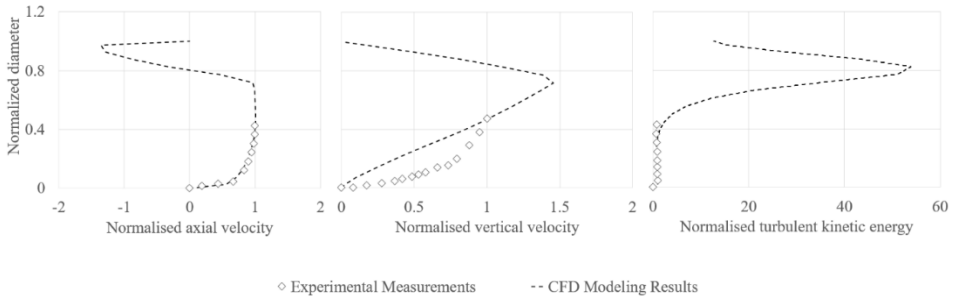
Roller
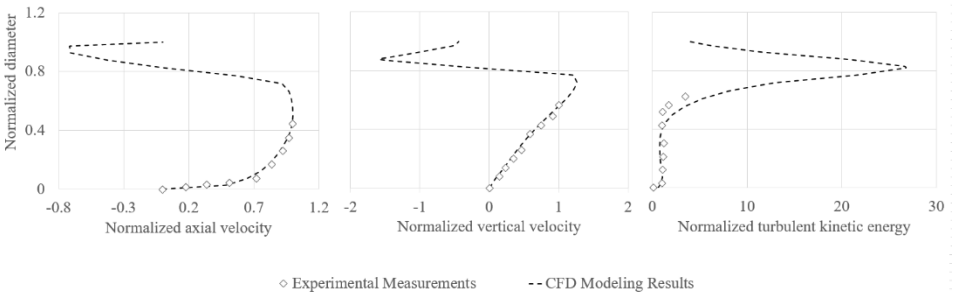
Slug flow
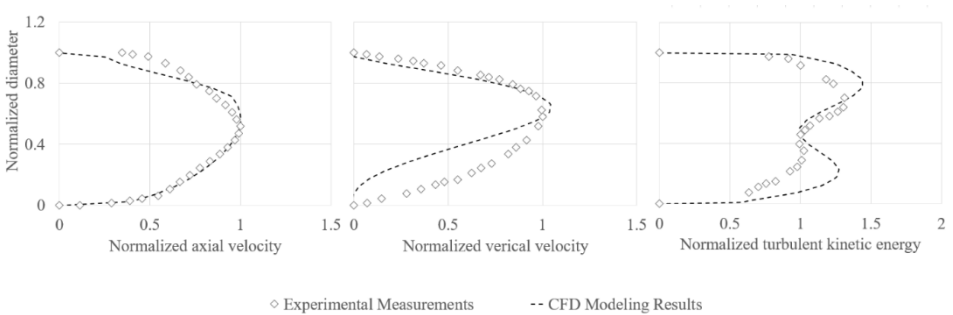
Figure 28. Normalised measured and modelled axial and vertical velocity, and turbulent kinetic energy at the different development stages of the flow in the 80 mm pipe filling experiments (Kaur et al., 2023).

The measured and modelled turbulent kinetic energy comparison in a non-normalised form, for flow region right behind the hydraulic jump region, was presented in Kaur et al. (2018). The modelled turbulent kinetic energy showed good concurrency with experimental data, when comparing the whole set of values captured on the streamwise central plane. In Figure 29, all of the turbulent kinetic energy data points (5300 in the image) captured over the PIV measurement domain of a width of 640 pixels (96 mm) behind the mobile hydraulic jump roller, are indicated with crosses. More than 90% of the data points fall between curves obtained from numerical simulation at the limits of the measurement domain (taking the distance from the roller as a reference).
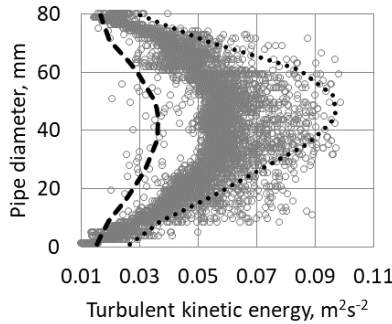
Figure 29. Turbulent kinetic energy of experimental results in comparison to numerical simulation in the bubbly flow region (Kaur et al., 2018).

In Laanearu & Kaur (2018), it was shown that the different air-water mixed flow patterns are crucially dependent on the pipeline layout and wall roughness. Three settings of the validated CFD model were tested to clarify the mobile hydraulic jump formation conditions. In the first case, the solver was used to investigate the formation of a mobile hydraulic jump in a hydraulically smooth pipe. In the second and third cases, the CFD solver was applied to investigate the formation of a mobile hydraulic jump for hydraulically rough pipes, with corresponding roughness heights of 1.0 mm and 0.5 mm. The same inlet and outlet boundary conditions were used as for the above-described case. Herein, the smooth pipe case and the case with a roughness height of 1 mm are presented.

In the hydraulically smooth pipe, the stratified flow developed along the pipeline until the intruding water-air front in the horizontal pipe reached the outlet pipe with a reduced diameter. After this time instant, the air-water interface elevation started to rise in the downstream part of the horizontal pipe. After filling the pipe cross-section up to the obvert, the interface formed a mobile hydraulic jump that moved backwards against the stratified flow current, i.e. toward the pipe bridge. In this phase, the formation of some slugs at the downstream face was detected. Figure 30a demonstrates the formation of a long air pocket trapped near the pipe bridge and the formation of slugs along the pipe obvert. Figure 30,b shows the evolution of the vertical distribution of the along-pipe (x-axis direction) velocity component through the hydraulic jump. As expected, the changes of velocity over the vertical cross-sections, where stratified and fully filled flows of the pressurised pipe merge, involve the velocity maximum reduction in the downstream face of the hydraulic jump, which is also associated with the development of a turbulent core at the pipe axis. The vertical distribution of eddy viscosity is shown in Figure 30c, for the same locations. The maximum eddy-viscosity is associated with the upstream roller of the hydraulic jump.
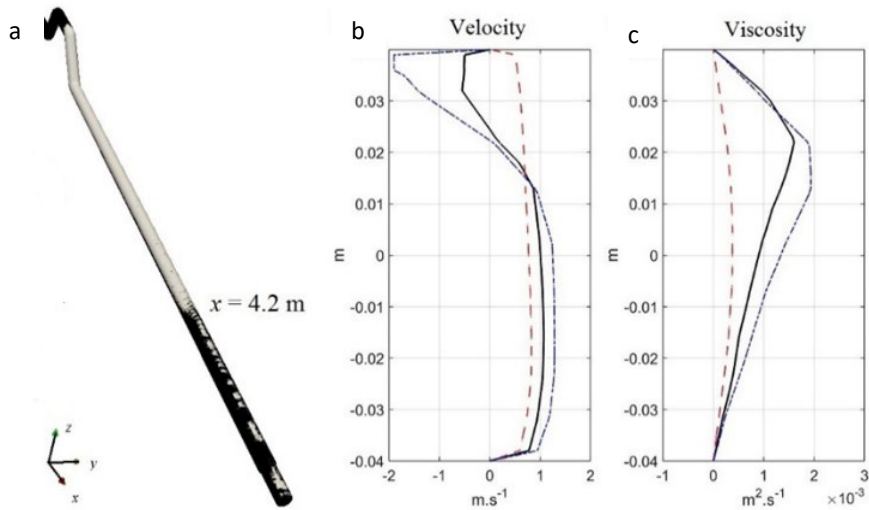
Figure 30. Smooth-pipe flow case. (a) Visual of the air pocket and slug flow formation. (b) Vertical distribution of along-pipe velocity (x-axis component) at cross-sections (dash-dotted curve at x = 4.0 m; continuous line at x = 4.2 m; dashed curve at x = 4.4 m). (c) Vertical distribution of eddy viscosity at cross-sections (dash-dotted curve at x = 4.0 m; continuous line at x = 4.2 m; dashed curve at x = 4.4 m) (Laanearu & Kaur, 2018).

For the rougher-pipe flow case the set-up was modified with the wall function, to investigate the formation of hydraulic jump in the rough pipe with a roughness height of 1 mm, corresponding to relative roughness 0.0125. The initial conditions and integration period are the same as for smooth-pipe flow. At the earlier integration stage, the stratified flow develops along the pipeline. An important difference from the smooth-pipe flow case is that, before the intruding water-air front can reach the outlet, a gradually varying flow with a comparatively steep slope develops inside the horizontal pipe. Therefore, a wavy flow forms at the interior of the horizontal pipe, the wave crest of which, after merging with a secondary water front from the outlet, forms the hydraulic jump with concurrent slug flow in the downstream region. The comparatively short air pocket entrapped near the pipe bridge and the formation of more-or-less periodic slug flow along the pipeline are presented in Figure 31a. A difference in velocity changes over the vertical cross-sections, where stratified and fully-developed flows in pressurised pipes merge (with respect to smooth pipe flow), is that the interface of the transition flow part is more suppressed in the along-pipe direction. This effect may be explained by the slightly modified formation of the slugs, which demonstrate a more-or-less periodic pattern. The vertical distribution of eddy viscosity is shown in Figure 31c. It can be seen that the maximum eddy-viscosity is associated with the surfaces of stratified flow at the hydraulic-jump region, where the velocity shear is substantially increased, compared to the smooth-pipe flow.
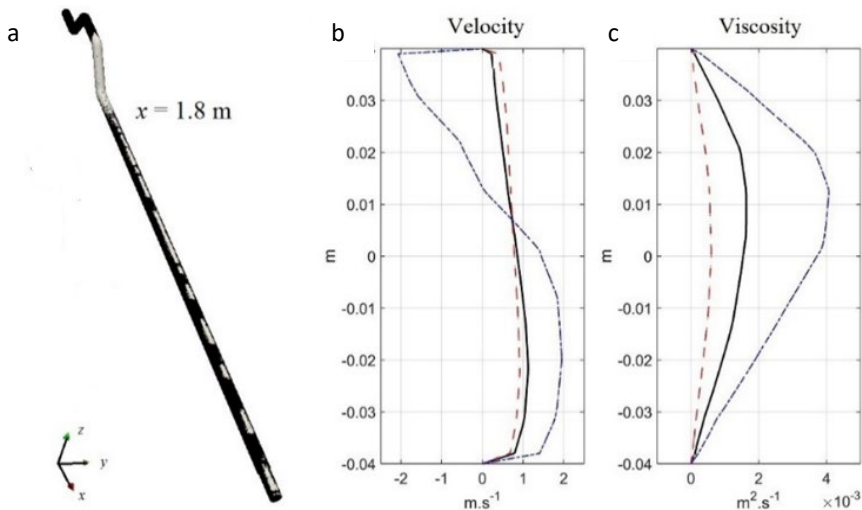
Figure 31. Rougher pipe flow case. (a) Visual of the air pocket and slug flow formation. (b) Vertical distribution of along-pipe velocity (x-axis component) at cross-sections (dash-dotted curve at x = 1.6 m; continuous line at x = 1.8 m; dashed curve at x = 2.0 m). (c) Vertical distribution of eddy viscosity at cross-sections (dash-dotted curve at x = 1.6 m; continuous line at x = 1.8 m; dashed curve at x = 2.0 m) (Laanearu & Kaur, 2018).

3.3.2 Flow in Complex Geometry Pipes

The roughness and geometry effects were numerically analysed in more detail for fully filled pipe flow in Annus et al. (2019) and Kaur et al. (2020).

A preliminary study of the pipe with an abrupt change in diameter was conducted in Annus et al. (2016), where the performance of solution algorithms of Ansys Fluent and OpenFOAM softwares and of standard k-ω and k-ε, realisable k-ε and Shear Stress Transport k-ω turbulence models were compared. In Annus et al. (2019) slight modifications were implemented in the standard k-ε turbulence model coefficients. Figure 32 contains images of the computational domains used in Annus et al. (2016) and Annus et al. (2019).
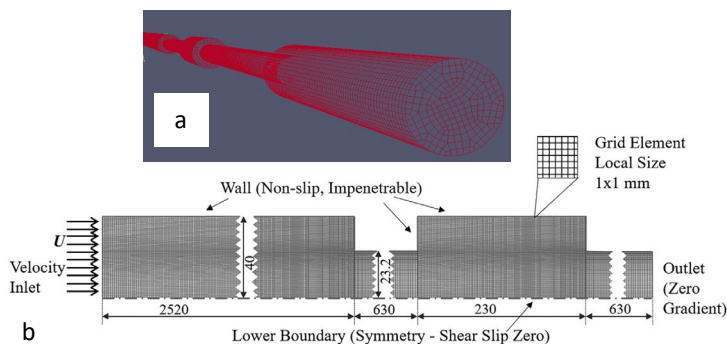
Figure 32. Computation domains of the pipe with abrupt change in diameter in (a) Annus et al. (2016) and (b) Annus et al. (2019).

For the numerical study of Annus et al. (2019), a two-dimensional model, representing the expanding and contracting pipeline, was constructed with physical dimensions. The computational domain was discretised by a structured grid. By comparing modelling results with different pipe segment lengths in the upstream and downstream end of the test section with PIV measurements, it was found that it is essential to include all geometrical elements that affect the flow in the study area in the model. Finally, a 4 m long section of the pipe was included in the numerical analysis. For a grid uncertainty study, the grid convergence index method was used. The numerical simulations were carried out, both in stationary and nonstationary model set-up conditions, and compared. It was concluded that, for this case, the models describe the developed flow in a similar way.

Two turbulence model closure coefficients were finally modified from $C_{1\varepsilon} = 1.44$, $C_{2\varepsilon} = 1.92$ to $C_{1\varepsilon} = 1.4$, $C_{2\varepsilon} = 2.0$ to slightly alter the turbulence dissipation behaviour. The effect of modifying the coefficients was investigated as the abrupt change in diameter generated additional vortices in the flow and the standard k-ε turbulence model is generally valid for simple boundary layer flow (Davidson, 2006). The flow through the middle section between the expansion and contraction behaves like a jet. Previous studies for round jet type flows (Launder et al., 1972; Pope, 1978) indicated that the usage of standard turbulence constants produces large errors and the constants are not universal (Smith et al., 2004). Figure 33 shows the change in axial velocity and turbulent kinetic energy for experiments 1 and 2 (Table 1), at the pipe axis. The horizontal axis represents the length of the PIV box (Figure 21a), where $x = 0$ mm is the inflow and $x = 230$ mm is the outflow from the box (Annus et al., 2019).
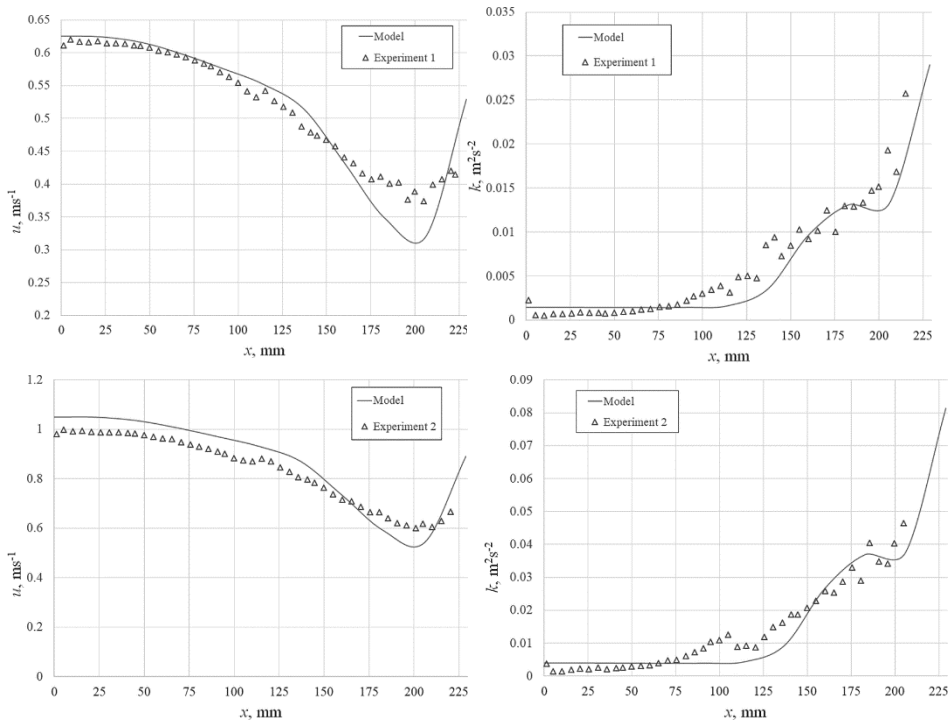
Figure 33. Comparison of the measured and modelled axial velocity and turbulent kinetic energy at the pipe axis. Exp. 1 Q=0.75 l/s and exp. 2 Q=1.245 l/s (Annus et al., 2019).

The uneven roughness build-up was classified in Annus et al. (2020) and the geometry of one roughness element was proposed. The impact of this element on the velocity field of water flow has been further investigated in Kaur et al. (2020). The view of the element situated on the invert of a pipe section is seen in Figure 34.
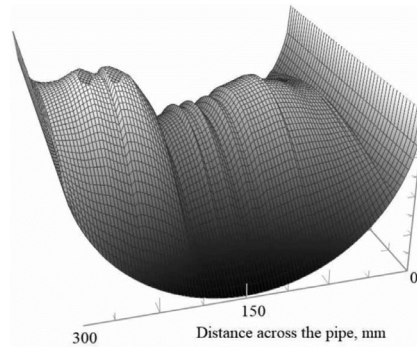
Figure 34. Roughness element (Kaur et al., 2020).

The elements were bruised into the pipe wall at two and four locations over the pipe length, to mimic the irregular inner surface of a typical old rough pipe (see Figure 21b). The surface pattern was applied to the test pipe, both on the top, and on the bottom side. The internal diameter of the analysed pipe was 300 mm and length 1500 mm. The CFD calculations were performed at six different pressure drops between the pipe segment inlet and outlet, ranging from 50 to 2500 Pa. The corresponding flow rates were calculated at each pressure drop, while the pipe surface sand-grain roughness was set to 1 mm. The numerical simulations were conducted using the SIMPLE algorithm and the flow was considered turbulent.

The grid sensitivity study was conducted, based on a slightly more complex computational domain configuration, with eight of the roughness elements inside the pipe, of 100 mm diameter. The way that the flowrate in the domain changes while the grid refinement level is raised was analysed. By comparing meshes with 0.56, 1.45 and 2.77 million elements (Figure 35), it was seen that the difference in the flow rate value for two higher resolutions was 1% and, therefore, the middle resolution was chosen; for the larger diameter pipe, the grid elements were scaled accordingly.
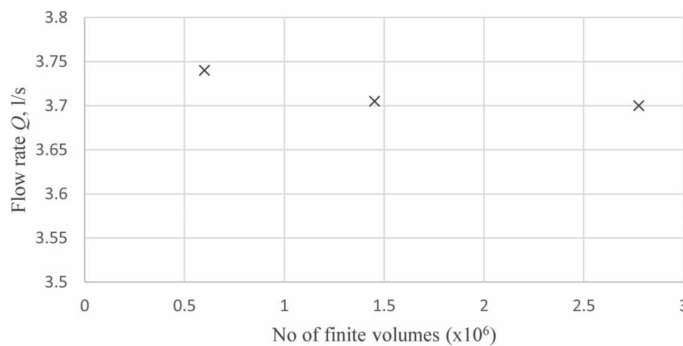
Figure 35. Calculated flow rate for three different grid sizes (Kaur et al., 2020).

The numerical analysis confirmed a qualitative similarity to experiments as the developing eddies behind the roughness elements change in size with different pressure drops for some configurations while, for others, they remain constant. This is dependent on the distance between the wall deformations. Therefore, depending on the spatial distribution, roughness elements nearing the radius of the pipe (in size) may be considered as local obstructions or as near-even sand grain roughness with a large height. Figure 36 shows the comparison of eddy formation for different numbers of roughness elements.
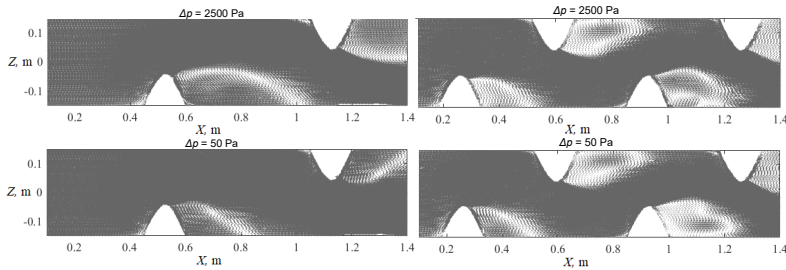
Figure 36. Comparison of eddy formation behind roughness elements for two and four elements (Kaur et al., 2020).

3.3.3 Inverted Siphon

The presence of an inverted siphon in a stormwater system is one of the causes of flow transitions (Hamam, 1982). To investigate the effect that the presence of sediment-loaded water has on the operating conditions of an inverted siphon, a numerical study was conducted by Kaur et al. (2017). It was demonstrated that the multi-phase flow processes are associated with the malfunctioning of stormwater systems during intense rain events. The inverted siphon under investigation here is located at Tallinn, Estonia (see Figure 37).
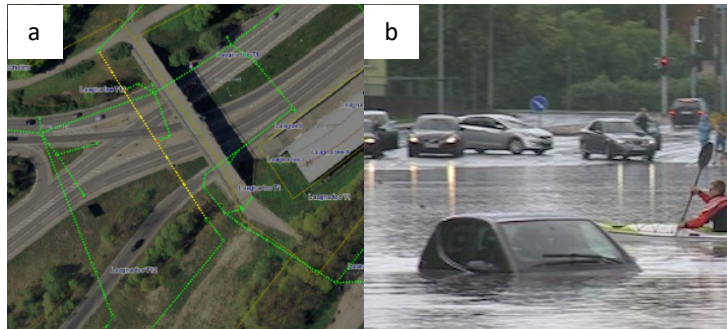
Figure 37. (a) 90 m single line inverted siphon under Laagna Road, Tallinn, Estonia, denoted with yellow line; image by K-projekt. (b) Flooding at Laagna Road, Tallinn, 10.07.2016; image by Estonian Public Broadcasting.

The hydraulic system (Figure 38) consists of two reinforced-concrete chambers at the inlet and outlet, which both include a manhole on top. The inlet and outlet chambers at the sides are equipped with inflow and outflow pipes, respectively. The inlet and outlet chambers are connected by the siphoned part, consisting of a pipeline with an inner diameter of 800 mm and a length of 90 m. The inverted siphon is constructed from centrifugally cast fiberglass-reinforced, polymer mortar pipes, which is characterised with an approximate Manning's roughness coefficient of n = 0.015 (Kaur et al., 2017).
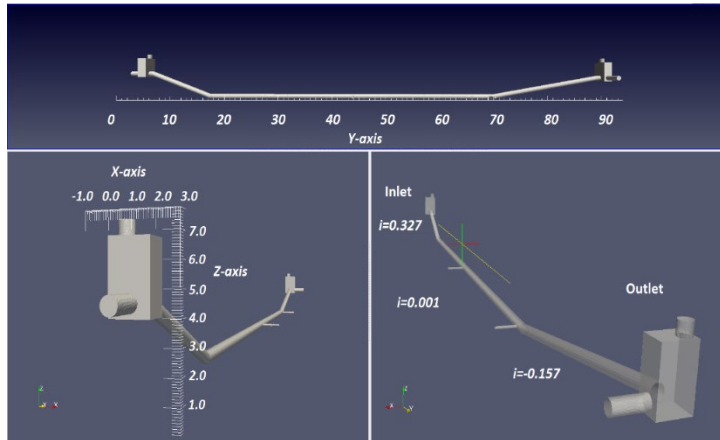
Figure 38. Geometric representation of the inverted siphon under Laagna Road in Tallinn, with dimensions and slopes indicated (Kaur et al., 2017).

Two approaches were used for the CFD investigation of flow dynamics in the inverted siphon. Initially, the OpenFOAM two-phase solver interFoam for two immiscible fluids was used to separately model air and water and water and slurry-fluid flows (Figure 39b). Secondly, to investigate the slurry-fluid's effect on flow dynamics more comprehensively, an OpenFOAM solver for n-phases (multiphaseInterFoam), developed on the logic of interFoam, was used (Figure 39a). This solver captures the interfaces and includes surface-tension and contact-angle effects for each phase pair. To increase consistency between hydraulic modelling results and CFD simulations, a rough wall function was also implemented in the modelling. Hydraulic modelling of a fully filled steady-state flow to determine head losses, hydraulic gradients and wall shear stresses at certain Reynolds numbers in the expected operational range, is presented in Kaur et al. (2016).
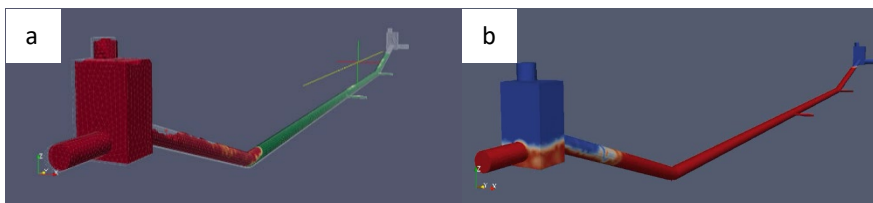
Figure 39. (a) modelling of three-phase flow in the inverted siphon; (b) modelling of two-phase flow in the inverted siphon.

Instead of the steady hydraulically driven flow, the computational results revealed unexpected unsteady two-phase flow dynamics with the design flow rates. The numerical study of the inverted siphon under Laagna road in Tallinn revealed quasi-stationary pressure oscillations with a characteristic period, while air-water-flow and fully filled water flow regimes alternated. When the driving pressure-head was high, the air was expelled effectively out of the siphoned part and the flow accelerated. The flow acceleration resulted in the water level drop in the inlet chamber, which, in turn, caused air intake into the pipeline. As a result, the pressure-head was raised until another cycle of flow acceleration.

Pluvial flooding associated with heavy rainfall and the capacities of the stormwater network can tentatively be classified into two categories: (1) street flooding induced by

water outflow from manholes; (2) street flooding induced by restricted inflow of rainwater through manhole gullies and grates due to the outflow of air, induced by multi-phase flow processes inside the pipeline. Based on the modelled behaviour in this study, it is concluded that the flooding induced by air outflow from the manholes will last for a short time interval and may be periodic in nature.

3.4 Discussion

In this chapter, the numerical and experimental investigation of the two-phase air-water flow in a horizontal pipe has been presented, together with studies related to roughness and geometry effects. It may be concluded that the behaviour of flow transition, from stratified to slug flow via mobile hydraulic jump, is dependent on filling ratio for different scale pipes, with a smaller filling ratio resulting in a relatively slower roller advancement in the pipe. For all cases, the mobile hydraulic jump will move inside the pipe with a changing velocity and may create vacuum conditions. Additionally, the air-water mixed flow patterns are dependent on the pipe layout and wall roughness. Changes in conduit geometry may cause a change in effective flow area and the occurrence of recirculation zones, for some cases resulting in adverse effects on upstream flow and initiating the flow regime transition. Furthermore, in terms of modelling, while additional vortices are generated in the flow, standard turbulence models (e.g. standard k-ε turbulence model) may result in velocity and turbulence fields not in accordance with empirical results.

Air trapped inside the sewer can cause a range of problems, which may result in the malfunctioning of urban infrastructure, e.g. lifting of manhole covers etc. Also, water flooding is possible, when the pressure is increased to a head that exceeds the grade elevation. It was demonstrated herein that, at a targeted inflow, the flow regime may undergo a transition from stratified to pressurised flow. Different types of pressurisation scenarios of a sewer are possible, resulting in volumetric water-flux differences between inflow and outflow. In the present study, the pipe bridge was used to produce the stratified flow which, during the rapid filling of a horizontal pipe, became unstable, resulting in the formation of mobile hydraulic jump that travelled upstream. Due to the formation of the pressurisation bore, a pressure difference across the jump is generated and, therefore, during the pipeline filling process, the outflow of water is possible. The alternative scenario, where a sloped pipeline section in the sewer becomes pressurised, is described by Politano et al. (2007). In this case, i.e. during the filling of an inclined pipe, pressurisation may be started due to restricted outflow. As the sewer is fed from the manholes, an air-water interface travels toward the upstream end. This less air-water-mixing dependent case can also result in pressurisation of the sewer with possible flooding.

Future works associated with this study should concern the improvement of the experimental procedure. In this thesis, the experimental measurements were conducted for the water phase only. To clarify the air entrainment process, measurement of the air phase in laboratory conditions is also needed. Furthermore, due to the apparent prevalence of the occurrence of transitional flow conditions, field tests should be considered. Flooding, damage to the sewer system, and possibly geysering (water jets shooting vertically up into the atmosphere) could be partially avoided by determining the transition conditions in sewers.

In newly designed sewers the pressure-testing conditions can be established by introducing supercritical flow in the pipeline section, which has no air-exchange through manholes. During the filling process, when the air-pocket forms, the velocity of the

pressurisation bore determines the hydraulic system testing period. For new systems making use of design operating conditions, it is also possible to carry out numerical testing of the dynamic multi-phase processes. The current confidence level of applicability to new systems highlights the practical limitations of this work. As the majority of experimental data presented herein was gathered on relatively small-scale apparatus and the comparison is made with few large-scale data points, the scalability may yet be considered to be an open question. Furthermore, as the operating conditions are controlled in the laboratory setting and are unknown in in-service systems, to some extent, drawing one-to-one conclusions may be premature. Conversely, as the urban water systems are an expensive and extensive infrastructure, most of the pipelines have been in use for many years, even decades, with rehabilitation (i.e. replacement and renovation) strategies aimed at extending the useful life span. Therefore, to further validate the applicability of numerical models, like the one applied to in-service systems herein, large-scale field testing would be needed.

Several national guidelines propose to subject storm sewers to leak-tightness (water) and pressure (air-tightness) tests in the pre-operation phase, after construction. Conventional testing of piping systems can be carried out by means of water or air under stationary conditions. Additional testing of piping sections, e.g. pipes with manholes, should be undertaken for dynamic conditions where air and water are mixed. The testing procedure would include the generation of the air-water process in a section between manholes. To detect the surcharging, pressure gauges should be installed in manhole covers during surge testing. Preferably, the surge tests could be carried out as a continuation of the leak-tightness test.

The mechanically closed covers can be equipped with pressure transducers. The recording of the pressure changes during the filling process of the specifically designed sewer experiment (Figure 40) would help avoid accidents with manhole cover displacements. In engineering practice, documentation about accidents with sewer manholes, sometimes with casualties, are well reported (Crimaldi & Ramos, 2016; Wright et al., 2011), but it is not common practice to record in situ measurements of flow conditions which would identify these hazardous situations. There can be different causes of air pressurisation in manholes, including the release of entrapped air pockets. It is apparent that such releases will result in the displacement of the free surface within the manholes, potentially creating enough air pressure to overcome the weight of an unfixed manhole cover.
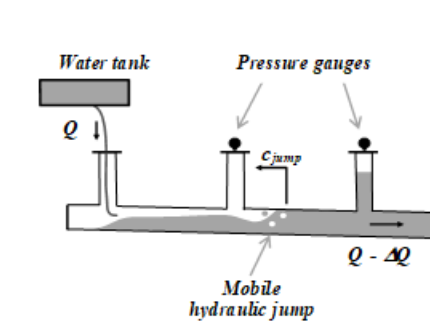
Figure 40. Schema of sewer surge test.

4 Concluding Remarks

This study has provided experimental evidence for the formation of an air pocket when a horizontal pipe is filled with water through a pipe bridge. The investigated filling process had three stages, distinguished as: air cavity formation, air pocket formation, and air entrainment. The formation of an air cavity was explained by the flow number. For the air pocket formation explanation, different dimensionless numbers were used in the parameterisation process. It was concluded that, in the case where air flow rate is negligible, the instability resulting in a mobile hydraulic jump can be predicted based on a single-phase flow concept and characterised based on the Froude number condition. For the mobile hydraulic jump roller, the mixing efficiency parameter was introduced for air-water mixed flow conditions in conduits, to explain the dissipation of turbulent energy in the transitional flow due to a suppressed hydraulic jump, which merged the stratified flow with slug flow. Based on the positive flux Richardson number, it was concluded that the buoyancy fluxes suppress the turbulence through the hydraulic jump development stage, facilitating the re-separation of the mixed phases. It was found that the pressurisation bore in the pipeline filling process is characterised by the mobile hydraulic jump speed, which is essentially determined by the pressure, the cross-sectional area of water flow, and the density jumps.

The experiments were used to validate the numerical model. The multi-phase model used in this thesis is based on the VOF-type method for immiscible fluids, such as air and water. The VOF method has been validated as being suitable for investigating the multi-phase flow in stormwater systems. The VOF model in this thesis was first coupled with the standard k- ε model but concurrency with experimental data was found to be insufficient and, therefore, the RNG k- ε model was taken into use. The full-scale two-phase model with RNG k-ε turbulence showed good agreement, in terms of air pocket formation. The measured and modelled values for velocity and the turbulent kinetic energy profiles during the stages of the transitional flow process were compared, and it was concluded that the modelling allowed for qualitative and quantitative interpretation of the air pocket dynamics during filling of the pipe.

The numerical modelling revealed that a pipe's internal geometry and roughness significantly affect the flow dynamics. Based on the analysis, the mobile hydraulic jump formation in closed conduits can tentatively be grouped according to four root causes: (1) local geometry change jump – occurs when there are local obstructions in the pipe that change the effective flow diameter. (2) Conduit roughness jump – forms with the gradually varied flow due to wall-roughness effects. (3) Pipe layout instability jump – the bridging due to flow instabilities is made possible by small perturbations in the flow being carried downstream. The conditions for the occurrence of the interfacial instabilities are directly linked with the pipe layout, such as pipe connections and alignments. (4) Pipe-slope jump – occurs due to sloping pipes and the more-or-less periodic flow behaviour. This will result in air flow oscillations near the slope, possibly causing air flowing out of manholes periodically and restricting water inflow.

List of Figures

References

Adams, T., Grant, C., & Watson, H. (2012). A simple algorithm to relate measured surface roughness to equivalent sand-grain roughness. *International Journal of Mechanical Engineering and Mechatronics*, *1*(2), 66–71. https://doi.org/10.11159/ijmem.2012.008

Andersson, B. (Ed.). (2012). *Computational fluid dynamics for engineers*. Cambridge University Press.

Annus, I., Kartushinsky, A., Vassiljev, A., & Kaur, K. (2019). Numerical and experimental investigation on flow dynamics in a pipe with an abrupt change in diameter. *Journal of Fluids Engineering*, *141*(10), 101301. https://doi.org/10.1115/1.4043233

Annus, I., Kaur, K., Vassiljev, A., Laanearu, J., & Šanin, M. (2016). Flow dynamics in a pipe with a sudden change in diameter. *14th International Computing and Control for the Water Industry (CCWI) Conference*.

Annus, I., Vassiljev, A., Kändler, N., & Kaur, K. (2020). Determination of the corresponding roughness height in a WDS model containing old rough pipes. *Journal of Water Supply: Research and Technology-Aqua*, *69*(3), 201–209. https://doi.org/10.2166/aqua.2019.080

ANSYS, Inc. (2011). *Ansys fluent theory guide*.

Axworthy, D. H., Karney, B. W., Cabrera, E., Izquierdo, J., Abreu, J., Iglesias, P. L., Liou, C. P., & Hunt, W. A. (1997). Discussions and closure: Filling of pipelines with undulating elevation profiles. *Journal of Hydraulic Engineering*, *123*(12), 1170–1174. https://doi.org/10.1061/(ASCE)0733-9429(1997)123:12(1170)

Bardina, J., Ferziger, J., & Reynolds, W. (1980, July 14). Improved subgrid-scale models for large-eddy simulation. *13th Fluid and Plasma Dynamics Conference*. 13th Fluid and Plasma Dynamics Conference, Snowmass, CO, U.S.A. https://doi.org/10.2514/6.1980-1357

Benjamin, T. B. (1968). Gravity currents and related phenomena. *Journal of Fluid Mechanics*, *31*(2), 209–248. https://doi.org/10.1017/S0022112068000133

Bird, R. B., Stewart, W. E., & Lightfoot, E. N. (2002). *Transport phenomena* (2nd ed.). John Wiley & Sons, Inc.

Bombardelli, F. A., Hirt, C. W., & García, M. H. (2001). Discussion on Computations of Curved Free Surface Water Flow on Spiral Concentrators. *Journal of Hydraulic Engineering*, *127*(7), 629–631. https://doi.org/10.1061/(ASCE)0733-9429(2001)127:7(629)

Boris, J., & Book, D. (1973). Flux-corrected transport. I. SHASTA, a fluid transport algorithm that works. *Journal of Computational Physics*, *11*, 38–69.

Bozkus, Z., & Wiggert, D. C. (1997). Liquid slug motion in a voided line. *Journal of Fluids and Structures*, *11*(8), 947–963. https://doi.org/10.1006/jfls.1997.0112

Brennen, C. E. (2005). *Fundamentals of multiphase flow*. Cambridge University Press.

Caretto, L. S., Gosman, A. D., Patankar, S. V., & Spalding, D. B. (1973). Two calculation procedures for steady, three-dimensional flows with recirculation. In H. Cabannes & R. Temam (Eds.), *Proceedings of the Third International Conference on Numerical Methods in Fluid Mechanics* (pp. 60–68). Springer. https://doi.org/10.1007/BFb0112677

Cebeci, T., & Bradshaw, P. (1977). *Momentum transfer in boundary layers*. Hemisphere Publishing Corporation.

Černe, G., Petelin, S., & Tiselj, I. (2001). Coupling of the interface tracking and the two-fluid models for the simulation of incompressible two-phase flow. *Journal of Computational Physics*, *171*(2), 776–804. https://doi.org/10.1006/jcph.2001.6810

Chadwick, A., Morfett, J., & Borthwick, M. (2004). *Hydraulics in Civil and Environmental Engineering* (4th ed.). CRC Press. https://doi.org/10.1201/9780203140130

Chaudhry, M. H. (1979). *Applied hydraulic transients*. Van Nostrand Reinhold Company.

Chitale, K. C., Rasquin, M., Sahni, O., & Jansen, K. E. (2014). *Boundary Layer Adaptivity For Incompressible Turbulent Flows*. 22.

Chow, V. T. (1959). *Open-channel hydraulics*. McGraw-Hill.

Courant, R., Friedrichs, K., & Lewy, H. (1928). Über die partiellen Differenzengleichungen der mathematischen Physik. *Mathematische Annalen*, *100*(1), 32–74.

Crimaldi, L., & Ramos, N. (2016, February 12). Answers sought in manhole cover fatality on expressway. *Boston Globe*. https://www.bostonglobe.com/2016/02/12/woman-struck-flying-manhole-cover-inside-neill-tunnel-suffers-fatal-injuries/Okpvg6Jx6VF86xsYrA2ZRN/story.html

Davidson, P. A. (2006). *Turbulence. An introduction for scientists and engineers*. Oxford University Press.

Davies Wykes, M. S., Hughes, G. O., & Dalziel, S. B. (2015). On the meaning of mixing efficiency for buoyancy-driven mixing in stratified turbulent flows. *Journal of Fluid Mechanics*, *781*, 261–275. https://doi.org/10.1017/jfm.2015.462

Derksen, J., & Van den Akker, H. (1999). Large eddy simulations of stirred tank flow. *Engineering Turbulence Modelling and Experiments 4*, 257–266.

Douglas, C. (2014). *OpenFOAM tutorial snappyHexMesh*. Calum Douglas. https://www.calum-douglas.com/openfoam-tutorial-snappyhexmesh/

Eldayih, Y., Cetin, M., & Vasconcelos, J. G. (2020). Air-pocket entrapment caused by shear flow instabilities in rapid-filling pipes. *Journal of Hydraulic Engineering*, *146*(4), 04020016. https://doi.org/10.1061/(ASCE)HY.1943-7900.0001711

ESI Group. (n.d.). *OpenFOAM*. Retrieved June 8, 2021, from https://www.openfoam.com/

Falvey, H. T. (1980). *Air-water flow in hydraulic structures* (A Water Resources Technical Publication No. 41; Engineering Monograph). United States Department of the Interior, Water and Power Resources Service, Engineering and Research Center.

Ferziger, J. H., & Peric, M. (2002). *Computational methods for fluid dynamics* (3rd ed.). Springer.

Frank, T. (2003). *Numerical simulations of multiphase flows using CFX-5*. CFX Users conference, Garmisch-Partenkirchen, Germany.

Ghorai, S., & Nigam, K. D. P. (2006). CFD modeling of flow profiles and interfacial phenomena in two-phase flow in pipes. *Chemical Engineering and Processing: Process Intensification*, *45*(1), 55–65. https://doi.org/10.1016/j.cep.2005.05.006

Hager, W. H. (1999). Cavity outflow from a nearly horizontal pipe. *International Journal of Multiphase Flow*, 16.

Hamam, M. A. M. (1982). *Transition of gravity to surcharged flow in sewers*. University of Windsor.

Harlow, F. H., & Welch, J. E. (1965). Numerical calculation of time-dependent viscous incompressible flow of fluid with free surface. *Physics of Fluids*, *8*(12), 2182. https://doi.org/10.1063/1.1761178

Hirt, C. W., & Nichols, B. D. (1981). Volume of fluid (VOF) method for the dynamics of free boundaries. *Journal of Computational Physics*, *39*(1), 201–225. https://doi.org/10.1016/0021-9991(81)90145-5

Höhne, T., & Vallée, C. (2010). Experiments and numerical simulations of horizontal two-phase flow regimes using an interfacial area density model. *The Journal of Computational Multiphase Flows*, *2*(3), 131–143. https://doi.org/10.1260/1757-482X.2.3.131

Holzmann, T. (2019). *Mathematics, Numerics, Derivations and OpenFOAM(R)* (Release 7.0). Holzmann CFD. https://Holzmann-cfd.de, DOI: 10.13140/RG.2.2.27193.36960

Hou, Q., Tijsseling, A. S., Laanearu, J., Annus, I., Koppel, T., Bergant, A., Vučković, S., Anderson, A., & van 't Westende, J. M. C. (2014). Experimental investigation on rapid filling of a large-scale pipeline. *Journal of Hydraulic Engineering*, *140*(11), 04014053. https://doi.org/10.1061/(ASCE)HY.1943-7900.0000914

Issa, R. I. (1986). Solution of the implicitly discretised fluid flow equations by operator-splitting. *Journal of Computational Physics*, *62*(1), 40–65. https://doi.org/10.1016/0021-9991(86)90099-9

Issa, R. I., & Kempf, M. H. W. (2003). Simulation of slug flow in horizontal and nearly horizontal pipes with the two-fluid model. *International Journal of Multiphase Flow*, *29*(1), 69–95. https://doi.org/10.1016/S0301-9322(02)00127-1

Jones, W. P., & Launder, B. E. (1972). The prediction of laminarization with a two-equation model of turbulence. *International Journal of Heat and Mass Transfer*, *15*(2), 301–314. https://doi.org/10.1016/0017-9310(72)90076-2

Kaur, K., Annus, I., & Laanearu, J. (2018). Experimental measurements of momentum changes at hydraulic jump in a transparent horizontal pipe. *13th International Conference on Pressure Surges*, *2*, 937–948.

Kaur, K., Laanearu, J., & Annus, I. (2016). Using CFD to simulate multiphase flow in a large-scale inverted siphon: Tallinn storm-water system case study. *14th International Computing and Control for the Water Industry (CCWI) Conference*.

Kaur, K., Laanearu, J., & Annus, I. (2017). Numerical study of Tallinn storm-water system flooding conditions using CFD simulations of multi-phase flow in a large-scale inverted siphon. *IOP Conference Series: Materials Science and Engineering*, *251*, 012128. https://doi.org/10.1088/1757-899X/251/1/012128

Kaur, K., Laanearu, J., & Annus, I. (2023). Air pocket dynamics under bridging of stratified flow during rapid filling of a horizontal pipe. *Journal of Hydraulic Engineering*, *149*(1), 04022030. https://doi.org/10.1061/(ASCE)HY.1943-7900.0002021

Kaur, K., Vassiljev, A., Annus, I., Kändler, N., & Roosimägi, J. (2020). Numerical investigation of the impact of irregular pipe wall build-up on velocity in the water distribution system. *Journal of Water Supply: Research and Technology-Aqua*, *69*(7), 647–655. https://doi.org/10.2166/aqua.2020.035

Kaur, K., Vassiljev, A., Annus, I., Truu, M., & Kändler, N. (2022). *Flow dynamics in a pipe containing uneven roughness elements*. 2nd WDSA/CCWI Joint Conference, Valencia, Spain.

Kent, J. C. (1952). *The entrainment of air by water flowing in circular conduits with downgrade slope*. University of California.

Kordyban, E. (1990). Horizontal slug flow: A comparison of existing theories. *Journal of Fluids Engineering*, *112*(1), 74–83. https://doi.org/10.1115/1.2909372

Kundu, P. K., Cohen, I. M., & Dowling, D. R. (2012). *Fluid mechanics* (5th ed.). Academic Press, Elsevier.

Laanearu, J., Annus, I., Koppel, T., Bergant, A., Vučković, S., Hou, Q., Tijsseling, A. S., Anderson, A., & van't Westende, J. M. C. (2012). Emptying of large-scale pipeline by pressurized air. *Journal of Hydraulic Engineering*, *138*(12), 1090–1100. https://doi.org/10.1061/(ASCE)HY.1943-7900.0000631

Laanearu, J., Hou, Q., Annus, I., & Tijsseling, A. S. (2015). Water-column mass losses during the emptying of a large-scale pipeline by pressurized air. *Proceedings of the Estonian Academy of Sciences*, *64*(1), 8. https://doi.org/10.3176/proc.2015.1.02

Laanearu, J., & Kaur, K. (2018). Two-phase CFD modelling of air-water flow transition in a horizontal circular pipe and comparison with experimental results. *13th International Conference on Pressure Surges*, *2*, 937–948.

Laanearu, J., & van't Westende, J. (2010). Hydraulic characteristics of test rig used in filling and emptying experiments of large-scale PVC pipeline. *Proceedings of the HYDRALAB III Joint User Meeting*, 4.

Launder, B. E., Morse, A. P., Rodi, W., & Spalding, D. B. (1972). Prediction of free shear flows—A comparison of six turbulence models. *NASA Report Number SP-311*. NASA Free Shear Flows Conference.

Launder, B. E., & Spalding, D. B. (1974). The numerical computation of turbulent flows. *Computer Methods in Applied Mechanics and Engineering*, *3*, 269–289.

Leon, A. S., Ghidaoui, M. S., Schmidt, A. R., & Garcia, M. H. (2010). A robust two-equation model for transient-mixed flows. *Journal of Hydraulic Research*, *48*(1), 44–56. https://doi.org/10.1080/00221680903565911

Li, J., & McCorquodale, A. (1999). Modeling mixed flow in storm sewers. *Journal of Hydraulic Engineering*, *125*(11), 1170–1180. https://doi.org/10.1061/(ASCE)0733-9429(1999)125:11(1170)

Lin, P. Y., & Hanratty, T. J. (1986). Prediction of the initiation of slugs with linear stability theory. *International Journal of Multiphase Flow*, *12*(1), 79–98. https://doi.org/10.1016/0301-9322(86)90005-4

Liou, C. P., & Hunt, W. A. (1996). Filling of pipelines with undulating elevation profiles. *Journal of Hydraulic Engineering*, *122*(10), 534–539. https://doi.org/10.1061/(ASCE)0733-9429(1996)122:10(534)

Malekpour, A., & Karney, B. W. (2011). Rapid filling analysis of pipelines with undulating profiles by the method of characteristics. *ISRN Applied Mathematics*, *2011*, 1–16. https://doi.org/10.5402/2011/930460

Marongiu, J. C., Leboeuf, F., & Parkinson, E. (2007). Numerical simulation of the flow in a Pelton turbine using the meshless method smoothed particle hydrodynamics: A new simple solid boundary treatment. *Proceedings of the Institution of Mechanical Engineers, Part A: Journal of Power and Energy*, *221*, 6.

Marongiu, J.-C., Leboeuf, F., Caro, J., & Parkinson, E. (2010). Free surface flows simulations in Pelton turbines using an hybrid SPH-ALE method. *Journal of Hydraulic Research*, *48*(sup1), 40–49. https://doi.org/10.1080/00221686.2010.9641244

Milne-Thomson, L. M. (1938). *Theoretical hydrodynamics*. Macmillan.

Moukalled, F., Mangani, L., & Darwish, M. (2016). *The finite volume method in computational fluid dynamics: An advanced introduction with openFOAM® and MATLAB®* (Vol. 113). Springer.

Oberkampf, W. L., & Trucano, T. G. (2002). Verification and validation in computational fluid dynamics. *Progress in Aerospace Sciences*, 64.

Ogden, K. A., & Helfrich, K. R. (2016). Internal hydraulic jumps in two-layer flows with upstream shear. *Journal of Fluid Mechanics*, *789*, 64–92. https://doi.org/10.1017/jfm.2015.727

OpenCFD Ltd. (n.d.). *OpenFOAM: User Guide v2112*. https://www.openfoam.com/documentation/guides/latest/doc/index.html

OpenFOAMWiki. (n.d.). *OpenFOAM guide/The SIMPLE algorithm in OpenFOAM*. Retrieved October 16, 2022, from https://openfoamwiki.net/index.php/OpenFOAM_guide/The_SIMPLE_algorith m_in_OpenFOAM

Orszag, Staroselsky, Flannery, & Zhang. (1996). Introduction to renormalization group modeling of turbulence. *Simulation and Modeling of Turbulent Flows*, 155–183.

Politano, M., Odgaard, A. J., & Klecan, W. (2007). Case study: Numerical evaluation of hydraulic transients in a combined sewer overflow tunnel system. *Journal of Hydraulic Engineering*, *133*(10), 1103–1110. https://doi.org/10.1061/(ASCE)0733-9429(2007)133:10(1103)

Pope, S. B. (1978). An explanation of the turbulent round-jet/plane-jet anomaly. *AIAA Journal*, *16*(3), 279–281. https://doi.org/10.2514/3.7521

Pope, S. B. (2000). *Turbulent flows*. Cambridge University Press. https://doi.org/10.1017/CBO9780511840531

Pothof, I. (2011). *Co-current air-water flow in downward sloping pipes* [Delft University of Technology]. http://resolver.tudelft.nl/uuid:9fb08bee-8443-48b5-a127-13544eed87a7

Pratt, L. J. (1986). Hydraulic control of sill flow with bottom friction. *Journal of Physical Oceanography*, *16*(11), 1970–1980.

Resch, F. J., & Leutheusser, H. J. (1972). Reynolds stress measurements in hydraulic jumps. *Journal of Hydraulic Research*, *10*(4), 409–430. https://doi.org/10.1080/00221687209500033

Ruder, Z., & Hanratty, T. J. (1990). A definition of gas-liquid plug flow in horizontal pipes. *International Journal of Multiphase Flow*, *16*(2), 233–242. https://doi.org/10.1016/0301-9322(90)90056-O

Schall, J. D., & Richardson, E. V. (1997). *Hydraulic design series no. 4 Introduction to highway hydraulics* (FHWA HI 97-028). Federal Highway Administration.

Schulz, H. E., Vasconcelos, J. G., & Patrick, A. C. (2020). Air entrainment in pipe-filling bores and pressurization interfaces. *Journal of Hydraulic Engineering*, *146*(2), 04019053. https://doi.org/10.1061/(ASCE)HY.1943-7900.0001672

Shih, T.-H., Zhu, J., & Lumley, J. L. (1996). Calculation of wall-bounded complex flows and free shear flows. *International Journal for Numerical Methods in Fluids*, *23*, 1133–1144.

Smith, E. J., Mi, J., Nathan, G. J., & Dally, B. B. (2004). *Preliminary examination of a 'Round jet initial condition anomaly' for the k–ε Turbulence model*. 15th Australasian Fluid Mechanics Conference, Sydney, Australia.

Smith, L. M., & Woodruff, S. L. (1998). Renormalization-group analysis of turbulence. *Annual Review of Fluid Mechanics*, *30*, 275–310.

Sussman, M., Smereka, P., & Osher, S. (1994). A level set approach for computing solutions to incompressible two-phase flow. *Journal of Computational Physics*, *114*(1), 146–159. https://doi.org/10.1006/jcph.1994.1155

Taitel, Y., & Dukler, A. E. (1976). A model for predicting flow regime transitions in horizontal and near horizontal gas-liquid flow. *AIChE Journal*, *22*(1), 47–55. https://doi.org/10.1002/aic.690220105

Tryggvason, G., Scardovelli, R., & Zaleski, S. (2011). *Direct Numerical Simulations of Gas–Liquid Multiphase Flows* (1st ed.). Cambridge University Press. https://doi.org/10.1017/CBO9780511975264

USACE. (1980). *Engineering and design: Hydraulic design of reservoir outlet works* (No. 1110-1–1602; Engineering Manual).

Vasconcelos, J. G., Klaver, P. R., & Lautenbach, D. J. (2015). Flow regime transition simulation incorporating entrapped air pocket effects. *Urban Water Journal*, *12*(6), 488–501. https://doi.org/10.1080/1573062X.2014.881892

Vasconcelos, J. G., & Wright, S. J. (2006). Mechanisms for air pocket entrapment in stormwater storage tunnels. *World Environmental and Water Resource Congress 2006*, 1–10. https://doi.org/10.1061/40856(200)9

Vasconcelos, J. G., & Wright, S. J. (2009). Investigation of rapid filling of poorly ventilated stormwater storage tunnels. *Journal of Hydraulic Research*, *47*(5), 547–558. https://doi.org/10.3826/jhr.2009.3390

Vasconcelos, J. G., Wright, S. J., & Roe, P. L. (2006). Improved simulation of flow regime transition in sewers: Two-component pressure approach. *Journal of Hydraulic Engineering*, *132*(6), 553–562. https://doi.org/10.1061/(ASCE)0733-9429(2006)132:6(553)

Wallis, G. B., & Dodson, J. E. (1973). The onset of slugging in horizontal stratified air-water flow. *International Journal of Multiphase Flow*, *1*(1), 173–193. https://doi.org/10.1016/0301-9322(73)90010-4

Weller, H. G. (2005). *Derivation, Modelling and Solution of the Conditionally Averaged Two-Phase Flow Equations* (TR/HGW/02; p. 30). CFD Direct Limited.

White, F. M. (2009). *Fluid mechanics* (7th ed.). McGraw-Hill.

Wiggert, D. C. (1972). Transient flow in free-surface, pressurized systems. *Journal of the Hydraulics Division*, *98*(1), 11–27. https://doi.org/10.1061/JYCEAJ.0003189

Wimhurst, A. (n.d.). *Fluid mechanics 101*. Retrieved October 16, 2022, from https://www.fluidmechanics101.com/pages/lectures.html

Wright, S. J., Lewis, J. W., & Vasconcelos, J. G. (2011). Physical processes resulting in geysers in rapidly filling storm-water tunnels. *Journal of Irrigation and Drainage Engineering*, *137*(3), 199–202. https://doi.org/10.1061/(ASCE)IR.1943-4774.0000176

Yadigaroglu, G., & Hewitt, G. F. (Eds.). (2018). *Introduction to Multiphase Flow: Basic Concepts, Applications and Modelling*. Springer International Publishing. https://doi.org/10.1007/978-3-319-58718-9

Yakhot, V., & Orszag, S. A. (1986). Renormalization-group analysis of turbulence. *Physical Review Letters*, *57*(14), 1722–1724. https://doi.org/10.1103/PhysRevLett.57.1722

Yakhot, V., Orszag, S. A., Thangam, S., Gatski, T. B., & Speziale, C. G. (1992). Development of turbulence models for shear flows by a double expansion technique. *Physics of Fluids A: Fluid Dynamics*, *4*(7), 1510–1520. https://doi.org/10.1063/1.858424

Yen, B. C. (2001). Hydraulics of sewer systems. In *Stormwater Collection Systems Design Handbook*. McGraw-Hill.

Zhou, F., Hicks, F. E., & Steffler, P. M. (2002). Transient flow in a rapidly filling horizontal pipe containing trapped air. *Journal of Hydraulic Engineering*, *128*(6), 625–634. https://doi.org/10.1061/(ASCE)0733-9429(2002)128:6(625)

Zhou, L., Cao, Y., Karney, B., Bergant, A., Tijsseling, A. S., Liu, D., & Wang, P. (2020). Expulsion of entrapped air in a rapidly filling horizontal pipe. *Journal of Hydraulic Engineering*, *146*(7), 04020047. https://doi.org/10.1061/(ASCE)HY.1943-7900.0001773

Zhou, L., Pan, T., Wang, H., Liu, D., & Wang, P. (2019). Rapid air expulsion through an orifice in a vertical water pipe. *Journal of Hydraulic Research*, *57*(3), 307–317. https://doi.org/10.1080/00221686.2018.1475427

Zhou, L., Wang, H., Karney, B., Liu, D., Wang, P., & Guo, S. (2018). Dynamic behavior of entrapped air pocket in a water filling pipeline. *Journal of Hydraulic Engineering*, *144*(8), 04018045. https://doi.org/10.1061/(ASCE)HY.1943-7900.0001491

Zhu, D. Z., & Lawrence, G. A. (2000). Hydraulics of exchange flows. *Journal of Hydraulic Engineering*, *126*(12), 921–928. https://doi.org/10.1061/(ASCE)0733-9429(2000)126:12(921)

Zukoski, E. E. (1966). Influence of viscosity, surface tension, and inclination angle on motion of long bubbles in closed tubes. *Journal of Fluid Mechanics*, *25*(4), 821–837. https://doi.org/10.1017/S0022112066000442

Acknowledgements

This work would not have been possible without constant support from my supervisors and colleagues at TalTech. I am ever grateful to my supervisor, Prof. Janek Laanearu for guiding me throughout my studies and always being ready for a thought-provoking discussion. I sincerely thank my co-supervisor, Prof. Ivar Annus, who has been irreplaceable in coaching me towards conducting experimental investigations at the Laboratory of Fluid Mechanics at TalTech, among so many other things. I also express my warmest gratitude to my colleagues from TalTech Urban Water Systems Research group for their support, feedback and for providing an excellent working and research environment. Last but not least, I owe my deepest gratitude to my ever-supportive family, and especially to Kristjan.

Abstract

Dynamic Processes of Air-Water Flows in Urban Water Systems

The focus of the thesis is the air–water interactions during pipe filling. The work was motivated by the objective of validating the applicability of finite volume method solvers for storm sewer flow analysis. For this purpose, a numerical and experimental investigation was performed. With a better understanding of the dynamic processes affecting the urban water infrastructure, it is possible to alleviate the risk of pluvial flooding.

Air-filled stormwater pipelines experience different filling ratios of water and, depending on the boundary conditions, the system may become surcharged, sometimes resulting in a mixed flow regime of gravity and pressurised flow. The air–water mixed flow is related to a mobile hydraulic jump in the horizontal pipe section.

There are no clear criteria for predicting the formation of mobile hydraulic jumps in poorly ventilated pipelines with concurrent air pocket entrapment during filling and the air flow velocity is insignificant. It is likely that several types of instabilities contribute in different proportions in different stages of the flow. It is proposed that the formation of the pipe layout-related instability jump is related to the stratified flow instability of long-wave type.

The mobile hydraulic jump that merges stratified flow and slug flow is characterised by the speed of the surge wave, which is determined by the pressure, cross-sectional area of water flow, and density changes. The flow transitions in storm sewers, and other urban water systems, may take place due to geometry effects or fluid and flow properties. Therefore, in this thesis, single, two and three-phase flow has been investigated under different geometrical configurations.

For the mobile hydraulic jump roller, the mixing efficiency parameter, based on the flux Richardson number, was introduced for air-water mixed flow conditions. The mixing efficiency was calculated based on modelled flow field data and a good concurrence was found, with the profile indicating a region of the roller where the phases were not well mixed and a region where the buoyancy fluxes suppress the turbulence.

The numerical modelling revealed how the pipe's internal geometry and roughness affect the flow dynamics. Based on the analysis, the mobile hydraulic jump formation in closed conduits can tentatively be grouped into types of local geometry change jump, conduit roughness jump, pipe layout instability jump, and pipe-slope jump. The latter may, under certain conditions, cause oscillating behaviour and cause the air to periodically flow out of manholes and restrict water inflow. This type of pluvial flooding contrasts with the state where water is escaping from the manhole to the street surface.

Lühikokkuvõte

Õhu ja vee koosvoolamise dünaamilised protsessid linna veesüsteemides

Doktoritöö keskendub õhu ja vee vastastikmõjudele torude täitmisel. Töö on ajendatud eesmärgist valideerida lõplike mahtude meetodi lahendusalgoritmi rakendatavust sademekanalisatsiooni voolamise analüüsis. Sel eesmärgil viidi läbi numbriline ja eksperimentaalne uurimus. Linna veeinfrastruktuuri mõjutavate dünaamiliste protsesside parema mõistmisega on võimalik maandada sademeveekanalisatsioonist lähtuva üleujutuse ohtu.

Õhuga täidetud sademeveetorustikud võivad piiritingimustest tulenevalt täituda erinevate suhtelise täite tasemeteni ja teatud tingimustel üle minna täistäitele. Selle tulemusena võib esineda vaba ja surve segavoolurežiim. Õhu ja vee segavoolurežiim on seotud liikuva vooluhüppe tekkega toru horisontaalses osas.

Seni puuduvad selged kriteeriumid, mis ennustaksid halvasti õhutatud torustike täitmisel liikuva vooluhüppe teket koos kaasneva õhukoti lõksu jäämisega tingimustel, kus õhukiirus on kaduvväike. On tõenäoline, et voolamise erinevates etappides omavad erinevates proportsioonides mõju eri tüüpi ebastabiilsused. Käesolevas töös pakutakse välja, et toruosade paigutusest tingitud ebastabiilsus areneb vooluhüppeks pikalaine tüüpi kihistunud voolamise ebastabiilsuse tõttu.

Liikuvat vooluhüpet, kus kihiline voolamine läheb üle režiimi, milles õhk voolab kottidena toru lae all, iseloomustab rõhulise laine kiirus, mille väärtuse määravad rõhu, veevoolu ristlõikepindala ja tiheduse muutused läbi hüppe. Sademeveekanalisatsioonis võivad üleminekut osaliselt torutäitelt täistäitele põhjustada nii geomeetria mõjud kui ka vedeliku ja voolamise omadused. Seetõttu on käesolevas töös uuritud ühe-, kahe- ja kolmefaasilist voolamist erineva geomeetriaga torudes.

Liikuva vooluhüppe valtsi jaoks toodi käesolevas töös õhu ja vee segavoolurežiimi tingimustel sisse segunemise efektiivsuse parameeter, mis põhineb voo Richardsoni arvul. Segamise efektiivsus arvutati modelleeritud voolamise andmete põhjal ja leiti hea kokkulangevus, kus profiilis on võimalik tuvastada valtsi piirkond, kus faasid ei olnud hästi segunenud, ja piirkond, kus ujuvuse voog surub turbulentsi maha.

Numbriline modelleerimine näitas, kuidas toru sisepinna geomeetria ja karedus mõjutavad voolamise dünaamikat. Analüüsi põhjal saab liikuva vooluhüppe tekkepõhjused torudes esialgses lähenduses rühmitada kohaliku geomeetria muutuse hüppe, kanali kareduse hüppe, toruosade paigutuse ebastabiilsuse hüppe ja toru kalde hüppe tüüpidesse. Viimane võib teatud tingimustel põhjustada eralduspinna võnkuvat dünaamikat ja õhu perioodilist väljavoolu kaevudest seeläbi piirates vee sissevoolu. Seda tüüpi sademeveekanalisatsioonist lähtuv üleujutus on erinev olukorrast, kus vesi pääseb kaevust tänavapinnale.

Appendix 1

Air Pocket Dynamics under Bridging of Stratified Flow during Rapid Filling of a Horizontal Pipe

Katrin Kaur[1]; Janek Laanearu, Aff.M.ASCE[2]; and Ivar Annus[3]

Abstract: This paper focuses on air–water interactions during pipe filling. The air–water mixed flow is related to a mobile hydraulic jump in the horizontal pipe section. The trapped water–air front at the crown of the pipe bridge determines the upstream boundary conditions for the stratified flow, suppressed hydraulic jump, and slug flow regions in the horizontal pipe section. The velocity field, the water level, and the pressure were measured at different stages of the transitional flow process. A full-scale two-phase computational fluid dynamics model, with two-equation eddy viscosity turbulence to account for small scales of motion, was used to predict the air pocket dynamics. The paper suggests that in the case of a frozen upstream water–air front, the formation of a hydraulic jump downstream can be explained by long-wave-type instability, which is confirmed by the free-surface supercritical flow Froude number condition. The hydraulic jump that merges stratified flow and slug flow is characterized by the speed of the surge wave, which is determined by the pressure, cross-sectional area of water flow, and density changes. A mixing efficiency parameter was introduced to explain the dissipation of turbulent energy due to the air–water mixing front of the suppressed hydraulic jump. **DOI: 10.1061/(ASCE)HY.1943-7900.0002021.** *This work is made available under the terms of the Creative Commons Attribution 4.0 International license, https://creativecommons.org/licenses/by/4.0/.*

Author keywords: Air–water interactions; Computational fluid dynamics; Froude number; Hydraulic jump; Mixing efficiency; Pipe Froude number; Turbulence; Zukoski number.

Introduction

Two-phase flow dynamics is important when dealing with conduits that are subjected to transitional gravity filling conditions, such as elements of an urban drainage system (UDS) during intense rainfall. If UDS tunnels are poorly ventilated, trapped air pockets may occur and become pressurized, negatively influencing the operating conditions of the system (Vasconcelos and Wright 2009). When a transition to pressurized flow in UDS sections occurs, an air–water front appears, resulting in a regime with both gravity and pressurized flow or mixed flow (e.g., Vasconcelos et al. 2006; Politano et al. 2007; Leon et al. 2010).

Pressure surges in pipelines can be associated with fast pressure fluctuations or prolonged pressure alterations. High pressure peaks in UDS during storm events can be induced by the release of trapped air pockets, which cause flow acceleration that may result in conduit failure or induce flooding. The formation of air pockets in sewers due to the bridging of stratified flow during the filling of the conduit may be accompanied by a mobile hydraulic jump. The flow transients, which are related to changes in flow depth, can act to entrain air into the water column, resulting in prolonged pressure change and deviations of the operating conditions of the system until the air pocket collapses.

When trapped air pockets are released, flow acceleration in the undulating pipeline can result in unexpected pressure surges (Liou and Hunt 1996). For example, if a rapidly advancing water column passes a knee point when undulating pipeline profiles are being filled, negative gauge pressures can arise (Liou and Hunt 1996; Malekpour and Karney 2011). This phenomenon can introduce intrusion of contaminants (Funk et al. 1999) or even structural buckling (Chaudhry 2014).

The transition from stratified to slug flow in a horizontal pipe is facilitated by the pressurization bore forming a nonstationary flow, which results in a mobile hydraulic jump. This hydraulic jump acts to entrain air from the air pocket until the fully filled condition is reached. Filling experiments on an industrial-scale pipeline carried out at Deltares (formerly Delft Hydraulics) (Hou et al. 2014) confirmed the intrusion of water–air fronts with different speeds along the pipeline, starting from a full vertical water–air front at the pipe bridge. The Deltares experimental apparatus also enabled the researchers to generate stratified flow, which touched the pipe obvert (i.e., bridged) due to the formation of a mobile hydraulic jump and the consequent occurrence of an air pocket during pipeline filling. Measurements of the flow rate, pressure, and water level along the horizontal polyvinyl chloride (PVC) pipeline, which was 261 m long and had an internal diameter of 236 mm (Hou et al. 2014), were used with camcorder recordings to quantify the transitional flow process. When air pockets form during the filling of a pipeline, a volumetric water flux difference can occur between the inflow and outflow. If the inflow rate is significantly larger than the outflow rate, the pressurization bore velocity may be considerable, and unexpected changes in the pressure gradient (i.e., subatmospheric conditions) can occur in the downward sloping pipe (Politano et al. 2007).

There are no clear criteria for predicting the formation of hydraulic jumps in closed conduits with concurrent air pocket entrapment during filling. Air pocket formation in the pipe may be related

[1]Ph.D. Student, Dept. of Civil Engineering and Architecture, Tallinn Univ. of Technology, Ehitajate tee 5, 19086 Tallinn, Estonia (corresponding author). ORCID: https://orcid.org/0000-0002-4111-9302. Email: katrin.kaur@taltech.ee

[2]Associate Professor, Dept. of Civil Engineering and Architecture, Tallinn Univ. of Technology, Ehitajate tee 5, 19086 Tallinn, Estonia. Email: janek.laanearu@taltech.ee

[3]Assistant Professor, Dept. of Civil Engineering and Architecture, Tallinn Univ. of Technology, Ehitajate tee 5, 19086 Tallinn, Estonia. ORCID: https://orcid.org/0000-0003-3081-3144. Email: ivar.annus@taltech.ee

to stratified flow instabilities: shear flow instability (SFI), and long wave instability. Currently, the shear flow instability criterion is used for pipe flow (Kordyban 1990; Li and McCorquodale 1999). Investigation of the advance of air cavities in pipes was introduced by Zukoski (1966) and Benjamin (1968). The Zukoski number was used by Laanearu et al. (2012) to characterize the air-cavity dynamics in the case of large-scale pipeline emptying in which air pockets do not form during stratified flow. The difference between an interfacial Froude-like parameter (Eldayih et al. 2020), which is related to the SFI, and the Zukoski number criterion, which is related to the air–water interaction in the closed conduit, is the definition of celerity. For the SFI criterion, the relative velocity (between air and water in the stratified-flow regime) is normalized by the square root of gravitational acceleration times the hydraulic depth, whereas for the Zukoski number, the velocity of the air cavity is normalized by the square root of gravitational acceleration times the pipe diameter. The validity of the stratified flow instability criteria in closed conduits is unclear with respect to the presence of a shear flow and a long wave, while the air flow is insignificant. In this study, the SFI condition of stratified flow is represented with respect to the Zukoski number. The long wave instability is based on the free-surface-flow Froude number that is defined herein for the conduit geometry.

The ability to predict and understand the phenomenon of air–water mixed flow in UDS is of great interest. It can be speculated that in a storm sewer pipe, a series of air pockets may form during filling, changing the operating conditions. The numerical study of the transition from stratified to slug flow via a pressurization bore raises a number of challenges in terms of solving the air–water interaction conditions. The Storm Water Management Model (SWMM) (Rossman 2015), which is used widely to simulate storm water flow conditions, is not able to capture the dynamics of rapid flow changes in hydraulic systems (Vasconcelos et al. 2018). Computational fluid dynamics (CFD) models that use the volume of fluid (VOF) method to solve the two-phase flow have been able to reproduce the pressurization bore and predict the behavior of the air–water mixed flow (Laanearu and Kaur 2018; Eldayih et al. 2020). The Reynolds-averaged Navier–Stokes (RANS) approach, which requires a solution to the Reynolds stress term, is one of the most widely used methods for turbulent-flow modeling. Two-equation models that simulate the eddy viscosity via turbulent kinetic energy production and dissipation (e.g., Launder and Spalding 1972; Shih et al. 1995) commonly are used. Air bubbles aggregate and decompose in the turbulent environment of a hydraulic jump, dissipating the mechanical energy of the flow process

(Chanson and Brattberg 2000). However, studies of turbulent kinetic energy profiles in air–water mixed flow are scarce (Pothof 2011), due to the presence of air bubbles, buoyancy, and turbulence.

This work explains the bridging conditions of stratified flow in a closed conduit using experimental and numerical model findings. Based on these findings, the pressurization bore in the closed conduit was quantified, and a parameter of the mixing efficiency of strongly coupled immiscible fluids was introduced.

Methodology

Experimental Method

Filling experiments were carried out on a horizontal pipeline containing a bridge which was used to accelerate the water flow. Transparent polymethyl methacrylate (PMMA) pipe segments 2 m long and with an inner diameter of 0.08 m were used to assemble a pipeline 18 m in length. During the experiments, this pipeline was fed from an upstream tank, and the pressure head was kept constant. The pipeline discharged into a base reservoir of 150 m^3, which was used to fill the upstream tank. The experimental apparatus is illustrated in Fig. 1. The numbered locations on the schematic of the experimental facility are used for reference in the descriptions of the instrumentation and procedure given herein.

The operating conditions of the experimental apparatus first were mapped in a series of tests. The intent was to operate the apparatus in a manner that resulted in the formation of a sufficiently large air pocket to be able to investigate the advance of the pressurization bore along the pipeline. We aimed to create a stratified flow interface bridging 5 m downstream of the pipe bridge, and to achieve a stationary inflow rate throughout the series of experiments. The inflow rate was adjusted by changing the initial pressure in the upstream tank (Fig. 1, 1) and the setting of the inflow valve (Fig. 1, 3). A suitable operating frequency was found for the pump supplying the tank (Fig. 1, 1) to keep the water level in the tank constant. The Reynolds number for fully filled flow at the target flow rate was $R = 56{,}000$.

In the initiation stage, the section of pipe (Fig. 1, 3–6) between the upstream tank and bridge was filled with water, i.e., all air was expelled. The outflow valve (Fig. 1, 13) was fully open, and the position of the inflow valve (Fig. 1, 3) was adjusted to achieve the target flow rate. Section 6–13, initially containing only air, was subjected to free-surface water inflow via the pipe bridge

		1 water tank	4, 12 electromagnetic flow meters
		2, 5, 7, 11 pressure transducers	6 pipe bridge
		3, 13 shut-off valves	8, 10 water-level meters
			9 PIV measurement section

Section	3–4	4–5	5–6	6–7	7–8	8–9	9–10	10–11	11–12	12–13
Length, m	1.1	1.6	7.8	1.8	1.2	0.55	1.7	0.25	1.0	0.65
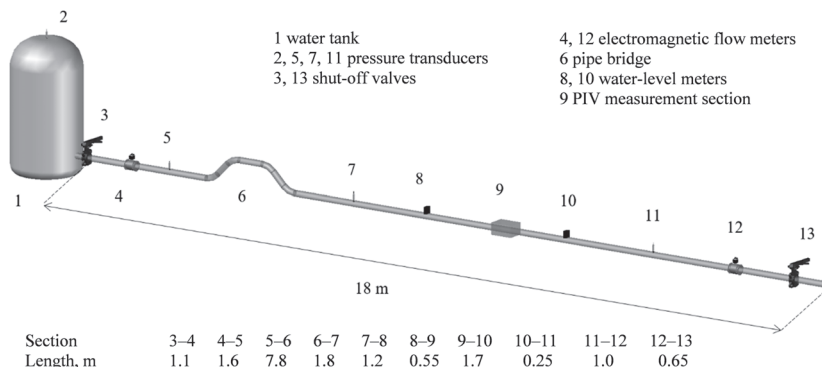
Fig. 1. Components and instrumentation of the experimental facility at Laboratory of Fluid Mechanics, Tallinn University of Technology.

(Fig. 1, 6) at a constant inflow rate $Q = 3.5\ \mathrm{l\,s^{-1}}$, corresponding to pipe Froude number $\mathrm{f} = Q/(A(gD)^{1/2}) = 0.8$ according to Hager (1999), where A = water flow cross-sectional area of partially filled case, yielding the formation of an air cavity. Bridging of the stratified flow occurred 5 m after the pipe bridge (Fig. 1, 6) at Section 10–11, resulting in the formation of an air pocket. The pressurization bore travelled upstream with celerity, c_{jump} as the air was mixed and entrained via the roller near the pipe obvert, thereby gradually decreasing the volume of the air pocket. The velocity distributions (at Location 9), water levels (at Locations 8 and 10), and pressure changes (at Locations 5, 7, and 11) were captured at different stages of development of the transitional flow process, for a constant inflow rate and varying outflow rate. Electromagnetic flow meters (Fig. 1, 4 and 12) were used to determine the water volumetric flux differences (data from the downstream meter were filtered after the measurements to account only for the full cross-section water flow portions). The flow development stages were defined with respect to Location 9, the section at which particle image velocimetry (PIV) measurements were taken, as follows:

1. stratified flow was when the bore was located 8 pipe diameters downstream of Location 9;
2. roller was when the bore was located at Location 9; and
3. slug flow was when the bore was located 3 pipe diameters upstream of Location 9.

After the first series of measurements of Stages 1–3, additional air was supplied to the air pocket through a valve at the crown of the pipe bridge (Fig. 1, 6), thus readjusting the bridging location to 5 m from the pipe bridge and restarting the advance of the pressurization bore along the horizontal pipe section. Fifteen repeat measurements were taken of each stage. Before ensemble averaging was conducted, the individual PIV frame sequences were analyzed in order to discard frames in which the roller was not precisely at the predetermined position. Additional measurements of fully filled flow were conducted for a numerical model sensitivity study (Fig. 2) after the pressurization bore reached the bridge crown, i.e., when all air was expelled from the pipeline. The instrumentation used in the experiments was as follows:

- Electromagnetic flow meters (Fig. 1, Locations 4 and 12) were used at the up- and downstream ends of the pipeline. The sampling frequency for both flow meters was set to 100 Hz. The uncertainty in the readings was ±0.6% for the upstream flow meter and ±0.5% for the downstream meter, for water-only conditions.
- Strain-gauge pressure probes were used on the pipe (Fig. 1, Locations 5, 7, and 11), and on the upstream tank (Fig. 1, 2). The sampling frequency for all pressure probes was set to 100 Hz, and the uncertainty in the pressure measurement readings was ±0.3%.
- A PIV system was used (Fig. 1, Location 9), consisting of a high-speed camera and a continuous-wave laser. The frequency of measurement varied from 1,155 to 2,982 images/s, depending on the Reynolds numbers for fully filled and stratified flow. The uncertainties in the captured PIV velocity field components and the derived values of turbulent kinetic energy were quantified using the uncertainty propagation techniques presented by Sciacchitano and Wieneke (2016). The uncertainties of the horizontal along-pipe and vertical cross-pipe velocity components, hereinafter corresponding to axial and vertical velocity components, and the turbulent kinetic energy at the different stages of flow development are presented in Table 1. The larger uncertainty in the vertical velocity component arose from the settings for the PIV sampling frequency; this depended on the mean axial velocity, which was more than 1 order of magnitude larger

Table 1. Uncertainties in PIV measurements of axial and vertical velocities and turbulent kinetic energy at different stages of flow development (%)

Quanitity	Stratified flow	Roller	Slug flow
Axial velocity	0.675	2.45	1.98
Vertical velocity	12.4	11.6	9.16
Turbulent kinetic energy	0.987	7.43	3.48

than the vertical velocity component for the measurements of stratified, roller, and slug flow.

- Capacitive sensors for water level metering (Fig. 1, 8 and 10) were placed at each side of Section 9. The sampling frequency for both was set to 100 Hz, and the accuracy of the measurement was 1 mm.
- Two synchronized data acquisition modules were used to collect flow rate, pressure, and water level data.

Numerical Procedure

To interpret the different stages of the pressurization bore development, CFD modeling was applied. A three-dimensional computational domain geometry was created based on the physical dimensions of the experimental apparatus. Simulations of the two-phase flow were conducted using the interFoam solver of OpenFOAM v1906 (OpenCFD Ltd.) software. The flow regime was turbulent, and the air and water phases were considered to be incompressible, isothermal, Newtonian, and immiscible fluids (Hou et al. 2014). Interface capturing for the air–water flow was resolved by applying the VOF phase fraction–based approach (Hirt and Nichols 1981; Bombardelli et al. 2001). The transport equations for continuity [Eq. (1)] and momentum [Eq. (2)], in which the two immiscible fluids are considered as a single joint fluid through the domain, are

$$\nabla \cdot \mathbf{U} = 0 \tag{1}$$

$$\frac{\partial(\rho\mathbf{U})}{\partial t} + \nabla \cdot (\rho\mathbf{U}\mathbf{U}) = -\nabla p' - \mathbf{g} \cdot \mathbf{x}\nabla\rho + \sigma\kappa\nabla\gamma$$
$$+ \nabla \cdot (\mu\nabla\mathbf{U}) + (\nabla\mathbf{U}) \cdot \nabla\mu \tag{2}$$

where $\mathbf{U} = \gamma\mathbf{U}_l + (1-\gamma)\mathbf{U}_g$ = velocity vector of two-phase fluid; $\rho = \gamma\rho_l + (1-\gamma)\rho_g$ = average density of the fluid within a cell; t = time; $\mu = \gamma\mu_l + (1-\gamma)\mu_g$ = average dynamic molecular viscosity; p' = pressure, modified to exclude hydrostatic contribution; $\mathbf{g} = (0, 0, -g)$, where g = acceleration due to gravity; $\mathbf{x}$ = position vector; σ = surface tension; $\kappa = \nabla \cdot \mathbf{n}$ = interface curvature, where $\mathbf{n} = -\nabla\gamma/|\nabla\gamma|$; and subscripts l and g correspond to liquid and gas, respectively.

To define the portion of the cell occupied by the fluid, the phase fraction γ is used as an indicator function. The transport of γ is expressed by an advection function $\partial\gamma/\partial t + \nabla \cdot (\gamma\mathbf{U}) = 0$. The phase fraction, γ, representing the excess density, can range within $0 \leq \gamma \leq 1$, with values 0 or 1 corresponding to regions entirely of air or water, respectively. To provide a sharper interface resolution, especially for large density difference two-phase flows, Weller (2002) introduced an extra term of artificial compression in the phase fraction equation, so the transport equation is

$$\frac{\partial\gamma}{\partial t} + \nabla \cdot (\gamma\mathbf{U}) + \nabla \cdot (\gamma(1-\gamma)\mathbf{U}_r) = 0 \tag{3}$$

where $\mathbf{U}_r = \mathbf{U}_l - \mathbf{U}_g$ = velocity field to compress interface.

Because the water in our experiments was circulated from an indoor reservoir, the physical properties in the numerical model

were chosen based on the laboratory air temperature of 20°C. The density and dynamic molecular viscosity of water were set to 998.2 kg m^{-3} and 1.002×10^{-3} kg m^{-1} s^{-1}, and those for air were set to 1.204 kg m^{-3} and 1.82×10^{-3} kg m^{-1} s^{-1}, respectively. The interfacial tension plays an important role in the two-phase flow of immiscible fluids that are strongly coupled due to the formation of the air pocket. The surface tension coefficient was set to $\sigma = 0.0728$ N m^{-1} for the air–water interfaces.

The performance of the RANS model for the transitional flow was analyzed by comparing the measured and modeled velocities, the turbulent kinetic energy distributions, the water levels and the location of formation and dynamics of the hydraulic jump. Based on the performance analysis, the renormalization group (RNG) k-ε model was used in the numerical experiments.

The RNG k-ε turbulence model was derived using a statistical technique called renormalization group theory (Yakhot and Orszag 1986; Smith and Reynolds 1992; Smith and Woodruff 1998). The RNG model contains an additional term in the equation for ε that improves the accuracy for rapidly strained flows. The effect of swirl on turbulence is included in the RNG model, which enhances the accuracy of swirling flows. In addition, the RNG theory provides an analytical formula for turbulent Prandtl numbers, whereas the standard k-ε model uses empirical, constant values (Launder and Sharma 1974). The values of the constants in the equations for k and ε stemming from the RNG analysis are $C_\mu = 0.0845$, $C_{\varepsilon 1} = 1.42$, $C_{\varepsilon 2} = 1.68$, and $\sigma_k = \sigma_\varepsilon = 0.72$ (Orszag et al. 1996; Pope 2000). The advantage of the RNG k-ε turbulence model is that it also accounts for small scales of fluid motion, and therefore it is more suitable for flows with a low Reynolds number.

In the present CFD solver, the wall functions approach is based on universal flow profiles in the boundary layer along a wall, which is divided into three regions based on the viscous, buffer, and inertial sublayers. The production of turbulence occurs at varying normalized distances from the wall, and depends on the Reynolds number. The turbulence model in the CFD solver used in this study places the first internal grid point in the vicinity of the pipe wall in the inertial sublayer and approximates the viscous sublayer by the wall function boundary condition.

At the domain inlet, initial values of the turbulent kinetic energy and turbulence dissipation rate are required. The initial values of k and ε were determined from the measurements and used in the setup of the model. These values were set to $k = 0.00124$ m^2 s^{-2} and $\varepsilon = 0.00128$ m^2 s^{-2}. Concurrently, a constant inflow rate boundary condition was set for the inlet, and a zero gradient boundary condition was set for the outlet, in accordance with the experiments.
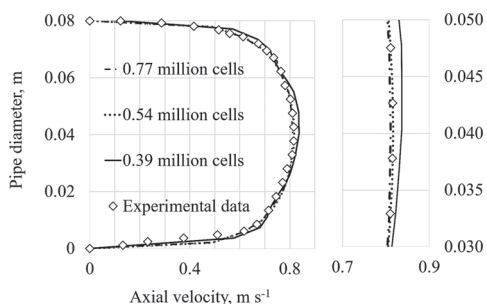
The computational domain was discretized using a hybrid grid containing a blend of structured and unstructured grid areas. The snappyHexMesh utility from OpenFOAM, which creates the grid using triangulated surface geometries, was used to generate the mesh. The domain was discretized more or less uniformly over the pipe cross-section, considering that the mixing processes of particular interest occur near the centerline, whereas the boundary layer was resolved by applying wall functions. A mesh convergence analysis was performed on the full-scale computational domain. Fig. 2 compares the measured axial velocity profile and the modeled profile obtained with three different grid resolutions for fully filled flow. It is apparent from the graph that the finer grid resolutions with 0.54 million and 0.77 million elements gave almost identical results for the velocity distribution, and therefore we used 0.54 million finite volumes in this study.

Parameterization of Stratified Flow

Eldayih et al. (2020) found that SFI during the regulated emptying of a pipeline was characterized by an interfacial Froude-like parameter (F_I), which depends on the relative velocity between the air and water, and on the hydraulic water depth (area/free-surface width) of the flow region in free-surface flow mode. If this value exceeded a critical value, defined as F_C, then SFI occurred during the emptying of the pipeline. The expressions for both F_I and F_C were adopted from Li and McCorquodale (1999) and Kordyban (1990). In the present study, a modified SFI criterion was tested for the formation of an air pocket during rapid filling of a horizontal pipe via a pipe bridge to clarify the conditions under which it occurs.

The onset of shear-flow-type instability can be characterized by the Zukoski number, which is defined as the ratio of the air cavity speed to the celerity of a shallow water wave, based on the pipe diameter. The Zukoski number represents a dimensionless speed that is related to the rate of change of the length of the water column due to the intrusion of air above the water layer. In the case of pipe filling, the air cavity speed is defined as the difference between the water inflow velocity of the fully filled section, U_{VF}, and the velocity of the upper water–air front at the upstream end of the cavity U_{VF1} (Fig. 3).

The Zukoski number then is defined as

$$\mathsf{Zu} = \frac{U_{VF} - U_{VF1}}{\sqrt{g \cdot D}} \qquad (4)$$

where D = internal diameter of pipe. In the case of a frozen water–air upstream front in the pipe, the upper-front velocity U_{VF1} is zero; the Zukoski number therefore is determined by the fully filled inflow velocity, U_{VF}, and is equal to $\mathsf{Zu} = 0.8$. In the present experiment, the instability appearing at the downward sloping section of the pipe bridge was thought to be of the Helmholtz type, modified

Fig. 2. Grid sensitivity study for fully filled flow, with detailed view of the flow core region.
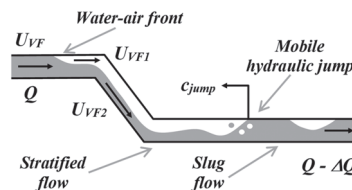
Fig. 3. Schema for the formation of an air pocket and the concurrent mobile hydraulic jump in a pipe.

by the influence of the gravitational field, which is not perpendicular to the air–water interface. Zukoski (1966) found that the amplitude of Helmholtz instability in the interface also increases with increasing cavity speed. While the upper water–air front is frozen, i.e., the cavity moves with a velocity equal and opposite with respect to the water column, the instability of the lower water–air front advancing into the horizontal pipe section results in a mobile hydraulic jump. The formation of the cavity, with respect to the pipe Froude number value, is in accordance with values mapped by Hager (1999) because the pipe bridge acts to trap the upper water–air front and mimics the pipe outlet conditions. In the

present study, the Zukoski number value that corresponds to the frozen interface case at the pipe bridge was found.

Based on the assumption that air is forcing the interface motion to create water waves, forming instability, Li and McCorquodale (1999) proposed a normalized condition for the transition of free-surface to pressurized flow by discontinuity. They built on the work of Milne-Thomson (1938), who proposed an equation for the instability condition based on the small-amplitude waves between water and air. A modification is proposed here in which the condition is normalized based on the square root of the gravitational acceleration and the pipe diameter

$$\frac{|U_{VF1} - U_{VF2}|}{\sqrt{g \cdot D}} \geq K_f \sqrt{\left(1 - \frac{\rho_a}{\rho_w}\right)\left(\frac{\rho_w}{\rho_a}\tanh\left(\frac{2\pi h_a}{\lambda}\right) + \tanh\left(\frac{2\pi h_w}{\lambda}\right)\right)}\sqrt{\frac{\lambda}{2\pi D}} \qquad (5)$$

where h_w and h_a = hydraulic depths of water and air, respectively; and ρ_w and ρ_a = densities of water and air, respectively. If the air velocity is zero, corresponding to a frozen water–air upstream front in the pipe, then the instability is determined by the lower-front water velocity in the stratified-flow regime $U_{VF2} = 1.15 \text{ m s}^{-1}$. The water–air front velocity U_{VF1}, the fully filled inflow velocity U_{VF}, and the water velocity in the stratified-flow regime U_{VF2} are related through the Laanearu et al. (2015)

formula, $U_{VF1} = U_{VF}/\alpha - U_{VF2}(1 - \alpha)/\alpha$, where α is the void fraction, representing the effective cross-sectional area of air. The void fraction is proportional to the cross-section average of the parameter $(1 - \gamma)$, represents the effective cross-sectional area of the air, and is equal to unity when the vertical water–air front exists over the cross-sectional area. Hence, U_{VF2} on the left-hand side of Eq. (5) can be expressed in terms of U_{VF} and U_{VF1}. Because U_{VF1} is assumed to be practically zero, the SFI criterion can be expressed as

$$\frac{U_{VF}}{\sqrt{g \cdot D}} \geq K_f(1 - \alpha)\sqrt{\left(1 - \frac{\rho_a}{\rho_w}\right)\left(\frac{\rho_w}{\rho_a}\tanh\left(\frac{2\pi h_a}{\lambda}\right) + \tanh\left(\frac{2\pi h_w}{\lambda}\right)\right)}\sqrt{\frac{\lambda}{2\pi D}} \qquad (6)$$

by making use of the definition of the Zukoski number. The Zukoski number is fundamentally related to the stratified flow, similar to an interfacial Froude-like parameter, and unlike the Froude number, which is related only to the water-layer mechanical energy. In this modified SFI criterion, λ is the wavelength of the free-surface water wave, which may vary from 20 mm (for capillary waves) to a few times the water depth. The correction factor K_f is due to the reduction in the air flow area, and the entrance and alignment conditions. According to this criterion, K_f should be on the order of magnitude of $1/10$ for the instability to arise, because the criterion value varies in the range 2.8–5.7, whereas λ varies from the capillary wave length to a wavelength equal to the pipe diameter (Li and McCorquodale 1999). The SFI criterion given here would be applicable to air pocket formation if the setup produced a significantly higher air velocity. Therefore, a criterion for the onset of instability that is governed by the Froude number, i.e., long-wave-type instability, is considered. Pratt (1986) described long-wave instability criteria for the sill flows resulting from supercritical solutions in which the propagation of the perturbed-flow interfacial waves is possible only in the downstream direction of flow. Based on the similarity criterion, long-wave instability was applied in this study.

The onset of long-wave-type instability during free-surface inflow that results in the formation of a pressurization bore is indicated by the supercritical Froude number. The equation form

[Eq. (7)] was derived by solving for the cross-section minimum specific energy, making use of the partially filled circular cross-section of flow area, and is expressed as follows:

$$\mathsf{Fr}^2 = \frac{2Q^2}{gA^3}\sqrt{h(D - h)} \qquad (7)$$

In the experiments, the water level above the pipe invert was $h = 0.045 \text{ m}$, $D = 0.08 \text{ m}$, and $Q = 3.5 \text{ l s}^{-1}$. The corresponding Froude number for the stratified flows stage then was $\mathsf{Fr} = 2$. This corresponds to supercritical flow, but is sufficiently small to facilitate the formation of a long air pocket. The value of the Froude number was calculated based on experimental data captured when the bore in the pipe had already formed.

Mixing

In the transitional flow process, air–water mixing and the formation of the mobile hydraulic jump are responsible for the entrainment of air into the water (the formation of air bubbles) and water into the air (formation of water droplets in air) inside the pipeline, which is quantified in the numerical model by the phase fraction γ. In the air–water mixing flow process, such as the hydraulic jump, the kinetic energy can be converted to potential energy due to increase of the water level and pressure. The concept of mixing efficiency can

be used to relate the amount of mixing in the stratified flow to the amount of energy available to support mixing (Davies Wykes et al. 2015). Mixing efficiency is used to characterize the internal hydraulic jumps of two-layer flows with a small density difference (Ogden and Helfrich 2016). However, the density variations inside the air–water roller are present due to external forcing, and the mixing efficiency therefore is applicable in a general way. As per its definition, the mixing efficiency for the air–water roller can be formulated based on the flux Richardson number, representing the ratio of the buoyant destruction to shear production. In the case of temperature-stratified single-phase flow, because the shear production is positive with the minus sign displayed, the sign of the flux Richardson number depends on the sign of the heat flux (Kundu et al. 2012).

The mixing efficiency parameter was introduced in this study to estimate the turbulence energy consumed in the air–water mixing process in the pressurization bore. In the case of horizontal flow with a vertical jump, the flux Richardson number can be given as

$$\mathsf{Ri}_f \approx \frac{-g\gamma U_3}{-\overline{u_1 u_3}\frac{dU_1}{dx_3}} \qquad (8)$$

where U_1 and U_3 = axial and vertical velocity components, respectively; and u_1 and u_3 = respective fluctuating velocity components. In the numerator of Eq. (8), the buoyant destruction is replaced with the loss to potential energy, the parameter that appears in the equation for the mean flow's kinetic energy per unit mass (Kundu et al. 2012).

The mixing efficiency of the air–water interface roller (i.e., at the bridging location) is determined based on the results of full-scale numerical modeling using the RANS equations. The maximum of the profile is located in the region in which the volume fraction gradients occur, i.e., near the interface (Fig. 4). If measurements indicate the presence of turbulent fluctuations, but at the same time the value of Ri_f is positive, then it can be concluded that the turbulence is decaying. The water level is increased due to long-wave instability forming a hydraulic jump that mixes the air and water phases, virtually mimicking a single-phase-like state in the roller. The experiments indicate that the fluid phases are not well mixed near the pipe obvert ($\mathsf{Ri}_f < 0$) (Fig. 4). In accordance with the positive flux Richardson number, the buoyancy fluxes are suppressing the turbulence through the hydraulic jump development stage, facilitating the separation of the mixed phases. The hydraulic jump roller is trailed by slug flow with mobile air pockets at the pipe obvert. The mixing efficiency parameter can be used to quantitatively assess the mixing regimes of stable and unstable two-phase flow.
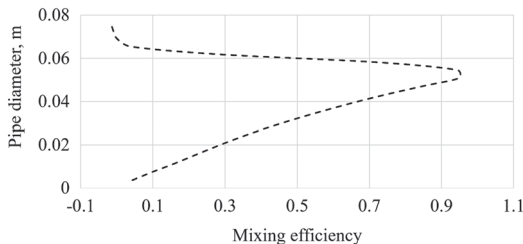
Fig. 4. Mixing efficiency at the air–water flow interface bridging stage.

Control-Volume Model

The stratified flow transition to slug flow is modeled within the framework of a control volume (CV) using the principles of conservation of mass and momentum. The aim of the CV analysis is to establish a relationship for the speed of the hydraulic jump. Based on a straightforward relationship between the CV mass and momentum equations, the speed of the mobile hydraulic jump can be expressed as:

$$c_{\text{jump}} = (U_u - U_d) - \sqrt{\frac{A_u \rho_u (A_u p_u - A_d p_d + R_x)}{A_d \rho_d (A_u \rho_u - A_d \rho_d)}} \qquad (9)$$

where (p_u, U_u, A_u, ρ_u) and (p_d, U_d, A_d, ρ_d) = average pressure and water velocity, water flow cross-section area, and density immediately upstream and downstream of jump, respectively; and R_x = friction force.

Therefore, the pressurization bore that occurs during the filling process of the pipe can be characterized by the surge wave speed, which essentially is determined by the pressure, the cross-sectional area of water flow, and the density jumps. The friction force at the hydraulic jump section can be omitted ($R_x \rightarrow 0$) as the mixing region length is on the order of magnitude of the pipe diameter, and the mixing-efficiency parameter value indicated that the buoyancy fluxes are suppressing the turbulence ($\mathsf{Ri}_f > 0$). Calculations based on experimental data captured during the measurements at the roller stage revealed the value of the hydraulic jump speed $c_{\text{jump}} \approx 0.04 \text{ m s}^{-1}$.

Results and Discussion

Formation of the Air Pocket

The filling process under investigation has three stages: air cavity formation, air pocket formation, and air entrainment. This three-stage mixed flow process lasts about half an hour, until the trapped air is entrained out from the pipeline.

The operating conditions of the experimental apparatus were chosen to produce an air pocket. The target flow rate resulted in the cavity formation, as two water–air fronts appeared, the upper water–air front becoming frozen at the pipe bridge crown and the lower front advancing into the horizontal pipe section. The prerequisite of the cavity formation corresponds well to the pipe Froude number that is associated with cavity formation at the horizontal pipe outlet (Hager 1999). In the present study, the pipe bridge mimicked the pipe outlet conditions. In terms of the cavity formation in the undulating pipe, the pipe bridge acts as a cavity trap. The pipe Froude number value corresponds to the range resulting in a trapped air cavity at the pipe bridge crown. The formation of the air cavity caused the stratified flow that led to the formation of a hydraulic jump in the horizontal pipe section.

As the mobile hydraulic jump advanced, two distinctive regions were observed behind the jump. The roller acted to entrain air, resulting in bubbles being propelled toward the pipe centerline, forming a bubbly flow [Fig. 5(c)], before aggregating near the obvert and resulting in slug flow. The region of bubbly flow spanned approximately 2 pipe diameters behind the roller.

The Deltares experiments, conducted on a pipe with a 235-mm diameter and used here for comparison, also manifested the three stages of the mixed flow process (Fig. 6). The scales of these two experiments were different; in the present experiment, for fully filled flow, the Reynolds number was 56,000, whereas in the
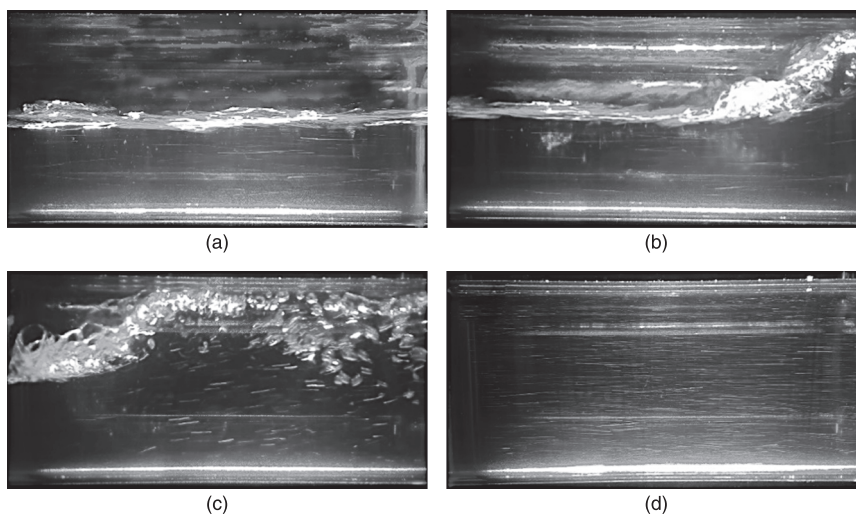
Fig. 5. Flow stages of pressurization bore advancement in an 80-mm pipe: (a) stratified; (b) roller; (c) bubbly; and (d) slug.
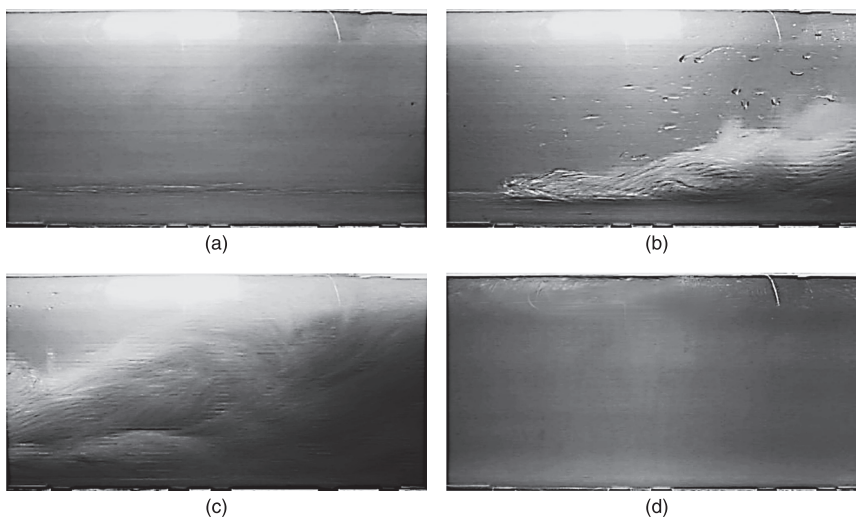
Fig. 6. Flow stages of pressurization bore advancement in a 235-mm pipe: (a) stratified; (b) roller; (c) bubbly; and (d) slug.

Deltares experiments the Reynolds number was 950,000. The length of the air pocket, the end of which was the bridging location, and the region of bubbly flow were dependent on the cross-sectional filling ratio of the pipe, h/D, and consequently on the Froude number. Stronger supercritical flow conditions correspond to smaller volumes of captured air. The size of the air pocket also is related to the volumetric water flux difference between the inflow and outflow of the pipeline.

Table 2 presents experimentally determined values of the normalized water–flux differences, air pocket volumes, hydraulic jump speeds, and Froude numbers. The hydraulic jump speed c_{jump} was calculated in the reference frame of the pipe, considering that the

bore moves on top of the stratified inflow. Two groups based on the filling ratio, at which point the air pocket formed, are apparent in Table 2. Experiments that resulted in mobile hydraulic jump formation from a filling ratio $h/D > 0.5$ corresponded to the comparatively less-supercritical Froude number and thus the higher hydraulic jump speed. The more supercritical Froude-number experiments with $h/D < 0.2$ had a lower air–water front speed. Because the two experimental facilities were of a different scale, the water flux differences between the inlet and outlet were normalized by the volumetric inflow rate, $(Q_{inflow} - Q_{outflow})/Q_{inflow}$, and the air pocket volumes were normalized based on the cube of the pipe diameter (V/D^3).

Table 2. Average normalized water flux differences, normalized air pocket volumes, hydraulic jump speeds, and Froude numbers for air pocket formation induced by weaker and stronger supercritical flow conditions

Pipe diameter (m)	Filling ratio	Normalized water flux difference	Normalized air pocket volume	c_{jump}	Fr
0.08	0.63	0.002	11.6	—	—
0.08	0.63	0.01	20.9	0.04	2
0.08	0.63	0.012	22.6	—	—
0.08	0.63	0.02	25.6	—	—
0.235	0.53	0.06	45	0.067	3.5
0.235	0.14	0.1	17.1	0.015	14.3
0.235	0.14	0.13	19.5	0.017	16.7
0.235	0.19	0.19	26.8	0.029	9.6

In the present experiments, the air entrained through the roller, and the jump approached the bridge with speed c_{jump}, which decreased during the two-phase process. The numerical modeling suggested that the speed of the hydraulic jump changes during the process. During the first 5 s after the bridging event $c_{jump} \approx 0.07$ m s^{-1}, which decreased to 0.01 m s^{-1} over the next 1.5 min. Formula-based calculations using Eq. (9), which included experimental data captured during the roller measurements, revealed that the value of the hydraulic jump speed was $c_{jump} \approx 0.04$ m s^{-1}. This relatively slow process investigated here had an approximate air entrainment rate of 7×10^{-5} m^3 s^{-1}. Pressure changes also were apparent, with a small vacuum forming in the air pocket. For the

laboratory-scale system, the pressure gradient through the jump was about 200 Pa. Subatmospheric conditions also were detected in measurements of the Deltares experiments during the mobile hydraulic jump's motion towards upstream.

Velocity and Turbulent Kinetic Energy Profiles

Figs. 7–9 show the measured and modeled velocities and turbulent kinetic energy profiles in normalized form. The PIV measurements were facilitated by flow visualization, which involved seeding the water flow with oxygen and hydrogen bubbles generated via electrolysis. However, for two-phase mixed flow, visualization of the air flow was not straightforward, and the air flow therefore was not captured with PIV, although in the comparative figures, modeling results are shown for both water and air.

Normalization consistently was done based on the maxima of the water flow profiles. The measured profiles were used as the basis, and the axial and vertical velocity profile maxima were found. The modeled axial and vertical velocities then were normalized based on the cell value corresponding to the coordinates of the experimentally determined maxima. Turbulent kinetic energies were normalized based on the cell value corresponding to the experimentally determined maxima of the axial velocity. The values of the normalization constants for the measured and modeled flow profiles and their differences are presented in Table 3.

The axial velocity component had better qualitative agreement than the vertical component between the measured and modeled transitional flow stage of stratified flow (Fig. 7). Comparison of
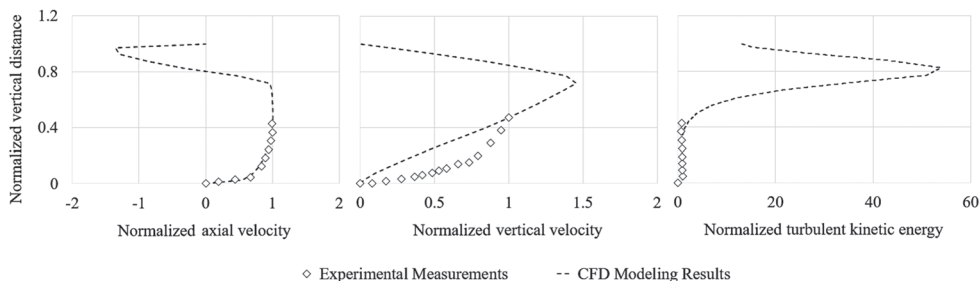
Fig. 7. Normalized measured and modeled axial and vertical velocity, and turbulent kinetic energy in the stratified flow stage of filling of a pipe 80 mm in diameter.
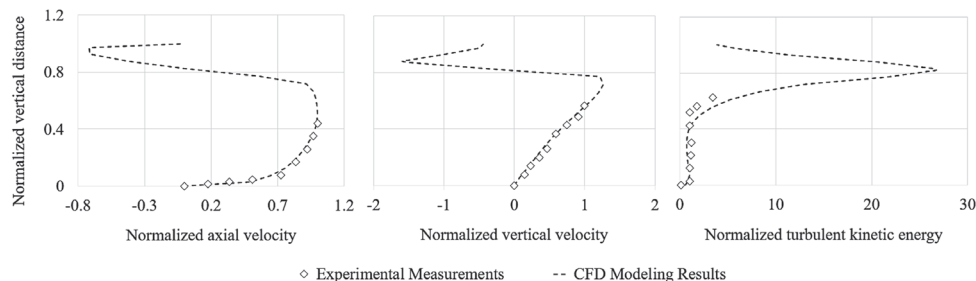
Fig. 8. Normalized measured and modeled axial and vertical velocity, and turbulent kinetic energy in the roller flow stage of filling of a pipe 80 mm in diameter.
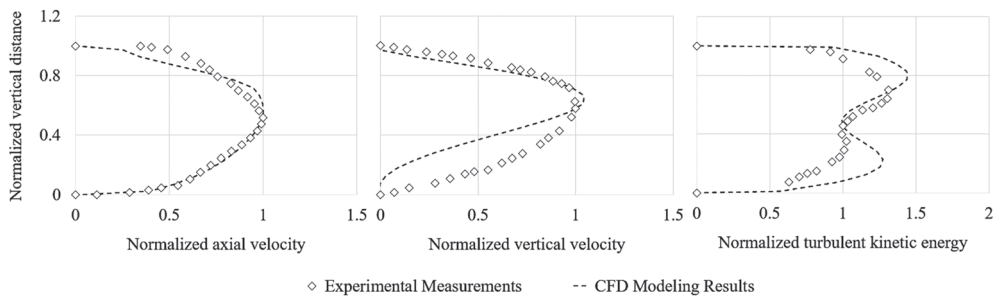
Fig. 9. Normalized measured and modeled axial and vertical velocity, and turbulent kinetic energy in the slug flow stage of filling of a pipe 80 mm in diameter.

Table 3. Values of normalization constants for measured and modeled flow profiles and their differences

Flow stage	Quantity	Normalization coefficient		Difference (%)
		Measured	Modeled	
Stratified flow	Axial velocity	1.364	1.185	13
	Vertical velocity	0.015	0.013	10
	Turbulent kinetic energy	0.012	0.014	14
Roller	Axial velocity	1.336	1.162	13
	Vertical velocity	0.107	0.118	10
	Turbulent kinetic energy	0.012	0.014	23
Slug flow	Axial velocity	0.982	1.005	2
	Vertical velocity	0.035	0.024	32
	Turbulent kinetic energy	0.017	0.011	32

the modeling and experiments of the stratified flow stage revealed slight differences in the interface behavior. In the experiments, it was observed that the vertical air–water mixing already was present in the stratified flow portion, and the mixing intensity increased gradually toward the roller. The numerical model had behavior more similar to that of a gradually varied flow, resulting in the same bridging location. Concurrently, the experiment revealed faster vertical component growth in this stage.

The measured and modeled axial and vertical velocity components in the roller flow stage had the overall best qualitative (Fig. 8) and quantitative (Table 3) agreement. Due to the model's ability to reproduce the roller's behavior consistently, it was possible to use the modeled velocities in mixing efficiency calculations.

The measured and modeled vertical velocity and turbulent kinetic energy of the slug flow stage (Fig. 9) had the lowest quantitative agreement (Table 3). This primarily was due to the frequency of PIV measurements, and secondly because the measurement results were affected by the mixed-in air releasing due to buoyancy. This also was apparent in the case of axial velocity in Fig. 9, in which the measured and modeled profiles coincide merely for the water phase.

The data in the figures and in Table 3 reveal that the qualitative similarity between the measured and modeled profiles is apparent. In addition, the distribution of turbulence energy is qualitatively similar to that of other studies. Turbulence intensity and Reynolds stress distributions measured in and behind the hydraulic jump in open channel rectangular flow by Resch and Leutheusser (1972) revealed turbulence energy maxima near the centerline of the flow behind the jump, as also was the case in the present study.

Conclusion

This study provided evidence of the formation of an air pocket under conditions of nearly-zero velocity of the air phase in a poorly ventilated conduit. Experiments, numerical modeling and parameterization were used to gain insight into the bridging conditions of stratified flow.

The upstream boundary condition in the experiments was regulated by pressure, measured by a flowmeter, and controlled with the water–air front at the pipe bridge. The experiments made it possible to validate the applicability of the VOF method of numerical modeling of the mobile hydraulic jump in a conduit with known geometry and filling conditions. However, the PIV velocity field measurements of the air phase in the two-phase flow process remain a challenge. Therefore, the numerical model was validated based on water-phase measurements and bridging dynamics, and the validated model was used to analyze the air behavior.

In general, the CFD results agreed with the observations of the experiments. Nevertheless, the modeling and experimental results revealed some differences in the interface behavior. The numerical modeling resulted in less-turbulent structures in the stratified flow region leading up to the hydraulic jump roller. Even though the sensitivity study conducted based on the experimental stage in which all air had been entrained had good agreement, higher resolutions might capture the air and water mixing more accurately. In terms of the bridging location of the stratified flow and the dynamics of the resulting mobile hydraulic jump in experiments, comparison with the standard k-ε turbulence model and RNG k-ε turbulence model indicated that the latter predicts the behavior more consistently. The transitional flow process produces rapid strain and streamline curvature. Due to the additional term in the transport equation of turbulent dissipation, the RNG model yields lower turbulent viscosity in rapidly strained flows than the standard k-ε turbulence model. It is assumed that, because the bridging location is set by the aggregation of the perturbation signals, the standard model results in an inaccurate location due to higher rates of turbulent kinetic energy.

The stratified flow was parameterized to explain the instability that results in air pocket formation. The results revealed that the SFI condition would hold if the velocity in the air cavity were significantly higher. Therefore it was concluded that the hydraulic jump formed in the closed conduit due to long-wave instability, supported by the Froude number value (Fr > 1). The experimental conditions that led to the air cavity and subsequent air pocket formation with a sufficient length were characterized by a relatively low supercritical Froude number. Comparison of the measurement results from pipelines with 80- and 235-mm internal diameters

confirmed that larger filling ratios with smaller Froude number values resulted in a comparatively higher mobile hydraulic jump speed, due to the lower water layer velocities.

The positive value of the mixing efficiency parameter showed that the buoyancy fluxes suppressed the shear production in the hydraulic jump roller stage. This in turn made it possible to neglect the friction force effects when determining the speed of the surge wave in the horizontal pipe. Thus, the surge wave speed is determined by the pressure, the cross-sectional area of water flow, and the density jumps. The surge-wave-speed formula [Eq. (9)] may be useful to assess the duration of the prolonged pressure alteration in a closed conduit when the hydraulic conditions are known.

It can be concluded that the VOF-based approach of two-phase flow makes it possible to simulate the transitional flow dynamics in the pipe under varied initial and boundary conditions. CFD modeling can be applied at different pipeline design and construction stages to estimate the conditions of surge wave formation. However, the turbulence modeling of the two-phase process is challenging in the numerical modeling of surge wave characteristics. Therefore, the experimental investigations support the understanding of the transitional flow process in the pipeline. The propagation speed of the surge wave in UDS pipes determines the pressure changes due to the transitional flow and the concurrent pressure head that may be related to the water column height in manholes. Field measurements would contribute to further advancing the CFD modeling, eventually providing a tool to assess UDS sections that are known to experience deviations from design conditions. Conducting field measurements under conditions similar to the herein-described laboratory experiments remains a challenge. Therefore, the robustness of the model under varied boundary conditions should be assessed in the future.

Data Availability Statement

All data, models, or code generated or used during the study are available from the corresponding author upon reasonable request, including numerical and experimental data.

Acknowledgments

Notation

The following symbols are used in this paper:

A = flow section of circular pipe;
A_d = flow section downstream of hydraulic jump;
A_u = flow section upstream of hydraulic jump;
c_{jump} = hydraulic jump speed;
D = pipe internal diameter;
F_C = critical interfacial Froude-like parameter;
F_I = interfacial Froude-like parameter;
Fr = Froude number;
f = pipe Froude number;
$\mathbf{g}$ = acceleration due to gravity;
h = water level;
h_a = hydraulic depth of air;
h_w = hydraulic depth of water;
K_f = correction factor;
k = turbulent kinetic energy;
$\mathbf{n}$ = normal vector of density interface;
p' = modified pressure;
p_d = pressure downstream of hydraulic jump;
p_u = pressure upstream of hydraulic jump;
Q = inflow rate;
R = Reynolds number;
R_x = friction force;
Ri_f = flux Richardson number;
t = time;
$\mathbf{U}$ = flow velocity vector of two-phase fluid;
U_d = water velocity downstream of hydraulic jump;
U_u = water velocity upstream of hydraulic jump;
U_{VF} = volumetric water inflow velocity;
U_{VF1} = air–water front velocity;
U_{VF2} = water velocity in stratified-flow regime;
U_1 = axial velocity component;
U_3 = vertical velocity component;
u_1 = axial velocity fluctuation component;
u_3 = vertical velocity fluctuation component;
$\mathbf{x}$ = position vector;
Zu = Zukoski number;
α = void fraction;
γ = phase fraction;
ΔQ = volumetric water flux difference;
ε = rate of dissipation of turbulent kinetic energy;
κ = interface curvature;
λ = wave length of water wave;
μ = dynamic molecular viscosity;
ρ = average density of fluid within cell;
ρ_a = air density;
ρ_d = air–water mixture density downstream of hydraulic jump;
ρ_u = water density upstream of hydraulic jump;
ρ_w = water density; and
σ = surface tension.

References

Benjamin, T. B. 1968. "Gravity currents and related phenomena." *J. Fluid Mech.* 31 (2): 209–248. https://doi.org/10.1017/S0022112068000133.

Bombardelli, F. A., C. W. Hirt, and M. H. Garcia. 2001. "Discussion: Computations of curved free surface water flow on spiral concentrators." *J. Hydraul. Eng.* 127 (7): 629–631. https://doi.org/10.1061/(ASCE)0733-9429(2001)127:7(629).

Chanson, H., and T. Brattberg. 2000. "Experimental study of the air–water shear flow in a hydraulic jump." *Int. J. Multiphase. Flow* 26 (4): 583–607. https://doi.org/10.1016/S0301-9322(99)00016-6.

Chaudhry, M. H. 2014. *Applied hydraulic transients*. New York: Springer.

Davies Wykes, M. S., G. O. Hughes, and S. B. Dalziel. 2015. "On the meaning of mixing efficiency for buoyancy-driven mixing in stratified turbulent flows." *J. Fluid Mech.* 781 (Sep): 261–275. https://doi.org/10.1017/jfm.2015.462.

Eldayih, Y., M. Cetin, and J. G. Vasconcelos. 2020. "Air-pocket entrapment caused by shear flow instabilities in rapid-filling pipes." *J. Hydraul. Eng.* 146 (4): 04020016. https://doi.org/10.1061/(ASCE)HY.1943-7900.0001711.

Funk, J. E., S. J. VanVuuren, D. J. Wood, M. LeChevallier, and M. Friedman. 1999. "Pathogen intrusion into water distribution systems

due to transients." In *Proc., 3rd ASME/JSME Joint Fluid Engineering Conf.* New York: ASME.

Hager, W. H. 1999. "Cavity outflow from a nearly horizontal pipe." *Int. J. Multiphase. Flow* 25 (2): 349–364. https://doi.org/10.1016/S0301-9322 (98)00046-9.

Hirt, C. W., and B. D. Nichols. 1981. "Volume of fluid (VOF) method for the dynamics of free boundaries." *J. Comput. Phys.* 39 (1): 201–225. https://doi.org/10.1016/0021-9991(81)90145-5.

Hou, Q., A. S. Tijsseling, J. Laanearu, I. Annus, T. Koppel, A. Bergant, S. Vučković, A. Anderson, and J. M. C. van't Westende. 2014. "Experimental investigation on rapid filling of a large-scale pipeline." *J. Hydraul. Eng.* 140 (11): 04014053. https://doi.org/10.1061/(ASCE) HY.1943-7900.0000914.

Kordyban, E. 1990. "Horizontal slug flow: A comparison of existing theories." *J. Fluids Eng.* 112 (1): 74–83. https://doi.org/10.1115/1 .2909372.

Kundu, P. K., I. M. Cohen, and D. R. Dowling. 2012. *Fluid mechanics.* New York: Elsevier.

Laanearu, J., I. Annus, T. Koppel, A. Bergant, S. Vučković, Q. Hou, A. S. Tijsseling, A. Anderson, and J. M. C. van't Westende. 2012. "Emptying of large-scale pipeline by pressurized air." *J. Hydraul. Eng.* 138 (12): 1090–1100. https://doi.org/10.1061/(ASCE)HY.1943-7900.0000631.

Laanearu, J., Q. Hou, I. Annus, and A. S. Tijsseling. 2015. "Water-column mass losses during the emptying of a large-scale pipeline by pressurized air." *Proc. Est. Acad. Sci.* 64 (1): 8–16. https://doi.org/10.3176/proc .2015.1.02.

Laanearu, J., and K. Kaur. 2018. "Two-phase CFD modelling of air-water flow transition in a horizontal circular pipe and comparison with experimental results." In *Proc., 13th Int. Conf. on Pressure Surges.* Washington, DC: BHR Group.

Launder, B. E., and B. I. Sharma. 1974. "Application of the energy-dissipation model of turbulence to the calculation of flow near a spinning disc." *Lett. Heat Mass Trans.* 1 (2): 131–137. https://doi.org/10 .1016/0094-4548(74)90150-7.

Launder, B. E., and D. B. Spalding. 1972. *Lectures in mathematical models of turbulence.* London: Academic Press.

Leon, A. S., M. S. Ghidaoui, A. R. Schmidt, and M. H. Garcia. 2010. "A robust two-equation model for transient-mixed flows." *J. Hydraul. Res.* 48 (1): 44–56. https://doi.org/10.1080/00221680903565911.

Li, J., and A. McCorquodale. 1999. "Modeling mixed flow in storm sewers." *J. Hydraul. Eng.* 125 (11): 1170–1180. https://doi.org/10.1061 /(ASCE)0733-9429(1999)125:11(1170).

Liou, C. P., and W. A. Hunt. 1996. "Filling of pipelines with undulating elevation profiles." *J. Hydraul. Eng.* 122 (10): 534–539. https://doi.org /10.1061/(ASCE)0733-9429(1996)122:10(534).

Malekpour, A., and B. W. Karney. 2011. *Rapid filling analysis of pipelines with undulating profiles by the method of characteristics.* London: Hindawi. https://doi.org/10.5402/2011/930460.

Milne-Thomson, L. M. 1938. *Theoretical hydrodynamics.* London: Macmillan.

Ogden, K. A., and K. R. Helfrich. 2016. "Internal hydraulic jumps in two-layer flows with upstream shear." *J. Fluid Mech.* 789 (Jan): 64–92. https://doi.org/10.1017/jfm.2015.727.

Orszag, S. A., I. Staroselsky, W. S. Flannery, and Y. Zhang. 1996. *Introduction to renormalization group modeling of turbulence.* Oxford, UK: Oxford University Press.

Politano, M., A. J. Odgaard, and W. Klecan. 2007. "Case study: Numerical evaluation of hydraulic transients in a combined sewer overflow tunnel system." *J. Hydraul. Eng.* 133 (10): 1103–1110. https://doi.org/10.1061 /(ASCE)0733-9429(2007)133:10(1103).

Pope, S. B. 2000. *Turbulent flows.* Cambridge, MA: Cambridge University Press.

Pothof, I. W. M. 2011. "Co-current air-water flow in downward sloping pipes." Ph.D. dissertation, Dept. of Sanitary Engineering, Technical Univ. of Delft.

Pratt, L. J. 1986. "Hydraulic control of sill flow with bottom friction." *J. Phys. Oceanogr.* 16 (11): 1970–1980. https://doi.org/10.1175/1520 -0485(1986)016<1970:HCOSFW>2.0.CO;2.

Resch, F. J., and H. J. Leutheusser. 1972. "Reynolds stress measurements in hydraulic jumps." *J. Hydraul. Res.* 10 (4): 409–430. https://doi.org/10 .1080/00221687209500033.

Rossman, L. A. 2015. *Storm water management model user's manual Version 5.1.* Washington, DC: US EPA.

Sciacchitano, A., and B. Wieneke. 2016. "PIV uncertainty propagation." *Meas. Sci. Technol.* 27 (8): 084006. https://doi.org/10.1088/0957 -0233/27/8/084006.

Shih, T.-H., W. W. Liou, A. Shabbir, Z. Yang, and J. Zhu. 1995. "A new k-ε eddy viscosity model for high Reynolds number turbulent flows." *Comput. Fluids* 24 (3): 227–238. https://doi.org/10.1016/0045-7930(94) 00032-T.

Smith, L. M., and W. C. Reynolds. 1992. "On the Yakhot–Orszag renormalization group method for deriving turbulence statistics and models." *Phys. Fluids A.* 4 (2): 364–390. https://doi.org/10.1063/1.858310.

Smith, L. M., and S. L. Woodruff. 1998. "Renormalization-group analysis of turbulence." *Annu. Rev. Fluid Mech.* 30 (2): 275–310. https://doi.org /10.1146/annurev.fluid.30.1.275.

Vasconcelos, J. G., and S. J. Wright. 2009. "Investigation of rapid filling of poorly ventilated stormwater storage tunnels." *J. Hydraul. Res.* 47 (5): 547–558. https://doi.org/10.3826/jhr.2009.3390.

Vasconcelos, J. G., S. J. Wright, and P. L. Roe. 2006. "Improved simulation of flow regime transition in sewers: Two-component pressure approach." *J. Hydraul. Eng.* 132 (6): 553–562. https://doi.org/10.1061 /(ASCE)0733-9429(2006)132:6(553).

Vasconcelos, J. G., E. Yasemin, Z. Yang, and J. A. Jalil. 2018. *Evaluating Storm Water Management Model accuracy in conditions of mixed flows.* Guelph, Canada: Computational Hydraulics Intl. https://doi .org/10.14796/JWMM.C451.

Weller, H. 2002. *Derivation modelling and solution of the conditionally averaged two-phase flow equations.* London: Nabla Ventures.

Yakhot, V., and S. A. Orszag. 1986. "Renormalization group analysis of turbulence. I. Basic theory." *J. Sci. Comput.* 1 (14): 3–51. https://doi .org/10.1007/BF01061452.

Zukoski, E. E. 1966. "Influence of viscosity, surface tension, and inclination angle on motion of long bubbles in closed tubes." *J. Fluid Mech.* 25 (4): 821–837. https://doi.org/10.1017/S0022112066000442.

Appendix 2

Numerical investigation of the impact of irregular pipe wall build-up on velocity in the water distribution system

Katrin Kaur, Anatoli Vassiljev, Ivar Annus, Nils Kändler
and Janet Roosimägi

ABSTRACT

This paper presents novel equations for different wall build-up types in old pipes developed for the estimation of real flow velocities in a water distribution system (WDS). This is important when estimating the contamination propagation rate in an operational WDS. Because the inner surface geometry of old rough pipes is complex, real velocities cannot be estimated by conventional WDS models. Therefore, a computational fluid dynamics (CFD) model was used to analyse the flow dynamics in old rough pipes with even and uneven roughness build-up. The developed equations for the velocity correction coefficients derive from the results of numerical simulations. Numerically obtained velocity fields show that in some cases, pipe wall build-up can affect the effective flow section significantly and the flow velocity can be underestimated by more than two times. Therefore, different velocity correction equations have to be used for different types of pipe wall build-up.

Key words | computational fluid dynamics, contamination propagation rate, pipe wall build-up, roughness, water distribution system modelling

Katrin Kaur (corresponding author)
Anatoli Vassiljev
Ivar Annus
Nils Kändler
Janet Roosimägi
Department of Civil Engineering and Architecture,
Tallinn University of Technology,
Tallinn 19086,
Estonia
E-mail: *katrin.kaur@taltech.ee*

HIGHLIGHTS

- Velocity correction coefficients for old water distribution pipes were developed.
- Velocity correction is significant when estimating the contamination propagation rate using water distribution system models.
- Existing models can underestimate the flow velocity in old pipes by more than two times.

INTRODUCTION

For decades, the water distribution systems (WDS) have been considered as resilient and reliant infrastructures, offering quality service at relatively low cost. On the other hand, we are entering into an era where the average life span of pipes laid down from the late 1800s to the 1950s is running out (e.g. AWWA 2001; Kanakoudis & Tolikas 2001; Lee & Meehan 2017; Barton et al. 2019). Kanakoudis & Tolikas (2001) reported that taking into account the hydraulic, economic and social aspects, the optimum replacement time for cast iron pipes is between 69 and 89 years, depending on the pipe diameter. This exceeds the estimations by Barton et al. (2019) who investigated the data of pipe brakes in 308 water companies in the USA and Canada. They concluded that the average life span of metal water pipes is about 50 years, independent of the type of metal. Studies conducted on the breaking data of copper and galvanized steel pipes have shown that the average lifespan of small diameter service line pipes can be as low as 35 years (Lee & Meehan 2017). The result of infrastructure ageing is an increase in structural failures (pipe bursts and rate of leakages) and operational shortcomings (increased energy consumption, water quality issues,

low pressure, etc.). The deviations from design operating conditions may indicate to the deviations of pipe characteristics inherent to old rough pipes.

The pipe wall build-up is not only time-dependent but is affected by a number of factors – pipe cross-section, material, water quality and flow velocity (Kändler 2002; Kanakoudis 2004; Vreeburg & Boxall 2007; Vreeburg *et al.* 2009). Design of the WDS has been dominated by the fire-fighting demand and the intuitive need for looping, leading to low velocities and long residence time. A field study carried out in Tallinn revealed that the pipe cross-sections of metal pipes (steel and cast iron) were reduced on average by 10% due to wall build-up. The specimens were 25–100 years old with diameters from 75 to 200 mm (Kändler 2002). Corrosion caused carrying capacity failures due to the pipe wall build-up may prevent WDS from constantly ensuring customer water needs with satisfying quality (Kanakoudis 2004). The side effect of corrosion and low velocity can be discolouration of the water, which has been the main customer complaint about the water quality in the UK (Vreeburg & Boxall 2007). The formation and growth of particles in the WDS is a complex process, but the sedimentation of the particles is related to the hydraulic conditions of the network. It was shown that at low velocities, the sediment settling will take place in the lower half of the horizontal pipe, while at higher velocities, the settling will cover the entire pipe wall (Vreeburg & Boxall 2007). Vreeburg *et al.* (2009) suggested that the daily maximum velocity in the WDS should be at least 0.4 m/s to prevent particles from accumulating and causing pipe wall build-up.

A number of studies have analysed the growth of the pipe roughness over time. Colebrook & White (1937) suggested that the pipe roughness grows linearly and the growth rate depends mostly on the pH of the water flowing inside the pipe. The reported values of the roughness growth rate ranged from 0.066 to 0.63 mm/yr. The latter is similar to the results reported by Willims & Hazen (1920). The range is in line with numerous investigations in the US (Walski *et al.* 1988); however, it is significantly underestimating the growth rate reported by Echávez (1997) for galvanized iron pipes (2.13 mm/yr) that are concurrently less often used in WDS compared to cast iron. Rapid growth rate will result in a rapid reduction in the flow area and growth of the

flow velocity. This is particularly important when estimating changes in the water quality in a WDS. The reason is that underestimation of the flow velocity will lead to considerable errors in the estimations of the propagation rate of the contaminated zones in a WDS (Boxall *et al.* 2004; Annus & Vassiljev 2015).

The numerical model of a WDS is commonly developed using nominal pipe diameters. Therefore, during the calibration of such a model, the pipe wall build-up is compensated by adjusting the roughness value (Lansey *et al.* 2001) or by adjusting the water consumption at the nodes (Kanakoudis & Gonelas 2015a, 2015b). The latter can be done only when the consumption in the nodes is not measured. The adjustment of the pipe roughness value is justified for surfaces whose geometry is easily described (Jimenez 2004). However, in real WDS, the shape of the inner wall can vary significantly over the pipe length, so that the pipe cross-section is not homogeneous. The irregular wall roughness elements greatly complicate the flow dynamics (Christensen *et al.* 2011), indicating that the usage of nominal pipe diameters in the modelling process is not always justified.

The roughness height, as well as the shape of the inner pipe surface, may significantly vary in old pipes, resulting in complex geometries. Annus *et al.* (2020) analysed the influence of irregular pipe wall roughness on the flow velocity in WDS old pipes. Three types of roughness build-up were investigated: Type 1 – evenly distributed roughness (roughness height <10 mm); Type 2 – unevenly distributed roughness (roughness height up to $0.5D$) and Type 3 – sediment settling in the lower part of the pipe. It was shown by Annus *et al.* (2020) that in pipes Type 1 and Type 3, the dependence between the relative roughness and the increase in the estimated velocity (so-called velocity correction coefficient) was similar. In Type 2 pipes, the velocity correction coefficient is dependent both on the shape and the number of local disturbances that reduce the effective pipe diameter. Measurements in Tallinn WDS have revealed that in some cases, the exponent describing the dependence between the pressure drop and the flow rate can be larger than 2, indicating that the actual flow behaviour is complex and simple expressions will lead to misjudgement of flow parameters. The main goal of this paper was to analyse the reason for such results. It is

proposed herein that when measurements at nodes reveal abnormal exponent values, pipe sections with irregular roughness elements may be present. This paper analyses the factors influencing the exponent based on computational fluid dynamics (CFD) simulations and presents an equation to estimate real flow velocities in a WDS containing pipes with uneven surface roughness.

METHODS

Existing network calibration data

Analysis of the WDS containing old rough pipes shows that in some cases, the exponent n describing the dependency between the pressure drop Δp and the flow rate Q is larger than 2 (i.e. $n > 2$ in $\Delta p = k \cdot Q^n$, where k is a constant characterizing the pipe). Figure 1 shows the values of the exponents in selected measurement points in a part of Tallinn WDS. These measurements were performed during collecting data for the calibration of the WDS. Pressures were measured in 18 points and flow rate in 13 points. Additional measurements were conducted at pumping stations supplying the WDS. For pressure measurements, portable data loggers of the 'Sensus' company with strain gauge pressure sensors were used. Absolute heights of all sensors were measured with high accuracy using geodetic levelling. Water flow rates were measured using turbine and electromagnetic

flow meters that had impulse output for using data. Some results of the calibration are presented in Vassiljev *et al.* (2015). Seventeen measurement points are shown in Figure 1. The exponent values are larger than 2 in three points.

Due to high costs and constructional restrictions, it is not possible to identify the effective pipe diameters in an operational WDS precisely. Pipe replacements in the operational WDS in Tallinn have revealed that the wall build-up has resulted in an uneven decrease of the diameter along the pipe length, sometimes acting as local obstruction (Kändler 2002). Local obstructions increase energy losses and affect the flow dynamics, making its description by a simple expression impossible. These local losses (Type 2 pipes) generate additional pressure drop that is dependent on the flow rate. In EPANET, the increase in the pressure drop is usually described with the increase of pipe roughness. This can lead to unrealistic pipe roughness values and underestimation of real flow velocities (Annus & Vassiljev 2015; Annus *et al.* 2020). Therefore, it has to be reckoned that the ageing process of pipes is expressed both in the increase of pipe roughness and the decrease of pipe diameter. Only under these conditions, it can be assumed that the modelled flow velocities are in a reasonable range and the model is reliable for analysing extreme conditions (e.g. fire flows) or changes in the water quality. The next section describes Type 2 pipe models and calculation methods to determine the actual flow velocity in the WDS containing this type of old rough pipe.
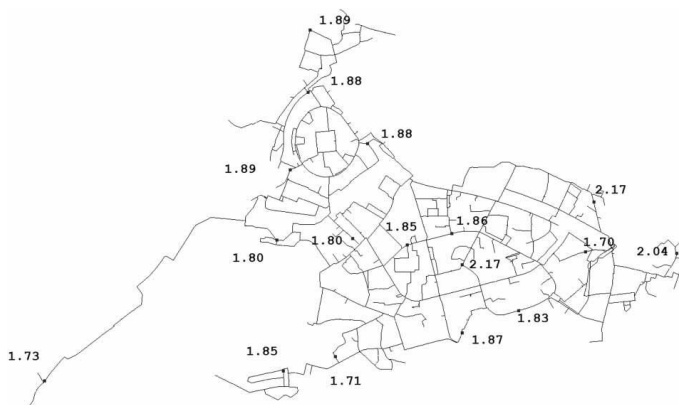
Figure 1 │ Exponents of dependence between the measured pressure drop and the flow rate in Mustamäe-Õismäe district, Tallinn.

Numerical procedure

CFD model was used to analyse the flow dynamics in a pipe where the diameter decreases unevenly along the pipe length (referred to as Type 2 pipe in Annus *et al.* (2020)) (Figure 2). In Type 2 pipes, the changes in average velocity are dependent both on the shape and the number of local obstructions that reduce the effective flow section. Therefore, CFD models are used as the complexity of the flow dynamics needs more attention to improve the estimation of real flow velocities in WDS.

   To analyse the flow dynamics, a random pattern was created (Figure 3) and 'bruised' into the pipe wall at two and four locations over the pipe length to mimic the irregular inner surface of a typical old rough pipe (Figures 4 and 5). The surface pattern was applied to the test pipe both on the top and bottom side. The CFD calculations were performed at six different pressure drops between the pipe segment inlet and outlet ranging from 50 to 2,500 Pa. The range of average flow velocities used in this study was 0.13…1.3 m/s. The corresponding flow rates were calculated at each pressure drop while the pipe surface sand-grain roughness was set to $e = 1$ mm.

   In Annus *et al.* (2016), the performance of the Reynolds-averaged Navier–Stokes (RANS) turbulence model in a complex pipe was analysed by comparing the measured and the modelled velocity and kinetic energy distributions

Figure 3 | 3D visualization of random surface pattern.

over a complex geometry pipe segment length and perimeter. The standard k–ω turbulence model by Wilcox (1998) showed the best qualitative and quantitative correlation. In this study, we used the experimentally validated solution algorithm with the k–ω turbulence model.

   In addition to the turbulent flow regime, the fluid was assumed incompressible, isothermal and Newtonian. In the validation process, numerical simulation results obtained from the stationary and nonstationary solution algorithms were compared. It was concluded that after a sufficiently large number of iterations (1,500 to 5,000, depending on the initial conditions), the flow becomes steady; nonstationary and stationary models gave similar results. A solver from OpenFOAM v1218 (OpenCFD Ltd) employing the Semi-Implicit Method for Pressure Linked Equations (SIMPLE) algorithm (Caretto *et al.* 1973) was used to solve continuity and momentum equations.

   In the current study, the pipe had a nominal diameter of 300 mm and a length of 1,500 mm for both configurations of the irregular pipe inner surface (i.e. two and four irregular roughness elements). Results for Type 2 pipe with 100 and 200 mm diameter are shown in Annus *et al.* (2020). The computational domains (Figures 4 and 5) were discretized by a hybrid grid containing a mixture of structured and unstructured grid portions. In the vicinity of local complex geometry, a more refined grid was applied. The pipe with two irregular roughness elements was meshed with

Figure 2 | Typical pipe wall build-up with unevenly distributed roughness – Type 2 pipe (Kändler 2002).
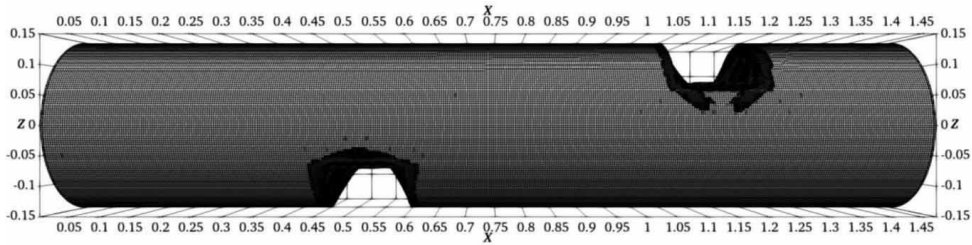
Figure 4 | Computational domain of the 1.5 m long pipe with two irregular roughness elements.
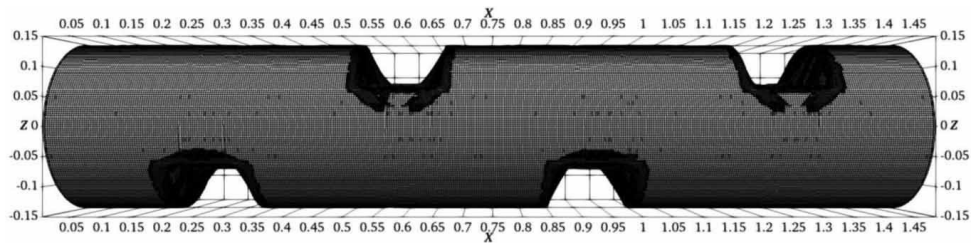
Figure 5 | Computational domain of the 1.5 m long pipe with four irregular roughness elements.

2.475×10^6 finite volumes, of which 2.333×10^6 were hexahedral. The pipe with four irregular roughness elements was meshed with 2.642×10^6 finite volumes, of which 2.404×10^6 were hexahedral. The convergence criteria for x-, y- and z-velocity components, ω and k were set to 0.0001.

Grid sensitivity

Grid sensitivity study was conducted for a more complicated geometry with eight irregular roughness elements and

100 mm nominal diameter, resulting in a smaller computational domain and therefore allowing higher numbers of finite volumes to be tested. Figure 6 presents simulation results for three mesh refinement levels. It can be seen that the difference in the calculated flow rate value for grids with 1.45 and 2.77 million elements is 1%. It was concluded that 2.77 million elements are sufficient and further refinement is not necessary. For the pipe with the nominal diameter 300 mm, the grid element size was scaled accordingly.
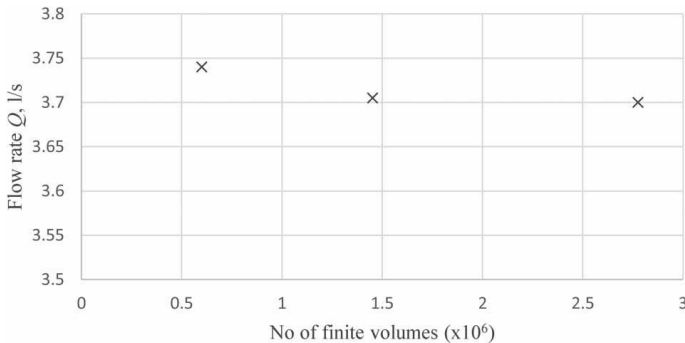
Figure 6 | Calculated flow rate for three grid sizes.

RESULTS AND DISCUSSION

CFD calculation results for different numbers of irregular roughness elements are given in Table 1. The exponent for the pressure drop is higher than 2 at two irregular roughness elements. In other cases, the exponent is lower than 2. It has to be reckoned that the exponent is calculated using the flow rate (not average velocity). At an average velocity (calculated using the estimated effective flow section), the exponent would be close to 2 for all configurations of irregular roughness elements.

Analyses show that in some pipe wall configurations, local disturbances have to be taken into account as they change the function between the pressure drop and the flow rate. Numerical investigations revealed that the complex pipe inner wall shape leads to complex flow dynamics and interactions between the developing vortices near the deformed wall elements. Analysis of the developing vortices shows that at some pipe configurations, the size of the eddies changes at different pressure drops, and in some cases, the size is constant (Table 2). This depends on the distance between the irregular roughness elements. Similar to

Table 1 │ Exponent of dependence $\Delta p = f(Q)$ for different numbers of irregular roughness elements

Number of irregular roughness elements	Exponent
0	1.95
2	2.27
4	1.93

Table 2 │ Dependence between the pressure drop and the size of vortices (% of computational domain volume) at different numbers of irregular roughness elements

	Volume of vortices (%)	
Pressure drop (Pa)	Number of irregular roughness elements 2	Number of irregular roughness elements 4
2,500	22	24
1,500	22	24
900	21	24
500	16	24
200	14	24
50	12	24

corrugated pipes, if the distance between the deformations is small enough, the vertical structures trapped between the deformations have a minimal influence on the core flow (Vijiapurapu & Cui 2007, 2010). The effective flow section of a pipe is equal to the free space between the irregular roughness elements, excluding the volume of the near-wall vortices. The interaction between the near-wall vortices and the jet-like flow at the pipe axis is low (Annus *et al.* 2019).

Flow structure in pipes with two and four irregular roughness elements is presented in Figures 7 and 8. In the case of two irregular roughness elements, the eddy size is significantly affected by the change in the pressure drop, and it is evident that the irregular roughness element acts as local obstruction. Calculations reveal that the exponent describing the dependence between the pressure drop and the flow rate is larger than 2 for this configuration.

Velocity field in the pipe with four irregular roughness elements shows no changes in the eddy size at the increase of the pressure drop.

It is proposed that the flow structure can be characterized according to the exponent while calibrating the model of a WDS. Figure 9 presents the dependence between the relative roughness and the velocity correction coefficient for the three types of old rough pipes with diameters of 100, 200 and 300 mm. The results for pipes with diameters of 100 and 200 mm are based on Annus *et al.* (2020).

When the roughness in the EPANET calibration process is large and the exponent is equal to or less than 2, it can be concluded that there are old pipes in the network that have uniform roughness build-up (in the form of reduced cross-section area – Type 1 or changed cross-section shape – Type 3). The velocity correction coefficient should be used taking into account a corrected pipe cross-section area:

$$v_{\mathrm{cor}} = 2.2 \cdot \frac{e_m}{D} + 1.3 \tag{1}$$

where e_m/D is relative roughness and e_m is pipe roughness gained from EPANET for pipe nominal diameter D.

When the roughness in the EPANET calibration process is large (i.e. equal to or larger than the pipe radius) and the exponent is more than 2, then there are Type 2 segments in the pipeline and the velocity should be recalculated

Figure 7 │ Comparison of vortex formation behind two irregular roughness elements.

Figure 8 │ Comparison of vortex formation behind four irregular roughness elements.

according to

$$v_{\text{cor}} = 0.8 \cdot \frac{e_m}{D} + 1.25. \tag{2}$$

CONCLUSIONS

Measurements on old operational WDS sections have revealed that in some cases, the exponent describing the relationship between the pressure drop and the flow rate yields values larger than 2. It is proposed herein that this indicates the presence of pipes with irregular roughness elements in-between measurement nodes. Due to high costs and constructional restrictions, it is not possible to identify the effective pipe diameters in operational WDS precisely. Therefore, numerical modelling was applied in the present study to investigate the effect of the shape of an irregular pipe wall on the flow velocity. Based on the computational analysis, velocity correction coefficients
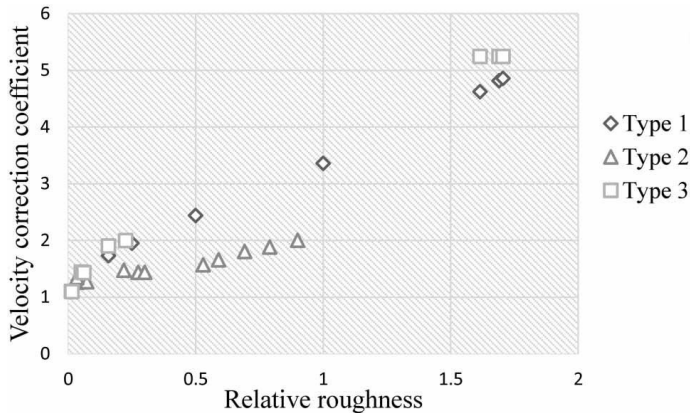
Figure 9 │ Relative roughness and velocity correction coefficient.

were estimated for WDS. The study showed that in some old rough pipes, the inner shape is changed such that the irregular roughness elements act as local obstructions. Formation of vortices is dependent on the number of obstructions and distance between them. These vortices reduce the effective flow section and an increase in volume with an increasing flow rate.

It was concluded that different equations hold for the types of wall build-up when finding the real flow velocity estimation. When the exponent is less than or equal to 2, it can be concluded that roughness build-up in the pipeline sections is uniform. Field studies in Tallinn have shown that the exponent in an operational WDS containing old rough pipes may in some cases be larger than 2. In this case, the wall build-up is inconsistent, which in the EPANET calibration process, is expressed by large roughness and an exponent value higher than 2. For the second type, it is shown via velocity field visualization that irregular roughness elements affect the eddy size significantly, and therefore also the effective flow section. In this case, the velocity correction coefficient is dependent on the number of local obstructions and their distance. The inner surfaces of old rough pipes presented here with two and four irregular roughness elements are simplifications. In real old pipes, more complex geometries are possible and the formation of the vortices is not straightforward, possibly resulting in further effective flow section reductions. The analysis here

showed that the flow velocity in old rough pipes can be underestimated by more than two times.

ACKNOWLEDGEMENTS

DATA AVAILABILITY STATEMENT

Data cannot be made publicly available; readers should contact the corresponding author for details.

REFERENCES

Annus, I. & Vassiljev, A. 2015 Different approaches for calibration of an operational water distribution system containing old pipes. *Procedia Engineering* **119**, 526–534. doi:10.1016/j.proeng.2015.08.900.

Annus, I., Kaur, K., Vassiljev, A., Laanearu, J. & Šanin, M. 2016 Flow dynamics in a pipe with a sudden change in diameter. In: *Proceedings of the 14th International CCWI Conference*, Amsterdam, The Netherlands, pp. 1–8.

Annus, I., Kartushinsky, A., Vassiljev, A. & Kaur, K. 2019 Numerical and experimental investigation on flow dynamics in a pipe with an abrupt change in diameter. *Journal of Fluids Engineering* **141** (10), 101301-1–101301-9. doi:10.1115/1.4043233.

Annus, I., Vassiljev, A., Kändler, N. & Kaur, K. 2020 Determination of the corresponding roughness height in a WDS model containing old rough pipes. *Journal of Water Supply: Research and Technology – AQUA* **69** (3), 201–209. doi:10.2166/aqua.2019.080.

AWWA 2001 *Dawn of the Replacement Era: Reinvesting in Drinking Water Infrastructure*. United States of America Water Works Association, Denver, USA.

Barton, N. A., Farewell, T. S., Hallett, S. H. & Acland, T. F. 2019 Improving pipe failure predictions: factors affecting pipe failure in drinking water networks. *Water Research* **164**, 1–16.

Boxall, J. B., Saul, A. J. & Skipworth, P. J. 2004 Modeling for hydraulic capacity. *Journal American Water Works Association* **96** (4), 161–169. doi:10.1002/j.1551-8833.2004.tb10607.x.

Caretto, L. S., Gosman, A. D., Patankar, S. V. & Spalding, D. B. 1973 Two calculation procedures for steady, three-dimensional flows with recirculation. In: *Proceedings of the Third International Conference on Numerical Methods in Fluid Dynamics*. Lecture Notes in Physics 19. Springer, Heidelberg. doi:10.1007/BFb0112677.

Christensen, R. T., Spall, R. E. & Barfuss, S. L. 2011 Application of three RANS turbulence models to aged water transmission pipes. *Journal of Hydraulic Engineering* **137** (1), 135–139. doi:10.1061/(ASCE)HY.1943-7900.0000288.

Colebrook, C. F. & White, C. M. 1937 Experiments with fluid friction in roughened pipes. *Proceedings of the Royal Society A* **161** (906), 367–381. doi:10.1098/rspa.1937.0150.

Echávez, G. 1997 Increase in losses coefficient with age for small diameter pipes. *Journal of Hydraulic Engineering* **123** (2), 157–159. doi:10.1061/(ASCE)0733-9429(1997)123:2(157).

Jimenez, J. 2004 Turbulent flow over rough wall. *Annual Review of Fluid Mechanics* **36**, 173–196. doi:10.1146/annurev.fluid.36.050802.122103.

Kanakoudis, V. 2004 A troubleshooting manual for handling operational problems in water pipe networks. *Journal of Water Supply: Research and Technology – AQUA* **53** (2), 109–124. doi:10.2166/aqua.2004.0010.

Kanakoudis, V. & Gonelas, K. 2015a Accurate water demand spatial allocation for water networks modelling using a new approach. *Urban Water Journal* **12** (5), 362–379. doi:10.1080/1573062X.2014.900811.

Kanakoudis, V. & Gonelas, K. 2015b Properly allocating the urban water meter readings to the nodes of a water pipe network simulation model. *Desalination and Water Treatment* **54** (8), 2190–2203. doi:10.1080/19443994.2014.934101.

Kanakoudis, V. & Tolikas, K. 2001 The role of leaks and breaks in water networks: technical and economical solutions. *Journal of Water Supply: Research and Technology – AQUA* **50** (5), 301–311. doi:10.2166/aqua.2001.0025.

Kändler, N. 2002 *Optimal Algorithm for Rehabilitation of a Water Distribution Network*. MSc Thesis, Tallinn University of Technology, Tallinn, Estonia.

Lansey, K. E., El-Shorbagy, W., Ahmed, I., Araujo, J. & Haan, C. T. 2001 Calibration assessment and data collection for water distribution networks. *Journal of Hydraulic Engineering* **127** (4), 270–279. doi:10.1061/(ASCE)0733-9429(2001)127:4(270).

Lee, J. & Meehan, M. 2017 Survival analysis of US water service lines utilizing a nationwide failure data set. *Journal AWWA* **109** (9), 13–21.

Vassiljev, A., Koor, M. & Koppel, T. 2015 Real-time demands and calibration of water distribution systems. *Advances in Engineering Software* **89** (2015), 108–113. doi:10.1016/j.advengsoft.2015.06.012.

Vijiapurapu, S. & Cui, J. 2007 Simulation of turbulent flow in a ribbed pipe using large eddy simulation. *Numerical Heat Transfer, Part A: Applications* **51** (12), 1137–1165. doi:10.1080/10407780601112829.

Vijiapurapu, S. & Cui, J. 2010 Performance of turbulence models for flows through rough pipes. *Applied Mathematical Modelling* **34** (6), 1458–1466. doi:10.1016/j.apm.2009.08.029.

Vreeburg, J. H. G. & Boxall, J. B. 2007 Discolouration in potable water distribution systems: a review. *Water Research* **41** (3), 519–529. doi:10.1016/j.watres.2006.09.028.

Vreeburg, J. H. G., Blokker, E. J. M., Horst, P. & van Dijk, J. C. 2009 Velocity-based self-cleaning residential drinking water distribution systems. *Water Science & Technology: Water Supply* **9** (6), 635–641. doi:10.2166/ws.2009.689.

Walski, T. M., Sharp, W. W. & Douglas Shields Jr., F. 1988 Predicting internal roughness in water mains. *Journal American Water Works Association* **80** (11), 34–40. doi:10.1002/j.1551-8833.1988.tb03132.x.

Wilcox, D. C. 1998 *Turbulence Modelling for CFD*. DCW Industries Inc., La Canada, USA.

Williams, G. S. & Hazen, A. 1920 *Hydraulic Tables*. John Wiley & Sons Inc., Brooklyn, USA.

Appendix 3

Ivar Annus
Department of Civil Engineering
and Architecture,
Tallinn University of Technology,
Ehitajate tee 5,
Tallinn 19086, Estonia
e-mail: ivar.annus@taltech.ee

Alexander Kartushinsky
Department of Civil Engineering and Architecture,
Tallinn University of Technology,
Ehitajate tee 5,
Tallinn 19086, Estonia
e-mail: aleksander.kartusinski@taltech.ee

Anatoli Vassiljev
Department of Civil Engineering and Architecture,
Tallinn University of Technology,
Ehitajate tee 5,
Tallinn 19086, Estonia
e-mail: anatoli.vassiljev@taltech.ee

Katrin Kaur
Department of Civil Engineering and Architecture,
Tallinn University of Technology,
Ehitajate tee 5,
Tallinn 19086, Estonia
e-mail: katrin.kaur@taltech.ee

Numerical and Experimental Investigation on Flow Dynamics in a Pipe With an Abrupt Change in Diameter

Flow dynamics in a pipe with an abrupt change in diameter was experimentally and numerically analyzed. Two-dimensional stationary Reynolds-averaged Navier–Stokes (RANS) k–ε epsilon model was used to describe the development of axial and radial velocity and turbulent kinetic energy in two cases. The theoretical results were compared with experimental findings gained in a transparent pipe test rig. Particle image velocimetry (PIV) technique was used to analyze the development of flow in a pipe with complex geometry. The measured and modeled velocities and turbulent kinetic energy were found to be in good agreement. The two-dimensional stationary RANS k–ε model is suitable for the analysis of the flow dynamics in real old rough pipes where the pipe wall build-up leads to changes in the actual diameter of the pipe but the flow can still be considered axially symmetrical. [DOI: 10.1115/1.4043233]

Introduction

Many engineering systems contain surfaces that can be considered hydrodynamically rough. Therefore, development of models capable of accurate prediction of turbulent flow dynamics over rough surfaces has attracted high interest. This problem is directly linked with pipe network modeling. The numerical models of existing water distribution systems (WDS) that contain old pipes are usually calibrated by estimating the roughness of the pipes. Due to the lack of information, nominal pipe diameters are generally used in the model development and the change in the pipe diameter due to pipe wall build-up is compensated by adjusting the roughness value [1]. This can lead to roughness values larger than pipe radius which are unrealistic. The shape of the pipe inner wall can vary in time and space due to uneven wall build-up. Pipe surfaces that were originally manufactured smooth can develop irregular wall roughness elements that greatly complicate the flow dynamics [2]. Therefore, it is not always reasonable to use nominal pipe diameters in the modeling process. Information about real pipe diameters and flow velocities is very important for estimating the propagation rate of the contaminated zones in WDS in cases of chemical or biological threats [3–5]. The assessment of real flow dynamics at irregular pipe wall geometry is a prevailing challenge.

Over the years, many investigations have focused on the analysis of the flow dynamics in pipes with regular roughness elements. Vijiapurapu and Cui [6,7] investigated the turbulent flow in ribbed pipes. Experimental data were compared with Reynolds-averaged Navier–Stokes (RANS) and large eddy simulation (LES) models. Three different pipe configurations were analyzed. It was shown

that when the distance between the ribs is small, the vortical structures trapped between the ribs have minimal influence on the core flow. On the other hand, if the distance between the ribs is larger, the core flow near the rib is significantly affected by the vortices developing between the ribs. It was concluded that both RANS and LES corresponded well with the experimental results for all three investigated rib roughnesses but RANS models had difficulties in predicting flow separation. In addition to the time-averaged flow pattern, LES was capable of accurately reproducing the three-dimensional statistics of turbulence, but taking into account complex vertical motions, the computational time was around five times longer. Stel et al. [8] and [9] analyzed the turbulent flow in corrugated pipes. The low-Reynolds number k–ε model was used to investigate the effect of rib roughness on friction factors. The numerical results were validated by comparing them with the differences in the measured pressure of corrugated pipes. The k–ε model results were found to be in good agreement with [6] LES results. It was concluded that the friction factor is higher in corrugated pipes as compared to smooth pipes and increases as both the Reynolds number and the groove length increase; at the same time, it is not affected by the groove height. Turbulent intensities tend to increase near the downstream corner of the groove and the main flow is not completely unaffected by the cavities. Calomino et al. [10] conducted an experimental and numerical study on the flow field, pressure drop, and friction factor in corrugated pipes. Measured pressures and velocity fields were compared with numerical results using the LES model. Good correlation between measured and modeled averaged velocities and pressures was found. LES modeling results were used to analyze the vorticities and velocity fluctuations in the area near the pipe wall.

These studies were conducted on a surface with relatively large roughness elements. However, the surfaces of real old pipes differ having generally a range of roughness scales. Therefore, Christensen et al. [2,11] conducted a series of numerical investigations

using three RANS models ($\overline{v^2} - f$, realizable k–ε and k–ω) at Reynolds numbers ranging from 6700 to 31,000 to model the flow through aged pipes. Darcy–Weisbach friction factors were calculated in all cases and compared to experimentally obtained values. It was concluded that dependent on Reynolds number and model used the computational fluid dynamics (CFD) models underestimated the friction factors 8–30%.

In old rough pipes, one of the roughness effects is an abrupt change in pipe diameter. Numerous experimental and numerical studies have been conducted in this field to analyze the stability in sudden expansion pipe flow [12–14] and over a backward-facing step [15,16] to determine the propagation of velocity and turbulent kinetic energy. The studies have been focused on analyzing the sequence of events in the transition from laminar to turbulent flow and establishing the critical Reynolds number that is not so firmly determined. The main difference in these studies compared to this paper is that the sudden expansion is not followed by an abrupt contraction, which is typical in real old pipes where the pipe wall build-up has an arbitrary manner and is significant compared to the pipe diameter.

In this study, an experimental investigation was conducted to analyze the flow dynamics in a pipe with an abrupt change in diameter where the sudden expansion is followed by a sudden contraction. The experimental results were compared with the CFD modeling results. The focus was on the applicability of the widely used RANS k–ε model for modeling a flow in ducts with complex geometry mimicking old rough pipes. The effect of the model coefficients and the setup was analyzed to increase the concurrence with experimental results. The model enables to determine mean flow velocity and effective diameter in any old rough pipe which is essential in case of analyzing water quality changes in WDS.

Test Rig and Instrumentation

A pipeline apparatus was setup at the Laboratory of Fluid Mechanics, Tallinn University of Technology to investigate

Table 1 List of experiments. Uncertainty of reading for flow rate measurements was ±0.5%.

Experiment number	Flow rate (Q, l/s)	Reynolds number in the test section ($D = 80$ mm)	PIV measurement frequency (f_s, Hz)
1	0.75	12,000	235
2	1.245	19,800	391

the flow dynamics in a pipe with an abrupt change in diameter. Velocity distributions and pressure changes were measured at two different flow rates (Table 1).

The layout of the experimental apparatus is shown in Fig. 1. It consisted of a tank at the upstream end, a horizontal transparent polymethyl methacrylate pipe of total length $L = 18.8$ m with the internal diameter $D = 80$ mm and a control valve at the downstream end. The pipeline was assembled of 2 m long pipes and was hydraulically smooth. In the case of a pipe with an abrupt change in diameter, the 2 m long test section consisted of two short pipes at both ends with an internal diameter $D = 80$ mm, two longer pipes with an internal diameter $D = 46.4$ mm, and a 0.23 m long transparent section with an internal diameter $D = 80$ mm in the middle. The test rig was pressure driven and the upstream-end tank had a constant water level during all tests. The flow rate was controlled by a downstream-end control valve and upstream-end pump frequency.

Changes in the velocity distribution at an abrupt change in diameter were measured in the middle of the test section using the two-dimensional particle image velocimetry (PIV). PIV measurements were carried out using a high-speed camera and a continuous-wave laser for lighting. The camera was adjusted to ensure that the whole area of the PIV box is covered. The size of a window used was 1280×800 pix. The measurement frequency of the camera was adjusted according to the Reynolds number (Table 1). A steady-state flow was measured for 10 s, which corresponded to 2350–3910 images per test. The data were recorded and processed by special software Dynamic Studio 4.0 (by Dantec Dynamics, Skovlunde, Denmark). The cross-correlation method was used to process the PIV data. As a result, velocity vector fields were calculated taking into account the displacement of the particles between the two frames. An interrogation window of 16×16 pixels with 50% overlap, decreasing the size with multiple passes (starting from 256×256 pixels) was used. No pre- or postprocessing of the images was carried out. A simple reference image with rulers inserted in the pipe was used to calibrate the PIV. No distortion was present in images because a Plexiglas PIV box was used in the tests, and the camera lens was mounted horizontally. From the calibration image, a scale of 1 pix = 0.16 mm was set and used in further calculations. Mean velocities, standard deviations, and turbulent kinetic energies were calculated using only valid vectors (i.e., gained from measured particle displacements not substituted by the software).

Uncertainties of PIV-measured velocity field components and derived values of turbulent kinetic energy were quantified using uncertainty propagation techniques presented in Ref. [17]. The uncertainties for axial velocity u, radial velocity v, and turbulent
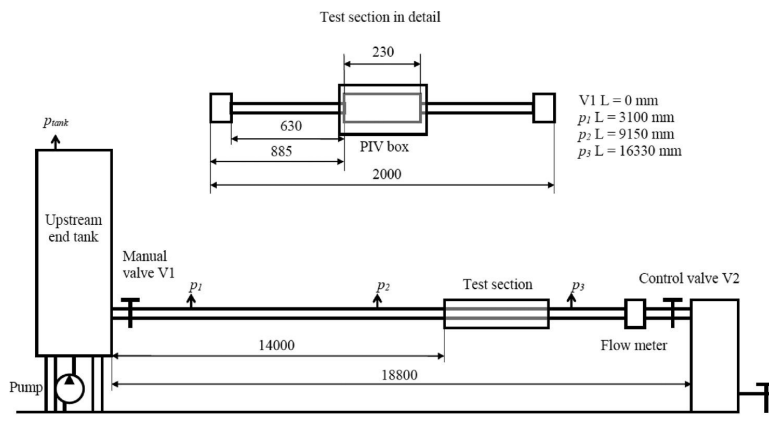
Fig. 1 Schematic of the test rig

kinetic energy k were $\pm2.4\%$, $\pm22.5\%$, and $\pm3.6\%$, respectively. Relatively larger uncertainty for the radial velocity component was induced by the PIV sampling frequency settings. The sampling frequency was adjusted according to axial velocity component which was more than an order of magnitude larger than the radial component.

Diode type continuous-wave laser with a maximum output power of 5 W was used and the settings were adjusted according to the test. Oxygen and hydrogen bubbles generated via electrolysis were used for seeding. The electrified wires were attached inside the pipe just before the test section.

In addition, pressures were measured at three different locations over the pipe length (three strain-gauge pressure probes, measuring range $-1\dots5$ bar), and the flow rate was measured with an electromagnetic flowmeter installed at the downstream end of the pipe. The instrumentation was carefully selected to have the response of suitable accuracy and frequency. Instruments were calibrated before the measurements in laboratory conditions. The sampling frequency for the pressure and flow rate was $f_s = 100$ Hz. Uncertainty of reading was $\pm0.5\%$ in flow measurements and $\pm0.3\%$ in pressure measurements.

Numerical Procedure

Reynolds-averaged Navier–Stokes standard k–ε turbulence model [18] was used to analyze the flow dynamics in a pipe with complex geometry. The flow regime was turbulent and the fluid was assumed to be incompressible, isothermal, and Newtonian. The flow was considered axially symmetrical and a two-dimensional cylindrical coordinate system was used.

Following the Boussinesq approximation concept, the dynamic eddy viscosity was modeled by the well-known relationship

$$\mu_t = \rho c_\mu \frac{k^2}{\varepsilon} \qquad (1)$$

where k is the turbulent kinetic energy, ε is the dissipation rate of turbulent kinetic energy, ρ is the fluid density, and c_μ is a closure coefficient.

The turbulent kinetic energy was calculated

$$\frac{\partial}{\partial x} r \left[\rho u k - (\mu_t + \mu) \frac{\partial k}{\partial x} \right] + \frac{\partial}{\partial r} r \left[\rho v k - (\mu_t + \mu) \frac{\partial k}{\partial r} \right]$$
$$= \frac{\partial}{\partial x} r (\mu_t + \mu) \frac{\partial k}{\partial x} + \frac{\partial}{\partial r} r (\mu_t + \mu) \frac{\partial k}{\partial r} + r (P_k - \rho \varepsilon) \qquad (2)$$

and the dissipation rate of the turbulent kinetic energy

$$\frac{\partial}{\partial x} r \left[\rho u \varepsilon - \left(\frac{\mu_t}{\sigma_\varepsilon} + \mu \right) \frac{\partial \varepsilon}{\partial x} \right] + \frac{\partial}{\partial r} r \left[\rho v \varepsilon - \left(\frac{\mu_t}{\sigma_\varepsilon} + \mu \right) \frac{\partial \varepsilon}{\partial r} \right]$$
$$= \frac{\partial}{\partial x} r \left(\frac{\mu_t}{\sigma_\varepsilon} + \mu \right) \frac{\partial \varepsilon}{\partial x} + \frac{\partial}{\partial r} r \left(\frac{\mu_t}{\sigma_\varepsilon} + \mu \right) \frac{\partial \varepsilon}{\partial r} + \frac{\varepsilon}{k} r (c_{\varepsilon 1} P_k - c_{\varepsilon 2} \rho \varepsilon) \qquad (3)$$

where

$$P_k = \mu_t \left\{ 2 \left[\left(\frac{\partial u}{\partial x} \right)^2 + \left(\frac{\partial v}{\partial r} \right)^2 + \left(\frac{v}{r} \right)^2 \right] + \left(\frac{\partial u}{\partial r} + \frac{\partial v}{\partial x} \right)^2 \right\} \qquad (4)$$

is the production term of turbulent kinetic energy.

The abrupt change in the pipe diameter generates additional vortices in the flow compared to a flow in a constant diameter pipe. The standard k–ε model with standard coefficients is only valid at a simple boundary layer flow [19]. Previous studies for round jet type flows [20,21] have indicated that the usage of standard turbulence constants produces large errors in the case of axisymmetric jets. The constants are not universal and need to be adjusted for different kinds of flows [22]. The comparison of the abilities of different

CFD packages to model a simple submerged jet type flow revealed that the discrepancy compared to the experimental velocity can be up to 40% [23]. In case of flows over a backward-facing step the standard k–ε model with standard coefficients usually under predicts the recirculation length of the flow leading to changes in the model coefficients more than five times [15]. Therefore, the impact of the values of turbulence closure coefficients $c_{\varepsilon 1}$ and $c_{\varepsilon 2}$ in the turbulent dissipation rate equation was analyzed during preliminary tests to gain consistency with the experimental results. It was found that in a pipe with an abrupt expansion followed by an abrupt contraction practically classical parameter values can be used.

The k–ε model constants used in this study for both cases were as follows: $c_\mu = 0.09$, $\sigma_\varepsilon = 1.3$, $c_{\varepsilon 1} = 1.4$, $c_{\varepsilon 2} = 2.0$.

Numerical simulations were carried out both in stationary and nonstationary conditions. The flow parameters of the two flow regimes presented in this study were analyzed in both cases, and it was concluded that after several thousand iterations, the initially unsteady flow becomes steady. Preliminary analysis (not presented in this paper) showed that the nonstationary and stationary models describe the developed flow dynamics similarly. Therefore, in this study, the results of a stationary model are presented.

Numerical Method. The finite volume method was applied to solve two-dimensional stationary partial differential equations together with the boundary conditions. The transport equations were solved using the implicit lower and upper matrix decomposition method [24,25]. The transport equations were solved using central differencing scheme. The model was initially used for corrugated pipes where the diameter change is incremental. In this study, it is shown that the same model is applicable in case of large ($\sim$2 times) diameter changes causing submerged jet type flows. Convergence criteria for implicit lower and upper matrix decomposition method weres monitored during the calculations by checking the decrease of the residuals norms of each calculated flow parameter with reduced value at least three orders of their magnitudes as proposed in Ref. [26]. The calculations were performed in the dimensional form for all flow conditions.

Computational Domain and Boundary Conditions. A two-dimensional model of the expanding and contracting pipeline apparatus section was constructed using physical dimensions. The dimensions of the computational domain, along with boundary conditions used in this study are presented in Fig. 2.

A structured grid was used to discretize the computational domain. The control volume dimension was chosen so that the dimensionless distance from the wall was $y^+ \approx 11.42$ control volumes were used in the radial direction, and the grid size over the cross section was uniform. The number of finite volumes was 168,420 for the pipe length of 50.125 diameters and pipe segments diameter of 80 and 46.4 mm.

It was found that for complex pipe geometry it is essential to include in the model all geometrical elements that affect the flow in the study area. Modeling results with different pipe segment lengths in the upstream and downstream end of the test section were compared with PIV measurements to find an optimal model configuration. In this study, a pipe with a total length of 4 m was included in the model to take into account all considerable flow disturbances in the upstream end of the PIV box.

For the axisymmetric flow in a circular pipe, the initial and boundary conditions were as follows:

$$u = u(t = 0, x, r), \quad v = v(t = 0, x, r),$$
$$k = k((t = 0, x, r), \quad \varepsilon = \varepsilon(t = 0, x, r) \qquad (5)$$

$$r = 0 : \frac{\partial u}{\partial r} = v = \frac{\partial k}{\partial r} = \frac{\partial \varepsilon}{\partial r} \qquad (6)$$

For the continuous phase using the finite volume method [24,26], the shear stress at the pipe wall is
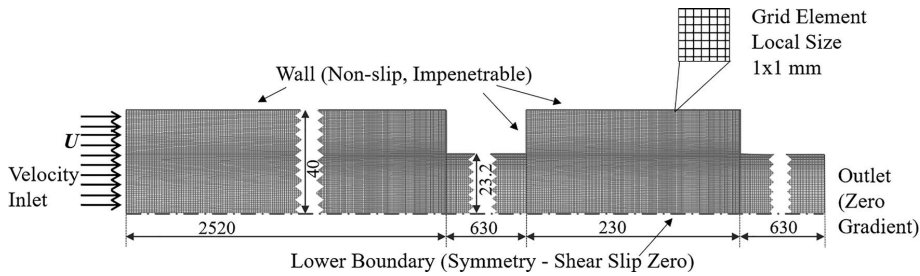
Fig. 2   Schematic of computational domain and boundary conditions

$$\tau_w = \begin{cases} \mu \dfrac{\partial u}{\partial r} = \mu \dfrac{2u}{\Delta r} & r^+ = \dfrac{\Delta r c_\mu^{0.25}\sqrt{k}}{\mu} \le 11 \\[3mm] \mu_t \dfrac{\partial u}{\partial r} = \dfrac{\psi \rho c_\mu^{0.25}\sqrt{k}u}{\ln(\sum \cdot r^+)} & r^+ > 11 \end{cases} \quad (7)$$

where r^+ is the distance from the pipe wall given in wall units, Δr is the computation mesh size, $\psi = 0.41$ is the von Karman constant, and $\Sigma = e^{\psi B} = 8.4371$ (is an empirical constant related to the sublayer thickness, $B = 5.2$). The roughness effect [27,28] has been accounted by taking the distance from the wall as $r^+ = \Delta r/s$, where s is the roughness value (2.5 mm). The value of the modified constant B was taken 8.5.

The friction velocity of the liquid, $v^+ = c_\mu^{0.25}\sqrt{k}$, is calculated using the wall function method, with the assumption of local equilibrium between the production and dissipation of the turbulent energy [24]. At the pipe wall, the production of the turbulent energy is

$$P_k = \tau_w \frac{\partial u}{\partial r} \cong 2\tau_w c_\mu^{0.25}\sqrt{k}/(\psi \cdot \Delta r) \quad (8)$$

where τ_w is the wall shear stress, a quantitative parameter implemented into the wall function definition and determined by the flow regime in the vicinity of the wall, either laminar or turbulent regime.

At the pipe wall, the dissipation rate of the turbulent energy is

$$\varepsilon = 2c_\mu^{0.75} \cdot k^{1.5}/(\psi \cdot \Delta r) \quad (9)$$

At the pipe inlet ($x = 0$), the following conditions are imposed: u is constant, determined by the flow Reynolds number and pipe diameter, $v = 0$, $k = u\cdot\text{const}_u\cdot 10^{-4}$, $\varepsilon = 20\cdot k^{1.5}/D$, where D is the pipe diameter and const_u may vary from 1 to 100 depending on a low, medium, or high inlet turbulence level. In this study, $\text{const}_u = 1$.

Finally, pipe outlet boundary conditions were as follows:

$$\frac{\partial u}{\partial x} = v = \frac{\partial k}{\partial x} = \frac{\partial \varepsilon}{\partial x} = 0 \quad (10)$$

For streamwise and radial average velocity components the boundary conditions were set as nonslip and impenetrable, correspondingly. Applying the finite volume method of calculations, the standard wall-function approach, which set logarithmic or laminar velocity profile depending on the value of normalized wall distance [26], was used.

Grid Uncertainty Study. Scheme efficiency was checked by using different numbers of finite volumes across and along the flow domain. The fine grid convergence index (GCI) method was used to estimate the discretization error. Three different grid sizes (total number of elements 39,710, 168,420, and 372,930) were

Table 2   Discretization error of axial velocity at the pipe axis

	u_3 at the pipe axis	u_7 at the pipe axis
N_1, N_2, N_3	39,710, 168,420, 372,930	39,710, 168,420, 372,930
r_{21}	1.909	1.909
r_{32}	1.476	1.476
u_1	0.590	0.446
u_2	0.601	0.429
u_3	0.561	0.388
p	4.278	3.749
u_{ext}^{21}	0.603	0.433
e_a^{21}	1.73%	3.87%
e_{ext}^{21}	0.43%	0.91%
$\text{GCI}_{\text{fine}}^{21}$	0.15%	0.47%
u_{ext}^{32}	0.553	0.370
e_a^{32}	6.56%	9.46%
e_{ext}^{32}	1.49%	0.50%
$\text{GCI}_{\text{fine}}^{32}$	1.91%	3.58%

analyzed. It was found that the average GCI for key variable u at the pipe axes was <5% for both cases (experiments 1 and 2, Table 1). The calculated discretization error for u_3 and u_7 at the pipe axis is presented in Table 2 and the calculated axial velocity and turbulent kinetic energy profiles for case 1 at $x = 69$ mm for grids 1, 2, and 3 are shown in Fig. 3. GCI was calculated for both experiments and for all three variables (u, v, k). The average discretization error for axial velocity was 15%, for radial velocity 7%, and for turbulent kinetic energy 19% corresponding to $\sim$0.02 m/s, $\sim$0.0005 m/s, and $\sim$0.0006 m^2/s^2, respectively.

Results and Discussion

The measured and modeled flow dynamics are presented for two cases (experiments 1 and 2, Table 1). First, Figs. 4 and 5 show the change in the axial velocity for experiments 1 and 2, respectively; and Figs. 6 and 7 the turbulent kinetic energy (TKE) at the pipe axis for experiments 1 and 2, respectively. The x-axis represents the length of the PIV box (test section), where $x = 0$ mm is the inflow to the box and $x = 230$ mm is the outflow from the box. The comparison of the measured and modeled axial velocities at the pipe axis shows good qualitative correlation in both test cases (Figs. 4 and 5). The model slightly overestimates the velocity near the inlet in both cases but predicts the minimum velocity near the outlet both qualitatively and quantitatively.

In case of a pipe with an abrupt change in diameter large primary recirculation bubbles evolve behind the sudden expansion and before the sudden contraction. The maximum velocity is highest at the inlet of the larger diameter pipe where the flow is typical to a submerged jet. The efficient diameter of the pipe is smallest, and the flow direction at the near wall region is the opposite. In the middle section, the velocity decrease is more-or-less linear
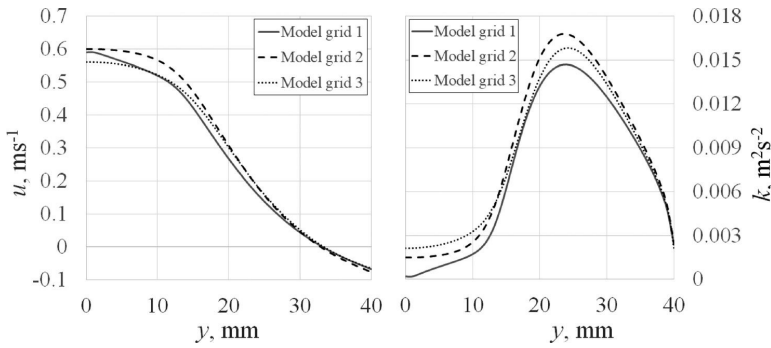
Fig. 3 Calculated axial velocity and turbulent kinetic energy profiles for three grid sizes (experiment 1, $x = 69$ mm)
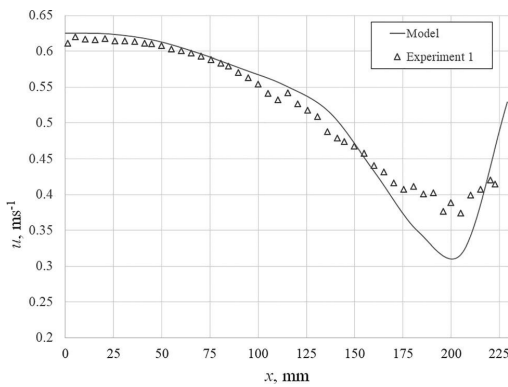
Fig. 4 Comparison of the measured and modeled axial velocity at the pipe axis (experiment 1). Uncertainty of measured axial velocity was ±2.4%.
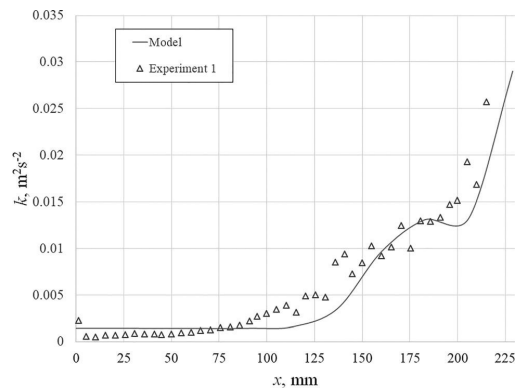
Fig. 6 Comparison of the measured and modeled turbulent kinetic energy at the pipe axis (experiment 1). Uncertainty of measured turbulent kinetic energy was ±3.6%.
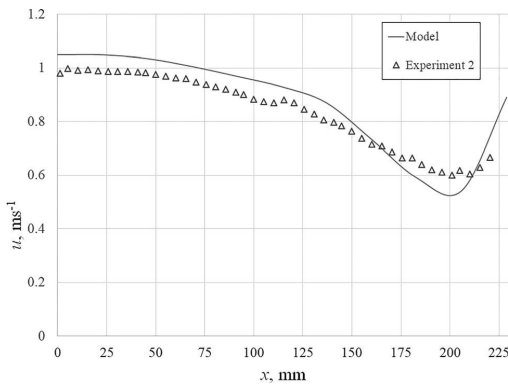
Fig. 5 Comparison of the measured and modeled axial velocity at the pipe axis (experiment 2). Uncertainty of measured axial velocity was ±2.4%.
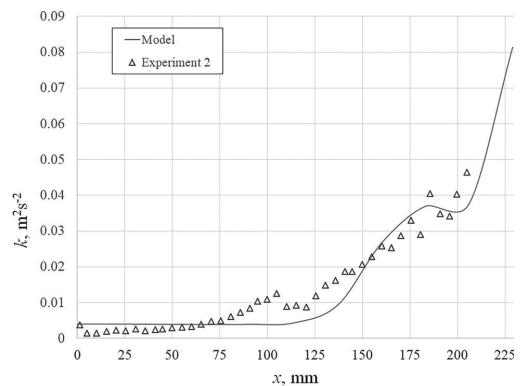
Fig. 7 Comparison of the measured and modeled turbulent kinetic energy at the pipe axis (experiment 2). Uncertainty of measured turbulent kinetic energy was ±3.6%.

due to turbulent mixing, reaching a minimum value at $x \sim 200$ mm. Thereafter, the streamlines curve strongly as the flow enters to the outflow pipe. This results in a rapid increase of both axial and radial velocity.

The comparison of the measured and modeled turbulent kinetic energy for both test cases (Figs. 6 and 7) reveals that near the inlet, the submerged jet acts like a solid body, and the turbulent intensities are low. In the midsection of the PIV box, the turbulent
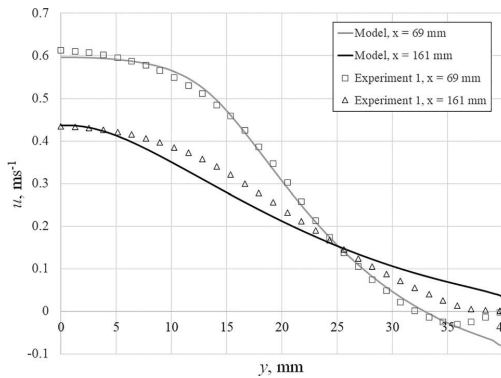
Fig. 8 Comparison of the measured and modeled axial velocity profiles near the inlet ($x = 69$ mm) and outlet ($x = 161$ mm) of the test section (experiment 1). Uncertainty of measured axial velocity was ±2.4%.

Fig. 10 Comparison of the measured and modeled radial velocity profiles near the inlet ($x = 69$ mm) and outlet ($x = 161$ mm) of the test section (experiment 1). Uncertainty of measured radial velocity was ±22.5%.

Fig. 9 Comparison of the measured and modeled axial velocity profiles near the inlet ($x = 69$ mm) and outlet ($x = 161$ mm) of the test section (experiment 2). Uncertainty of measured axial velocity was ±2.4%.

Fig. 11 Comparison of the measured and modeled radial velocity profiles near the inlet ($x = 69$ mm) and outlet ($x = 161$ mm) of the test section (experiment 2). Uncertainty of measured radial velocity was ±22.5%.

effects and shear forces start to grow, resulting in an increase of velocity fluctuations. The effective diameter starts to increase, bringing along a decrease in the radial velocity component.

The change in the turbulent kinetic energy at the pipe axis is exponential, leading to around 30–50 times higher values near the outlet compared to the inlet. One of the possible reasons for the high level of the turbulent intensity is an abrupt change of the pipe diameter, which obviously generates additional smaller-scale turbulent vortices interacting with larger-scale turbulent vortices generated at the wall of the larger diameter pipe. The exponent in both cases is similar. This is similar to flow over backward-facing step where the maximum of turbulent kinetic energy is between the main flow and the secondary recirculation bubble [16]. In the present case, the TKE does not decay as the recirculation bubbles evolve at the both ends of the abrupt pipe diameter change. Measurements show that turbulence intensity is larger near the sudden contraction bringing along an exponential growth of the TKE along the pipe length.

Figures 8 and 9 show the axial velocity distribution at two locations ($x = 69$ mm near the inlet and $x = 161$ mm near the outlet) for experiments 1 and 2, respectively. At the inlet of the test section, convectional deceleration takes place and the velocity
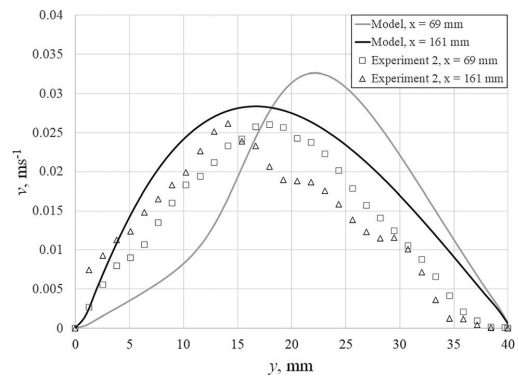
distribution in the core is uniform, resulting in large velocity gradients in the near wall region. Similarly, to the flow through sharp extension, a backflow occurs close to the wall. Due to inertial effects, the flow retains its plug-like behavior in the core [29–31] until the inertial influences become weaker than the turbulence-decay influences [31]. This results in a significant change in the velocity profile as the maximum velocity decreases and the shape of the velocity profile reveals that the increase in the axial velocity from the pipe axis to the pipe wall is linear. The modeling results match the experimental results both qualitatively and quantitatively.

The comparison of the development of the radial velocity (Figs. 10 and 11) reveals that near the inlet, the turbulent vorticities in the near-wall region are more compressed, resulting in a larger maximum velocity value. The decay of the inertial influences results in larger turbulent vorticities that propagate toward the pipe axis. Still it can be seen that at larger initial velocities (and therefore larger inertial forces, experiment 2), the magnitude of the radial velocity remains practically the same throughout the test section, only the shape of the profile "leans" toward the pipe axis.

The model captures the development of the radial velocity component very well. In experiment 1, the model slightly
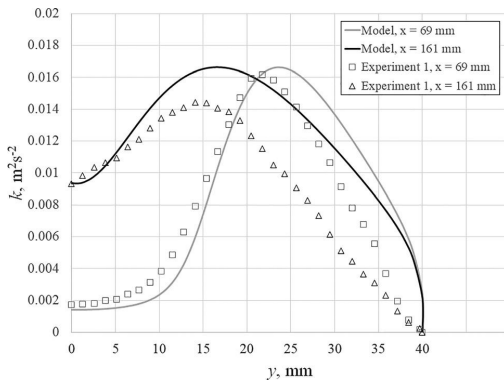
Fig. 12 Comparison of the measured and modeled turbulent kinetic energy profiles near the inlet ($x = 69$ mm) and outlet ($x = 161$ mm) of the test section (experiment 1). Uncertainty of measured turbulent kinetic energy was ±3.6%.
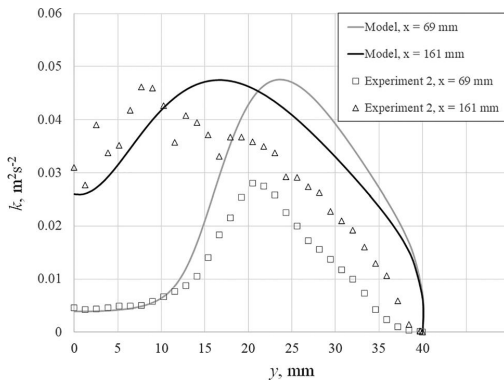
Fig. 13 Comparison of the measured and modeled turbulent kinetic energy profiles near the inlet ($x = 69$ mm) and outlet ($x = 161$ mm) of the test section (experiment 2). Uncertainty of measured turbulent kinetic energy was ±3.6%.

underestimates the maximum velocity near the inlet and the experiments reveal that the changes in the velocity are evenly distributed over the pipe radius. This results in a small mismatch between the measured and modeled radial velocities in the core region.

For experiment 1 (Fig. 10), quantitative comparison of the measured and modeled radial velocity profiles reveals that near the inlet (at $x = 69$ mm) the modeled peak value is higher than measured by 3.65%, and near the outlet (at $x = 161$ mm) by 23.23%. Concurrently for experiment 2 (Fig. 11) near the inlet model overestimates the peak by 20.30% and near the outlet by 7.83%. Meanwhile, the uncertainty of measured radial velocity was ±22.5% and the average discretization error for radial velocity was 7%. Therefore, the mismatch is within the uncertainty limit.

Finally, the distribution of the turbulent kinetic energy at two locations in the test section is presented (Figs. 12 and 13). Turbulent kinetic energy is useful in illustrating the interactions between the core flow and the developing vortices. Measurements of average velocity fluctuations help to understand the complex nature of the flow. It can be seen from Figs. 12 and 13 that in both test cases, the peak value in the turbulent kinetic energy near the inlet is at $y \sim 22$ mm, corresponding to the location of the wall of the

smaller diameter pipe. Convectional decelerations cause a rapid growth of velocity fluctuations at the boarders of the entering jet. The velocity fluctuations grow and spread over the cross section of the smaller diameter pipe as the jet-type uniform flow dissipates and mixes with the rest of the flow. This corresponds to the growth of the turbulent kinetic energy in the core region. Near the outlet, the streamlines curve strongly as the flow accelerates and enters the smaller diameter pipe. As a result, the peak in the turbulent kinetic energy shifts toward the pipe axis. This is similar to the flow dynamics in corrugated pipes with larger groove widths where a high concentration of TKE spreads to the core near the end of the rib [8].

The model predicts the experimental turbulent kinetic energy behavior qualitatively. The model fails to predict the TKE in the near wall region because of the modified flow structure caused by the interaction of the jet-like flow and the pipe wall after the abrupt expansion of the pipe diameter. The qualitative behavior of TKE is similar in both cases. The model predicts the point where the TKE has its maximum value in both experiments 1 and 2 but fails to calculate the exact value. The maximum TKE is close to the reattachment point where the flow approaches to equilibrium. The discrepancy between the experimental and modeling results is due to the incorrect supposition that turbulence is isotropic and the inability of the model to calculate rotational strains, which are the source of extra turbulence kinetic energy dissipation, thus smaller values of TKE [32]. Similar numerical results were presented for slurry flows in a sudden expansion [33] where the model overestimated the TKE in the core region compared to experimental data by as much as 53%. At lower Reynolds numbers (experiment 1), the turbulent kinetic energy dissipates in the test section but at higher Reynolds numbers, there is a growth of TKE along the larger diameter pipe test section caused by the larger vorticities developing in the near wall region.

For experiment 1 (Fig. 12) quantitative comparison of the measured and modeled TKE profiles reveals that near the inlet (at $x = 69$ mm) the modeled peak value is higher than measured by 2.71%, and near the outlet (at $x = 161$ mm) by 13.41%. Concurrently for experiment 2 (Fig. 13) near the inlet model overestimates the peak by 41.16% and near the outlet by 2.6%. As the uncertainty of measured TKE was ±3.6% and the average discretization error for TKE was 19%, the discrepancy is outside of uncertainty limits for one presented profile. However, the model overestimates TKE similarly to Ref. [33].

Conclusions

Flow dynamics in a pipe with an abrupt change in diameter were analyzed both experimentally and numerically. Detailed two-dimensional PIV measurements were used to examine the flow dynamics in pipes with a complex geometry and to determine the impact of the standard k–ε model turbulence closure coefficients and model setup on the modeling results of a jet-like flow.

The comparison of the measured and modeled axial velocities indicated that the model slightly overestimates the maximum velocity at the pipe axis but captures the change of the velocity in the test section very well. The correlation between the measured and modeled velocity profiles was very good. At radial velocities, the model slightly underestimates the magnitude of the velocity in experiment 1 near the inlet but captures the development of the radial velocity in experiment 2 throughout the test section. The developed vortices near the inlet are more compressed, resulting in a higher maximum radial velocity in the core region. Both experimental and numerical investigations confirm that near the inlet, the turbulent kinetic energy at the pipe axis of the test section is 30–50 times lower than at the outlet of the test section. Near the inlet, the submerged jet acts like a solid body, resulting in low turbulent intensities. Due to the convectional deceleration, the growth of the shear forces is declined and a rapid growth of the velocity fluctuations takes place at the boarders of the submerged jet. This results in a maximum value of the TKE near the

location of the wall of a smaller diameter pipe. The RANS k–ε model predicts the development of the TKE profiles both qualitatively and quantitatively.

The results of the steady and unsteady modeling were found to be similar after several thousand iterations. This confirms that the implementation of a steady model in the present case was justified and enabled the analysis with lower computation time and resources.

The sensitivity analysis of the model geometry revealed that it is essential to include to the model all geometrical elements that affect the flow in the study area. In this study, a pipe with a total length of 4 m was included to the model to take into account all considerable flow disturbances in the upstream end of the PIV box. As a result, the standard RANS k–ε model allows for the prediction of the flow dynamics in pipes with complex geometry at moderate changes in the turbulence closure coefficients. On proper setup, the standard RANS k–ε model is capable of accurately modeling the pressurized submerged yet-type flow in pipes. This enables the analysis of the flow dynamics in real old rough pipes where the pipe wall build-up leads to changes in the actual diameter of the pipe but the flow can still be considered axially symmetrical.

Acknowledgment

Funding Data

Nomenclature

$c\varepsilon_1$, $c\varepsilon_2$, c_μ = closure coefficient
const_u = turbulence intensity constant
D = pipe diameter (mm)
f = elliptic relaxation function
f_s = sampling frequency (Hz)
k = turbulent kinetic energy (m^2/s^2)
L = pipe length (m)
P_k = production term of turbulent kinetic energy (kg/m·s^3)
Q = flow rate (l/s)
r = radial coordinate (m)
r^+ = distance from the pipe wall given in wall units
Re = Reynolds number
s = roughness (mm)
t = time (s)
u = axial velocity (m/s)
v = radial velocity (m/s)
v^+ = friction velocity (m/s)
$\overline{v^2}$ = velocity fluctuation normal to streamlines (m^2/s^2)
x = axial coordinate (m)
y^+ = distance from the wall normalized by the viscous length scale

Greek Symbols

Δr = computation mesh size (mm)
ε = dissipation rate of turbulent kinetic energy (m^2/s^3)
μ = dynamic viscosity (kg/m·s)
μ_t = dynamic eddy viscosity (kg/m·s)
ρ = fluid density (kg/m^3)
σ_ε = closure coefficient
$\sum$ = empirical constant related to sublayer thickness
τ_w = shear stress at the pipe wall (kg/m·s^2)
Ψ = von Karman constant
ω = specific dissipation rate (1/s)

References

[1] Lansey, K. E., El-Shorbagy, W., Ahmed, I., Araujo, J., and Haan, C. T., 2001, "Calibration Assessment and Data Collection for Water Distribution Networks," J. Hydraul. Eng., **127**(4), pp. 270–279.
[2] Christensen, R. T., Spall, R. E., and Barfuss, S. L., 2011, "Application of Three RANS Turbulence Models to Aged Water Transmission Pipes," J. Hydraul. Eng., **137**(1), pp. 135–139.
[3] Vassiljev, A., and Koppel, T., 2015, "Estimation of Real-Time Demands on the Basis of Pressure Measurements by Different Optimization Methods," Adv. Eng. Software, **80**, pp. 67–71.
[4] Annus, I., and Vassiljev, A., 2015, "Different Approaches for Calibration of an Operational Water Distribution System Containing Old Pipes," Proc. Eng., **119**, pp. 526–534.
[5] Boxall, J. B., Saul, A. J., and Skipworth, P. J., 2004, "Modeling for Hydraulic Capacity," J. Am. Water Works Assoc., **96**(4), pp. 161–169.
[6] Vijiapurapu, S., and Cui, J., 2007, "Simulation of Turbulent Flow in a Ribbed Pipe Using Large Eddy Simulation," Numer. Heat Transfer, Part A, **51**(12), pp. 1137–1165.
[7] Vijiapurapu, S., and Cui, J., 2010, "Performance of Turbulence Models for Flows Through Rough Pipes," Appl. Math. Modell., **34**(6), pp. 1458–1466.
[8] Stel, H., Morales, R. E. M., Franco, A. T., Junqueira, S. L. M., Erthal, R. H., and Gonçalves, M. A. L., 2010, "Numerical and Experimental Analysis of Turbulent Flow in Corrugated Pipes," ASME J. Fluids Eng., **132**(7), p. 071203.
[9] Stel, H., Franco, A. T., Junqueira, S. L. M., Erthal, R. H., Mendes, R., Gonçalves, M. A. L., and Morales, R. E. M., 2012, "Turbulent Flow in D-Type Corrugated Pipes: Flow Pattern and Friction Factor," ASME J. Fluids Eng., **134**(12), p. 121202.
[10] Calomino, F., Tafarojnoruz, A., De Marchis, M., Gaudio, R., and Napoli, E., 2015, "Experimental and Numerical Study in the Flow Field and Friction Factor in a Pressurized Corrugated Pipe," J. Hydraul. Eng., **141**(11), p. 04015027.
[11] Christensen, R. T., 2009, "Age Effects on Iron-Based Pipes in Water Distribution Systems," Ph.D. thesis, Utah State University, Logan, UT.
[12] Mullin, T., Seddon, J. R. T., Mantle, M. D., and Sederman, A. J., 2009, "Bifurcation Phenomena in the Flow Through a Sudden Expansion in a Circular Pipe," Phys. Fluids, **21**(1), p. 014110.
[13] Sanmiguel-Rojas, E., del Pino, C., and Gutiérrez-Montes, C., 2010, "Global Mode Analysis of a Pipe Flow Through a 1:2 Axisymmetric Sudden Expansion," Phys. Fluids, **22**(7), p. 071702.
[14] Sanmiguel-Rojas, E., and Mullin, T., 2012, "Finite-Amplitude Solutions in the Flow Through a Sudden Expansion in a Circular Pipe," J. Fluid Mech., **691**, pp. 201–213.
[15] Ding, D., and Wu, S., 2010, "Numerical Application of k–ε Turbulence Model to the Flow Over a Backward-Facing Step," Sci. China: Technol. Sci., **53**(10), pp. 2817–2825.
[16] Schäfer, F., Breuer, M., and Durst, F., 2009, "The Dynamics of the Transitional Flow Over a Backward-Facing Step," J. Fluid Mech., **623**, pp. 85–119.
[17] Sciacchitano, A., and Wieneke, B., 2016, "PIV Uncertainty Propagation," Meas. Sci. Technol., **27**(8), p. 084006.
[18] Launder, B. E., and Spalding, D. B., 1974, "The Numerical Computation of Turbulent Flows," Comput. Methods Appl. Mech., **3**(2), pp. 269–289.
[19] Davidson, P. A., 2006, Turbulence. An Introduction for Scientists and Engineers, Oxford University Press, New York.
[20] Launder, B. E., Morse, A. P., Rodi, W., and Spalding, D. B., 1972, "The Prediction of Free Shear Flows—A Comparison of Six Turbulence Models," NASA Free Shear Flows Conference, VA, Report No. NASA SP-311.
[21] Pope, S. B., 1978, "An Explanation of the Round Jet/Plane Jet Anomaly," AIAA J., **16**(3), pp. 279–281.
[22] Smith, E. J., Mi, J., Nathan, G. J., and Dally, B. B., 2004, "Preliminary Examination of a 'Round Jet Initial Condition Anomaly' for the k–ε Turbulence Model," 15th Australasian Fluid Mechanics Conference, Sydney, Australia, Dec. 13–17, pp. 1–4.
[23] Mackenzie, A., Lopez, A., Riros, K., Stickland, M. T., and Dempster, W. M. A., 2015, "Comparison of CFD Software Packages' Ability to Model a Submerged Jet," 11th International Conference on CFD in the Minerals and Process Industries CSIRO, Melbourne, Australia, Dec. 7–9, pp. 1–4.
[24] Fertziger, J. H., and Perić, M., 2002, Computational Methods for Fluid Dynamics, Springer-Verlag, Berlin, Germany.
[25] Kartushinsky, A., Michaelides, E., Hussainov, M., and Rudi, Y., 2009, "Effects of the Variation of Mass Loading and Particle Density in Gas-Solid Particle Flow in Pipes," Powder Technol., **193**, pp. 176–181.
[26] Perić, M., and Scheuerer, G., 1989, "CAST—A Finite Volume Method for Predicting Two-Dimensional Flow and Heat Transfer Phenomena," GRS Technische Notiz, Köln, Germany, Report No. GRS-TN-SRR-89-01.
[27] Kartushinsky, A., Rudi, Y., Stock, D., Hussainov, M., Shcheglov, I., and Tisler, S., 2013, "3D RANS-RSTM Numerical Simulation of Channel Turbulent Particulate Flow With Wall Roughness," 11th International Conference Numerical Analysis and Applied Mathematics, Rhodes, Greece, Sept. 21–27, pp. 1067–1070.

[28] Kartushinsky, A., Rudi, Y., Hussainov, M., Shcheglov, I., Tisler, S., Krupenski, I., and Stock, D., 2014, "RSTM Numerical Simulation of Channel Particulate Flow With Rough Wall," *Computational and Numerical Simulation*, Intech, London, pp. 41–63.

[29] Annus, I., and Koppel, T., 2011, "Transition to Turbulence in Accelerating Pipe Flow," ASME J. Fluids Eng., **133**(7), p. 071202.

[30] Annus, I., Koppel, T., Sarv, L., and Ainola, L., 2013, "Development of Accelerating Pipe Flow Starting From Rest," ASME J. Fluids Eng., **135**(11), p. 111204.

[31] Ariyaratne, C., He, S., and Vardy, A. E., 2010, "Wall Friction and Turbulence Dynamics in Decelerating Pipe Flows," J. Hydraul. Res., **48**(6), pp. 810–821.

[32] Koronaki, E. D., Liakos, H. H., Founti, M. A., and Markatos, N. C., 2001, "Numerical Study of Turbulent Diesel Flow in a Pipe With Sudden Expansion," Appl. Math. Modell., **25**(4), pp. 319–333.

[33] Frawley, P., O'Mahony, A. P., and Geron, M., 2010, "Comparison of Lagrangian and Eulerian Simulations of Slurry Flows in a Sudden Expansion," ASME J. Fluids Eng., **132**(9), p. 091301.

Appendix 4

Publication IV
Kaur, K.; Annus, I.; Laanearu, J. (2018). **Experimental measurements of momentum changes at hydraulic jump in a transparent horizontal pipe.** 13th International Conference on Pressure Surges, *2*, 925–936. BHR Group.

Experimental measurements of momentum changes at hydraulic jump in a transparent horizontal pipe

K Kaur, I Annus, J Laanearu
School of Engineering, Tallinn University of Technology, Estonia

ABSTRACT

Two-phase flow experiments are conducted on a laboratory-scale pipeline apparatus to investigate the momentum changes that result from stratified flow transition to slug flow in a pressurized pipe. The PIV velocity fields are used to explain the two-phase flow processes associated with the formation of non-stationary hydraulic jump. The velocity field in the pressurized pipe is measured in three stages: 1) stratified flow (upstream of hydraulic jump); 2) slug flow (downstream of hydraulic jump) and; 3) transitional flow (at hydraulic jump location). The aim of study is to provide experimental data for the validation of advanced numerical models dealing with the air-water interactions in pipelines. The estimated turbulent kinetic energy reveals that the air-water interface breaking is the dominating turbulent process during stratified flow transition to slug flow. It is found that the vacuum inside the entrapped air pocket is responsible for the air intrusion into the hydraulic jump.

NOTATION

A	- cross-section area of flow	Q	- volumetric flux of water
c	- speed of bore wave	Re	- Reynolds number
D	- pipe diameter	t	- time
Fr	- Froude number	$\vec{u}$	- flow velocity
g	- gravitational acceleration	$\langle \vec{u} \rangle$	- velocity mean
h	- interface height above pipe invert	$\overline{u'}$	- velocity fluctuation
k	- turbulent kinetic energy	ρ	- fluid density
p	- pressure		

1   INTRODUCTION

There is a wide range of industrial applications where complex two-phase flow dynamics may substantially hinder the proper prediction of operating conditions. Tunnel spillways, drainage engineering and sewer technology are all areas where transitional processes of two-phase flow are significant. Such applications are designed for free-surface flow with co-current airflow above the water flow. Abrupt transition from high-velocity stratified flow to slug flow in pressurized pipe with air pockets left entrapped in the system is associated with consequences such as large pressure fluctuations and conduit failure.

Presence of stratified flow significantly modifies the flow dynamics during filling and emptying of a large-scale pipeline (Hou et al. (1), Laanearu et al. (2)). Air-water dynamics in undulated pipelines is investigated in many studies to understand the fast pressure fluctuations due to the two-phase flow processes (see Liou and Hunt (3), Axworthy and Karney (4), Hou et al. (5), Malekpour and Karney (6), Vasconcelos and Wright (7)). In pipelines with an undulating elevation profile, column separation may occur at high points, and air pockets can be entrapped (Hou et al. (5)). According to Liou and Hunt (3) and Axworthy and Karney (4), a flow acceleration in pipeline, when trapped air pockets are released, can result in unexpected pressure surges. The present study aims to contribute to development of understanding the mixed flow, where air-water interactions are important for pressure changes in the pipeline.

A large number of controlled pipeline filling experiments were performed within the EC Hydralab III project that provided access to a Deltares large-scale experimental facility in Delft, The Netherlands. Hou et al. (1) have carried out design, construction and detailed experimental investigations of two-phase unsteady flows in an industrial-scale pipeline during 2009. The test section of the industrial-scale pipeline consisted of a 250 mm external diameter and 275 m long PVC pipeline. The PVC pipeline, which was built of 10 m long PVC pipes that were connected with 45° and 90° bends of different radii, had a rather complicated layout configuration over the ~0.3 km distance between different laboratories at Deltares buildings.

The industrial-scale pipeline was fed with water from the supply tower during the filling experiments, i.e. the air at atmospheric pressure initially present in the test section was replaced with water by keeping the upstream control valves completely open. Seventy-eight full-pipe steady-flow measurements were carried out between the pipeline filling and emptying experiments to determine the system's hydraulic characteristics. According to Laanearu et al. (8) the frictional head loss of 11.9 m at a Reynolds number of 948'170 corresponded to a slope 0.0475 of the hydraulic gradient, representing the major loss in the 251 m long test section. The reasons of the formation of mobile and suppressed hydraulic jump (Figure 1) that appeared during several experimental runs with the industrial-scale pipeline are still not fully understood.
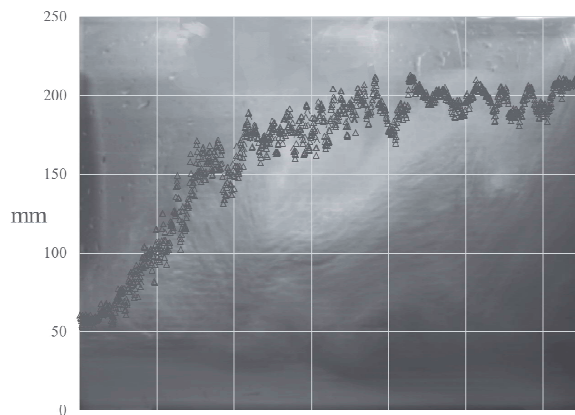
Figure 1. Hydraulic jump observed at the transparent section of industrial-scale pipeline at Delft experimental facility (data points of interface height above invert are denoted with triangles)

The goal of the present study is to investigate the formation of hydraulic jump caused by combined effect of pipe layout (pipe bridge, horizontal pipe and outlet) to provide data for numerical model calibration and validation. For this purpose, experiments were conducted on a laboratory-scale pipeline apparatus (Figure 2). Varying initial conditions are used to determine system operating conditions that result in the non-stationary hydraulic jump in the outlet pipe section, and then fixed initial conditions are applied to measure velocity profiles in the jump region.
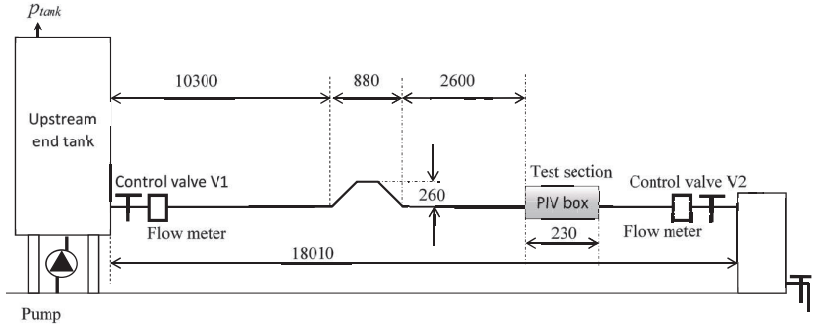
Figure 2. Schematic of laboratory-scale pipeline apparatus

Actually, the pipeline under investigation in the present study is designed as a downscaled version of the industrial-scale pipeline, which was used to carry out the filling and emptying experiments on the Deltares dynamic multi-phase test rig by Laanearu et al. (2). The experiments reveal dynamics of the formation of the non-stationary hydraulic jump (Figure 3), occurring at a transition zone where stratified and slug flow in the pressurized pipe are merged.
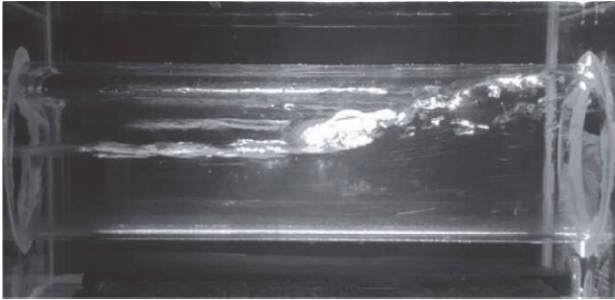
Figure 3. Hydraulic jump in laboratory-scale pipe

To investigate the multi-phase flow dynamics in the laboratory-scale horizontal pipe and provide data for advanced numerical analysis, velocity fields are measured at different flow stages. The experiments are conducted to aid qualitative and quantitative interpretation of the two-phase flow processes that are associated with the behaviour of hydraulic jump.

The plan of the present study is as follows. First, the experimental setup of the laboratory-scale pipeline apparatus used for multi-phase flow investigations is described in detail. Then some results of the two-phase flow experiments are demonstrated. Three

stages of flow development are presented: first, the stratified flow in the upstream of the hydraulic jump; second, the slug flow in the downstream of the hydraulic jump and; third, the transitional flow in the hydraulic jump region, which all have slightly different volumetric flow rate. The turbulent flow behaviour through the jump is explained by analysing the changes of turbulent energy profiles. The propagation speed of the intruding front of air-water transition part, where stratified flow and slug flow inside the pressurized pipe are merged, is analysed with simplified 1D Control Volume (CV) model. Finally, the experimental findings are concluded and discussed in respect to the numerical simulation results presented in Laanearu and Kaur (9).

2 EXPERIMENTAL STUDY

To measure the changes of pressurized flow during the stratified flow transition to the slug flow via hydraulic jump, the experiments are conducted on a transparent horizontal pipeline at the Laboratory of Fluid Mechanics at Tallinn University of Technology (Figure 4).

First, the experiments are conducted on a lab-scale apparatus (Figure 2) with varying initial conditions to determine system operating conditions that result in the formation of non-stationary hydraulic jump in the horizontal pipe (Figure 3), and then with fixed initial conditions to measure axial and radial velocity profiles and its fluctuations in the jump region. Initial conditions were set to correspond to supercritical flow according to Froude number criterion. In the stratified flow part upstream of the non-stationary hydraulic jump the Froude number Fr = 2.2 is computed using the following equation:

$$Fr^2 = \frac{\langle u \rangle^2 (3D - 4h)}{g \, h \, 2(D - h)} \tag{1}$$

It should be noted that Eq. (1) holds for circular pipe while the interface height above pipe invert is less than half a diameter: $0 < h \leq D/2$.

The pipeline apparatus depicted in Figure 2 consists of a basement reservoir, a water tank with control valve at the upstream end, an 18 m long conduit made up from a horizontal pipe, a pipe bridge, and an outlet pipe with a test section and a control valve at the downstream end. The pipeline is built of 2 m long transparent PMMA (PolyMethyl MethAcrylate) pipes with inner diameter of 80 mm.
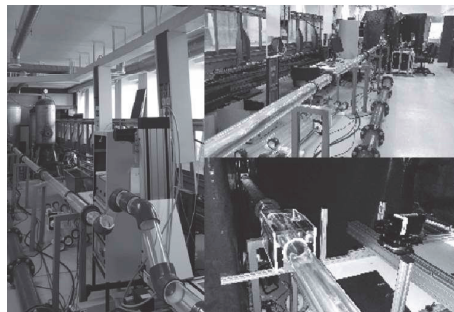
Figure 4. Images of the pipeline apparatus in the fluid mechanics laboratory of Tallinn University of Technology

The test section of the horizontal pipe is filled through the pipe bridge with the height of 0.26 m and the length of 1.68 m, and depleted through the outlet pipe with the diameter of 75 mm and the length of 0.2 m. The test rig is pressure driven and the upstream-end tank water level is kept constant during velocity field measurements. The flow rate is controlled by upstream-end control valve position and pump frequency. It is possible to re-adjust the position of the hydraulic jump during experiments by supplying additional air into the air pocket through a valve on top of the pipe bridge.

Velocity fields are measured with two-dimensional Particle Image Velocimetry (PIV) using high-speed camera and continuous-wave laser. The camera is adjusted so that it covers the whole pipe diameter. The size of the window is 640 × 800 pixels. The measurement frequency varies from 1155 to 2982 images per second and is adjusted according to Reynolds number. The Reynolds number ranges from 45'700 to 111'200, where the latter corresponds to stratified flow and is computed using hydraulic diameter dependant on wetted perimeter. The data recording and processing is done using software Dynamic Studio 4.0 (Dantec Dynamics). The adaptive cross-correlation method is used to process the PIV data. As a result, velocity vector fields are calculated taking into account the displacement of the particles between two frames. An interrogation window of 16 × 16 pixels with 50% overlap is used. There is no pre- or post-processing of the images carried out. A simple reference image with a ruler inserted into the measurement domain is used to calibrate the PIV. Image distortion is absent in the calibration because an acrylic glass PIV box is used in the measurement domain and the camera lens is mounted horizontally. From the calibration image a scale of 1 pixel = 0.15 mm is set and used in further calculations. Mean velocities, standard deviations and turbulent kinetic energies are calculated using only valid vectors (i.e. gained from measured particle displacements not substituted by the software). Oxygen and hydrogen bubbles are used for seeding of PIV. Therefore, multiple electrified wires are inserted into the pipe. Voltage difference between the wires causes electrolysis and oxygen and hydrogen bubbles are released. The wires are mounted inside the pipe just before the pipe bridge.

In addition, pressures and water levels are monitored at different locations over the pipeline. Flow rate is measured with an electromagnetic flowmeter installed at the upstream end of the pipe, with the option of control measurements with a second one at outlet pipe. The instrumentation is carefully selected to have the response of suitable accuracy and frequency. All instruments are calibrated before they are used for the measurements in the laboratory.

3   RESULTS

Three illustrative stages are presented: firstly, the stratified flow upstream of hydraulic jump; secondly, the slug flow downstream of hydraulic jump and; thirdly, the transitional flow in the hydraulic jump region. The hydraulic jump measurements are conducted in two short time intervals. During the first short interval (Transitional flow I in Figure 6 & Figure 7) the roller (see Figure 5) velocity field, where recirculation and air entrainment occurs, is captured. During the second short interval (Transitional flow II in Figure 6 & Figure 7) the velocity field twenty centimetres downstream of the roller is captured, where the interface intersects the pipe obvert, but the turbulence generation is still dominated by air-water interface and mixing as opposed to wall-generated turbulence.

Figure 5. Image of roller structure, which is captured with high-speed PIV camera

Change of vertical distribution of the along-pipe velocity component u_x for water flow is presented in four diagrams (Figure 6), which correspond to illustrative stages of flow transition from the stratified flow to the slug flow. As expected, the changes of velocity over the vertical cross-sections, where the stratified and the slug flows merge inside the pipe, demonstrate the flow velocity distribution changes between the interfacial flow and slug flow. In the case of the stratified flow the velocity maximum is near interface, and in the case of the slug flow the velocity maximum is at the turbulent core.
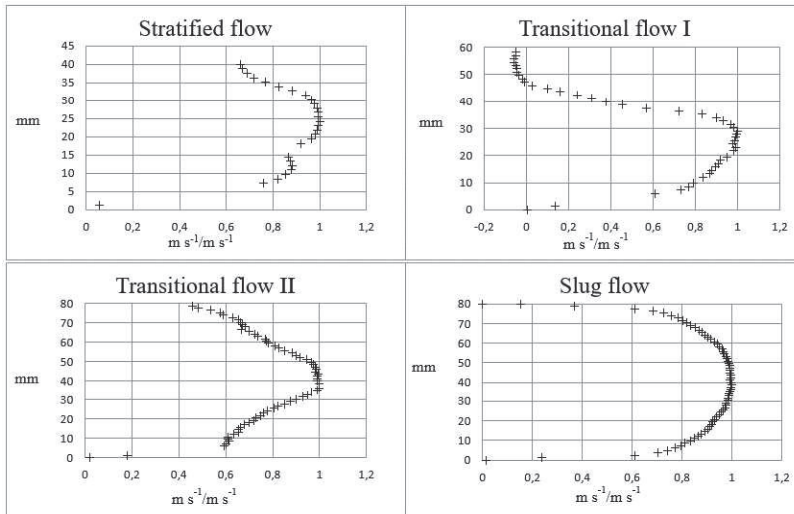
Figure 6. Change of vertical distribution of the along-pipe normalized velocity component u_x at four illustrative stages of flow transition from stratified flow to slug flow in pressurized pipe

The turbulent flow behaviour through the hydraulic jump is interpreted according to changes of turbulent kinetic energy profile (Figure 7). The turbulent kinetic energy carried by the velocity fluctuations is defined

$$k = \frac{1}{2}\left(\langle {u'_x}^2 \rangle + \langle {u'_y}^2 \rangle + \langle {u'_z}^2 \rangle\right).$$ (2)

It is proposed that the axial velocity fluctuations are larger in magnitude as compared to the radial velocity fluctuations such that $\langle {u'_x}^2 \rangle > \langle {u'_y}^2 \rangle = \langle {u'_z}^2 \rangle$ and therefore the following approximation is used

$$k \approx \frac{1}{2}\left(\langle {u'_x}^2 \rangle + 2\langle {u'_y}^2 \rangle\right)$$ (3)

Change of vertical distribution of the turbulent kinetic energy for water flow is presented in four diagrams (Figure 7) for illustrative stages of flow transition from stratified flow to slug flow in pipe. It can be observed that the maximum of turbulent kinetic energy is associated with the air-water interface breaking, which is part of hydraulic jump in the transitional flow region, and with wall-generated turbulence at the slug flow region. It can be also noted that the maximum of turbulent kinetic energy is associated with air-water interface breaking and around order of magnitude larger than the maximum turbulent kinetic energy at the core of flow dominated by wall-generated turbulence.
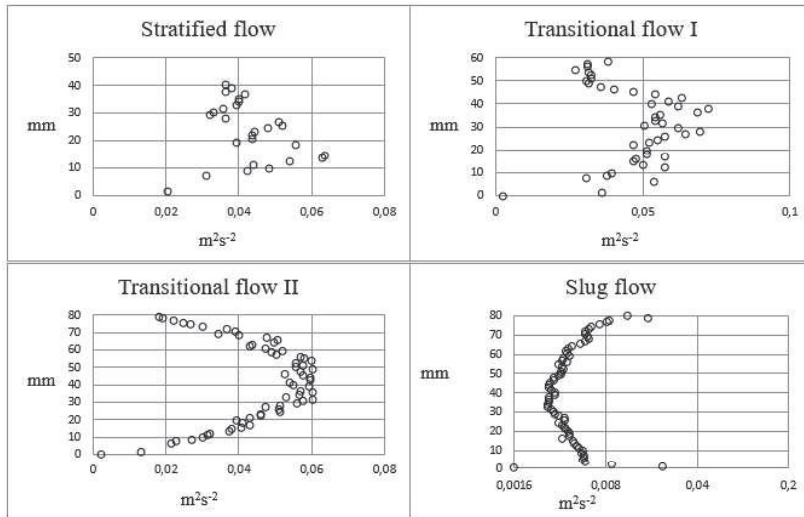
Figure 7. Turbulent kinetic energy change through flow transition from stratified to slug flow in pressurized pipe

3.1 1D Control Volume (CV) model

Presence of pressurized air on top of the water column inside the horizontal pipeline can result in flow transition between stratified flow and slug flow. The production of slugs at the flow transition region was apparent in the filling experiments of laboratory-scale pipeline under investigation here. The Zukoski dimensionless number can be used to parameterize the relative shortening of the water column associated with the unidirectional movement of the fronts along the pipeline (see Zukoski (10)). Using the CV approach, the water-column mass losses due to intrusion of air on top of the water column during two-phase flow are theoretically analysed and parameterized (implementing Zukoski number) by Laanearu et al. (8), (11).

In present study the 1D CV model is developed to interpret the experimental results, especially the momentum changes resulting from the motion of hydraulic jump (see sketch in Figure 8). The aim is to characterize the water front's motion on top of stratified flow.
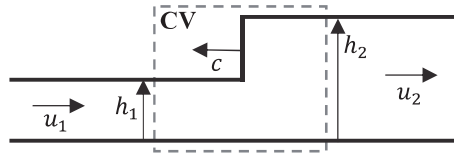
Figure 8. Hydraulic jump in Control Volume (CV)

In the simplified 1D CV model, the hydraulic jump is approximated as mathematical discontinuity between two uniform flows (A_1, u_1) and (A_2, u_2), where $u = |\vec{u}| = u_x$ and A is the cross-sectional area of stratified flow (sub-notation 1) or fully-filled flow (sub-notation 2). In reality, the uniform flow exist at some distance upstream and downstream of the jump. It is mathematically approximated that the uniform flows merge at the discontinuity. Mass change through the control volume is given as

$$0 = \frac{\rho(c-u_1)\Delta t}{\Delta t}(A_2 - A_1) + \rho A_2 u_2 - \rho A_1 u_1, \qquad (4)$$

where $(c - u_1)\Delta t$ corresponds to the finite length Δs of CV. Assuming the length of the discontinuity is sufficiently short, the force arising from frictional stress acting along the bottom should be negligible. Herein it is considered that no external forces due to the gravity in the flow direction act on the fluid discontinuity. However, an additional pressure force due to the air pressure changes is possible. Hence, for the momentum change through the control volume can be given as

$$-\Delta pA = \frac{\rho(c-u_1)\Delta t}{\Delta t}(A_2 u_2 - A_1 u_1) + \rho A_2 u_2^2 - \rho A_1 u_1^2. \qquad (5)$$

The hydraulic jump herein is considered as a transition from the stratified flow, with a height of half the pipe diameter, to fully-filled flow. Taking the centroid of flow section at partially- and fully-filled sections into consideration when determining the pressure forces, the result yields

$$\Delta pA = \frac{1}{6}g(4h_1 A_1 - 3h_2 A_2). \qquad (6)$$

Considering a propagating bore wave with stagnant fluid to the left ($u_1 = 0$) we can write a solution for relative speed c. This represents no loss in generality since the frame of reference can always be translated to $u_1 = 0$. Consequently, discontinuity's moving speed at given conditions in a circular pipe

$$c^2 = -\frac{gA_2(4h_1 A_1 - 3h_2 A_2)}{A_1(6A_1 - A_2)} \qquad (7)$$

It should be noted that if $A_1 = \frac{1}{6}A_2$ then $h_1 = \frac{9}{2}h_2$ has to hold.

The water-filled area of the partially filled circular pipe is given as

$$A(\xi) = \tfrac{1}{8}\pi D^2 \left[1 + \tfrac{2}{\pi}\sin^{-1}(2\xi - 1) + \tfrac{4}{\pi}(2\xi - 1)\sqrt{\xi - \xi^2}\right], \quad (8)$$

where $\xi = h/D$ is the ratio of interface height above invert to pipe diameter. Denoting the term in square brackets with φ_1 and φ_2 accordingly, the formula for air-water-front speed yields:

$$c^2 = \frac{g\varphi_2(3h_2\varphi_2 - 4h_1\varphi_1)}{\varphi_1(6\varphi_1 - \varphi_2)}. \qquad (9)$$

In the case of a jump from half-filled ($h_2 = 2h_1$) to fully-filled pipe, $\varphi_1 = 1$ and $\varphi_2 = 2$. This approximation yields a square-root relationship between the relative bore propagation speed and the interface height above invert upstream of the hydraulic jump:

$$c = \sqrt{4gh_1}. \qquad (10)$$

It can be concluded that the bore wave moving on the top of water column, which fills half of pipe cross-section, has a speed two times larger as in the shallow-water approximation. In the experiment, the bore propagation speed varies in the range of 1.2 … 1.5 m/s, which depends on a number of factors. It should be noted here that the estimated bore wave speed using the visual changes of the jump position, yielding Δs, during the time interval Δt are somewhat dependent on the stratified flow accelerations and deceleration, which are arising from the formation of the downstream slug flow. Because $h_1 = \tfrac{1}{2}h_2 = \tfrac{1}{2}D = 0.04$ m the simple relationship (Eq. 10) yields $c = 1.25$ m/s. Thus additional pressure force due to the air pressure changes in the air pocked entrapped between the jump and the pipe bridge, can be considered relatively small. However, it is proposed that the agreement can be further improved. Herein the simple solution is derived for free-surface bore using interface heights above pipe invert on both sides of the hydraulic jump. Herewith if corrections for surge wave would be implemented i.e. height would be substituted with pressure head for the fully-filled flow part, therefore taking into account surge conditions behind the discontinuity, the speed c would increase slightly (12).

4   DISCUSSION

The two-phase flow experiments revealed the formation of the non-stationary hydraulic jump, which had excess momentum available for different flow processes. It can be pointed out that the non-stationary hydraulic jump during the filling of horizontal pipeline is associated with the excess flow-momentum, which is divided between the dissipation at jump, transferred to the motion of jump upstream and production of slug flow at the downstream face of the jump. However, the excess energy is essentially spent to the air-water mixing and the motion of hydraulic jump along the pipeline.

An interesting result appearing from the present experiments conducted in the laboratory-scale pipeline, is the removal of air from the formed stratified flow part via air pockets moving downstream near the pipe obvert. It is also observed that the appearance of more-or-less periodic slug flow alters the velocity of bore wave, which is moving on the top of water column and fills approximately half of pipe cross-section.
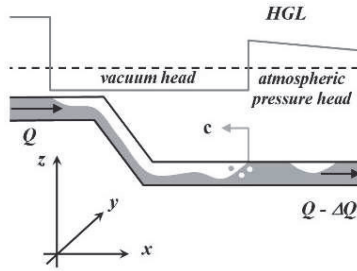
Figure 9. Schematic of contracting air pocket, hydraulic jump and slug flow

It should be outlined that the additional momentum change, resulting from pressure drop due to vacuum inside of air pocket, is transferred to air-water interactions such as air-water mixing and slug flow. It is proposed that the additional pressure drop is balanced by air-water mixing and surface tension force processes at the roller and therefore does not tangibly contribute to increase of the bore wave speed. It is apparent that downstream of hydraulic jump the unsteady flow exists. The slug flow is accelerating while the air pocket is diminishing and bore wave speed decreasing. It is found that the difference in kinetic energy in stratified flow and slug flow at the time of non-stationary hydraulic jump formation is virtually balanced by motion of it. It is deduced that the dynamics of the hydraulic jump is dominated by the entrapped air pocket and more-or-less periodic air entrainment via slug flow.

Figure 10 presents a good concurrency between experimental and numerical simulation (see Laanearu and Kaur (9)) results. With crosses, all the turbulent kinetic energy data points captured over the PIV measurement domain of width of 640 pixels (96 mm) in transitional flow (II) are indicated. It can be seen that virtually all points fall between curves obtained from numerical simulation at the limits of the measurement domain (taking the distance from roller as reference).
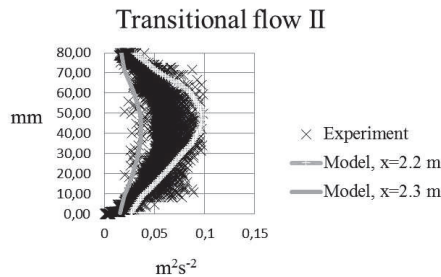
Figure 10. Turbulent kinetic energy of experimental results in comparison to numerical simulation

As the future objective, the established experimental results of the pipeline apparatus in the fluid mechanics laboratory of Tallinn University of Technology, Estonia, and the Deltares large-scale experimental facility in Delft, The Netherlands (Hou et al. (1)) will be compared and used to verify the 3D CFD solution developed in Laanearu and Kaur (9) more comprehensively.

REFERENCES

(1) Hou Q, Tijsseling AS, Laanearu J, Annus I, Koppel T, Bergant A, Vučković S, Anderson A, van 't Westende JMC (2014) Experimental Investigation on Rapid Filling of a Large-Scale Pipeline. ASCE *Journal of Hydraulic Engineering* **140**(11), 1−14.

(2) Laanearu J, Annus I, Koppel T, Bergant A, Vučković S, Hou Q, Tijsseling AS, Anderson A, van 't Westende JMC (2012) Emptying of large-scale pipeline by pressurized air. ASCE *Journal of Hydraulic Engineering* **138**(12), 1090−1100.

(3) Liou CP, Hunt WA (1996) Filling of Pipelines with Undulating Elevation Profiles. ASCE *Journal of Hydraulic Engineering* **122**, 534−539.

(4) Axworthy DH, Karney BW (1997) Discussion: Filling of Pipelines with Undulating Elevation Profiles. ASCE *Journal of Hydraulic Engineering* **123**, 1170−1174.

(5) Hou Q, Zhang LX, Tijsseling AS, Kruisbrink ACH (2011) Rapid filling of pipelines with SPH particle method. *International Conference on Advances in Computational Modeling and Simulation. Procedia Engineering* **31**, 38−43.

(6) Malekpour A, Karney BW (2011) Rapid Filling Analysis of Pipelines with Undulating Profiles by the Method of Characteristics. ISRN *Applied Mathematics* DOI: 10.5402/2011/930460

(7) Vasconcelos JG, Wright SJ (2009) Investigating rapid filling of poorly ventilated stormwater storage tunnels. *Journal of Hydraulic Research* **47**(5), 547–558.

(8) Laanearu J, Hou Q, Annus I, Tijsseling AS (2015) Water-column mass losses during the emptying of a large-scale pipeline by pressurized air. *Proceedings of the Estonian Academy of Sciences* **64**(1), 8–16.

(9) Laanearu J, Kaur K (2018) Two-phase CFD modelling of air-water flow transition in horizontal circular pipe and comparison with experimental results. *13th International Conference on Pressure Surges, Bordeaux, France.*

(10) Zukoski EE (1966) Influence of viscosity, surface tension, and inclination on motion of long bubbles in closed tubes. Journal of Fluid Mechanics 25(4) 821–837.

(11) Laanearu J, Hou Q, Tijsseling AS (2015) Experimental and analytical modelling study of water-front dynamics of two-phase unsteady flows in a large-scale pressurized pipeline. *12th International Conference on Pressure Surges, Dublin, Ireland,* 625−637.

(12) Wiggert DC (1972) Transient flow in free-surface, pressurized systems. *Journal of Hydraulics Division* **98**(1), 11−27.

Appendix 5

Publication V
Laanearu, J.; Kaur, K. (2018). **Two-phase CFD modelling of air-water flow transition in a horizontal circular pipe and comparisons with experimental results.** 13th International Conference on Pressure Surges, *2*, 937–948. BHR Group.

Two-phase CFD modelling of air-water flow transition in a horizontal circular pipe and comparisons with experimental results

J Laanearu, K Kaur
School of Engineering, Tallinn University of Technology, Estonia

ABSTRACT

The dynamics of air-water mixed flow in a laboratory-scale pipeline are explained using a 3D CFD tool. Filling of an initially empty horizontal pipe with fixed volumetric inflow rate and varying wall roughness is investigated numerically. The numerical experiments are designed to aid qualitative and quantitative interpretations of the formation of a non-stationary hydraulic jump. Essentially two different types of air-water flow transitions are detected during the pipe pressurization. It is found that the dynamics of the hydraulic jump, where stratified and fully-filled flows merge inside pressurized pipe, are related to the production of more-or-less periodic air pockets (associated with slug flow). It is shown that the turbulent-kinetic-energy maximum at a cross sections of the hydraulic jump is essentially related to the air-water mixing at the interface. The numerical findings are compared with the experimental results obtained in a laboratory-scale pipeline.

NOTATION

k - turbulent kinetic energy
u_x, - horizontal along-pipe velocity (x-axis component)
u_y - horizontal cross-pipe velocity (y-axis component)
u_z - vertical cross-pipe velocity (z-axis component)
α - air-fraction parameter (void-fraction parameter)
β - water-fraction parameter ($\beta = 1 - \alpha$)
ε - turbulent energy dissipation
v_T - eddy viscosity

1   INTRODUCTION

Air entrapped inside storm-water system can cause a range of problems, which usually result in malfunctioning urban infrastructure. Two-phase flow is also present in various hydraulic applications, such as water-distribution networks, fire-fighting systems and sewers, where pipeline cleaning and priming are performed. There is a wide range of industrial applications, complex multiphase flow dynamics, which are poorly understood until today due to absence of experimental data. Hou et al. (1) and Laanearu et al. (2) demonstrated experimentally that the presence of stratified flow significantly modifies

the dynamics of two-phase flow during water-air and air-water front intrusions along empty and filled large-scale pipelines, respectively. Water-column mass losses due to intrusion of an air cavity on top of the water column are experimentally justified and parameterized (making use the Zukoski number) in Laanearu et al. (3), (4). Air-water dynamics in undulated pipelines have been investigated in numerous studies at varying levels of process modelling (Liou and Hunt (5); Axworthy and Karney (6); Hou et al. (7); Malekpour and Karney (8); Vasconcelos and Wright (9); Izquierdo et al. (10); Pozos et al. (11); Leon et al. (12)). In a pipeline with an undulating elevation profile, column separation can occur at the high point, and an air pocket can be entrapped. A flow acceleration in pipeline, when an entrapped air pocket is released, can result in an unexpected pressure surge. A number of different numerical models have been developed to simulate free-surface flows, pressurized flows and their simultaneous occurrence (mixed flows) under single-liquid and two-phase flow conditions (entrapment and release of air pockets). Two-phase flow, viz. transient individual liquid slug motion in a voided line and the associated pressure peaks due to impacting slugs at the elbow were experimentally and theoretically investigated by Bozkus and Wiggert (13). The present study aims at contributing to understanding of mixed flows, where air-water interactions are important for the flow dynamics inside the pressurized pipeline.
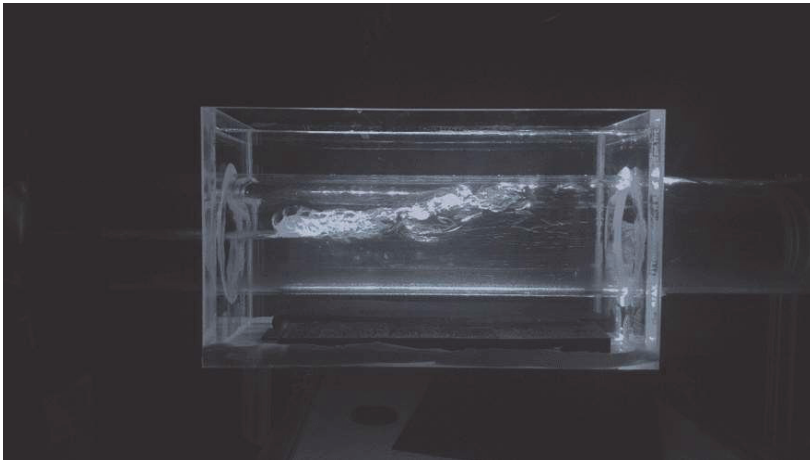
Figure 1: Hydraulic jump observed inside the visualization box of a laboratory-scale pipeline in the fluid mechanics laboratory at Tallinn University of Technology

The goal of the present study is to investigate the formation of a hydraulic jump due to a combined effect of pipeline layout (pipe bridge, horizontal pipe and outlet pipe) and wall roughness for fixed volumetric inflow rate. For this purpose also two-phase flow experiments are performed using the laboratory-scale pipeline of Tallinn University of Technology (TTÜ) (see Kaur et al. (14)). Computational Fluid Dynamics (CFD) simulations with the package OpenFOAM solver are performed to investigate the observed air-water mixed flow. The whole computational domain is meshed using a standard elements of varying sizes. The numerical experiments are conducted with a fixed volumetric inflow rate allowing qualitatively compare the formation of non-stationary hydraulic jumps under different wall-boundary roughness conditions in the horizontal pipe with restricted outflow. The numerical experiments are designed to

explain the turbulent mixing effects that are important for the formation of a hydraulic jump inside the pipeline. An image of the non-stationary hydraulic jump, which has been observed inside the visualization box of a horizontal pipe is shown in Figure 1. TTÜ's pipeline apparatus under investigation represents a downscaled version of the industrial-scale pipeline apparatus, and consisted of a Plasticized Polyvinyl Chloride (PVC) pipeline of external diameter 250 mm and is 275 m long. This pipeline was used to carry out the filling and emptying experiments on the Deltares dynamic multi-phase test rig (Laanearu et al. (2)), where mobile hydraulic jumps during filling stages eventually appeared at short transparent section near the pipe bridge. It should be noted that the Deltares pipeline was built of non-transparent PVC pipes of 10 meters length, and the two-phase flow was visualized at three transparent sections of 0.5 meters length. In the present study, the CFD simulations are used to investigate dynamically similar solutions for the breaking of the air-water interface during the filling of the laboratory-scale pipeline. The resulting non-stationary hydraulic jump represents a transition of rapid flow through air-water mixing front to a reduced-velocity flow that include air bubbles, which at certain instant form buoyant air pockets between water slugs. It is anticipated that the CFD simulations also provide an important insights into the air-water interactions taking place in storm-water systems during intense rain events, when also comparatively rapid filling of hydraulic system arises and system malfunctioning (urban flooding) can occur due to two-phase flow transitions (Kaur et al. (15)).

The Deltares non-transparent pipeline was fed with water from the supply tower and the air at atmospheric pressure initially present in the pipeline was replaced with water. Due to poor visualization of the stratified flow process that occurred inside the industrial-scale pipeline, the formation of non-stationary hydraulic jump during specific experimental runs has not been fully understood and interpreted until now. The TTÜ's laboratory-scale pipeline is constructed of fully transparent pipes, made of acrylic glass i.e. PolyMethyl MethAcrylate (PMMA) pipes of 2 meters length. A transparent pipeline allows the visualization a series of two-phase processes.

The plan of the present study is as follows. First the setup of the CFD 3D-flow model is presented for the investigation of the patterns of air-water mixed flow in the laboratory-scale pipeline. Then the two-phase (air and water) flow CFD solver is used to investigate the formation of a hydraulic jump due to the combined effects of pipeline layout and wall roughness. Three numerical case-studies are analysed; one smooth pipe-flow and two rough pipe-flow situations, which all have same volumetric inflow rate. The numerical results of the three case studies are used to demonstrate an evolution of the eddy viscosity of a *k-epsilon* turbulence model at the transitions flow part of the pressurized pipe, where stratified and fully-developed flows merge.

Subsequently the numerical findings from the less-rough-pipe flow case are compared with the experimental results by Kaur et al. (14). Finally the overall findings are summarized and discussed with respect to future improvements making use advanced numerical modelling tools.

2   MODEL SETUP

The pressure vessel is used for filling the empty pipeline with water that enters through the pipe bridge, and replaces air at atmospheric pressure initially present inside the pipeline (as shown in Figure 2 plot i). The horizontal pipe is depleted into the outflow vessel through the outlet pipe with a reduced diameter. The modelling domain of the

pipeline is three-dimensional, and consists of three parts: pipe-bridge, horizontal pipe and outlet pipe with reduced diameter. (For a detailed description of the laboratory-scale pipeline apparatus see Kaur et al. (14)). In Figure 2 plot ii), the dimensions of the laboratory-scale pipeline are shown: the pipe bridge has a diameter of 0.08 m, a height of 0.26 m and a length of 1.68 m; the horizontal pipe has the diameter 0.08 m and a length of 5 m; and the outlet pipe has a diameter of 0.07 m and a length of 0.2 m. The modelling domain of the horizontal-pipe part between the pipe bridge and the outlet pipe is shortened by 1.4 meters. The reason is that a shortened pipe allows an increase the meshing efficiency of the modelling domain due to a reduced number of cells needed for the numerical calculations, and therefore reducing the integration time.
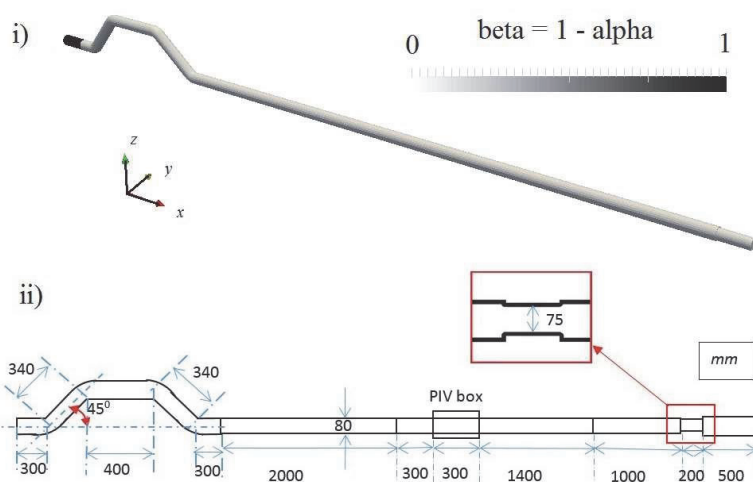
Figure 2: Laboratory-scale pipeline information: i) 3D CAD solution of modelling domain, where the initial condition for filling is shown, and ii) 2D sketch of the assembled pipeline (pipe bridge, horizontal pipe and outlet pipe) with dimensions

The numerical technique used by the CFD model is the Volume Of Fluid (VOF) method. The model uses a pressure-based solver that considers the relationship between velocity and pressure corrections by following mass conservation and momentum changes of immiscible fluids. The momentum equation includes the surface tension force, which acts at interfaces of mixed fluids. Numerical modelling convergence can be obtained by progressively tracking the imbalances in the numerical calculations of the algebraic equations, through each iteration step. These imbalances measure the overall conservation of residuals and convergent solutions can be achieved when these residuals are reduced under pre-set tolerances. The CFD model consists of three main elements: pre-processing, processing and post-processing. In the pre-processing step the geometry and mesh are generated, fluid phases and turbulence properties are defined, and the initial and boundary conditions are selected. The percentage of each fluid phase defines the density and viscosity of the mixture in each cell. The volume of fluid in a cell is computed as the fraction of fluid phase, defined for the phase of air as α (cf. Laanearu et al. (2)) and for the phase of water as $\beta = 1 - \alpha$ (cf. Laanearu et al. (4)). The values of α in each cell range between 0 and 1, and correspondingly the values of β in each cell range between 1 and 0. For instance, if the cell is completely filled with water then $\beta = 1$ (and correspondingly $\alpha = 0$) and if it is filled with air (void phase) then its value is 0. At the

interface, the value β (or correspondingly $\alpha = 1 - \beta$) is between 0 and 1 (1 and 0). It can be mentioned that for slug flow the air-fraction parameter corresponds to the hold-up parameter (cf. Bozkus and Wiggert (13)). The accuracy of a computational result can be affected by the number of cells in the grid, and here around 165'000 cells with varying sizes are generated for the pipeline modelling domain. The Computer Aid Design (CAD) solution includes walls with no-slip condition (pipe walls are considered both hydraulically smooth and rough in different cases), one end with constant inflow (pipe-bridge inlet) and one end with an open boundary (outlet). In the processing step, the flow variables such as velocity-vector components, pressure and density are approximated by means of simple algebraic functions. In the post-processing step the variables (velocity components (u_x, u_y, u_z), pressures, parameter β (corresponding also to density excess, cf. Cuthbertson et. al. (16)), turbulent kinetic energy (k), turbulent energy dissipation (ε) and eddy viscosity (υ_T)) are numerically determined and visualized.

3   CASE STUDIES

The relative proportions of air and water flowing through the pipeline gives rise to a range of different air-water mixed flow patterns. It is shown here that these flow patterns are crucially dependent on the pipeline layout and wall roughness. Three wall-boundary generated turbulence conditions of the two-phase flow solver are used to investigate the dynamics of air-water mixed flow in the horizontal pipe. In the first case, the two-phase flow CFD solver is used to investigate the formation of a hydraulic jump for the hydraulically smooth pipe. In the second and third cases, the CFD solver is used to investigate the formation of a hydraulic jump for hydraulically rough pipes, with roughness heights of 1 mm and 0.5 mm, correspondingly. To compare the air-water mixed flow patterns obtained in the CFD simulations under different wall-boundary generated turbulence conditions, the constant volumetric inflow rate 3.5 l.s^{-1} for water is used, and the flow at the outlet is fixed as a zero-gradient pressure flow. The density and molecular viscosity of water and air in all CFD simulations are set to 1000 kg.m^{-3} and 1.0×10^{-6} m^2.s^{-1}, and 1.2 kg.m^{-3} and 1.5×10^{-5} m^2.s^{-1}, respectively.

3.1   Case 1 (smooth-pipe flow)
Here the two-phase flow CFD solver is used to investigate the formation of a hydraulic jump for the hydraulically smooth pipe. Initially the computational domain is filled with water at the short inlet pipe of the pipe bridge (see water part ($\beta = 1$) in Figure 2 plot i)), and thus the pipeline filling process for a constant water volumetric inflow rate 3.5 l.s^{-1} is integrated 30 seconds. The stratified flow develops along the pipeline at the initial integration stage, this while the intruding water-air front in the horizontal pipe reaches the outlet pipe with reduced diameter. After this time instant the water-surface elevation starts to rise in the downstream part of the horizontal pipe, which after filling the pipe cross-section up to obvert forms a bore wave that is moving backwards against the stratified flow direction i.e. toward the pipe bridge, including the formation of some slugs at the downstream face. The co-ordinate position (i.e. $x = 4.2$ meters from the inlet of the pipe bridge) of the non-stationary hydraulic jump interface, which reaches the pipe obvert, at the time instant 30 seconds, is indicated in Figure 3 plot i). In the latter plot also the long air pocket entrapped near the pipe bridge and the formation of some slugs along the pipeline are in clear evidence. An evolution of the vertical distribution of the along-pipe (x-axis direction) velocity component u_x is shown for the co-ordinates $x = 4.0$, 4.2, 4.4 m; $y = 0$; $z = -0.04 \ldots 0.04$ m in Figure 3 plot ii). As expected, the changes of velocity over the vertical cross-sections, where stratified and fully-filled flows of the pressurized pipe merge, involve the velocity maximum reduction in the downstream face

of the hydraulic jump, which is also associated with the development of a turbulent core at pipe axis. The vertical distribution of eddy viscosity v_T is shown for the co-ordinates x = 4.0, 4.2, 4.4 m; y = 0; z = –0.04 … 0.04 m in Figure 3 plot iii). It can be recognized that the maximum eddy-viscosity is associated with the upstream face of hydraulic jump, where stratified flow is present due to the entrapped air pocket near the pipe bridge, and the air-water surface breaking is possible due to the increased velocity shear as compared to the fully filled pipe flow where the surface is transformed to slug flow.
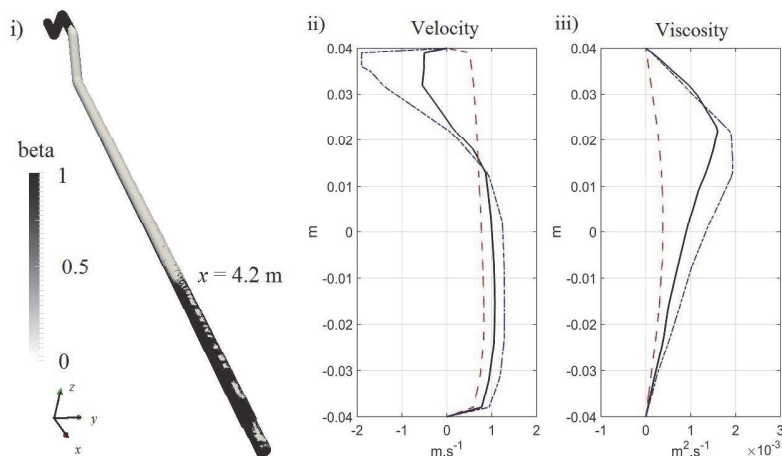
Figure 3: Smooth-pipe flow case: i) parameter β variation along the pipe at time instant 30 seconds, ii) vertical distribution of along-pipe velocity (x-axis component u_x) at cross-sections (dash-dotted curve at x = 4.0 m; full curve at x = 4.2 m; dashed curve at x = 4.4 m), and ii) vertical distribution of eddy viscosity v_T at cross-sections (dash-dotted curve at x = 4.0 m; full curve at x = 4.2 m; dashed curve at x = 4.4 m)

3.2   Case 2 (more-rough-pipe flow)

Here the CFD solver is modified with the wall function to investigate the formation of hydraulic jump in the rough pipe with a roughness height of 1 mm. The initial conditions and integration period are the same as in Case 1 (smooth-pipe flow). Again at the initial integration stages the stratified flow develops along the pipeline. An important difference as compared with the smooth-pipe flow case is that before the intruding water-air front extends to the outlet pipe with a reduced diameter, a gradually varying flow with comparatively steep slope develops inside the horizontal pipe. Therefore an undulating surface wave forms at interior of the horizontal pipe, the wave crest of which, after merging with the water front from the outlet, forms the hydraulic jump, with formation of slug flow in the downstream face. The co-ordinate position (i.e. x = 1.8 meters from the inlet of pipe bridge) of the non-stationary hydraulic jump interface, which reaches to the pipe obvert, at time instant 30 seconds, is indicated in Figure 4 plot i). The comparatively short air pocket entrapped near the pipe bridge and the formation of more-or-less periodic slug flow along the pipeline are in clear evidence. An evaluation of the vertical distribution of the along-pipe (x-axis) velocity component u_x is shown for the co-ordinates x = 1.6, 1.8, 2.0 m; y = 0; z = –0.04 … 0.04 m in Figure 4 plot ii). A difference of the velocity changes over the vertical cross-sections, where stratified and fully-developed flows in pressurized pipe merge, with respect to Case 1, is that the interface of the transition flow part is more supressed in the along-pipe direction. This effect may be

explained by the slightly modified formation of the slugs, which demonstrate a more-or-less periodic pattern in Figure 4 plot i). The vertical distribution of eddy viscosity v_T is shown for the co-ordinates $x = 1.6, 1.8, 2.0$ m; $y = 0$; $z = –0.04 … 0.04$ m in Figure 4 plot iii). It can be recognized that the maximum eddy-viscosity is associated with the surfaces of stratified flow at the hydraulic-jump region, where the velocity shear is substantially increased as compared to the smooth-pipe flow, having the maximum $\sim 4 \times 10^{-3}$ m^2.s^{-1}, 0.2 meters apart from the intersecting interface with the pipe obvert. (The eddy viscosity maximum of the vertical distribution is shown by the dash-dotted curve at $x = 4.0$ m in Figure 3 plot iii) is $\sim 2 \times 10^{-3}$ m^2.s^{-1}.)
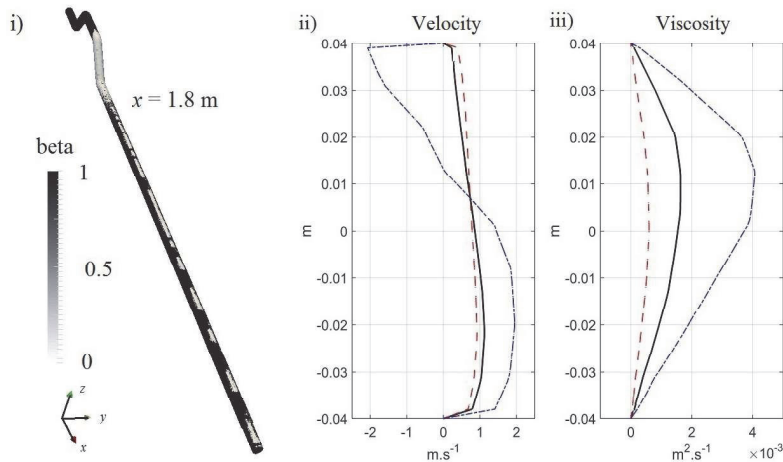
Figure 4: More-rough-pipe flow case: i) parameter β variation along the pipe at time instant 30 seconds, ii) along-pipe velocity (x-axis component u_x) vertical distribution at cross-sections (dash-dotted curve at $x = 1.6$ m; full curve at $x = 1.8$ m; dashed curve at $x = 2.0$ m), and ii) eddy viscosity v_T vertical distribution at cross-sections (dash-dotted curve at $x = 1.6$ m; full curve at $x = 1.8$ m; dashed curve at $x = 2.0$ m)

3.3   Case 3 (less-rough-pipe flow)

Here the CFD solver configured for Case 2 (more-rough pipe) is slightly modified to investigate the formation of a hydraulic jump for the rough pipe with a roughness height of 0.5 mm. The initial conditions and integration period are the same as in Case 1 (smooth-pipe flow) i.e. the constant water volumetric inflow rate 3.5 l.s^{-1} is integrated 30 seconds. At the initial integration stages the stratified flow develops along the pipeline. Similarly to the more-rough-pipe flow, a gradually varying flow with a comparatively milder slope appears inside the horizontal pipe, before the intruding water-air front extends to the outlet with a reduced diameter. The undulating surface-wave forms at the interior of the horizontal pipe, the wave crest of which, after merging with the water front from the outlet, forms a more downstream-side hydraulic jump as compared to the surface development processes of Case 2, with a similar pattern of slugs at the downstream face of hydraulic jump. The co-ordinate position (i.e. $x = 2.2$ meters from the inlet of pipe bridge) of the non-stationary hydraulic jump interface, which reaches to the pipe obvert at time instant 30 seconds, is indicated in Figure 5 plot i). An evaluation of vertical distribution of the along-pipe (x-axis) velocity component u_x is shown for the

co-ordinates x = 2.0, 2.2, 2.4 m; y = 0; z = –0.04 … 0.04 m in Figure 5 plot ii). Essentially, the velocity changes over the vertical cross-sections, where the stratified and fully-filled flows in the pressurized pipe merge, are similar to the Case 2 velocity changes. The vertical distribution of eddy viscosity v_T is shown for the co-ordinates x = 2.0, 2.2, 2.4 m; y = 0; z = –0.04 … 0.04 m in Figure 5 plot iii). The maximum of eddy-viscosity ~ 3 × 10^{-3} m^2.s^{-1}, shown with the dash-dotted curve in the Figure 5 plot iii) is apparently associated with the instabilities developing the surface of the stratified flow.
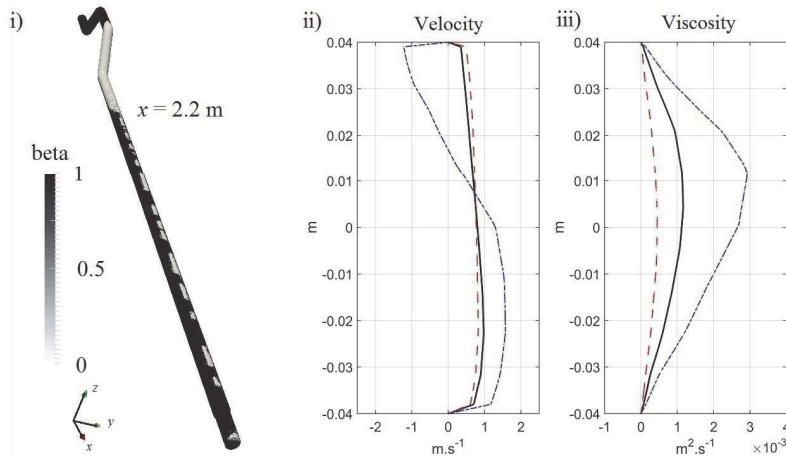
Figure 5: Less-rough-pipe flow case: i) parameter β variation along the pipe at time instant 30 seconds, ii) along-pipe velocity (x-axis component u_x) vertical distribution at cross-sections (dash-dotted curve at x = 2.0 m; full curve at x = 2.2 m; dashed curve at x = 2.4 m), and ii) eddy viscosity v_T vertical distribution at cross-sections (dash-dotted curve at x = 2.0 m; full curve at x = 2.2 m; dashed curve at x = 2.4 m)

4   EXPERIMENTAL ASSESSMENTS

The experiments of two-phase flow are conducted in a laboratory-scale pipeline, which is built in the TUT's fluid mechanics laboratory. The pipeline apparatus consisted of a number of elements: pressure vessel, centrifugal pump, pipe-bridge, horizontal pipe, outlet pipe with reduced diameter, outflow vessel, etc., and measurement equipment: electromagnetic flow meters, Particle Image Velocimetry (PIV) system, etc. (For a detailed description of the pipeline apparatus see Kaur et al. (14)). The overall dimensions of the laboratory-scale pipeline are shown in Figure 2 plot ii). During the filling of the pipeline, the flow rate was chosen so that the non-stationary hydraulic jump formed due to flow transition between the stratified flow and fully-filled flow (see the image in Figure 1). To check the repeatability of the non-stationary hydraulic jump, a series of runs were carried out with the same driving pressure and outflow conditions. In the present section the numerically modelled variables of the air-water mixed flow are compared with the experimental findings by Kaur et al. (14). Two-dimensional PIV is used to measure the velocity fields that resulted from vertically illuminated xz-coordinates plane of the water flow, employing one side-mounted digital CCD camera to record instantaneous flow velocity fields within specific regions of interest, i.e. across the 0.096 m-long and 0.120 m-high window, corresponding to 640 × 800 pixels per

image inside the visualization box. The recording frequency of the camera is adjusted according to the Reynolds number, and varied between 1155 and 2982 images per second. These PIV measurements are obtained at time periods when the two-phase flow corresponded to the motion of hydraulic jump between the downstream and upstream edges of visualization box (Figure 1), allowing synoptic (i.e. time-averaged) velocity fields to be generated for the regions of interest. Post-processing of the velocity field measurements is conducted using the PIV standard software Dynamic Studio 4.0 (Dantec Dynamics).
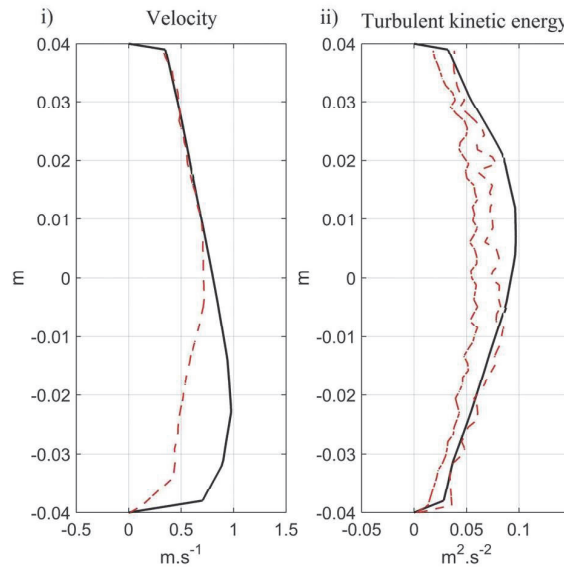
Figure 6: Turbulent flow characteristics at the transitional flow part of the pressurized pipe: i) along-pipe velocity (*x*-axis component u_x) vertical distribution at cross-sections from the numerical model (full curve at $x = 2.2$ m) and from the experiment (dashed curve), and ii) turbulent kinetic energy *k* vertical distribution at cross-sections from numerical model (full curve at $x = 2.2$ m) and from the experiment (dashed and dotted curves correspond to the isotropic and non-isotropic approximations of *k*, respectively)

The vertical distribution of the along-pipe (*x*-axis direction) modelled and measured velocity component u_x for the transitional flow part of pressurized pipe are shown in Figure 6 plot i). The modelled velocity distribution in the hydraulic-jump region corresponds well to the measured velocity distribution in the upper pipe-part of flow. The correlation between the modelled and measured velocities in the lower pipe-part of pressurized flow is less satisfying. The vertical distribution of modelled and measured turbulent kinetic energy *k* is shown at the same co-ordinate position in Figure 6 plot ii). It can be noted that the modelled *k* distribution follows better the isotropic approximation of the turbulent kinetic energy, according to the measurements. It should be considered that a standard *k-epsilon* turbulence model is used in the CFD model of two-phase flow.
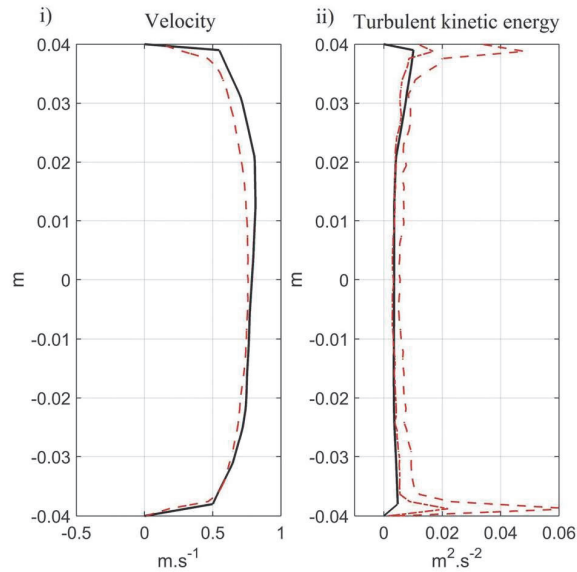
Figure 7: Turbulent flow characteristics at the downstream fully-developed flow part of pressurized pipe: i) along-pipe velocity (x-axis component u_x) vertical distribution at a cross-section from the numerical model (full curve at $x = 2.8$ m) and from the experiment (dashed curve), and ii) turbulent kinetic energy vertical distribution at a cross-section from the numerical model (full curve at $x = 2.8$ m) and from the experiment (dashed and dotted curves in the plot correspond to the isotropic and non-isotropic approximations of turbulent kinetic energy k, respectively)

The vertical distribution of the along-pipe (x-axis direction) modelled and measured velocity component u_x for the downstream fully-developed flow part of pressurized pipe is shown in Figure 7 plot i). The modelled velocity distribution in the fully-developed flow region corresponds well to the measured velocity distribution in the whole cross-section of flow in the pipe. The vertical distribution of modelled and measured turbulent kinetic energy k is shown at the same co-ordinate position in Figure 7 plot ii). It can be concluded that the modelled k distribution follow better the non-isotropic approximation of turbulent kinetic energy, estimated from the measurements.

5   CONCLUDING REMARKS

The numerical results presented in this study represent a laboratory-scale pipeline filling process for fixed water inflow rate and varying wall-boundary conditions. One aim of the numerical investigations was to show that the two-phase CFD solver can be a useful tool when explaining the dynamics of air-water mixed flow in horizontal pipes. The numerical case studies demonstrated that the non-stationary hydraulic jump inside the pressurized pipeline can be generated essentially due to two mechanisms; 1) formation of a bore wave at geometrical constriction and 2) water surface intersection with the pipe obvert due to wall-roughness effects. Thus it can be concluded that the numerical experiments performed here aid essentially a qualitative interpretation of the formation

of a non-stationary hydraulic jump. It was found that the dynamics of the hydraulic jump, where stratified and fully-filled flows merge inside a horizontal pipeline (consisting of pipe bridge, horizontal pipe and outlet pipe with a reduced diameter), was related to an entrapped air pocket near the pipe bridge and a more-or-less periodic production of air pockets, associated with slug flow in the downstream face of the jump. It was also shown that the turbulent kinetic energy at a cross section of the hydraulic jump was essentially related to the air-water mixing at the interface. It can be concluded that the numerical model variables follow quantitatively well the experimental results by Kaur et al. (14). However, in future work the turbulence model results apparently can be improved in some respects, e.g. 1) using more fine non-triangular cells at the wall boundaries of the modelling domain and 2) using the adaptive mesh at the pipe interior to capture interfacial processes.

ACKNOWLEDGEMENTS

REFERENCES

(1)   Hou Q, Tijsseling AS, Laanearu J, Annus I, Koppel T, Bergant A, Vučković S, Anderson A, van 't Westende JMC (2014) Experimental Investigation on Rapid Filling of a Large-Scale Pipeline. *ASCE Journal of Hydraulic Engineering* **140**(11), 1-14.
(2)   Laanearu J, Annus I, Koppel T, Bergant A, Vučković S, Hou Q, Tijsseling AS, Anderson A, van 't Westende JMC (2012) Emptying of large-scale pipeline by pressurized air. *ASCE Journal of Hydraulic Engineering* **138**(12), 1090-1100.
(3)   Laanearu J, Hou Q, Annus I, Tijsseling AS (2015) Water-column mass losses during the emptying of a large-scale pipeline by pressurized air. *Proceedings of the Estonian Academy of Sciences* **64**(1), 8-16.
(4)   Laanearu J, Hou Q, Tijsseling AS (2015) Experimental and analytical modelling study of water-front dynamics of two-phase unsteady flows in a large-scale pressurized pipeline. *12th International Conference on Pressure Surges, Fluid Transients and Water Hammer* 625-637.
(5)   Liou CP, Hunt WA (1996) Filling of Pipelines with Undulating Elevation Profiles. *ASCE Journal of Hydraulic Engineering* **122**, 534-539.
(6)   Axworthy DH, Karney BW (1997) Discussion: Filling of Pipelines with Undulating Elevation Profiles. *ASCE Journal of Hydraulic Engineering* **123**, 1170-1174.
(7)   Hou Q, Zhang LX, Tijsseling AS, Kruisbrink ACH (2011) Rapid filling of pipelines with SPH particle method. *International Conference on Advances in Computational Modeling and Simualtion. Procedia Engineering* **31**, 38-43.
(8)   Malekpour A, Karney BW (2011) Rapid Filling Analysis of Pipelines with Undulating Profiles by the Method of Characteristics. *ISRN Applied Mathematics* DOI: 10.5402/2011/930460
(9)   Vasconcelos JG, Wright SJ (2009) Investigating rapid filling of poorly ventilated stormwater storage tunnels. *IAHR Journal of Hydraulic Research* **47**(5), 547-558.
(10)   Izquierdo J, Fuertes VS, Cabrera E, Iglesias PL, Garcıa-Serra J (1999) Pipeline start-up with entrapped air. *IAHR Journal of Hydraulic Research* **37**(5), 579-590.

(11) Pozos O, Gonzalez CA, Giesecke J, Marx W, Rodal EA (2010) Air entrapped in gravity pipeline systems. *IAHR Journal of Hydraulic Research* **48**(3), 338-347.

(12) Leon AS, Ghidaoui MS, Schmidt AR, Garcia MH (2010) A robust two-equation model for transient-mixed flows. *IAHR Journal of Hydraulic Research* **48**(1), 44-56.

(13) Bozkus Z, Wiggert DC (1997) Liquid slug motion in a voided line. *Journal of Fluids and Structures* **11**(8), 947-963.

(14) Kaur K, Annus I, Laanearu J (2018) Experimental measurements of momentum change through hydraulic jump in a transparent horizontal pipe. *13th International Conference on Pressure Surges.*

(15) Kaur K, Laanearu J, Annus I (2017) Numerical study of Tallinn storm-water system flooding conditions using CFD simulations of multi-phase flow in a large-scale inverted siphon. *IOP Conference Series: Materials Science and Engineering*, **66**(6), 469-480.

(16) Cuthbertson A, Laanearu J, Carr M, Sommeria J, Viboud S (2018) Blockage of saline intrusions in restricted, two-layer exchange flows across a submerged sill obstruction. *Environmental Fluid Mechanics*, **18**(1), 27-57.

Appendix 6

Numerical study of Tallinn storm-water system flooding conditions using CFD simulations of multi-phase flow in a large-scale inverted siphon

K Kaur[1], J Laanearu[1] and I Annus[1]

[1]Department of Civil Engineering and Architecture, School of Engineering, Tallinn University of Technology, Tallinn, 19086, Estonia

E-mail: katrin.kaur@ttu.ee

Abstract. The numerical experiments are carried out for qualitative and quantitative interpretation of a multi-phase flow processes associated with malfunctioning of the Tallinn storm-water system during rain storms. The investigations are focused on the single-line inverted siphon, which is used as under-road connection of pipes of the storm-water system under interest. A multi-phase flow solver of Computational Fluid Dynamics software OpenFOAM is used for simulating the three-phase flow dynamics in the hydraulic system. The CFD simulations are performed with different inflow rates under same initial conditions. The computational results are compared essentially in two cases 1) design flow rate and 2) larger flow rate, for emptying the initially filled inverted siphon from a slurry-fluid. The larger flow-rate situations are under particular interest to detected possible flooding. In this regard, it is anticipated that the CFD solutions provide an important insight to functioning of inverted siphon under a restricted water-flow conditions at simultaneous presence of air and slurry-fluid.

1. Introduction

Flooding in urban areas is a serious hazard that can obstruct functioning of the public services due to breakdown of city transport, cutoff of electricity, etc. The storm-water system can experience considerable changes in flow, which can range from large volumetric flows during intense rains to longer periods of much smaller flows. The sediments such as sand, mud, etc. depositions take place in the storm-water system, and a multi-phase flow may develop at depressions under certain circumstances. Sediments deposition can generate problems such as hydraulic overloading due to a reduction in flow capacity, which may result in flooding during a storm event. Thus, the issue of designing storm-water systems to be self-cleaning becomes very important. Hou et al. [1] and Laanearu et al. [2] have demonstrated experimentally that the presence of air inside water column can significantly modify the flow dynamics during filling and emptying of large-scale pipeline, respectively. Water-column mass changes during two-phase flow are theoretically analyzed and parameterized in Laanearu et al. [3] [4]. According to Hou et al. [5], rapid filling of an empty pipeline with undulating elevation profile can occur under gravity and if the generated flow is not seriously blocked, the water column grows with little adverse pressure and can attain a high velocity. According to Laanearu et al. [2], emptying of initially filled pipeline is associated with stratified flow due to development of air cavity. Apparently, the presence of heavier substances in the pipeline in addition to air may considerably change the water-flow

dynamics e.g. due to the propensity of sediments depositions. Therefore, sand traps are used to reduce sand amount in the storm-water system. Nabil et al. [6] demonstrated that there is a satisfactory agreement between CFD simulation results of slurry-fluid flow and experimental data in case of fine slurries. In the preliminary study of Kaur et al. [7], several CFD simulations were used to determine two-phase flow dynamics in a large-scale storm-water system part i.e. the inverted siphon also under interest in the present study. In latter study two cases: 1) rapid filling of the system containing a stagnant water at constant water inflow rates, and 2) emptying the initially, partially filled system from slurry-fluid at constant inflow rates of water, were investigated. Instead of the steady hydraulically-driven flows, the computational results revealed unexpected unsteady two-phase flow situations with the design flow rates (air and water: 1000 lps and less). When the driving pressure-head was high, which is associated with an ascending water level in the inlet chamber of siphon, air from the inverted siphon was effectively expelled out, after which the flow was accelerated, and if the water level in the inlet chamber was descending below the upper invert of siphon then the air intake occurred. Apparently quasi-stationary pressure oscillations in the inverted siphon are a cause of this phenomenon, where the air-water-flow stage is replaced with water-flow stage and vice versa with a characteristic period.

Until present the restricted water-flow conditions in the Tallinn storm-water system due to simultaneous presence of air and sediments have been poorly examined. To investigate the three-phase flow dynamics in the storm-water system, more advanced numerical study of a restricted water flow through the large-scale inverted siphon is herein conducted. In addition of three phases of flow also the inverted-siphon walls representation in the CFD solutions is modified. For this purpose a rough-wall function is activated in the applied multi-phase flow solver to better simulate realistic conditions. An aim of the present study is to determine flooding conditions in the case of emptying the initially, partially filled inverted siphon from slurry-fluid at constant inflow rates of water. It is anticipated that the presence of slurry-fluid in the inverted siphon reduces the flow capacity, and modifies significantly the water-flow dynamics through the inverted siphon as compared by the previous results by Kaur et al. [7].

The plan of the current study is following. Firstly the CFD solver structure is briefly presented. The numerical simulations are investigated for two cases: 1) designed flow rate and 2) larger flow rate, for emptying the initially filled inverted siphon from slurry-fluid. Specifically, the case (2) is presented in two stages to detected flooding. For consistency check the stationary flow conditions in the numerical simulations are compared with the hydraulic results. Finally the overall results are discussed and concluded.

2. CFD solver setup

2.1. Inverted siphon
The hydraulic system (figure 1) consists of two reinforced-concrete chambers at inlet and outlet, which both include a manhole on top. The inlet and outlet chambers at sides are equipped with inflow and outflow pipes, respectively. The inlet and outlet chambers are connected by the siphoned part, consisting of pipeline with the inner diameter of 800 mm and the length of 90 m. The inverted siphon is constructed from centrifugally cast fiberglass-reinforced, polymer mortar pipes, which is characterized with an approximate Manning's roughness coefficient $n = 0.015$. The reinforced-concrete chambers have dimensions of 1.5 m × 2.0 m × 3.0 m. The siphoned part consists of three sections: inflow pipe with a positive slope $i_0 = 0.327$ and length $l = 13.3$ m, the middle section at the lowest part with a minor positive slope $i_0 = 0.001$ and $l = 55.3$ m and outflow pipe with the adverse slope $i_0 = -0.157$ and $l = 21.2$ m. Extra pipe connections are designed at the lowest pipe of siphon for maintenance purposes. In this regard, the use of flushing devices that generate controlled flush waves into the system are considered as a possible solution to remove the flow-restricting substances from the lower part of the inverted siphon. The designed flow rate of the system is 1000 lps. Hydraulic modelling of fully filled steady-state flow to determine head losses, hydraulic gradients and wall shear stresses at Reynolds numbers in the expected operational range is presented by Kaur et al. [7].
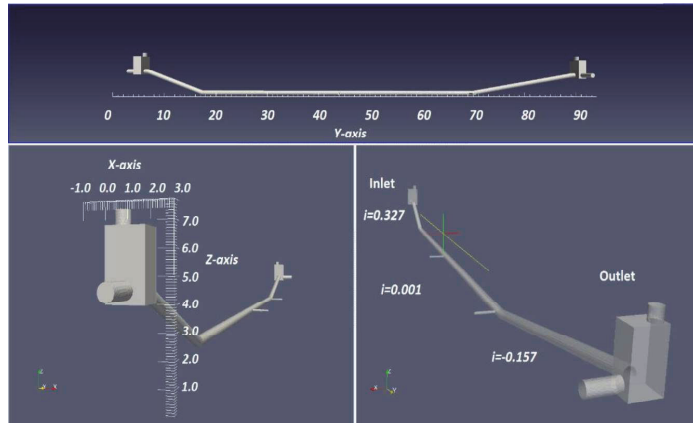
Figure 1. Full-scale CAD model of the inverted siphon under Laagna Road.

2.2. Multi-phase flow solver

A multi-phase flow solver of Computational Fluid Dynamics software OpenFOAM for a number of fluids is used. The solver includes surface-tension and contact-angle effects for each phase. The numerical technique used in the CFD modelling is the Volume of Fluid (VOF) method. A pressure-based solver considering the relationship between velocity and pressure corrections, following mass conservation and momentum changes is used. Convergence can be obtained by progressively tracking the imbalances in numerical calculations of algebraic equations, through each iteration step. These imbalances measure the overall conservation of residuals and convergence solutions can be achieved when these residuals are reduced under pre-set tolerances. In the processing step, the flow variables such as velocity, pressure and density are approximated by means of simple functions. In the post-processing step these variables are visualized.

A full scale three dimensional model of the inverted siphon (figure 1) is constructed and meshed in the pre-processing phase. Also, in this phase, fluid, pipe wall material and turbulence properties are defined and initial and boundary conditions are selected. Fields are set to clearly define the initial distribution of fluids: water at the inflow, slurry-fluid in the bottom of the inverted siphon as a stagnant pool up to a level that represents real-life conditions, and air, as default, everywhere else in the computational domain.

In the processing step a solver for n incompressible fluids is implemented for the three-phase flow of interest in this study. At appropriate boundaries of the computational domain wall-function for turbulent flow over rough walls is applied. The roughness parameter for the wall shear stress in this model is defined via equivalent sand-grain roughness, which can be calculated from the Darcy friction factor by a relation defined by Adams et al. [8]:

$$k_s = 3.7D \left(10^{-\frac{1}{1.8\sqrt{\lambda}}} - \frac{6.9}{Re} \right)^{1/1.11} \tag{1}$$

where D is the pipe diameter in meters, λ is the friction factor (set to 0.03) as the flow is operated in a fully turbulent regime, and Re is the Reynolds number.

2.2.1. Volume of Fluid method.

The multi-phase flow solver is based on the VOF method and calculates a multiphase mixture that is used to find physical properties as weighted averages based on phase fraction α_q that can take any value between 0 and 1.

The VOF method can be classified as a Surface Capturing technique which implies that the free-surface is not exactly tracked by the mesh like in Surface Tracking methods, but its position is approximated by a phase fraction function [9]. The momentum equation

$$\frac{\partial}{\partial t}(\rho_m \vec{u}) + \vec{\nabla} \cdot (\rho_m \vec{u} \otimes \vec{u}) = -\vec{\nabla} p_{rgh} + \vec{\nabla} \cdot \left[\mu_m (\vec{\nabla} \vec{u} + \vec{\nabla} \vec{u}^T) \right] - (\vec{g} \cdot \vec{x}) \vec{\nabla} \rho_m + \sigma \kappa \vec{\nabla} \alpha_q \quad (2)$$

The continuity equation

$$\vec{\nabla} \cdot \vec{u} = 0 \quad (3)$$

The phase fraction α_q for a phase-pair can be computed from a separate transport equation that takes the form

$$\frac{\partial \alpha_q}{\partial t} + \vec{\nabla} \cdot (\alpha_q \vec{u}) = 0 \quad (4)$$

To achieve the necessary compression of the surface an extra artificial compression term is introduced into the latter equation

$$\frac{\partial \alpha_q}{\partial t} + \vec{\nabla} \cdot (\alpha_q \vec{u}) + \vec{\nabla} \cdot [\alpha_q (1 - \alpha_q) \vec{v}_{qp}] = 0 \quad (5)$$

where $\vec{v}_{qp}$ is a velocity field suitable to compress the interface. This artificial term is only active in the interface region.

The density at any point in the domain is calculated as a weighted average of the volume fraction

$$\rho_m = \alpha_q \rho_i + (1 - \alpha_q) \rho_j \quad (6)$$

The curvature κ in the momentum equations surface tension term $\vec{F}_\sigma = \sigma \kappa \vec{\nabla} \alpha_q$ is given by equation

$$\kappa = \vec{\nabla} \cdot \left(\frac{\vec{\nabla} \alpha_q}{|\vec{\nabla} \alpha_q|} \right) \quad (7)$$

The treatment of the pressure is done using modified pressure p_{rgh} that is related to the pressure gradient via the equation

$$-\vec{\nabla} p + \rho_m \vec{g} = -\vec{\nabla} p_{rgh} - (\vec{g} \cdot \vec{x}) \vec{\nabla} \rho_m \quad (8)$$

where $\vec{x}$ is the position vector.

2.2.2. Turbulence model. The standard k-ε model of Jones and Launder [10], based on Boussinesq approximation with the turbulent viscosity μ_t is used in the multiphase solver. The turbulent viscosity equation is

$$\mu_t = \rho C_\mu \frac{k^2}{\varepsilon} \quad (9)$$

The transport equation for turbulent kinetic energy k, that determines the energy in the turbulence, takes the form

$$\frac{\partial}{\partial t}(\rho k) + \frac{\partial}{\partial x_i}(\rho k u_i) = \frac{\partial}{\partial x_j} \left[\left(\mu + \frac{\mu_t}{\sigma_k} \right) \frac{\partial k}{\partial x_j} \right] + P_k + P_b - \rho \varepsilon - Y_M + S_k \quad (10)$$

The transport equation for turbulent dissipation ε, that determines the scale of the turbulence, takes the form

$$\frac{\partial}{\partial t}(\rho \varepsilon) + \frac{\partial}{\partial x_i}(\rho \varepsilon u_i) = \frac{\partial}{\partial x_j} \left[\left(\mu + \frac{\mu_t}{\sigma_\varepsilon} \right) \frac{\partial \varepsilon}{\partial x_j} \right] + C_{1\varepsilon} \frac{\varepsilon}{k}(P_k + C_{3\varepsilon} P_b) - C_{2\varepsilon} \rho \frac{\varepsilon^2}{k} + S_\varepsilon \quad (11)$$

where the model constants are assigned the following standard values:

$$C_{1\varepsilon} = 1.44, C_{2\varepsilon} = 1.92, C_{3\varepsilon} = -0.33, C_\mu = 0.09, \sigma_k = 1.0, \sigma_\varepsilon = 1.3$$

Also, a boundary condition is provided for turbulent kinematic viscosity for rough walls, based on turbulence kinetic energy. This condition manipulates a parameter to account for roughness effects. The modified law of the wall that incorporates surface roughness, proposed by Cebecci and Bradshaw [11], based on sand-grain mean roughness height k_s takes the form:

$$u^+ = \frac{1}{K} \ln(y^+) + B - \Delta B(k_s^+) \quad (12)$$

where ΔB is a roughness function of $k_s^+ = {k_s u_\tau}/{\nu}$ based on experimental data, B=5.2, and K is von Karman's constant.

3. Case study

In the Tallinn city areas under interest the functioning of storm-water system during intense rains can yield floods. The aim of CFD simulations herein is to investigate a restricted water flow through the siphon with presence of air and slurry-fluid simultaneously. The geometry of the inverted siphon is constructed using a standard CAD software, and the computational domain is meshed with over 100'000 cells.

3.1. Three-phase flow simulations

To determine flooding conditions, the CFD simulations are performed for five different cases, which correspond to flow rates 500, 1000, 1500, 2000 and 3000 lps. All numerical experiments are conducted under same initial conditions, where the inverted siphon is initially partially filled with slurry-fluid up to a level of 2 meters from the lowest part of the pipe, which is determined appropriate to simulate real conditions of the storm-water system. The overall dynamics of different cases is found to be similar, and therefore the computational results are essentially compared for two cases 1) designed inflow rate: 1000 lps and 2) large inflow rate: 2000 lps, for emptying the initially filled inverted siphon from slurry-fluid. Lasting inflows of water into the partially slurry-fluid filled inverted siphon are simulated until the stationary flow conditions are reached.

The density and viscosity of water is 1000 kg/m^3 and 1.0×10^{-6} m^2/s, respectively, and for air is 1.2 kg/m^3 and 1.5×10^{-5} m^2/s, respectively. According to Engineering ToolBox the density and viscosity of slurry-fluid is 1200 kg/m^3 and 1.0×10^{-6} m^2/s, respectively. Fluids in the numerical modelling are considered incompressible and immiscible.

3.1.1. Design flow rate.
To investigate a restricted water flow patterns, which correspond to designed flow rate, the numerical test is conducted for 1000 lps. As expected, the siphon is self-cleaning at the designed flow rate, and during the simulation no flooding occurs. The numerical solution reveals a steady-state fully filled pipe flow during the iteration period of 300 000 steps. The steady flow through the siphon in the inflow chamber is characterized with the water level 5.7 m from the reference level, which corresponds to the lowest point of the inverted siphon, and the corresponding pressure-head drop is 1.25 m (figure 2). The corresponding Darcy friction factor $\lambda = 0.0551$ and Reynolds number $Re = 1.5915 \times 10^6$.
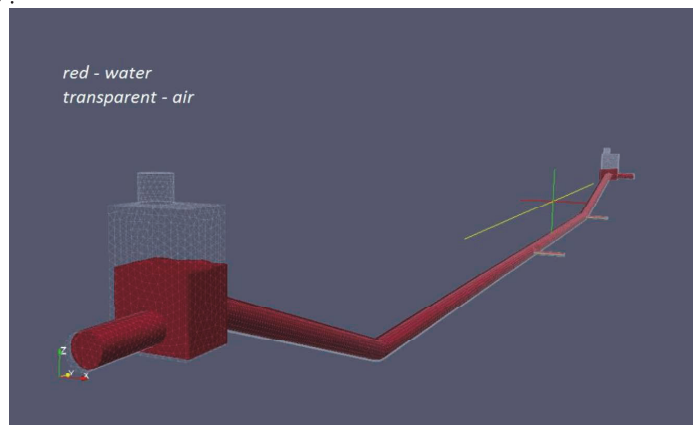
Figure 2. A CFD solution for design flow rate: steady flow stage.

3.1.2. Larger flow rate. The numerical test is conducted for 2000 lps, which correspond to the larger flow rate as compared to the designed flow rate. Now a restricted water flow patterns reveals more complicated dynamics. Initially the three-phase flow develops inside the inverted siphon and also the water outflow occurs from the manhole of concrete chamber. The unsteady two-phase flow for the larger flow rate is temporally associated with presence of flooding. After removal of the slurry-fluid from the inverted siphon i.e. in the final stage, the flow reveals the stationary flow conditions with the increased water level in the inlet concrete chamber, and the increased pressure drop as compared to the numerical test with the designed flow rate.

3.1.2.1   *Unsteady flow stage.* The computational results initially reveal that the unsteady three-phase flow situation causes the increasing pressure-head, which is associated with an ascending water level in the inlet chamber of the inverted siphon. Before the slurry-fluid is expelled out from the inverted siphon, the water level is reaching to the outlet level of the inlet chamber manhole (figure 3). Apparently the increased pressure-gradient due to mixed fluids in the inverted siphon are a cause of this phenomenon. Thus initially, before the slurry-fluid is being flushed out by water inflow, flooding occurs. It can be concluded that during the initial period of unsteady flow, the hydraulic gradient is significantly increased, and until self-cleaning occurs, the pressure in the inlet chamber is large enough to produce flooding.
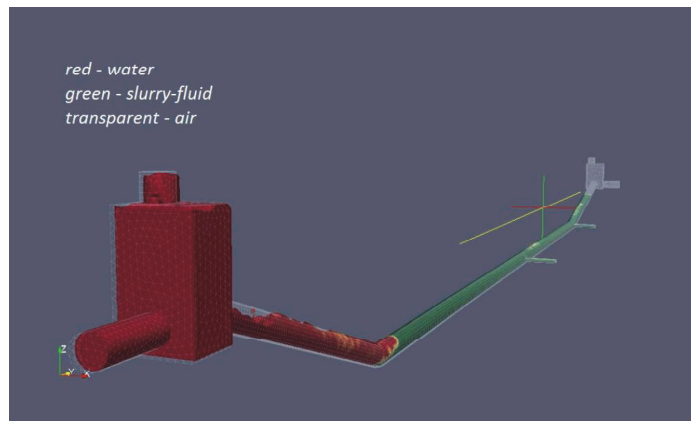
Figure 3. A CFD solution for larger flow rate: unsteady flow stage.

3.1.2.2   *Steady flow stage.* After the initial period of unsteady flow, when the self-cleaning occurs, the computational results reveal that the unsteady flow situation causes the decreasing pressure-head, which is associated with a descending water level in the inlet chamber of siphon. After the slurry-fluid is effectively expelled out from the inverted siphon, the water level is descending below the outlet level of the inlet chamber manhole. The numerical solution reveals a steady-state fully filled pipe flow during the iteration period of 300 000 steps. The steady flow through the siphon in the inflow chamber is characterized with the water level 7.0 m from the reference level, which corresponds to the lowest point of the inverted siphon, and the corresponding pressure-head drop is 2.2 m (figure 4). The corresponding Darcy friction factor $\lambda = 0.0242$ and Reynolds number $Re = 3.1831 \times 10^6$.
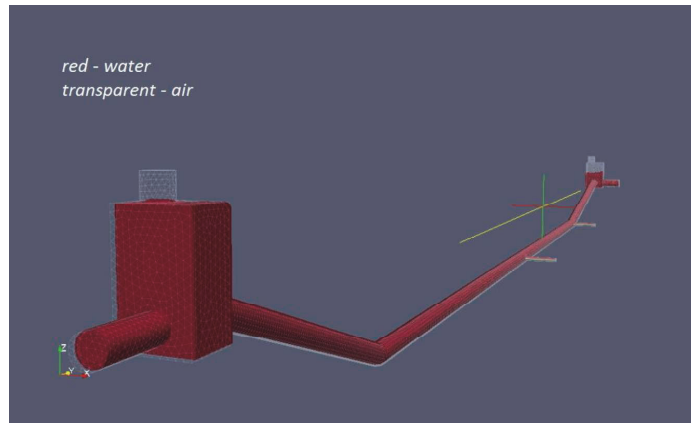
Figure 4. A CFD solution for larger flow rate: steady flow stage.

4. Conclusions and discussion

CFD solutions are used to determine the two- and three-phase flow dynamics in the large-scale inverted siphon, which is part of the storm-water system under road in Tallinn. The initially slurry-fluid filled inverted siphon flushing with water is investigated to find flooding conditions. The computational results demonstrate that no flooding occurs at flow rates smaller than 2000 lps even when the slurry-fluid is present in the system. Flooding does occur at 2000 lps at the inlet chamber in the computational phase where the slurry-fluid is still being flushed out and resides when it is discharged and fully-filled steady state pipe water flow develops.

An interesting result that is not presented above, but definitely merits discussion and further investigation is a simulation result at a small flow rate of 500 lps. In that case free surface flow is observed and a steady hydraulic jump seemingly occurs at the approximate height of 3.8 m with a zero level at the lowest part of siphoned part.

The next step of the investigation will be to use the extensive capabilities of CFD solvers and increase computational accuracy with dynamic meshing. Another step is to experimentally specify turbulence model constants for multi-phase flow. It would be also of interest to conduct experiments for different slurry fluid properties in addition to the here considered fine slurry, that can be modelled as a Newtonian fluid. Uncertainty of hydraulic resistance was estimated to be 0.02 and therefore, the hydraulic verification of the numerical boundary functions need more attention in any future work.

References

[1]   Hou Q, Tijsseling A S, Laanearu J, Annus I, Koppel T, Bergant A, Vučković S, Anderson A and Van 't Westende J M C 2014 Experimental investigation on rapid filling of a large-scale pipeline *ASCE J. Hyd. Eng.* **140** (11), 1−14
[2]   Laanearu J, Annus I, Koppel T, Bergant A, Vučković S, Hou Q, Tijsseling A S, Anderson A and van 't Westende J M C 2012 Emptying of large-scale pipeline by pressurized air *ASCE J. Hyd. Eng.* **138** (12), 1090−100

[3]   Laanearu J, Hou Q and Tijsseling A S 2015 Experimental and analytical modelling study of water-front dynamics of two-phase unsteady flows in a large-scale pressurized pipeline *12th Int. Conf. on Press. Surg., Fluid Trans. and Water Hammer* pp 625−637

[4]   Laanearu J, Hou Q, Annus I and Tijsseling A S 2015 Water-column mass losses during the emptying of a large-scale pipeline by pressurized air *Proc. Estonian Acad. Sci.* **64**(1), 8−16

[5]   Hou Q, Zhang L X, Tijsseling A S and Kruisbrink A C H 2011 Rapid filling of pipelines with SPH particle method *Proc. Eng.* **31**, 38-43

[6]   Nabil T, El-Sawaf I and El-Nahhas K 2014 Sand-water slurry flow modelling in a horizontal pipeline by computational fluid dynamics technique *Int. Water Tech. J.* **4**(1)

[7]   Kaur K, Laanearu J and Annus I 2016 Using CFD to simulate multiphase flow in a large-scale inverted siphon: Tallinn storm-water system case study *14th Int. CCWI Conf.* (Amsterdam: International Water Conferences)

[8]   Adams T, Grant C and Watson H 2012 A Simple Algorithm to Relate Measured Surface Roughness to Equivalent Sand-grain Roughness *Int. J. Mech. Eng. Mech.* **1**(2), 66-71

[9]   Carrica P, Wilson R and Stern F 2006 An unsteady single-phase level set method for viscous free surface flows *Int. J. Num. Meth. in Fluids* **53**(2), 229−56

[10]   Jones W P and Launder B E 1972 The prediction of laminarization with a two-equation model of turbulence *Int J Heat Mass Transf.* **15**(2), 301−14

[11]   Cebeci T and Bradshaw P 1977 *Momentum Transfer in Boundary layers* (New York: Hemisphere Publishing Corporation)

Curriculum vitae

Personal data

Name:	Katrin Kaur
Date of birth:	18.12.1990
Place of birth:	Tallinn
Citizenship:	Estonian

Contact data

E-mail:	katrin.kaur@taltech.ee

Education

2015 – …	Tallinn University of Technology, School of Engineering, environmental and coastal engineering, PhD
2013 – 2015	Tallinn University of Technology, Faculty of Science, Applied Physics, MSc
2009 – 2013	Tallinn University of Technology, Faculty of Science, Engineering Physics, BSc
2006 – 2009	Tallinn Art Grammar School, High school

Language competence

English	Fluent
Estonian	Native

Professional employment

2017 – …	Tallinn University of Technology, School of Engineering, Department of Civil Engineering and Architecture, engineer
2015 – 2016	Tallinn University of Technology, Faculty of Civil Engineering, Department of Mechanics, engineer
2013 – 2015	Tallinn University of Technology, Faculty of Science, Research Laboratory of Multiphase Media Physics, engineer
2013 – 2015	Tallinn Centre of Industrial Education, General Education Department, teacher
2012 – 2013	Konesko Ltd, Department of Wind Turbines, designer

Elulookirjeldus

Isikuandmed

Nimi:	Katrin Kaur
Sünniaeg:	18.12.1990
Sünnikoht:	Tallinn
Kodakondsus:	Eesti

Kontaktandmed

E-post:	katrin.kaur@taltech.ee

Hariduskäik

2015 – …	Tallinna Tehnikaülikool, Inseneriteaduskond, keskkonna ja rannikutehnika, PhD
2013 – 2015	Tallinna Tehnikaülikool, Matemaatika-loodusteaduskond, Rakendusfüüsika, MSc
2009 – 2013	Tallinna Tehnikaülikool, Matemaatika-loodusteaduskond, Tehniline füüsika, BSc
2006 – 2009	Tallinna Kunstigümnaasium, keskharidus

Keelteoskus

Inglise keel	Kõrgtase
Eesti keel	Emakeel

Teenistuskäik

2017 – …	Tallinna Tehnikaülikool, Inseneriteaduskond, Ehituse ja arhitektuuri instituut, insener
2015 – 2016	Tallinna Tehnikaülikool, Ehitusteaduskond, Mehaanikainstituut, insener
2013 – 2015	Tallinna Tehnikaülikool, Matemaatika-loodusteaduskond, Mitmefaasiliste keskkondade füüsika teaduslaboratoorium, insener
2013 – 2015	Tallinna Tööstushariduskeskus, Üldainete osakond, õpetaja
2012 – 2013	AS Konesko, Tuulegeneraatorite osakond, projekteerija